UNIVERSITAT POLITÈCNICA DE CATALUNYA BARCELONATECH

Bedforms and associated sediment dynamics on the inner shelves at different spatio-temporal scales

Queralt Guerrero Sánchez

BEDFORMS AND ASSOCIATED SEDIMENT DYNAMICS ON THE INNER SHELVES AT DIFFERENT SPATIO-TEMPORAL SCALES

PROGRAMA DE DOCTORAT EN CIÈNCIES DEL MAR

Memòria presentada per:

QUERALT GUERRERO SÁNCHEZ

Per optar al grau de Doctora per la Universitat Politècnica de Catalunya

Dirigida per

Dr. Jorge Guillén Aranda

Barcelona, Desembre 2018

The presented Thesis has been funded by the Spanish National Project FORMED (Ref. CGL2012-33989). The author was supported by a FPI grant (Ref. BES-2013-066261) from the Spanish Ministry of Economy and Competitiveness. The two periods abroad, at the National Oceanography Centre (NOC-NERC) of Liverpool (UK) were founded by two fellowships (EEBB-I-15-10201 and EEBB-I-17-11989) related to the FPI grant.

Abstract

This Thesis conducts the study of bedform development and dynamics in the inner shelf integrating observations at different spatial and temporal scales. An initial assumption is that different scales of sedimentary processes strongly interact between them and small-scale sedimentary processes intended to foster those of larger scale. The potential contribution of small-scale bedforms to the sediment transport is particularly addressed. The study includes the monitoring and analysis of sand ridges, ripples and near-bottom suspended sediment variations at the Ebro Delta (NW Mediterranean Sea) and Perranporth (Atlantic Ocean) inner shelves.

A sand ridge field with maximum ridges heights of 2.5 m and 400 m spaced is located over a retreating lobe in the Ebro Delta. Ridges are mostly symmetric arranging obliquely to the shoreline. The change of the main Ebro River channel led to the progressive abandonment of the former river mouth and to the severe coastal retreatment, providing large amount of sediment available in the coastal zone. In addition, NW winds induce strong near-bottom currents flowing towards the SE, which are able to transport sediment and produce ridge formation and migration towards the SE at ~10 m/y. The characteristics of the Ebro sand ridges match well with those of shoreface-connected sand ridges and, particularly, with the initial stages of sand ridge development on storm-dominated continental shelves. Time-scales related to their genesis can be within a few decades.

The study reveals that the presence of ripples on the inner shelf is the most usual situation under low- to moderate-energetic conditions in different shelves. In the wave-dominated and tideless coast of the Ebro Delta ripples were observed superimposed on sand ridges. Four types were identified: small undulations that were the precursor of larger ripples, 2D wave-ripples, current-dominated 2D-3D-ripples, and combined wave-current 3D-ripples. The wave-ripples were static while the current-dominated ripples migrated at ~10 cm/h. In a macro-tidal sandy beach exposed to high-energetic Atlantic storms (Perranporth), only wave-ripples were developed arranging orthogonal to wave approach and they were static. The size of ripples changed from larger (developed in equilibrium conditions) to smaller ripples, the latter interpreted as degraded ripples in wash-out conditions. In general, ripple prediction did not well-adjust to neither ripple appearance nor dimension. However, if the observed thresholds of seabed states are applied the model improves ripple appearance forecast.

The near-bottom suspended sediment variability from seconds to months in the Ebro Delta is described distinguishing between waves, currents, and combined wave-currents conditions. In general, waves dominated the sediment resuspensions although strong currents also have an important contribution in the suspended sediment concentration (SSC) increases. The time-

averaged SSC usually showed redundant structure by forming three layers with different patterns. In the lower and intermediate layers the SSC oscillated at gravity and infragravity wave frequencies. Time-varying and instantaneous profiles exhibit sediment patterns potentially related to ripples presence.

The potential role of ripple migration as an additional long-term mechanism of sediment transport was analysed. In Perranporth, wave ripples are stationary and did not contribute to beach recovery because of wave orbital symmetry. The sediment transport is alongshore during low-energetic regimes and cross-shore during more energetic regimes when ripples are washed-out. In the Ebro Delta, 3D-ripples migration agrees with sand ridges migration direction towards the SE. The respective migration rates and their differences in size, support that a subordinate part of sand ridge migration can be the result of ripple migration contribution under low-, moderate-regimes. This suggests that in specific environments, dynamics of small-scale bedforms can play a subordinate but not negligible role in the evolution of larger bedforms.

Resum

La Tesi estudia el desenvolupament i dinàmica de les formes de fons a la plataforma continental somera mitjançant la integració d'observacions a diferents escales espacials i temporals. Es parteix de la hipòtesi en què els processos sedimentaris a diferents escales estan relacionats i que els de petita escala fomenten als majors, fent especial èmfasi a la contribució de les formes de fons petites al transport de sediments. L'estudi inclou la monitorització i anàlisi de *sand ridges*, *ripples* i de les variacions de concentració de sediment en suspensió (CSS) prop del fons a la zona somera de les plataformes continentals del Delta de l'Ebre (NO Mar Mediterrània) i a Perranporth (oceà Atlàntic).

Un camp de *sand ridges* amb crestes de fins 2.5 m d'alçada i 400 m espaiades es troba en un antic lòbul al Delta de l'Ebre. Les crestes són simètriques i obliqües respecte a la línia de costa. El canvi del canal principal del riu va suscitar l'abandonament progressiu de l'antiga desembocadura amb el retrocés sever de la línia de costa, proporcionant gran quantitat de sediments per formar els *sand ridges* que actualment migren ~10 m/any. Les característiques dels *sand ridges* de l'Ebre son anàlogues a les de *sand ridges* connectats a la costa i especialment a les seves etapes inicials a plataformes continentals dominades per tempestes. Les escales temporals relacionades amb la seva formació poden comprendre dècades.

Les petites formes de fons observades inclouen: *ripples* superposats als *sand ridges* a la costa amb marees ínfimes dominada per tempestes de l'Ebre i *ripples* a la costa macro-mareal esposada a tempestes atlàntiques de Perranporth. Ambdues àrees, la presència de *ripples* és la situació habitual en condicions de baixa i mitja energia. A l'Ebre, es van diferenciar quatre morfologies: petites ondulacions precursores de 2D-*ripples* d'onatge, 2D-3D-*ripples* de corrents i 3D-*ripples* de la combinació d'onatge i corrents. Els *ripples* d'onatge eren estàtics mentre que els dominats per corrents migraven ~10 cm/h. A Perranporth, es van observar dues mides de *ripples* d'onatge amb crestes perpendiculars a la direcció de l'onatge i també estàtics. Els *ripples* més petits s'interpreten com la degradació dels grans. El model de predicció de *ripples* no s'ajusta ni per la seva formació ni dimensions. Tanmateix, quan els llindars d'estat de fons observats s'apliquen, el model millora el seu pronòstic.

Les CSS prop del fons al Delta de l'Ebre es distingeix entre condicions d'onatge, corrents i la combinació d'onatge i corrents. En general, l'onatge domina la resuspensió de sediments tot i que els corrents també hi contribueixen de forma important. Les estimacions d'estrès total de cisallament és un bon indicador de pics de CSS i assenyala llindars d'inici de resuspensió de sediments. Les CSS van oscil·lar entre freqüències d'onatge gravitacional i infragravitacional. Les mitjanes dels perfils de CSS mostren una estructura vertical de tres capes mentre que els

perfils instantanis mostren patrons en els CSS potencialment relacionats amb la presència de *ripples*.

La migració de *ripples* en direcció a la costa com a mecanisme addicional a la recuperació de la platja a llarg termini a Perranporth va ser descartat degut a la estacionalitat del *ripples* i a la simetria de les velocitats orbitals de l'onatge. El transport de sediment és paral·lel a la costa durant condicions de baixa energia i perpendicular en condicions d'alta energia quan els *ripples* són erosionats. A l'Ebre, els *sand ridges* i de *ripples* migren cap a la mateixa direcció (SE). La relació entre velocitat de migració i dimensions entre les dues morfologies refermen que una part subordinada de la migració dels *sand ridges* podria ser conseqüència de la migració de *ripples* durant períodes de baixa i mitja energia. Llavors, en entorns específics, la dinàmica de les formes de fons petites podrien tenir un paper subordinat, però no menyspreable, en l'evolució de les formes més grans.

Contents

Chapter I. Introduction

1. The study of bedforms

Bedforms are depositional morphologies formed by the interaction between a fluid and a mobile sediment bottom. They are composed of gravel, sand or mud of siliciclastic or carbonate sediment. The variability in the geometry and the spatial and temporal scale of bedforms is striking ranging five orders of magnitude in spacing, from a few centimetres to over 1 km; from centimetres to tens of meters in height; and time scales ranges from seconds to decades and centuries.

The first studies of bedforms were undertaken in the field of aeolian and river geomorphology and subsequently expanded to the coastal area, the deep ocean and the marine environment in general. The onset of continental shelf morphology studies, sediment distribution patterns and material composition started in the 1950s (e.g. Shepard, 1948). The knowledge and understanding of the morphological observations and the processes involved in sediment dynamics was progressively improved accompanied by an important advance in new instrumentation and technology designed to seafloor observations, hydrodynamic and sediment dynamics measurements such as: the incorporation of the high-resolution seafloor mapping by multibeam echosounder, bathymetric Laser-LIght Detection and Ranging (LIDAR), side scan sonar, Remote Operating Vehicles (ROVs), Autonomous Underwater Vehicles (AUVs); the improvement in the resolution of observations of the internal structure of the continental shelf with seismic sub-bottom profiling technics; improving hydrodynamic measurements with high-frequency correntimeters such as Acoustic Doppler Velocimeters (ADV) or Acoustic Doppler Correntimeter Profiler (ADCP); refining the technics and resolutions of suspended sediment concentrations measurements with Optical Backscatter Systems (OBS), Laser In Situ Scattering and Transmissometry (LISST) and Acoustic Backscatter Systems (ABS) and a long etcetera. These innovative technology has allowed to advance in the knowledge on fluid dynamics of a range of bedforms (Bridge & Best 1988; Nelson and Smith, 1989; Wiberg and Nelson, 1992; McLean et al., 1994), the quantification of bedform dimensions in relation to flow forcing (Baas, 1993, 1994; van Rijn 1993), the integration of bedform into stability diagrams (Southard & Boguchwal 1990; van den Berg and van Gelder, 1993), the relationships between cross-strata

thickness and bedform size (Best & Bridge 1992; Storms et al. 1999), and the morphodynamics of bedforms generated under combined flows (Li et al., 1996).

When the flow intensity exceeds a threshold value generally known as the critical condition for initiation of sediment motion, sediment grains start to move instantaneously. It is function of the amount exceeded that the plane bottom will no longer remain plane becoming unstable, deforming and developing bedforms. Numerous scientists have investigated bed defects and the first expression of bedform development on a flat sediment bed, and their relation to coherent structures in the near-bed flow (e.g. Allen 1968, Kennedy 1969; Dingler and Inman, 1976; Southard, 1991; Venditti et al., 2005; Perillo et al., 2014). Accordingly, the principal physical parameters that control bedforms development include flow velocity and depth, fluid density and viscosity, particle size and density, sediment supply, and bed roughness. The main groups of mechanisms able to generate or maintain bedforms in different marine environments include: (i) waves, tides and wind-induced currents (e.g. Swift et al., 1978; Kleinhans et al., 2004; Li and King, 2007) (ii) thermohaline oceanic currents, contour currents and other specific bottom currents (e.g. Wynn and Stow, 2002a; Masson et al., 2004;); (iii) density flows and turbidity currents (e.g. Trincardi and Normark, 1988; Lee et al., 2002); and (iv) internal waves (e.g. Puig et al., 2007; Ribó et al., 2016). Particularly, in shallow waters of the continental shelf, the trigger mechanisms for bedform development are restricted to the oscillatory movement generated by waves and currents induced by tides, winds or asymmetrical waves (storms and wind-driven currents). Additionally, the complex interactions between the parameters that control bedforms development can also create morphological feedbacks and lead to patterns assumed as self-organized (Coco and Murray, 2007; Coco, 2017). However, despite the progress achieved on sediment dynamics to date, the potential trigger mechanisms responsible to generate bedforms and the associated sediment transport processes is still incomplete and therefore the models limited (Davies and Thorne, 2008) because of the wide variability of these features and sedimentary environments.

Large and small scale bedforms play an important role on bottom boundary layer processes through the interaction between hydrodynamics, seabed sediment particles and sediment transport. The bedload sediment transport is normally attributed to bedforms transport by the growth, morphological change, dynamism and migration of these features. Therefore, bedforms migration rates provide valuable information on the local and regional hydrodynamic patterns and sediment transport. In addition, it has been demonstrated that the bedforms (small and large) roughness increases the amount of the suspended sediment (Naqshband et al., 2014) and modifies the pattern and dynamics of the suspended sediment e.g. vortex shedding entrainment (O'Hara Murray et al., 2012).

The study of bedforms is therefore important for the advance in knowledge of bottom boundary layer processes, such as sediment transport and seabed roughness changes. Moreover, bedforms can be used to interpret the geological record and infer the past hydrodynamics processes. Bedforms can also host specific habitats; offer exploitable mineral resources; provide sand deposits for beach nourishment; or analogues of possible reservoir rock. Finally, the dynamism of bedforms may have impacts and even damages on coastal and offshore structures such as harbours, estuaries and offshore wind farms. Therefore, the understanding of the distribution and mobility of sediment and bedforms can be important for the sustainable development and integrated management of some marine environments.

2. Bedforms classification

There is a comprehensive amount of bedforms with large diversity on sizes, geometries and sedimentological characteristics which has encouraged various attempts in classifications based on morphological, sedimentological or genetic criteria, albeit a generic classification that covers all this notable variety is still missing. Large-scale bedforms are ubiquitous in modern sandy environments where water depths are greater than 1 m, sediment sizes are coarser than ~0.15 mm (very fine sand), and mean current velocities are greater than ~0.4 m/s (Ashley, 1990). A large amount of terms describing bedforms are used. In shallow water, usual observed bedforms include ripples, megaripples, dunes, shoreface-connected sand ridges and nearshore bar systems (McBride and Moslow, 1991; Masselink et al., 2006; Bell and Thorne, 2007; Miles et al., 2014). On the continental shelf, shoreface-detached sand ridges, sorted bedforms, sand banks, sand waves, sand ridges, dunes and ribbons have been described (Dyer and Huntley, 1999; Goff et al., 1999; Murray and Thieler, 2004; Barrie et al., 2009; Durán et al., 2013). Finally, the most common bedforms observed in the outer shelf, slope and deep areas are large-scale sediment waves, large scale dunes and cyclic steps (Wynn and Stow, 2002b; Wynn and Masson, 2008; Cartigny et al., 2011; Ribó et al., 2016). Focusing in shallow marine environments, the most commonly used classification is that of Ashley (1990) that proposes *dunes* as the name for large-scale flow-transverse bedforms (Table I). The classification is based on bedform spacing using the term *subaqueous* when it is important to distinguish them from the aeolian dunes (Table I). First order descriptors of shape (e.g. 2D or 3D, Fig. 1) and second order descriptors such as sediment size and bedforms superposition were recommended to use to complete the description more thoroughly (Table I). When flow-transverse bedforms spacing are less than 0.6 m then the bedforms are named ripples (Yalin 1964; Allen 1968). Despite subaqueous dunes are the general term suggested by Ashley (1990) for sandy dynamic, flow-transverse bedforms on shallow waters, megarriples or sand waves are also used to describe the same type of bedforms, the latter usually related to tidal currents (Allen, 1980).

Table I. Classification scheme recommended by the SEPM Bedforms and Bedding Structures Research Symposium (Ashley, 1990).

Subaqueous Dune					
First Order Descriptors (necessary)					
Size	Spacing	small 0.6-5 m	medium 5-10 m	large 10-100 m	very large > 100 m
	Height*	0.075-0.4 m	0.4-0.75 m	0.75-5 m	> 5 m
Shape	2-Dimesional				
	3-Dimensional				
Second Order Descriptors (Important)					
- Superposition: simple or compound (sizes and relative orientation) - Sediment characteristics (size, sorting)					
Third Order Descriptors (useful)					
- Bedform profile (stoss and lee slope lengths and angles) - Fullbeddedness (fraction of bed covered by bedforms) - Flow structure (time-velocity characteristics) - Relative strengths of opposing flows - Dune behaviour-migration history (vertical and horizontal accretion)					

*Height calculated using the equation $H = 0.0677L^{0.8098}$ (Flemming 1988)

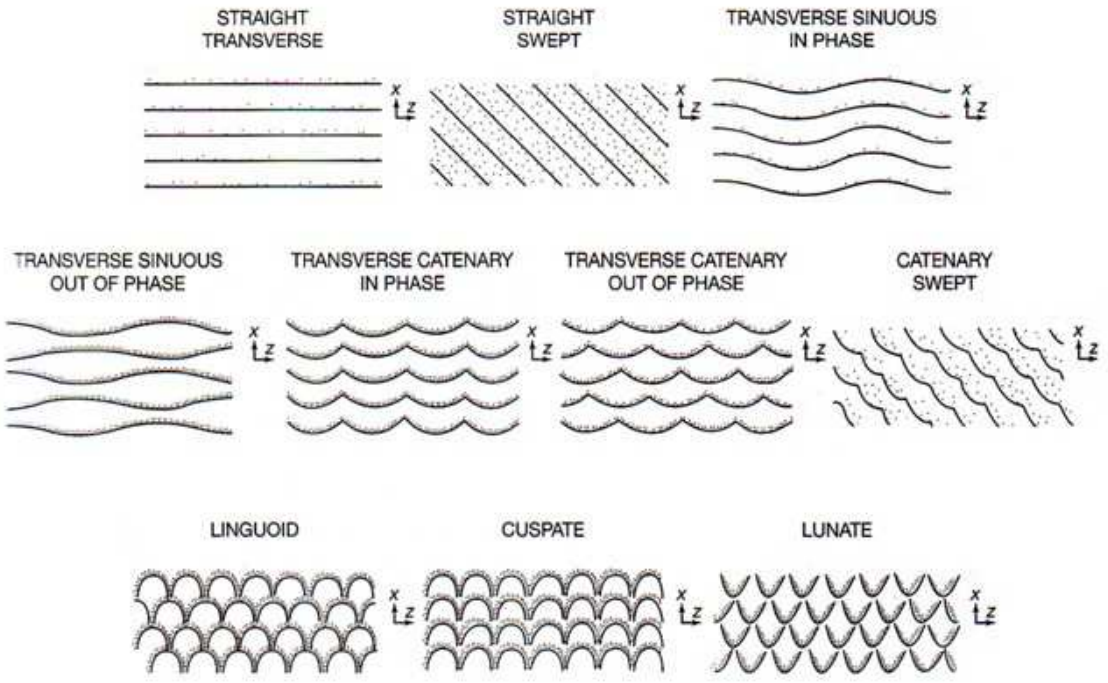

Fig. 1. Idealized classification of current ripples and dunes on the basis of plan-view shape. Flow is from the bottom to the top in each case (Allen, 1968).

Other classifications for continental shelf bedforms are based on *bed phase* states diagrams (Baas et al., 2016). These diagrams define a sequence of equilibrium bedforms states as the flow velocity increases for a given sediment-size, based on data collected in laboratory flumes and field conditions (Rubin and McCulloch, 1980). The bedform states defined from less to more

flow energy typically comprise: lower-stage plane bed, ripples, dunes, upper-stage plane bed, and antidunes (Fig. 2). Ripples and dunes are replaced by upper-stage plane bed conditions via a transitional phase of wash-out (van Rijn 1993; Camenen and Larson, 2006). Bed phase diagrams have been defined in function of three principal types of flow: (i) unidirectional currents, using dimensional (e.g. Southard & Boguchwal, 1990) (Fig. 2 a) and non- dimensional parameters (e.g. van den Berg & van Gelder, 1993) (Fig. 2 b); (ii) short-period oscillatory flows, which generate wave-ripples, hummocks and upper-stage plane beds (e.g. Kleinhans, 2005) (Fig. 2 c); and (iii) combined flows, in which unidirectional and oscillatory currents work together to reshape the seabed (Fig. 2 d).

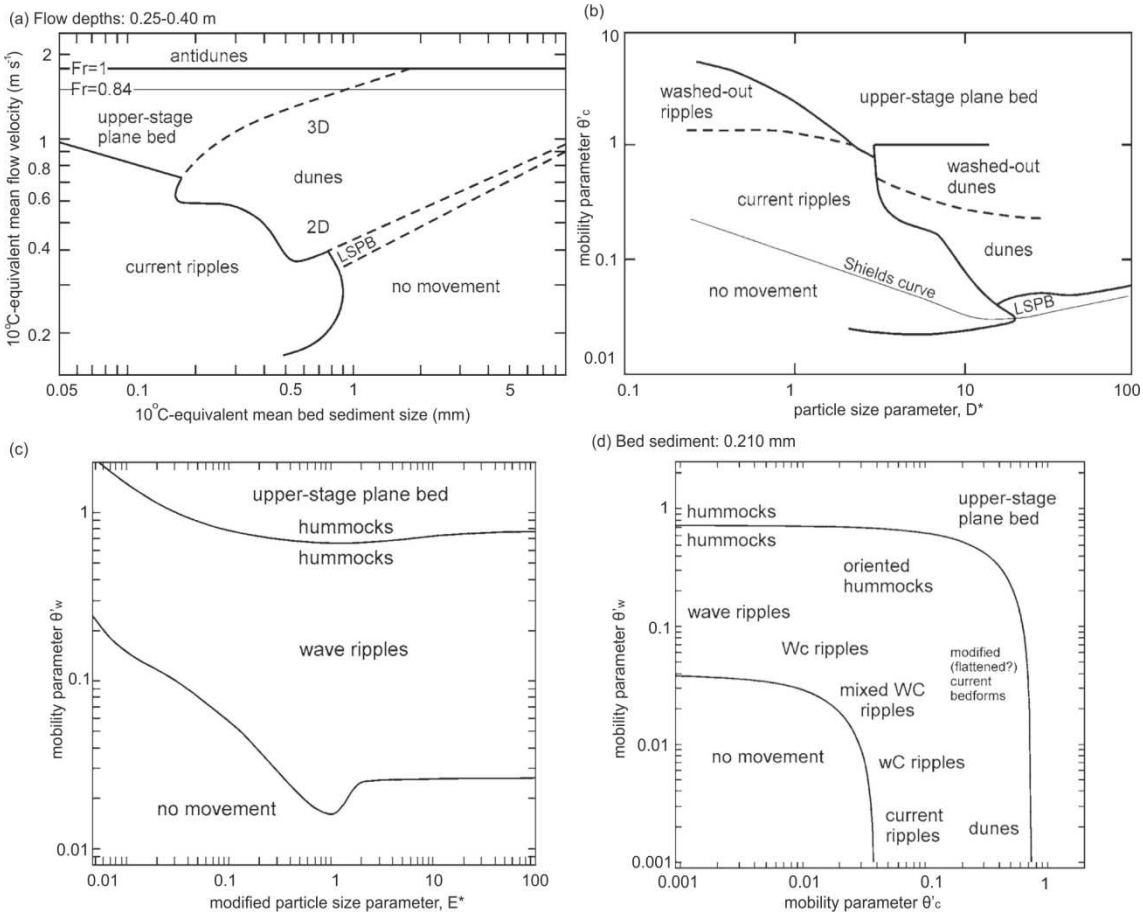

Fig. 2. Bedforms phase diagrams for: (a) current-generated bedforms, 2D section of the bedform phase diagram of Southard & Boguchwal (1990), showing 10°C-equivalent mean bed sediment sizes against 10°C-equivalent mean flow velocity between 0.25 and 0.4 m flow depths; (b) current-generated ripples of van den Berg & van Gelder (1993); (c) wave-generated bedforms of Kleinhans (2005) $E^* = 0.04789D^*$; (d) bedforms generated by combined waves and currents of Kleinhans (2005) for sand sizes between 90 and 250 μm. LSPB, lower-stage plane bed; Fr, Froude number; and WC, Wc and wC, waves and current of similar strength, wave-dominated and current-dominated, respectively. Dashed and continuous lines denote gradual and abrupt boundaries, respectively. Modified after Southard & Boguchwal (1990), van den Berg & van Gelder (1993), and Kleinhans (2005).

3. Ripples and sand ridges on the inner shelf

This study is focused on ripples and sand ridge characterisation and dynamics, which correspond to small and large subaqueous dunes in the Ashley (1990) classification. Small-scale bedforms (ripples) are the most common and the smallest-scale transverse bedform type on the seabed surface, which represents low-velocity flow conditions (Kennedy, 1969). It is the first flow-transverse bedform to develop for sediment sizes finer than coarse sand. The maximum height and wavelength of current ripples are 0.06 and 0.6 m, respectively (Ashley 1990), although most current ripples are less than 0.03 m high and 0.3 m wide (Baas et al., 2016). Ripples can be asymmetric or symmetric features with their down-current surfaces slopes usually at or near the angle of repose of the sediment (Kennedy, 1969), and their up-current slopes usually gentler (Southard, 1991). They are generated by wave-, current- or wave- current-induced flows (Flemming, 1980; Baas et al., 2016) and can be dynamic bedforms migrating usually down-stream (Traykovski et al., 1999; Crawford and Hay, 2001). Ripples are generally classified as straight-crested (2D-ripples), or no-straight-crested (3D-ripples) (Fig. 1) based on their crest alignment; and as very small ($\eta \sim 1$ cm), small ($\eta < 10$ cm), medium ($\eta > 10$ cm) and large or megaripples ($\eta > 1$ m) based on their height (η). Note that, large ripples or megaripples can be also called “small dunes” in Ashley (1990) classification (Table I).

Sand ridges are large scale bedforms widespread on many continental shelves world-wide. They are also referred as large or very large subaqueous dunes when they are active bedforms (Ashley, 1990). Sand ridges have elevations ranging from 1-30 m, widths from 700-8000 m and can be up to 60 km long (Amos and King, 1984). They show linear, elongated shape and predominantly asymmetric transverse profile, with steeper down-current flanks (Amos and King, 1984; Bassetti et al., 2006; Li and King, 2007). They have lineal to sinuous crest line in plan view and are oblique (or parallel) to the current flow. Exist two generic sand ridges types: “tidal-current ridges” (Dyer and Huntley, 1999; Liu et al., 2007), which are formed by strong, prevailing tidal currents, such as those in the North Sea; and storm-generated ridges implying an intermittent process of development usually associated with storm wave activity and storm/wind driven currents such as those in the Mid-Atlantic Bright (Goff, 2009; Swift et al., 1978). When sand ridges are located from the foot of the shoreface to the inner part of continental shelves (depths lower than ~20 m) they are defined as shoreface-connected (or attached) sand ridges (SFCRs); otherwise they are defined as shoreface-detached sand ridges (SFDRs). The presence of superimposed bedforms over sand ridges is frequently used as an indicator of active bedforms.

The inner shelf sediment transport, the associated morphological changes and the modifications induced by ripples and sand ridges in the bottom boundary layer can be examined at very

different time-scales, from the instantaneous motion of single grains (seconds) to seasonal and longer term movement of large sand bodies (Larson and C. Kraus, 1995). The spatio-temporal scales of bedform and the sediment transport are closely related. For example, the sediment transport rate over wave-ripples is estimated as the net result of the oscillatory motion (Traykovski et al., 1999; Hurther and Thorne, 2011) while the mesoscale sediment transport should be estimated from longer periods including seasonal, decadal and secular trends in presence of large scale bedforms (dunes, sand ridges) (e.g. Larson and C. Kraus, 1995; Masselink et al., 2006; Snedden et al., 2011; Nnafie et al., 2014; Miles and Thorpe, 2015; Scott et al., 2016).

Small-scale bedforms are usually observed superimposed on larger bedforms, typically dunes (Knaapen et al., 2005; Barnard et al., 2011). Because of the volume of sediment stored in them, the larger bedforms are relatively stable on time scales of months or years, whereas the smaller, ubiquitous, superimposed bedforms are more dynamic, sometimes even ephemeral, responding to minutes, daily and/or spring-neap tide fluctuations (Venditti et al., 2005; Reesink and Bridge, 2007; Barnard et al., 2011; Naqshband et al., 2014). In spite of these differences, when small bedforms are superimposed to a larger one, it is envisaged a close relation between both.

4. Aims and objectives

The scope of the Thesis deals about the study of contemporary sediment dynamic processes on the inner shelf at different temporal and spatial scales in presence of bedforms, based on field observations. To achieve this goal, a large amount of data, a wide variety of observational methods and techniques have been used and integrated.

In shallow environments dominated by the combined action of waves and currents, the presence of ripples (the smallest categorized bedform) is recurrent and frequently superimposed on larger scale bedforms. However, ripple contribution to the sediment transport on the inner shelf is poorly understood. It is commonly assumed that large-scale sediment transport can be attributed, at least partially, to the sum of the small-scale sediment processes. Therefore, delve into the detailed knowledge of small-scale processes is essential to interpret the larger-scale ones because small and large scale sediment dynamics are somehow connected. This Thesis evaluates these sediment processes interactions in time-scales from seconds to decades and spatial-scales from centimetres to kilometres. Field observations from two study sites are used, the Ebro and Perranporth inner shelves located at the NW Mediterranean and SW of England respectively, providing examples of two distinct environments. The study of the initial stages of shoreface-connected sand ridges formation attempts to improve our understanding of the timing and processes involved in shoreface-detached sand ridges development, particularly for the middle and outer shelf of the Mediterranean Sea. Moreover, the study of the morphology and

dynamics of ripples can provide new insights on the contribution of small-scale bedforms to the migration rates of larger bedforms and to the sediment exchanges between the inner shelf and the nearshore.

The main specific research questions involved are:

- ✓ What is the temporal scale for the development of shoreface connected sand ridges? Which are the particular conditions required for their formation and potential preservation?
- ✓ What is the morphological expression and variability of ripples on the inner shelf under waves, currents and wave-currents conditions? Are they morphologically and/or dynamically different between tideless and macro-tidal environments?
- ✓ Does simple model of ripple prediction satisfactory agree with observations?
- ✓ What are the main mechanisms responsible of the near-bottom suspended sediment variability over flat and rippled bed?
- ✓ What is the contribution (if any) of ripple dynamics to the migration of sand ridges?
- ✓ What is the contribution (if any) of ripple dynamics in the onshore sediment transport from the inner shelf to the nearshore as a potential mechanism of beach recovery?

5. Outline of the Thesis

This Thesis is divided into the following chapters:

In ***Chapter II***, the two study areas are described focussing on the geological and oceanographic settings.

Chapter III describes and explains the methodology followed to conduct the research of this Thesis.

The purpose of ***Chapter IV*** is to analyse the contemporary formation of a sand ridge field on the shoreface of a tideless erosional deltaic system: the Ebro Delta. It is characterised the morphodynamics, geological setting and timing of development of the sand ridges, and the processes associated with the onset of the field. Finally, the potential analogies with SFCRs and SFDRs on storm-dominated shelves are discussed.

In ***Chapter V***, the dynamics of ripples superimposed on the sand ridges in the Ebro Delta shoreface are studied. The development and dynamism of ripples under waves and/or currents and the feasibility of ripple migration as a potential contributor to the sand ridges migration are analysed. The reliability on using ripple predictors and sediment transport estimations is also discussed.

In ***Chapter VI***, the ripple occurrence and dynamics at the macro-tidal site of Perranporth is analysed. The feasibility of ripple migration as a potential contributor to onshore sediment transport and beach recovery is evaluated. Finally, the reliability on using ripple predictors and sediment transport is also discussed.

In ***Chapter VII***, the near-bottom SSC variability under low- to moderate- energetic hydrodynamic conditions induced by waves, currents and combined wave-currents in the Ebro Delta inner shelf is examined. The main mechanisms controlling SSC variability are discussed as well as the potential role of sediment transport processes using simultaneous measurements of SSC, waves and currents, wind field, suspended particle grain size and ripple observations.

Chapter VIII, the conclusions and future research lines are proposed.

Chapter II. Study areas

Large-scale bedforms (sand ridges) and near-bottom suspended sediment variability studies were based on observations collected in the Ebro Delta inner shelf while small-scale bedforms (ripples) development and dynamics were founded on field observations acquired at two sites: the Ebro Delta and Perranporth inner shelves, representing distinct morphologic and hydrodynamic environments.

1. Ebro Delta

The Ebro Delta is the third largest delta of the Mediterranean Sea (Fig. 3 a), with an emerged area of 325 km^2. The submerged Ebro Delta (prodelta) covers an area of ~2300 km^2 of the continental shelf and extends alongshelf up to 110 km southwards from the present river mouth (Díaz et al., 1996).

The Ebro Delta is located in a micro-tidal, wave-dominated coast with a maximum astronomical tidal rage of 0.25 m. As the tidal currents are negligible with very weak intensities and only detectable in absence of waves and winds, the Mediterranean Sea is frequently considered as a tideless sea (King and Williams, 1949). However, meteorological tides (storm surges) play an important role as they cause increases in sea level of up to ~1 m (Bolaños et al., 2009). This area is characterised by persistent strong, dry and usually cold winds that blow from the NW (Mistral wind) through the Ebro valley (offshore wind) during autumn and winter. The Mistral wind influenced by the orography, is channelized into a limited band, forming a seaward wind jet usually developed in a ~50 km wide band offshore (Grifoll et al., 2016). The NW winds have a clear seasonal pattern with the most intense and persistent winds during winter and autumn. However, during spring and summer, offshore winds can also flow with high- intensities (Cerralbo et al., 2015; Grifoll et al., 2016). The NW wind regime results on relatively small waves because the short fetch (< 50 km) along the Ebro coast. On the other hand, the most intense swell-dominated storms come from the eastern sectors (E or ENE) where stronger winds coincide with a maximum fetch of approximately 700 km (Bolaños-Sanchez et al., 2007; Sánchez-Arcilla et al., 2008). These storms have an average duration of less than 24 h, and typically occur more than 10 times per year, basically concentrating in the periods of October-

December and March-April (Sánchez-Arcilla et al., 2008). These eastern wave storms have an annual return period significant wave height (H_s) of 3.5 m (Bolaños et al., 2009).

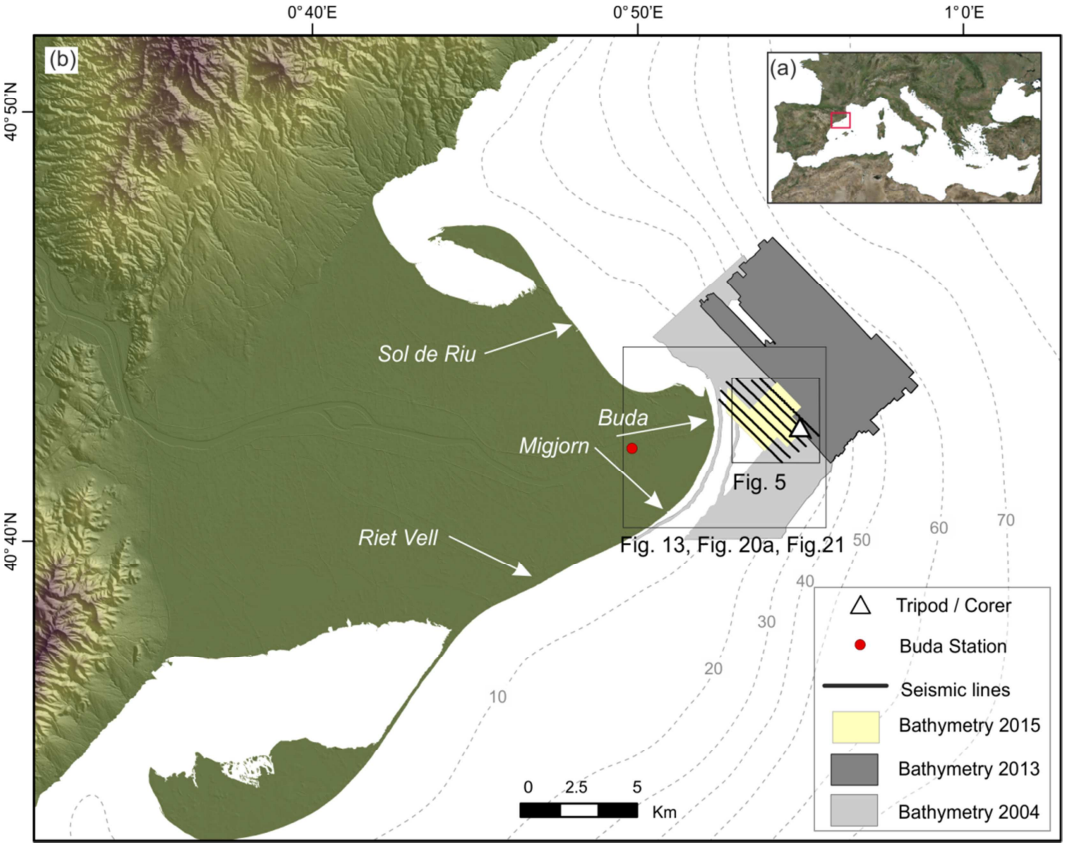

Fig. 3. (a) Ebro Delta location. (b) Subaerial Ebro Delta shaded-relief and bathymetric contours offshore with location of swath-mapped areas during the three cruises. Location of tripod, sediment sample, Buda Island meteorological station and high-resolution sub-bottom profiles. The location of the former Ebro Delta lobes and channels (white arrows) is also shown. Location of the view for Fig. 5, Fig. 13, Fig. 20 a, Fig. 21.

Morphodynamics in the Ebro delta nearshore are dominated by the easterly waves that generate net alongshore currents directed towards the NW and SW at the north and south of Cape Tortosa respectively (Jiménez and Sánchez-Arcilla, 1993). The nearshore along most of the coast is characterized by a morphodynamic beach state of "longshore bar and trough" with the presence of 1-2 dynamics bar systems in the profile (Guillén and Palanques, 1993). Small-scale bedforms (1 cm high and 8-14 cm spaced) also appear during fair-weather conditions at ~10 m depth on the shoreface of the Ebro Delta with their further vanishment because of seabed bioturbation (Guillén et al., 2008). Based on single-beam bathymetric profiles, Guillén and Palanques (1997 b) identified a number of bars (interpreted as relict nearshore bars) on the shoreface of the eroded Cape Tortosa mouth. They showed that the sediment size over these bars was more or less uniform and composed by fine sands with grain size slightly decreasing

towards deeper areas of the lobe (250 to 125 µm). Furthermore, they also indicated that mud sediments outcrop along the troughs of the bars (figure 4 P-24 in Guillén and Palanques,1997 b). Later, Urgeles et al. (2011) described the morphology of a subaqueous dune field based on a multibeam bathymetric survey that located the dune field from 7 to 15 m water depth (area of 3.7 km^2). The dunes made of sandy sediment were 0.2 to 2 m high, spaced 145 to 320 m apart and 480 to 1300 m long. They were reported to be asymmetric and arranged perpendicular to the bathymetric contours. In view of the crest alignment with respect to the shoreline of the Ebro River mouth, Urgeles et al. (2011) suggested that longshore currents generated by wind storms were the main mechanism responsible for development of the dune field.

2. Perranporth

The study area is located at the SW of England, off the Perranporth town (Fig. 4 a). This Atlantic coastal region typically consists on hard rock cliffs and embayed sandy beaches exposed to macro- to mega-tidal ranges (mean spring tide range (MSR) from 4 to 12 m) and medium- to high-energy waves (Scott et al., 2016). Located on the west coast of Cornwall (north Cornish coast), Perranporth beach is a macro-tidal, sandy beach with a semi-diurnal tidal regime and mean neap and spring tidal range of 3.1 m and 6.1 m, respectively (Austin et al., 2010; Inch et al., 2017). The beach is 3.5 km long and has an intertidal area ~200-300 m wide which widens at the southern end to ~400 m close to the Perranporth town location (Fig. 4 b). The beach is backed by an eroding sand dune system and Devonian hard rock cliffs at the north and south extremes of the beach, the steep vegetated dunes field reach nearly a mile inland (Fig. 4 b) (Poate et al., 2014; Scott et al., 2016).

Perranporth is straight beach facing the W-NW towards the Atlantic so it is fully exposed to the dominant westerly waves approach, receiving both Atlantic swell and locally generated wind waves (Austin et al., 2010; Inch et al., 2017). The mean annual significant wave height (H_s) and mean peak period (T_p), measured with the nearshore Perranporth buoy during the period 2006-2015, were 1.6 m and of 10.5 s, respectively, and significant wave height with an annual return period of 7 m (data from the Channel Coastal Observatory online 2016 report, www.channelcoast.org). Dominant wave directions come from the W formed during the passage of Atlantic low pressure systems; however there is also a small, but significant, amount of energy from northerly waves which often occur following sustained high pressures and northerly winds (Poate et al., 2014). The wave climate has a marked seasonality, with wave height and wave periods increasing during winter months, e.g. the monthly averaged H_s and T_p values from the nearshore wave buoy of Perranporth (representing the same as previous 9-year record from 2006 to 2015) range from 1.19 m and 8.5 s in July to 2.26 m and 12.5 s in January (www.channelcoast.org). The shoreline location also shows high variability as a consequence of

this weather seasonality (Davidson et al., 2017). From November to February shoreline retreat occur in response to a succession of erosive storms, while beach recovery begins in late March, at slower rate (~1/4) than the retreat, often persisting until October (Davidson et al., 2017).

The modal morphodynamic classification of Perranporth beach is low-tide bar and rip with typically single-double subtidal bars located around the seaward limit on the surf zone, however, winter periods are often typified by highly dissipative beach states (Austin et al., 2010; Poate et al., 2014; Scott et al., 2016; Davidson et al., 2017). The wide and highly dissipative beach has a low tide beach gradient of $\tan\beta = 0.012$ being the intertidal beach relatively flat ($\tan\beta = 0.015$-0.025), with concave-shaped profile. The sediment is composed of medium quartz sand ($d_{50} = 0.35$ mm) with a relatively high carbonate content (~50%) which suggests the influence of the offshore sediment sources (Austin et al., 2010; Poate et al., 2014; Inch et al., 2017). Perranporth beach is relatively featureless throughout the upper intertidal region and homogeneous alongshore, but the well-developed bar system interspaced with rip channels is exposed at spring low water combined with a linear to crescentic subtidal system (Austin et al., 2010, 2013; Poate et al., 2014; Inch et al., 2017).

Research on surf zone currents at Perranporth has been well established through a number of field deployments (Austin et al., 2009, 2010, 2014, 2013; Scott et al., 2014; Pitman et al., 2016). The beach system is dominated by cross-shore surf zone driven sediment transport and shore-normal waves (Scott et al., 2016). The flow of rip currents is stronger at low waters and appears to cease until a threshold depth of ~3 m under low-energy waves conditions. At depths where rip circulation are not active, longshore currents govern (Austin et al., 2010). Under shore-normal storm conditions, bed return flow currents, aided by (mega-) rip currents are the dominant mechanism driving offshore sediment transport by advection of sediment from the intertidal mid-upper beach and depositing it in systems of single and sometimes double subtidal sand bars located around the seaward limit of the surf zone (Scott et al., 2016). Perranporth is occasionally affected by extreme wave storms periods when significant amount of sediment is eroded from the emerged and intertidal beach, and mainly deposited in large subtidal bar and even sometimes reaching offshore deeper water depths (> 14 m) (Masselink et al., 2016; Scott et al., 2016). Under low energy conditions, wave ripples (heights ~2 cm and lengths ~20 cm) were observed to develop on the nearshore (between 1-6 m depth) and superimposed to megaripples (heights ~10-30 cm and lengths ~1-1.8 m) (Miles et al., 2014). In higher energy conditions the wave ripples flattened and the megaripples dominated the seafloor morphologies displaying the largest sizes when the orbital velocities ranged between 0.5-0.8 m/s (Miles et al., 2014). Onward migrations of the megaripples and wave ripples contributed to the onshore sediment transport (Miles et al., 2014).

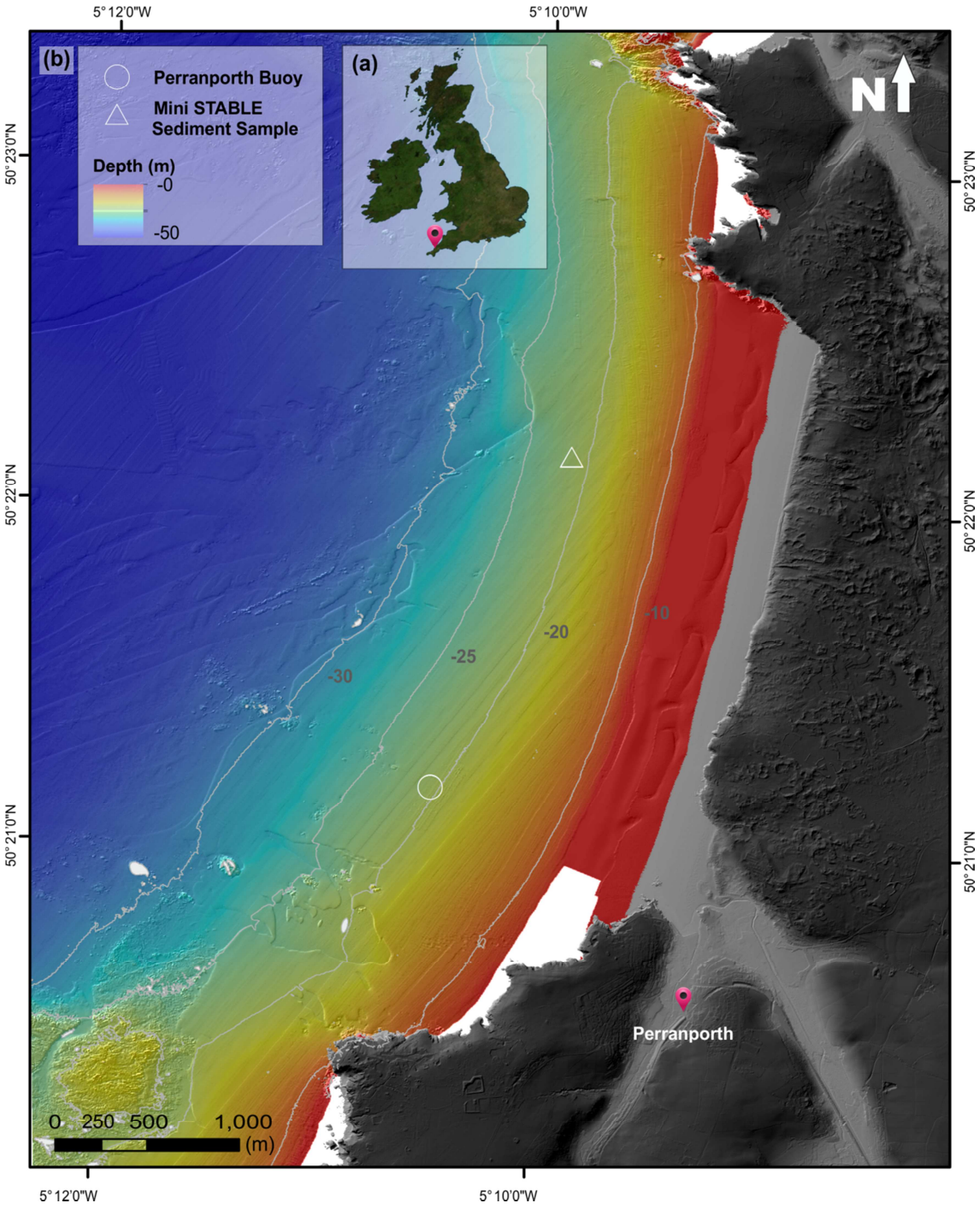

Fig. 4. (a) Location of Perranporth study area and (b) shaded-relief of Composite Digital Terrain Model (DTM) at 1 m of resolution from LIDAR data available at http://environment.data.gov.uk and bathymetry at 2m resolution from UKHO INSPIRE Portal & Bathymetry DAC. The bathymetric contours are displayed every 5 m. The Mini-STABLE rig location is indicated with a white triangle and the offshore Buoy of Perranporth location is indicated with a white circle.

Chapter III. Data acquisition, methodology and materials

1. Seafloor characterisation and analysis

1.1. Bottom sediment samples

Sediment samples were collected using a HAPS bottom corer on the sand ridge field at the same location than the benthic tripod before the deployment at the shoreface of the Ebro Delta (see location in Fig. 3 b). The corer was 13 cm long, and it was sampled every centimetre.

Two sediment samples were recovered at the same location than the Mini-STABLE deployment using a Van Veen Grab during the tripod recovery on the 12th of March of 2017 at the inner shelf of Perranporth (Fig. 4 b). The grabs were subsampled.

All samples were analysed at ICM-CSIC facilities. They were first dried in an oven at 80°C for 24 hours. The sediment fraction finer than 2000 μm was examined using an LA-950V2 laser scattering particle size distribution analyser (HORIBA), while the coarser fraction was sieved using a column with three sieves (6000, 4000 and 2000 μm). The grain size distribution and the median gain size (d_{50}) were estimated.

1.2. Topo-bathymetry data

1.2.1. Ebro Delta site

High-resolution multibeam bathymetric data were collected in three different surveys (Fig. 3 b). The first survey (hereafter referred as B-2004) was carried out in summer 2004 using a Simrad 300 kHz Kongsberg EM3002d multibeam echo-sounder and was gridded at 4 m node-spacing (Fig. 3 b). The area covered by this survey was ~47 km^2 (Urgeles et al., 2011). Two additional cruises were carried out in the framework of the FORMED project: The second (hereafter B-2013) was carried out in October 2013 using an ELAC NautikSeaBeam 1050D multibeam echo-sounder system on board the R/V García del Cid. The swath-mapped area (40 km^2) was gridded at 1 m resolution with a spatial arrangement that was complementary to that of the previous survey (Fig. 3 b). The third (hereafter B-2015) was carried out in November 2015 using an R2SONIC 2024 broadband multibeam echo-sounder system. This third bathymetric dataset,

used in this study for the morphometric analysis of the sand ridges, was gridded at 0.5 m node-spacing; it overlaid the previous two surveys and partially extended them landward, covering a total area of ~5.5 km^2 (Fig. 3 b).

The bathymetric data were processed by correcting heading, heave, pitch and roll, and filtering and manual cleaning of spurious depth records. The processed digital terrain models were imported into a Geographic Information System (ArcGIS© desktop v. 10.3) for analysis. The detailed geo-referenced shaded-relief images have sun-illumination with an azimuth of 315° and an elevation of 20° with two times vertical exaggeration to highlight the morphological details of the seabed. All images are displayed using a Universal Transverse Mercator (UTM 31 N zone) projection in the World Geodetic System (WGS-84) geographic coordinate system.

1.2.2. Topo-bathymetry of Perranporth site

The geomorphological setting of the study site between the nearshore and the continental shelf was put in context by a Digital Elevation Model (DEM) constructed by combining LIDAR data at 1 m of resolution and multi-beam bathymetry data at 2 m resolution. LIDAR was provided by the "Environmental open-data applications and datasets" of the Department of Environment Food & Rural Affairs of UK (http://environment.data.gov.uk) and the multibeam was provided by United Kingdom Hydrographic Office (UKHO) INSPIRE Portal & Bathymetry DAC. The DEM was corrected and referenced to Ordnance Datum Newlyn (ODN) using the Vertical Offshore Reference Frame model (VORF) facilitated by the United Kingdom Hydrographic Office, courtesy of Nieves García Valiente from the Centre for Coastal and Ocean Science and Engineering (CCOSE), University of Plymouth. According to the web site the bathymetric data were collected during surveys between the 20th of April of 2009 and the 3rd of March of 2011 by Fugro aboard MV Meridian for UKHO using a Reson Seabat 7125 MBES and Starfix HP/XP (0.2 m 2σ vertical) to IHO Order 1a. The DEM was imported into Geographic Information System (ESRI's ArcGIS© desktop v. 10.3) (Fig. 4 b). The detailed geo-referenced shaded-relief images had sun-illumination with an azimuth of 315° and an elevation of 20° and two times vertical exaggeration of bathymetry dataset to highlight the morphological details of the seabed. The bathymetry and the topography were displayed using a Universal Transverse Mercator (UTM 30N zone) projection in World Geodetic System (WGS-84) geographic coordinate system and Datum.

1.3. Morphometric parameters

A morphological characterisation of the sand ridges of the Ebro Delta was evolved. An automated morphobathymetric analysis procedure that detects the location of the crests and the troughs of the sand ridges was developed to characterize the ridge geometry in surveys B-2004 and B-2015. Based on the methodology of Knaapen (2005), 250 transects orthogonal to the

crests and spaced 11 m apart were used for the morphobathymetric analysis of the swath-mapped sand ridges (Fig. 5 a). Coordinates and elevations were sampled every 4 m along each profile (the lowest resolution of the different bathymetric data sets). The crests and the troughs were identified as local maxima or minima along each profile when a new maximum/minimum elevation was preceded by a maximum/minimum elevation higher/lower than 0.5 m in order to avoid undesirable values (noise) (Fig. 5 b).

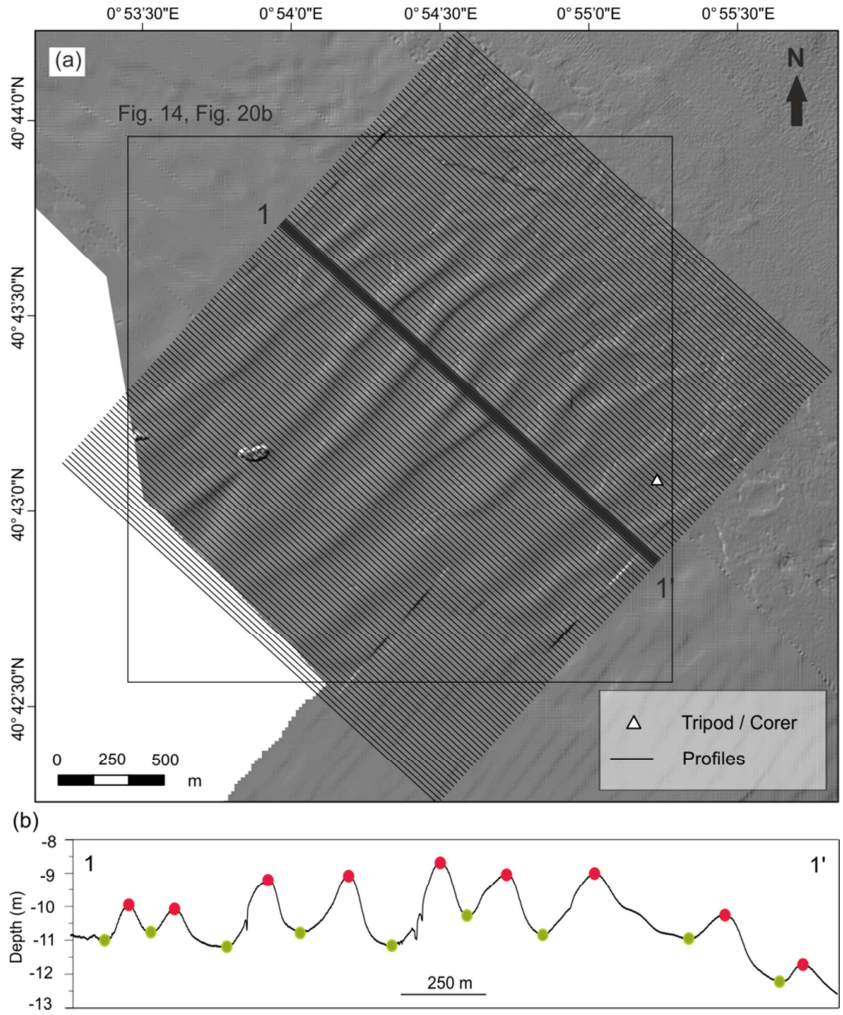

Fig. 5. (a) Detail of the 250 profiles oriented perpendicular to the sand ridge crests used for the morphobathymetric analysis. The triangle indicates the location of the tripod and the sediment sample. (b) An example of a bathymetric profile showing the geometry of the ridges and the location of the crests and troughs extracted automatically. The location of the profile is indicated with a black bold line in (a). Note vertical exaggeration of 100.

The wavelengths (L) and the heights (H) were calculated as the horizontal distance between two consecutive troughs (Fig. 6), as follows:

$$L = x_3 - x_1 \qquad \text{(eq. 1)}$$

$$H = \sqrt{Q^2 - {L_2}^2} \quad \text{(eq. 2)}$$

The asymmetry index (AI) and the steepness (Sp) were calculated as

$$AI = (L_1 - L_2)/(L_1 + L_2) \quad \text{(eq. 3)}$$

Note that AI positive values indicate that the lee side of the sand ridges faces to the SE whereas negative values indicate that the lee side faces to the NW.

$$Sp = H/L \quad \text{(eq. 4)}$$

Statistical parameters characterizing the bedforms were determined using morphometric histograms.

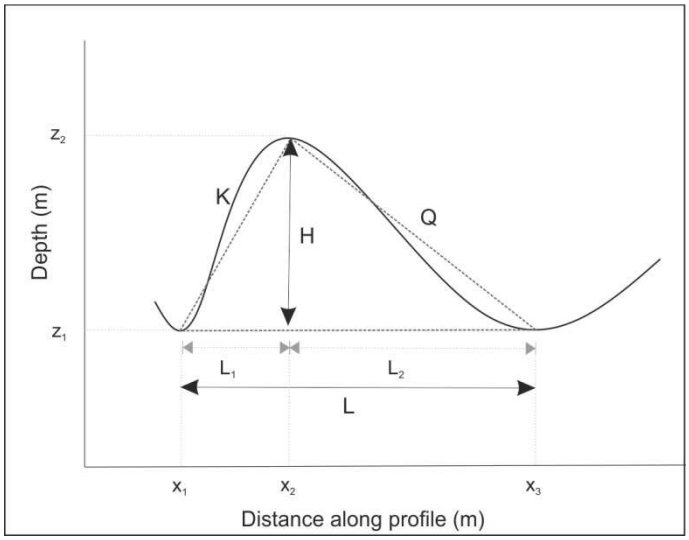

Fig. 6. Sand ridge geometric parameters. L, wavelength; L_1 and L_2, sequential distances from troughs to crest; H, ridge height; z_1, z_2, depth of the relative maxima and minima detected; x_1, x_2, x_3, position of the troughs and crests along the bathymetric profile.

1.4. Sand ridge migration

Ebro Delta ridge migration was estimated as the distance between the crest point positions on the bathymetries B-2004 and B-2015. This approach was used to estimate the mean migration, the migration rate, the differential migration along each crest and the variation of these values with depth. The migration rate was calculated by dividing the mean migration by the time span between the two cruises (11.33 years), considering both the whole sand ridge field (mean value) and each ridge separately.

1.5. Delta plain evolution

We used a nautical chart from 1880 and aerial photographs of 1947, 1957 and 2014 from the Cartographic and Geologic Institute of Catalonia (ICGC) to study the morphological changes in the Ebro River mouth during the last century. After geo-referencing the old nautical chart using ArcGIS software, by superimposing images and bathymetries we identified changes in the river mouth configuration and its morphological evolution from 1880 to the present.

1.6. Seismic dataset

Six high-resolution seismic profiles were acquired over the study area in the Ebro Delta on the 9th of November of 2015 with an INNOMAR SES-2000 Compact parametric sub-bottom profiler (Fig. 3 b). This profiler uses the parametric principle that generates a secondary low frequency of 4-12 KHz, capable of providing a layer resolution of up to 5 cm, and emits at a ping rate of up to 40 pings/s. The profiles were collected along NW-SE–oriented lines (Fig. 3 b). The dataset was analysed using the Kingdom Suite Software. The depth of the tracked horizons was transformed from two-way travel time in seconds to metres, assuming a constant sound travel velocity in sea-water of 1550 m/s. The thickness and volume of sediments involved in the sand ridges were obtained from the horizons tracked along the six profiles using ArcGIS software.

2. Winds and waves

2.1. Ebro Delta site

Wind field measurements from the *Buda* Island meteorological station (Latitude (Lat): 40.707° N, Longitude (Lon): 0.834° E) were supplied by the Catalan Meteorological Service (SMC) (see location in Fig. 3 b). The time series data provided wind speed intensities (gust velocity) and directions every 30 minutes during the study period.

Wave field measurements and statistics data were obtained from the offshore buoy of Tarragona available online and provided by the Spanish Ports Authority with hourly sampling interval (www.puertos.es). The buoy of Tarragona is located at approximately 50 km to the east of the tripod location at 688 m of water depth, Lat: 40.680° N and Lon: 1.47° E.

For the large-scale analysis, the wave data were propagated from the buoy location to the tripod position considering only the shoaling effect. While for the more detailed smaller-scale analysis the wave field was propagated using and integrated model considering the bathymetry, the waves and the wind fields.

2.2. Perranporth site

The wave field information was obtained from the Directional Waverider Buoy off Perranporth (Datawell; Directional Waverider MkIII) online available via Channel Coastal Observatory (www.channelcoast.org). The buoy was located at a water depth of ~20 m (ODN) at (WGS-84): Lat: 50º21.18' N; Lon: 05º 10.48' W. Because of the location of the Perranporth buoy and the location of the Mini-STABLE frame deployment there was no need to propagation (see location in Fig. 4 b).

3. Benthic tripod instrumentation

Instrumented bottom frames have been used since the 1960s to investigate bottom boundary layer processes and sediment dynamics without significant flow interference near the seafloor (Sternberg, 2005). Instruments attached at the benthonic tripod structures allow scientists to obtain measurements and observations of seabed micro-bathymetry, seafloor images, sediment characteristics, near-bottom hydrodynamics and suspended sediment concentrations.

Substantial part of this work is based on time series and datasets obtained by two benthonic tripods deployments: (i) at 13 m depth in the shoreface of the Ebro Delta shelf (NW Mediterranean) from the 13th of October of 2013 to the 8th of April of 2014; and (ii) at 20 m depth Ordnance Datum Newlyn (ODN) in the inner shelf of Perranporth (SW of England) from the 18th of January to the 12th of March of 2017.

3.1. Ebro Delta benthic tripod instrumentation

An instrumented benthic tripod was deployed off Cape Tortosa at the Ebro Delta inner shelf over a sand ridge field at approximately 13 m water depth from 13 October 2013 to 8 April 2014 in the framework of the FORMED project (Fig. 3 b).

The frame is a three-legged structure standing ~2.50 m high and the feet forming an equilateral triangle of 3 m on each side, with weights at each foot to maintain structure stability (Fig. 7). The frame was self-contained, fully submerged and it was attached various batteries, instruments and dataloggers. The attached instruments used in this Thesis were basically measuring current intensities and directions (currentmeter), turbidity (tubidimeters), suspended sediment concentration and grain size (Laser In Situ Scattering Transmisometer), suspended sediment concentration along the water column (Acoustic Backscatter System), direct seafloor images (video camera), and topographic seabed variability (altimeter). Instrument basics characteristics, location above the bottom (deck of the ship) and sampling strategy are shown in (Fig. 7 and Table II). The main instruments technical characteristics and set up are described below.

› *Currentmeter*

An Aanderaa currentmeter (RCM-9) recorded the current intensity and direction at 0.94 meters above the bottom (mab) every 30 minutes using and acoustic Doppler sensor emitting at 2 MHz and a magnetic compass (Table II). The instrument also was equipped with a turbidity sensor that measure suspended sediment concentrations at 0.852 mab (Table II).

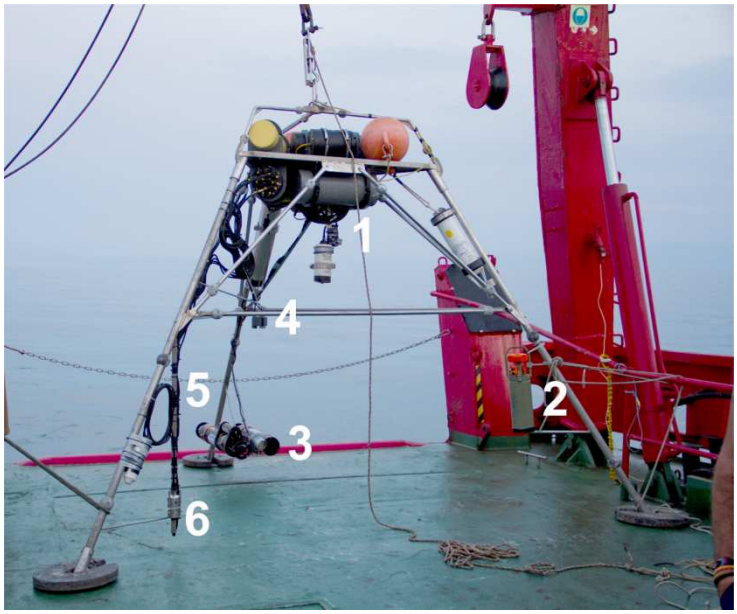

Fig. 7. Image of the tripod structure during the deployment manoeuvres on the deck of the ship on the 13th of October of 2013. Number indicate the position of the instruments used here: (1) video camera; (2) currentmeter; (3) LISST; (4) ABS; (5). Turbidimeters; and (6) altimeter.

› *AQUASCAT*

An AQUASCAT system provided with down-looking Acoustic Backscatter Sensor (ABS) measured the backscattered acoustic wave intensities along the water column from ~1.14 mab to the seabed. The ABS recorded vertical profiles of backscatter amplitude at 64 Hz, averaging the 64 profiles and storing 1 profile every second (profile/s). The resolution was 1 cm storing the backscattered received signal for each centimetre through the profile distributed along 110 cells (high temporal and spatial resolution). The ABS run bursts of 9 minutes every hour (540 profiles per burst), and had three channels emitting at 1, 2 and 4 MHz frequencies and powers of 30, 30 and 40 dB, respectively. Damping coefficients of 0.2, 0.2, and 0.25 dB/cm were used for the corrections, respectively. Acoustic sensors are sensible to sediment grain size mostly as a function of its own frequencies. The choice of the appropriate frequency/channel is function of the desired resolution and the in situ sediment grain size. In this work, channel 2 (2 MHz) was used because of it provided the most suitable resolution to work with the sediment of the area.

Four Seapoint turbidimeters connected to the ABS measured the turbidity at 0.29, 0.42, 0.56, and 0.76 mab in Formazin Turbidity Units (FTU) with a sampling interval of 6 s every hour (range of 0-500 FTU).

› *Altimeter*

An altimeter ALTUS measured the topography variability of the seabed as the distance from an acoustic transducer located at a 0.2 mab to the seabed every 15 minutes (Table II). This instrument was designed specifically to non-disturbance of the field area, with millimetre resolution of the elevation changes of the seabed (2 mm resolution), autonomous operating to be placed on isolated coastal areas and measurements recording facilities (Jestin et al., 1998). ALTUS operation is based on emitting 2 MHz acoustic wave. The echo signal is filtered, amplified, rectified, and then it is compared with the programmed threshold to give a detection signal (Jestin et al., 1998). The travel time of the acoustic wave corresponds to two times the distance from the transducer to the target. The altimeter also had a pressure sensor which provided information about the water level variations.

The altimeter time series was post-processed in order to remove automatically the spikes that appeared along the time series. The condition applied consisted in comparing point by point with the standard deviation of a 5-points window and substituting the point by its previous when it was bigger than the deviation.

› *Digital Image Sequences*

A GOPRO Hero3-Black Edition version 1.1 recorded sequences of 10 seconds (s) every 4 hours (h) at 1.6 mab. The digital video camera provides oblique images at 12-120 frames per second (fps), video effective pixels (k) of 12 MP. Providing an oblique image, the camera has 1920x1080 resolution and micro HDMI with field of view modes: narrow (90°), medium (127°), and ultra-wide (170°). The seabed coverage was approximately of 1.9 m^2.

› *Laser In-Situ Scattering Transmissometry*

A LISST-100X type B (Laser In-Situ Scattering Transmissometry) recorded turbidity and sediment grain size distribution at 0.27 mab (Table II). The grain size measurement, angular scattering distribution, is obtained over 32 ring-detectors whose radii increase logarithmically from 102 to 20000 µm (LISST-100X Particle Size Analyser User's Manual v5 available at https://www.sequoiasci.com/product/lisst-100x/). The rings cover an angular range from 0.0017 to 0.34 radians that correspond to grain size ranges from 1.25 to 250 µm. The measurements were recorded at 1 Hz during one minute every hour obtaining bursts of 60 measurements every hour. Finally, particle concentration was measured by optical transmission as the portion of light transmitted through a turbid medium which can be attenuated due to absorption in the medium

or scattered out of the beam. The LISST also has a pressure sensor which provides information about the water level variations.

Table II. Technical characteristics and specifications of the instruments deployed at the Ebro Delta Tripod

Instruments	Measurement used	Sampling interval	Location
AANDERAA RCM-9 Recording Current Meter	Horizontal Current Speed (cm/s)	30'	At a 94 cmab
	Current Direction (Deg.M)		
ALTUS 26001	Depth (m)	15'	At a 20 cmab
	Altitude (mm)		
GO-PRO	Video images	10'' every 4h	At a 163 cmab
AQUASCAT	ABS (output)	60'	At a 114 cmab
	Turbidity (FTU)	6"	Seapoint 4: 76.5 cm Seapoint 3: 56 cm Seapoint 2: 42 cm Seapoint 1: 29 cm
LISST Laser In Situ Scattering Transmissometry	Turbidity, sediment diameter (µm)	1h	27 cmab

3.2. Perranporth Mini-STABLE tripod instrumentation

The data used at Perranporth site was provided from the Marine Physics & Ocean Climate Group at the National Oceanography Centre (NOC, part of the Natural Environment Research Council) of Liverpool. The data are in the frame of BLUEcoast project, a UK national project, and specifically as part of the Work Package 1 which focus on high-energetic open coast and the measurement of the suspended and bedload sediment transport from beach to the inner shelf and vice versa (http://projects.noc.ac.uk/bluecoast/).

The data used were acquired during the Mini-STABLE deployment at approximately ~20 m depth (ODN) from the 18th of January to the 12th of March of 2017 at Perranporth inner shelf (Fig. 4 b). The Mini-STABLE is a compact version of the Sediment Transport Layer Experiment (STABLE) series of the seabed scientific lander systems produced by NOC Liverpool to study the near-bed turbulent currents and the associated sediment dynamics designed and built at the Proudman Oceanographic Laboratory (POL). The Mini-STABLE is the small version of the benthic landers, three-legged structure rig which stands about 1.8 m and 2 m in diameter and has a triangular shape with each side about 1.5 m (Fig. 8 a) (Bolaños et al., 2011). The rig was equipped with different instruments to measure currents, waves, suspended sediment concentration, sediment size, temperature; and seabed morphology (Fig. 8). This work is based on the measurements of the three dimensional Acoustic Ripple Profiler (3D-ARP) (Fig. 8 b, c) and the Acoustic Doppler Velocimetry (ADV) (Fig. 8 b, d), mounted on the Mini-STABLE (Fig. 4 b).

› *3D-Acoustic Ripple Profiler (3D-ARP)*

The 3D Acoustic Ripple Profiler (3D-ARP) is an instrument used to obtain the seabed morphology and its changes along time (3D bathymetry time series). By collecting regular time series scans of the seabed, the evolution of the bed morphology can be related to the changing hydrodynamic conditions (Thorne and Hanes, 2002). The 3D-ARP was clamped to the underside of the frame at a nominal height of 1.2 m above the deck floor. The acoustic pulses backscattered from the bed, the signal level is used to identify the bed location (x,y,z coordinates) and thereby measure the local bed level and morphology (Table III).

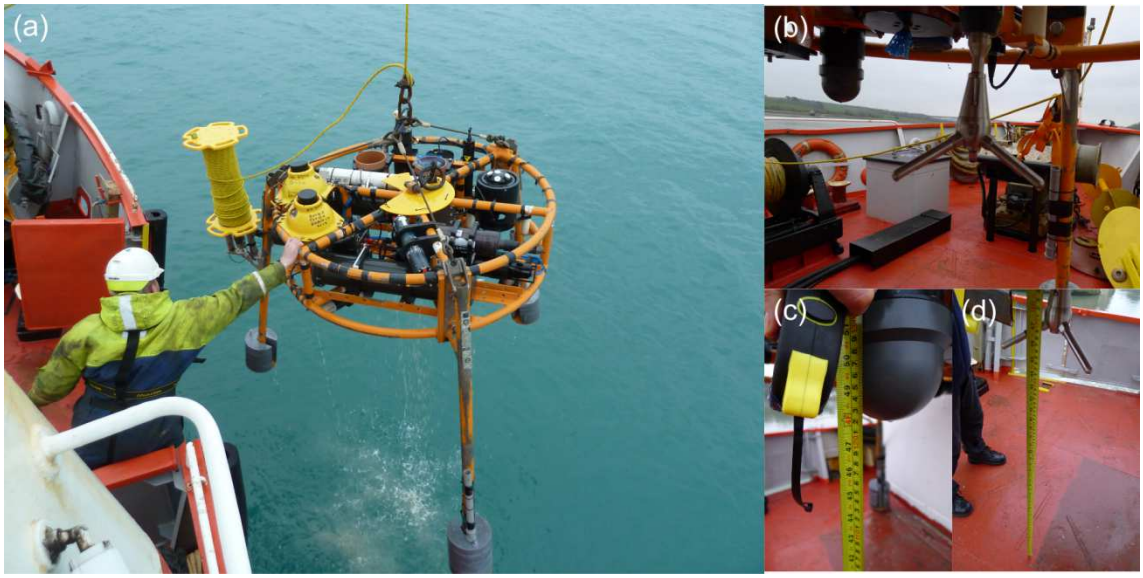

Fig. 8. (a) Recovery of the Mini-STABLE frame on the 12th of March of 2017 at Perranporth inner shelf; (b) location of the 3D-ARP and the ADV clamped at the underside of the Mini-STABLE rig; (c) detail of the distance from the head of the 3D-ARP to the deck floor; (d) detail of the distance from the three acoustic receivers of the ADV to the deck floor.

The 3D-ARP is a dual axis pencil-beam sonar scanning with an internally rotated transducer operating at 1.1 MHz which scans mechanically a circular area of the seabed (Marine Electronics Ltd., 2009). The sonar is mounted vertically, looking down at the seabed (Fig. 8). In a stepwise procedure, it scans a complete circular area underneath the sonar dome. A full backscatter profile is stored over a pre-programmed sector and once swath is completed, the head rotates about the vertical axis 0.9° ready to perform the next vertical swath. This process is repeated until the complete area beneath the system has been scanned over 360°. For every scan, there are 200 swaths (180° in 0.9° steps) and every scan takes about 12 minutes. Swath arc or width was set at 120° and the range was set at 2.5 m. It has an effective beam width of 1.8°. Other integrated sensors on the 3D-ARP are pressure (depth measurement); ±20° pitch and roll; conductivity; and temperature. The pitch and roll sensors provide attitude correction so that the

3D surface data is orientated correctly. A full bathymetry scan was recorded every 2 hours. With the sensor at 1.2 mab, the circular area covered by the scans was ~4 m of diameter.

The average speed of sound in water considered to calculate the 3D-ARP ranges was 1480 m/s. The blank distance was set at 0.4 m, to exclude the high echo level close the transducer due to the ringing, and the stop range at 2.4 m resulting on a total range of 2 m. The vertical resolution was 2 mm directly below the transducer (or beneath the nadir or central vertical beam). The scattered data points were gridded with a horizontal resolution of $\Delta x = \Delta y = 5$ mm resulting in a digital elevation model (DEM) with consistent grid cells.

In general, the ARP images showed that the seabed morphology was altered by the frame at the surroundings of the legs of the structure (see Chapter VI). The frame weight and the flow-structure interaction formed relatively large scour around the legs of the frame with 1-1.5 m of diameter and ~0.1-0.15 m deep reaching maximum values around 2.5 m and 0.30 m respectively and in some occasion even merging the scour from the different legs during the highest energy hydrodynamic conditions (see Chapter VI). Despite the scour formation, ripples continued developing over the recorded area. Although ripples formation were observed simultaneously with the scour, the time series data were evaluated during periods when the scour were not present or small enough to consider that they did not affect the hydrodynamics and the processes related to the ripples formation and dynamics (from the 18th of January to the 3rd of February of 2017).

› *Acoustic Doppler Velocimeter (ADV)*

The Nortek Vector is an Acoustic Doppler Velocimeter (ADV), which is a single point, high-resolution and high-accuracy 3D Doppler currentmeter. ADV uses pulse-coherent process: the instrument sends two pulses of sound separated by a time lag, to measure the further phase of the return signal from each pulse. The change in the phase divided by the time between pulses is directly proportional to the velocity of the particles in the water and it provides the best possible spatial and temporal resolution. The signal strength reaches a maximum when the pulse crosses the centre of the receive beam which belong to the sampling volume. The ADV uses one transmitter and two or three acoustic receivers (2D or 3D, three in our case). Then, the ADV combines velocity measurements from each receiver, knowing the relative orientation of the three bi-static axes, to calculate the 3D water velocity at the sampling volume at 14 cm below the transmitter (vertical centre of the sampling volume). For 3D probes, each receiver is slanted at 30° off the transmitted and the receivers are rotated at 120° relative azimuth angles. ADV measures bi-static velocities, each along axes 15° off the vertical axis, and converts them to Cartesian velocity using probe geometry. Then ADV output provides the three velocity components, three signal strength values (for each receiver) and three correlation values (for

each receiver). The ADV is configured with XYZ coordinate system by default. A rotation of the axis was applied considering the mean heading angle recorded by the own instrument during the first 400 bursts (period of the study) and then, the velocity components were referenced with respect to the ENU (East North Up) coordinate system (relative to the true North). The ADV was configured with a sampling rate of 16 Hz and nominal velocity range of 1 m/s. The sampling interval was set at 1 h recording during 12.5 minutes of burst of 12000 samples. The ADV transducer was located at 119 cm above deck floor (Table III).

ADV pressure sensor measured the pressure of the water column in decibars (dbar) at the same frequency sampling than the velocities. However, a fail in frequency recording at mid-deployment (beginning of February) occurred. The depth variable could be used for the further calculations and estimations during the specific study period (from the 18th of January to 3rd of February), although depth representation during the whole time series was not available. Alternatively, a Signature 1000 Acoustic Doppler Pulse-Coherent (ADCP) was also deployed and here used to performance the water depth time series along the whole period of the Mini-STABLE frame deployment. The instrument was up-looking attached to the upper side of the frame at a nominal height of 1.82 m above the seabed (Table III).

ADV quality measurements were verified, tested and processed by applying a quality data control procedure and a despiking method based on the exclusion of spikes from the ADV data using a phase-space threshold method proposed by (Goring and Nikora, 2002).

Table III. Details of the setting of the instruments attached at the Mini-STABLE frame and the buoy of Perranporth

Instrument	Measurement used	Sampling interval	Location
ADV	Velocity intensity and direction	1h	1.19 mab (Mini-STABLE)
3D-ARP	Seabed micro-bathymetry scans	2h	1.2 mab (Mini-STABLE)
ADCP Signature	Water depth	0.25 s	1.82 mab (Mini-STABLE)
Directional Waverider Buoy	H_s, T_z, T_p	30 min	20 m of water depth (ODN)

4. Time series data

Specific data quality controls were evaluated for each instrument and sensor following their own protocol and recommendations in order to assess the validity of the measurements. In addition, data were processed to obtain the desired variables as follows:

4.1. Seabed time series

4.1.1. Ebro seabed definition

At the Ebro Delta study area, the altimeter provides direct information about the seabed variability as the distance from the transducer to the target or seafloor. However, the definition of the seabed position from the ABS output data is not obvious. Different approaches have been proposed for bed detection in echo data (Krämer and Winter, 2016). In general, the water-sediment interface is assumed to be characterized by the maximum of the backscattered signal, followed by a more gentle decline towards a constant background noise level (Bell and Thorne, 1997a). Therefore, we define the seabed position as the maximum acoustic backscatter signal measured along each profile subtracting one centimetre.

4.1.2. Perranporth bed detection and mean bed level

The acoustic profiler can be used to record the range at which a threshold backscatter level is encountered for each head position that under ideal conditions, should be used to pick out the position of the seabed as a simple set of coordinates (Bell and Thorne, 1997a, 1997b). The simplest method to bed detection is then to pick the maximum value of echo intensity. However, in practice the threshold sea bed level can be triggered by suspended sediment, marine life or other instrumentation that can contribute also to strong reflectors acting as a noise for the bed detection and in other cases the required signal level is not reached from the bed echo. In order to solve these issues and because of the importance on the seabed location when micro-bathymetry and ripples bedforms morphology are the target of this sensor in our study, the data were processed using the bed recognition algorithm suggested by (Bell and Thorne, 1997b) which extracts the precise position of the bed echo and obtain the coordinates (x,y,z) of the sea bed for each scan. The method compares the signal with a desirable pattern and select the best match between both (Bell and Thorne, 1997a). The bed level in a single water column ping is found along-beam. Furthermore, a routine is applied which detects anomalous points and replace them with the best guess based on values from the adjacent space and time bins avoiding then the bed echoes that are completely masked by i.e. the reflection of the echoes with suspended sediment along the water column (weaker signal). In addition, with increasing range from the transducer, the backscattered echo level declines due to signal losses to reverberation and scattering in the water column. To reduce noise, the echo signals were smoothed by a five-point window moving average at the bed profile stage after the bed detection.

The seabed topographic variation at the study site was calculated by averaging the z-coordinate of each scan from the 3D-ARP data during the whole period studied (including the periods with the scour formation around the frame legs). This variable gives information about the distance from the 3D-ARP transducer relative to the seabed level.

4.2. Ripple observations

Ripple geometry and dimensions are here described as the orientation of the crestlines, and the cross-sectional ripple height and wavelength (η and λ, respectively). In general, to obtain ripple height and wavelength the morphology is usually simplified and schematized as a regular train of triangles or a sinusoidal wave train because of their rhythmic behaviour and appearance. However, field works show that in general ripples are far from these regular shapes and they can be highly irregular in size, shape and spacing (Mark and Blom, 2007). To determine the spatial variability and the geometric properties of ripples, a method that determines the locations of the crests and troughs in a measured bed elevation profile is needed and then, the geometric properties of individual ripples can be determined.

4.2.1. Ripples at the Ebro Delta

The seabed morphology and evolution were analysed using images from the video sequences recorded with the digital video camera located at 1.6 mab. The images provided a useful tool to identify changes on seabed morphologies and particularly to identify periods of ripples development. Seabed configurations were schematized and summarized along time. Periods with biological activity were also observed although they were not included in the time series. About the 18 % of the video sequences were quality poor or unclear (those classified as “no data”) because of technical failures of the camera, high turbidity levels or biological activity that cover the visual field of the camera.

Ripple heights were estimated from the topographic oscillations of the seabed level, recorded with the altimeter. The seabed position during each period of ripple formation was detrended using a polynomial fit to estimate ripple height from fluctuations of the bed elevations around a horizontal reference level removing bigger and smaller bed undulations or irregularities or other morphologies not related with the ripples. Then ripple height was estimated statistically by using the root mean square of the elevation multiplied by a factor equal to $2\sqrt{2}$. This is based on assuming a sinusoidal ripple cross section, since for a sine wave the height is equal to $2\sqrt{2}$ times the elevation of the standard deviation (Traykovski et al., 1999).

The instantaneous images were acquired from the videos and were first geometrically corrected using ground control points. Then, the ripples wavelengths were measured as the distance between successive ripples crests, mostly measured at the central areas of the images where the resolutions as well as deformations were the most optimum.

Migration rates were estimated as the time between the pass of two crests recorded with the altimeter. The ripple crests were first detected (considering a vertical threshold of 0.3 cm) and the distance between the two crests were assumed to be the time between the pass of a ripple

crest. Then the wavelength divided by the time of a crest pass resulted on ripple migration estimation. However, robustness of the method depended on where the measure was taken along the ripple crest which was unknown. It is worth noting that the altimeter data time series did not allow identify the direction of the ripple crest pass. Therefore, guarantee that the migration estimations is based on the orthogonal pass of the ripple crests cannot be tested leading to be cautious with the interpretations of these results.

4.2.2. Ripples at Perranporth

The ripple dimensions are here estimated from the small-scale gridded bathymetry dataset from the 3D-ARP by the following steps:

1. The central area of the scans was cropped considering only a square of 0.6 x 0.6 m in order to consider only the points directly below the central beam or nadir angle where each scan provides the best resolution (Fig. 9 a and b) according to Bell and Thorne (1997b).

2. The global trend was subtracted from the bathymetry in order to focus only on the fluctuations of the seabed elevations around a horizontal reference level ignoring other morphologies not related with ripples (Fig. 9 c and d). A fifth order polynomial based on least squares were computed and removed profile by profile (swath by swath) for each scan. The resulting residual bathymetry is a zero-mean bathymetry.

3. A first approximation of ripple wavelengths was estimated by using the transect method. This method evaluates for the local extrema (crest and trough) between zero up- and down- crossings and measure the distance between. Therefore, the crest orientation of the ripples was considered by selecting the direction which ripples crests were closer (the smallest wavelength).

4. The scans were rotated perpendicular to the ripples crests-lines. Ripple crests were detected at each profile or transect.

5. Ripple height was estimated statistically by using the standard deviation of the elevation multiplied by a factor equal to $2\sqrt{2}$. This is based on assuming a sinusoidal ripple profile, since for a sine wave the height is equal to $2\sqrt{2}$ times the elevation of the standard deviation (Traykovski et al., 1999).

6. Ripple wavelength was another time estimated by using the same transect method but now considering transects perpendicular to the ripple crests. Smooth window was applied at each transect to remove small irregularities of the seabed not related to ripples. The wavelengths larger than 40 cm were also removed considered bigger seabed undulations or irregularities. Finally, the mean wavelengths for each transect and for each scan, were calculated and defined as the mean ripple wavelength.

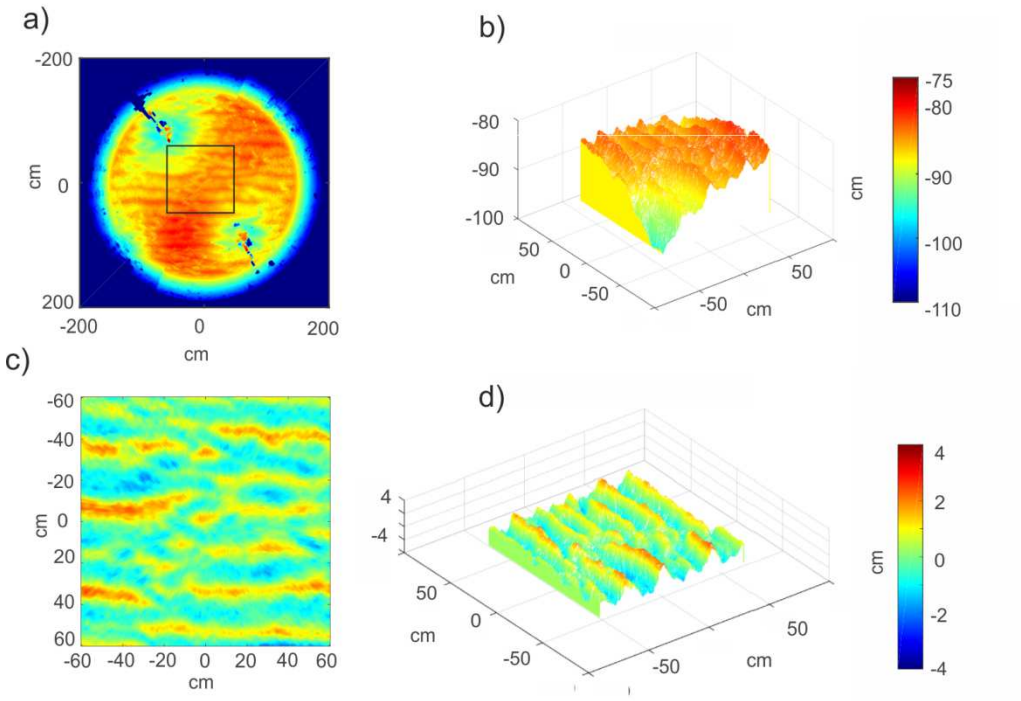

Fig. 9. Example of the pre-process automatically applied to each scan before ripple dimensions analysis: (a) complete scan measured with the 3D-ARP on the 31st of January at 0 h, the black square at the centre is the cropped area of 0.6 x 0.6 m; (b) three-dimensional view of the cropped area; (c) zero-mean residual bathymetry after subtract the global trend where from the ripples dimensions and dynamism analysis were evaluated; (d) three-dimensional view of c).

Ripple migration was evaluated by using 2D cross-correlation method, which accounts for tidal rotation and wave forcing at different angles (Lichtman, 2017). The migration distances were calculated from spatial difference between successive (2-hourly) 3D-ARP bed scans, determined by 2D cross-correlation. The distance migrated between two scans divided by the 120 minutes gave the migration rate. The area used for the 2D cross-correlation were the copped square of 0.6 x 0.6 m in order to use the best resolution area and remove the potential influence of the frame and the scour formed around the frame legs. The subsampled areas were detrended in order to remove large-scale bed topography as previously explained in the dimension estimations procedure (Fig. 9).

The 2D cross-correlation function gave small migration rates under the resolution of the scans being these values uncertain. Furthermore, stationary artefacts in the scans, like the hemisphere line, could also be affecting the 2D cross-correlation. In addition, no ripples migration was visually observed from the scans. All these reasons led to consider stationary ripples during the studied period.

4.3. Wave field time series

4.3.1. Ebro wave field

The wave field variables here used from the buoy data source were the significant wave height (H_s), the wave peak period (T_p) and the wave direction (Dir) and the wind variables used here were the maximum half-hourly gust-velocity and the respective direction.

The Tarragona buoy location is at 688 m of water depth at approximately 50 km to the east from the tripod location while wind data meteorological station (Illa de Buda Meteorological station) is located inland at ~5 km to the west from the tripod location. From October to December 2013, when the strong Mistral winds (NW winds) flew intensively, the Tarragona buoy measured high significant wave heights mostly because of the long fetch. However, at the tripod location, the NW wind had not enough fetch to develop relatively big waves because it is very close to the coast. Actually, the former Cape Tortosa buoy had been recorded during years wave filed data and showed a blank region or a lack of waves in a window between 220°-310° with respect to N (the former Cape Tortosa buoy was situated at 25 m of water depth relatively close to the tripod location). Therefore, wave field transformation and wind conditions were highly recommended to be integrated in a model able to transform waves, propagating them from the Tarragona buoy to the tripod location but also generating and accounting wind-induced waves from inland winds. To overcome the problem, the wave field data time series at the tripod location was obtained using SWAN model by simulations of wave generation and propagation along the Ebro Delta shelf from the 1st of October to the 31st of December of 2013, courtesy of Angels Fernandez-Mora.

The simulations were carried out with the SWAN Cycle III v. 41.20 model. The SWAN model (Simulating WAves Nearshore) is a third-generation wave model for simulating wave generation and propagation (shoaling, refraction and diffraction) in coastal and estuarine areas from given wind, wave and current conditions and bathymetric geometry (Booij et al., 1999). The model is based on the wave action balance equation (energy balance in the absence of currents) with sources and sinks. The simulations were run using the standard values of all parameters recommended in the SWAN user manual. For further information of the physical processes, the numerical schemes and model setup refer to the SWAN Scientific and Technical Documentation and SWAN User Manual. The wind forcing was considered throughout the entire domain to account for wave generation. The wave forcing was defined by the parametric wave spectra: the significant wave height (H_s), the peak period (T_p), the wave direction and the coefficient of directional spreading, interpreted as the directional standard deviation in degrees. The wave spectrum employed in the simulations considered 20 frequencies that were

logarithmically distributed over the frequency range of 0.05–1 Hz and 36 directional bins of 10º each bin.

The analysis area comprised the continental shelf and shoreface of the Ebro Delta. The computational domain in UTM coordinates ranges from 311778 to 340000 m E and from 4494043 to 4521327 m N (Fig. 10 a). The bathymetry has 90 m of grid resolution and it ranges from -100 m at the deepest outer region (E) to -5 m at the Ebro Delta (W). The bathymetry data were extracted from the Catalano-Balearic Sea bathymetric chart (Farrán, 2018). A uniform regular grid was used (cell size: 140 x 140 m), that conformed more than 43000 computational cells (Fig. 10 b).

SWAN was run in stationary mode ($\partial N/\partial t = 0$), for each hourly wind and wave conditions during the study period (October-December 2013), assuming that waves propagate instantaneously throughout the model domain with an immediate response to wind field changes.

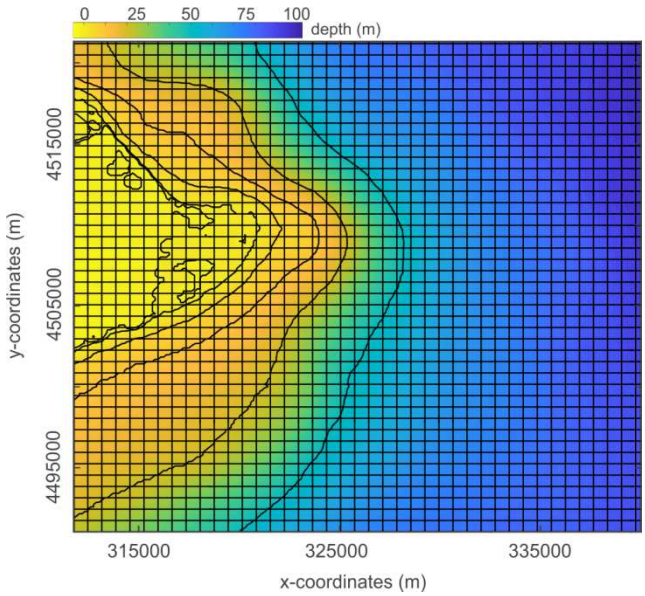

Fig. 10. Computational domain and bottom elevation showing the used regular computational grid (one of each five grid lines in both directions are shown).

4.3.2. Perranporth wave field

The data used from the directional buoy off Perranporth were: the significant wave height (H_s) (which later was transformed to the root mean square wave height (H_{rms}) by the equation $H_{rms} = H_s/\sqrt{2}$); the zero up-crossing wave period (T_z) defined spectrally and often referred as the mean wave period (T_m); the peak period (T_p); and the peak wave direction (direction of the

waves with the highest energy) all of them provided data every 30 minutes sampling interval (Table III).

4.4. Wave orbital velocity

The wave orbital velocity was calculated following small-amplitude linear wave theory considering regular waves. The orbital velocity just above the wave boundary layer over the bed due to monochromatic (single frequency) wave height (H) and period (T) in water depth (h) is:

$$U_w = \frac{\pi H}{T sinh(k\mathrm{h})} \quad \text{(eq. 5)}$$

where $sinh$ is the hyperbolic sine, $k = 2\pi/L$ is the wave number, L is the wavelength and $H = H_{rms}$ and $T = T_z$ from the wave buoy (Soulsby, 2006). The wave number k, was determined by applying the Newton-Rapshon iteration method to the dispersion equation following (Fenton and McKee, 1990) algorithm, which accounts for the effect of the currents and includes the wave-current angle correction. The wave-current angle is 0º when waves and currents are travelling in the same direction and 180° when they are travelling in opposite directions.

For most practical applications, waves are generally specified by spectral parameters such as H_s and one (or more) of zero-crossing period or spectral mean period (T_z), or peak period (T_p). However, values of wave period often yield much less statistically robust values of T_p than T_z because the first is picked as the single highest spectral (T_p) whereas T_z is derived from the whole spectrum. It is therefore preferable to use T_z when calculating the wave orbital velocity (Soulsby, 2006). However, the most relevant period for use in force, shear-stress or sediment transport calculations is T_p, because this is the period at which the energy is centred (Soulsby, 2006).

4.5. Velocity Skewness

When waves travel and propagate across the inner shelf from deep water towards the shore, waves transform from sinusoidal to skewed in the shoaling zone, to highly asymmetric shape in the inner surf and swath zone to finally run-up on the beach (Ruessink et al., 2011). Skewed waves are characterized by a high narrow crest and a broad shallow trough. The skewness (as well as the asymmetry) is reflected in the local near-bed orbital velocity beneath the waves, resulting in onshore sediment transport because of higher flow velocities in the onshore direction under the crest of waves (Ruessink et al., 2011).

The velocity skewness is defined as (Elgar, 1987):

$$U_{sk} = \frac{\overline{(u(z,t)-\bar{u})^3}}{u_{rms}(z)^2} \quad \text{(eq. 6)}$$

Where $u(z,t)$ is the cross-shore horizontal velocity (instantaneous or intraburst); the overbar denotes the time-averaged (over a burst) and z is at the depth of measurements.

$$u_{rms}(z) = \overline{(u(z,t)-\bar{u})^2}^{1/2} \quad \text{(eq. 7)}$$

4.6. Bed roughness

When small bedforms are present in the seabed generate form-drag due to the pattern of dynamic pressure distribution over their surface. The form-drag may be many times larger than the skin friction acting on the sand grains and is often the dominant cause of resistance felt by sea flow (Soulsby 1997). For sediment transport purposes, the skin friction is responsible for bedload transport and entrainment of sand from the bed, while the form-drag is associated to turbulence which diffuses the suspended sediment up into the flow (Soulsby 1997). Sediment transport roughness component should be also take into account, as it is related to the intensity of transport, at very high flow speeds, the momentum extracted by the flow to move the sand grains arises in this third roughness component. Therefore, the total roughness length (z_0) is the sum of the grain-related or skin-friction (z_{0s}), form-drag (z_{0f}) and sediment transport components (z_{0t}):

$$z_0 = z_{0s} + z_{0f} + z_{0t} \quad \text{(eq. 8)}$$

Where

$$z_{0s} = k_s/30 = 2.5d_{50}/30 = d_{50}/12 \quad \text{(eq. 9)}$$

$$z_{0f} = a_r \frac{\eta^2}{\lambda} \quad \text{(eq. 10)}$$

$$z_{0t} = \frac{5\tau_{0s}}{30g(\rho_s-\rho)} \quad \text{for currents} \quad \text{(eq. 11)}$$

$$z_{0t} = 0.00533 \cdot U_w{}^{2.25} \quad \text{for the waves} \quad \text{(eq. 12)}$$

τ_{0s} is the skin-friction shear stress according to Soulsby 1997, and a_r is an empirical coefficient a_r =0.533 according to Raudkivi (1988), η is the ripple height and λ is the ripple wavelength.

Note that in the Ebro there was not continue data of ripple dimensions along the period studied (see Chapter V) and the drag-form roughness component could not be considered (eq. 13 and 15). At Perranporth, form-drag was only considered for waves but not for currents, because of

ripple arrangement and currents flow direction were parallel and therefore ripple effects can be negligible (see Chapter VI) (eq. 13 and 14).

$$z_{0c} = z_{0s} + z_{0t} \quad \text{(eq. 13)}$$

$$z_{0w} = z_0 = z_{0s} + z_{0f} + z_{0t} \quad \text{(eq. 14)}$$

$$z_{0w} = z_0 = z_{0s} + z_{0t} \quad \text{(eq. 15)}$$

Where z_{0c} is the total roughness length accounting for currents contribution and z_{0w} is the total roughness length accounting for waves contribution

4.7. Bed shear stress

The bed shear stress is defined as the frictional force exerted by the flow per unit area of the bed because of the fluid-sediment interaction (Soulsby and Clarke, 2005). The forcing flow conditions are generally induced by waves and/or currents. The wave-current interaction is non-linear causing bed shear stress greater than the sum of the individual components (Soulsby and Clarke, 2005). When waves flow in opposite direction than currents, wavelength becomes shorter (decreases) and wave height becomes larger (increases) than the no-current case and the reverse happen when waves and currents travel towards the same direction. On the other hand, when currents and waves travel perpendicularly the direction has no effect on the waves (Soulsby et al., 1993).

The bed shear stress was calculated following the methodology proposed by Soulsby and Clarke (2005) and modified by Malarkey and Davies (2012) under combined waves and currents for hydrodynamic rough bed conditions and under the approximation of z_0 << BL << h where z_0 is the bed roughness length; BL is the wave boundary layer thickness; h is the depth. The method is based on laboratory and field measurements of the cycle-mean bed shear-stress (Soulsby and Clarke, 2005). The mean bed shear stress due to combined flow (τ_m) over hydrodynamic rough beds (sand and gravel beds) is:

$$\tau_m = \tau_c \left[1 + 1.2 \left(\frac{\tau_w}{\tau_c + \tau_w}\right)^{3.2}\right] \quad \text{(eq. 16)}$$

Where τ_c is the bed shear stress considering currents alone and τ_w is the bed shear stress due to waves alone

$$\tau_c = \rho C_D \overline{U}^2 \quad \text{(eq. 17)}$$

Where $\overline{U}$ is the depth averaged current speed, in our case the current measured at the currentmeter or ADV depth; C_D is the drag coefficient defined as:

$$C_D = \left[\frac{0.40}{\ln(h/z_{0c})-1}\right]^2 \quad \text{(eq. 18)}$$

For a sinusoidal wave of period T, and orbital velocity U_w, the amplitude of the bed shear stress is given by

$$\tau_{wr} = \frac{1}{2}\rho f_{wr} {U_w}^2 \quad \text{(eq. 19)}$$

Where r denotes rough bed; $f_{wr} = 1.39(A/z_{0w})^{-0.52}$ is the rough-bed wave friction factor and $A = U_w\, T/2\pi$ is the orbital amplitude of wave motion at the bed, and z_{0w} is the bed roughness length of waves.

Finally, the maximum bed shear stress due to combined flow (Soulsby, 1997) is:

$$\tau_{max} = [(\tau_m + \tau_w|cos\phi|)^2 + (\tau_w|sin\phi|)^2]^{1/2} \quad \text{(eq. 20)}$$

Where ϕ is the angle between the current and the wave travel directions.

4.8. Shields parameter and its thresholds

The Shields parameter (θ), also called Shields criterion or number is a non-dimensional variable used to identify or determine when seabed states change typically the initiation of motion of sediment in a fluid flow (van Rijn, 2007a). The Shields evaluation gives also an approximation of the boundaries or limits of seabed morpho-states in relation with the incident hydrodynamic conditions (eq. 21) considering in our case a constant sediment size along the studied period and evaluated during waves and currents separately (Soulsby et al., 2012).

$$\theta = \frac{\tau}{g(\rho_s-\rho)d_{50}} \quad \text{(eq. 21)}$$

Particle movement occurs when the instantaneous fluid force on a particle is just larger than the instantaneous resisting force related to the submerged particle weight and the friction coefficient (van Rijn, 2007a). The initiation of motion also known as the threshold of motion or critical Shields parameter is defined when the dimensionless bed shear stress (Shields parameter) is larger than the threshold value or critical Shields parameter ($\theta \geq \theta_{cr}$). The critical Shields parameter (θ_{cr}) using the formula of Soulsby and Whitehouse (1997) is given as:

$$\theta_{cr} = \frac{\tau_{cr}}{g(\rho_s-\rho)d_{50}} = \frac{0.3}{(1+1.2D*)} + 0.055[1 - exp(-0.02D^*)] \quad \text{(eq. 22)}$$

where τ_{cr} is the critical threshold for the bed shear stress, $D^* = d_{50}[(s-1)g/v^2]^{1/3}$ is the dimensionless sediment size being $D^* = 5.24$ at the Ebro site and $D^* = 6.64$ at Perranporth site; $v = 10^{-6}$ (m^2/s) is the kinematic viscosity coefficient; $g = 9.81$ (m/s^2) the gravity acceleration; and d_{50} the median grain size.

The Shields parameter due to waves is defined as:

$$\theta_w = \frac{\frac{1}{2} f_w {U_w}^2}{g(s-1)d_{50}} \quad \text{(eq. 23)}$$

The Shields parameter due to currents is defined as:

$$\theta_c = \frac{C_D \overline{U}^2}{g(s-1)d_{50}} \quad \text{(eq. 24)}$$

During strong energetic hydrodynamic conditions ripples can be washed-out. According to (Soulsby et al., 2012), the effect of wash-out at large current speeds can be included using a criteria given in terms of skin-friction Shields parameters as function of D*. Then, the limit of wash-out is:

$$\theta_{wo} = 1.66 {D_*}^{-1.3} \text{ when } D^* > 1.58 \quad \text{(eq. 25)}$$

It corresponds to the inception of the sheet flow regime where most of the sediment transport occurs in a thin layer close to the bed (Camenen and Larson, 2006). Sheet flow regime occurs when the Shields parameter reach some threshold value that may vary between 0.2 and 2 (Camenen and Larson, 2006; Camenen, 2009). The skin-friction sheet flow threshold as function of D* proposed by (Soulsby et al., 2012) is:

$$\theta_{sf} = 2.26 {D_*}^{-1.3} \text{ when } D^* > 1.58 \quad \text{(eq. 26)}$$

The transition to sheet flow state is usually described in empirical predictors. Camenen (2009) reviewed some of the expressions purposed since 1955 and developed an evaluation about sheet flow estimations. Because of the expressions are based on empirical equations it resulted on large variability in this value depending on the formula used (0.2-2). Camenen (2009) purposed an expression for the inception of sheet flow Shields parameter as:

$$\theta_{sf} = 10 {D^*}^{-3/4} \sqrt{\frac{d_{50}}{\delta_w}(1 + r_w)^2} \quad \text{(eq. 27)}$$

Where $\delta_w = \sqrt{\frac{\upsilon T}{\pi}}$ is the thickness of Stokes boundary layer and $r_w = \frac{u_{w,max} - u_{w,min}}{u_{w,max} + u_{w,min}}$ the wave asymmetry with $u_{w,max}$ the maximum velocity onshore and $u_{w,min}$ the minimum velocity offshore.

Other sheet flow criteria are:

$$60 < \left(\frac{A_w}{d_{50}}\right)_{sf} < 6000 \quad \text{(Soulsby and Whitehouse, 2005)} \quad \text{(eq. 28)}$$

$\theta_{sf} = \theta_w + \theta_c = 1$ (Kleinhans, 2005) (eq. 29)

$\theta_{sf} = 0.413 D^{*-0.396}$ (Li and Amos, 1999) (eq. 30)

$\theta_{sf} = 1$ (Nielsen, 1981) (eq. 31)

4.9. Ripple prediction

Ripple predictors to estimate the bedforms characteristics are mostly exclusively focussed on ripple geometry parameters: height and wavelength. These predictors usually are defined for current-generated, wave-generated or combined flows ripples while the orientation, shape and slope of ripples are much more rarely considered (Wiberg and Harris, 1994; Soulsby and Whitehouse, 2005; van Rijn, 2007b; Camenen, 2009; Maier and Hay, 2009; Soulsby et al., 2012; Nelson and Voulgaris, 2014). The capability to forecast the development and appearance of ripples is of practical importance because rippled seabed causes larger resistance to flow (larger bed roughness) which modifies the flow field; the roughness can also influence the wave dissipation, promote and increase sediment suspension enhancing the sediment transport; and the acoustic signals are reflected and absorbed differently than plane beds (Soulsby et al., 2012).

Soulsby et al., (2012) methodology of the theory of equilibrium ripples dimensions is here used because its simplicity and because it is based on the comparison of the Shields parameter thresholds obtained with the hydrodynamic measurements. From the methodology for equilibrium ripple predictor, different morpho-states are expected to develop under different hydro-states. The hydro-states are here differentiated by the thresholds proposed from the Shields parameter: (i) the threshold of initiation of sediment motion (θ_{cr}), sediment starts to move and therefore ripples can start to form. This limit is theoretically evaluated for a given sediment size and then, ripples develop with a constant height and wavelength if the hydrodynamic conditions are constant during enough time (Soulsby et al., 2012). (ii) wash-out of ripples (θ_{wo}) and (iii) sheet flow (θ_{sf}). The Shields thresholds are compared with Shields due to waves (θ_w) driving to wave-generated ripples and with Shields due to currents (θ_c) leading to current-generated ripples:

› *Wave-generated ripples*

When waves dominated, the estimated ripple dimensions changed, growing when the energy increased and decaying when the energy decreased because of they are directly function on the wave orbital velocity. If $\theta_w \geq \theta_{cr}$ ripples height and wavelengths (η and λ, respectively) are defined as:

$$\frac{\lambda}{A} = [1 + 1.87 \times 10^{-3} \Delta (1 - exp\{-(2 \times 10^{-4} \Delta)^{1.5}\})]^{-1} \quad \text{(eq. 32)}$$

$$\frac{\eta}{\lambda} = 0.15[1 - exp\{-(5000/\Delta)^{3.5}\}] \quad \text{(eq. 33)}$$

Where $\Delta = A/d_{50}$

Otherwise, λ and η are taken as the pre-existing values (relict ripples).

› *Current-generated ripples*

If $\theta_c \geq \theta_{cr}$ current-generated ripple develop. The method suggests constant and maximum bedform dimensions under current dominion. For a given grain-size that developed ripples of constant height and wavelength if the current speed is maintained during sufficiently time then:

$$\eta_{max} = d_{50} 202 {D_*}^{-0.554} \quad \text{for } 1.2 < D^* < 16 \quad \text{(eq. 34)}$$

$$\lambda_{max} = d_{50}\left(500 + 1881 {D_*}^{-1.5}\right) \quad \text{for } 1.2 < D^* < 16 \quad \text{(eq. 35)}$$

Soulsby et al., (2012) defined a linear reduction in ripple height between θ_{wo} and θ_{sf} assuming that the wavelength is unaffected by wash-out and is equivalent to the maximum value indicated above. Then, the equilibrium ripple height including wash-out is:

η_{eq} = pre-existing value (relict or frozen ripples) $\quad 0 < \theta_c < \theta_{cr}$ (eq. 36)

$$\eta_{eq} = \eta_{max} \quad \theta_{cr} < \theta_c < \theta_{wo} \quad \text{(eq. 37)}$$

$$\eta_{eq} = \eta_{max}\left(\frac{\theta_{sf} - \theta_c}{\theta_{sf} - \theta_{wo}}\right) \quad \theta_{wo} < \theta_c < \theta_{sf} \quad \text{(eq. 38)}$$

$$\eta_{eq} = 0 \quad \theta_c > \theta_{sf} \quad \text{(eq. 39)}$$

One important point to be considered in prediction of ripple characteristics is the Shields parameter for the inception of sediment movement θ_{cr} and for the inception of sheet flow θ_{sf}, which should border the limit for the ripple existence (Camenen, 2009). When currents governed over waves, these boundaries of ripples are well-stablished by imposing ripple dimensions decrease ($\theta_{wo} < \theta_c < \theta_{sf}$) until they completely wash-out imposing flatbed ($\theta_c > \theta_{sf}$; $\eta,\ \lambda = 0$) (Soulsby et al., 2012). However, if waves dominated over currents the method did not attempt for wash-out of ripples nor sheet flow.

› *Wave-current dominance criterion*

When crossing wave trains, large and abrupt changes in wave direction or the presence of waves and currents at the same time can lead to complicated three-dimensional ripple patters. However, for simplicity, Soulsby et al. (2012) ripple prediction model for waves and currents acting together assumes that only one ripple train is present at any time, and this is the dominant between both (Li and Amos, 1998).

If $\theta_w \geq \theta_c$ the wave-generated ripple expressions are used

If $\theta_w < \theta_c$ the current-generated ripple expressions are used

4.10. Sediment transport rate

The sediment transport rate was estimated following the van Rijn (2007a, 2007b) methodology because of its simplicity to obtain estimations of the bedload and suspended load sediment transport in coastal flows. The method only requires the basic hydrodynamic parameters (depth, current velocity, wave height, wave period, etc.) and the basic sediment characteristics (d_{50}) (van Rijn, 2007a). In addition, the (van Rijn, 2007c) transport formula is universal in the sense that it can be applied to the full range of sediment sizes (8-2000 μm) and the full hydrodynamic regimes (included coastal flows).

In theory, when flow and sediment characteristics combine to produce Shields parameters greater than the critical value, sediment is set to motion resulting the initiation of a non-zero transport of sediment (van Rijn, 2007a). It is known that the transport of the near-bed material particles may be in the form of bed load or suspended load (van Rijn, 2007a). Basically, the depth-integrated sediment transport is in the form of either bedload and/or suspended load, depending on the sediment size and the flow conditions (van Rijn, 2007a). The bedload transport is the transport of sediment particles in a thin layer close to the bed (of the order of 0.01 m) dominated by flow-induced drag forces and by gravity forces acting on the particles. The suspended load transport of sediment particles is above the bedload layer considered as the irregular motion of the particles through the water column derived by turbulence-induced drag forces on the particles. The net (averaged over the wave period) total sediment transport rate in coastal waters is defined as the vector sum of net bedload (q_b) and net suspended load (q_s) transport rates:

$$q_{total} = q_b + q_s \quad \text{(eq. 40)}$$

For coastal flow (steady flow with or without waves) the bedload transport according to (van Rijn, 2007a) is defined as:

$$q_b = \alpha_b \rho_s U h (d_{50}/h)^{1.2} {M_e}^{1.5} \quad \text{(eq. 41)}$$

Where q_b is the bedload transport rate (in kg/s/m); α_b =0.015; $M_e = (U_e - U_{cr})/[(s-1)g d_{50}]^{0.5}$ is the adimensional mobility parameter; $U_e = U + \gamma U_w$ the effective velocity (m/s) with γ =0.4 for irregular waves; U is the depth averaged flow velocity (m/s); U_w is the orbital velocity (m/s) (eq. 5); $U_{cr} = \beta u_{cr,c} + (1-\beta) u_{cr,w}$ the critical velocity (m/s) with

$\beta = U/(U + U_w)$; $u_{cr,c}$ is the critical velocity (m/s) for currents based on Shields; $u_{cr,w}$ is the critical velocity (m/s) for waves, which when 0.00005< d_{50} <0.0005 m, are:

$$u_{cr,c} = 0.19(d_{50})^{0.1} log(12h/3d_{90}) \quad \text{(eq. 42)}$$

$$u_{cr,w} = 0.24[(s-1)g]^{0.66} {d_{50}}^{0.33} {T_p}^{0.33} \quad \text{(eq. 43)}$$

h is the water depth (m); $d_{50}$the mean particle size (m); and $s = \rho_s/\rho_w$ is the relative density.

The simplified suspended load transport rate formula proposed by (van Rijn, 2007c) for coastal flows defined as the current-related suspended transport which is the transport of sediment by the mean current including the effect of wave stirring on the sediment load is:

$$q_s = 0.012\rho_s U d_{50} {M_e}^{2.4} (D*)^{-0.6} \quad \text{(eq. 44)}$$

For high current velocities (> 0.5 m/s) the formulations tend to overestimate sediment transport rate estimations (van Rijn, 2007c).

4.11. Suspended sediment concentration (Ebro Delta site)

4.11.1. At one point above the bottom

The turbidity data from the currentmeter time series was used to obtain the suspended sediment concentration at ~1 mab. The data were processed to correct non-consistent values (peaks with physical meaningless) by three steps: (i) check values larger than the average of the two preceded measurements plus 100; (ii) measurements larger than the previous and following values plus 20; (iii) the values that accomplish the two conditions were replaced by their average.

4.11.2. Suspended sediment concentration profiles

Suspended sediment concentration time series were inferred from the ABS and the 4 turbidimeters. Each instrument provided measurements in different output units and specific calibration curves for each device were required in order to transform units from instrument outputs to suspended sediment concentration (mg/l).

The four Seapoint turbidimeters measured in Formazin Turbidity Units (FTU). They were calibrated in the laboratory using mili-Q water and known concentrations from clean water (0 mg/l) to 5000 mg/l using in situ bottom sediment samples (Fig. 11). Transformations from output signal into SSC units (mg/l) were estimated by linear regression obtaining one equation for each turbidimeter and r^2=0.99:

$y_{0.29\ mab}=18.522x-21.511$ (eq. 45)

$y_{0.42\ mab}=16.476x-18.382$ (eq. 46)

$y_{0.56\ mab}=16.881x-19.439$ (eq. 47)

$y_{0.76\ mab}=16.582x-20.188$ (eq. 48)

Fig. 11. Laboratory calibration of the four turbidimeters using in situ bottom sediment sample and known concentration.

Suspended sediment and seabed detection is sensitive to the selected frequency of ABS channels (Meral, 2008). The higher frequency (4 MHz) favours the detection of finer particles, but offers less penetration capacity into the seabed. The lower frequency (1 MHz) provides lower suspended sediment concentrations (detection of coarser sediment) and deeper seabed position. The suitable frequency/channel is then function of the in situ sediment grain size and the resolution (Thorne and Hanes, 2002; Thorne and Hurther, 2014). In this study, after a first general overview of the SSC time series, ABS channel 2 (2 MHz) gave reasonable results compared with the other two frequencies detecting all the SSC peaks at the desired resolution. Therefore, hereafter we refer to channel 2 with 2 MHz of frequency emission as the ABS data and for all the further analysis and results.

The ABS down-looking profiler recorded the backscattered signal from the transducer to the seafloor every centimetre and every second during 9 minutes every hour. The signal was recorded as a voltage and automatically converted into “ABS output” units which are proportional to the Suspended Sediment Concentration (SSC) after range and damping corrections. The ABS output signal was transformed into mg/l by calibration using the four

turbidimeters. The ABS cells corresponding to turbidimeters at 29, 42, 56 and 76 cmab, were obtained at the beginning of the deployment and then, SSC measured with the turbidimeters in mg/l and the "ABS output" signal was compared and the best-fit equation by linear regression during an specific period was calculated (Fig. 12 a). In order to consider in the calibration the sensor response during changing conditions it was selected a period with an increase, a peak and decrease of the turbidity. The coefficient of determination obtained using the four turbidimeters was low, because the closest and furthest turbidimeters from the seabed introduced outlier points in the calibration (Fig. 12 a). When only the two turbidimeters located in the middle of the array were used, they improved the coefficients of determination (Fig. 12 b). Because of the turbidimeter located at 42 cmab showed some bimodal behaviour (Fig. 12 b), if only the turbidimeter located at 56 cmab was used, the obtained linear regression equation is similar and the coefficient of determination slightly improves (0.65) although scarce number of points are used. Consequently, the calibration was finally developed using the two intermediate turbidimeters.

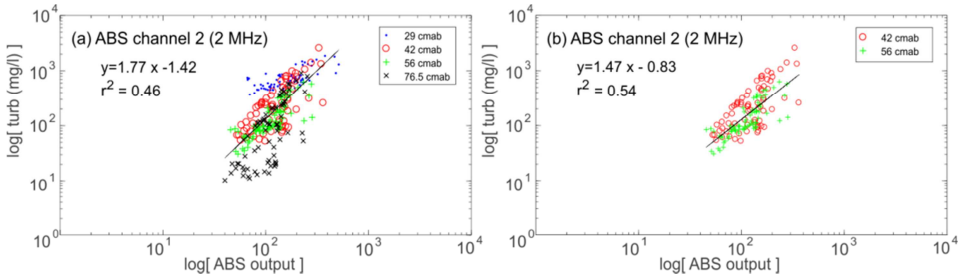

Fig. 12. Linear regression to calibrate from ABS output signal of channel 2 of 2 MHz to mg/l using (a) the four turbidimeters located at 29, 42, 56 and 76 cmab; and (b) only two turbidimeters located at 42 and 56 cmab; considering only the period between the 16th and the 19th of November 2013. The respective equations and the Coefficient of determination (r^2) are indicated.

The equation obtained and applied for the channel 2 (2 MHz) calibration to transform from output backscatter data to mg/l was:

$$SSC(mg/l) = 10^{1.47 * \log(ABSdata\_chan2) - 0.83} \quad \text{(eq. 49)}$$

The time series of SSC profiles in mg/l from the seabed to the cell 85 cm of the ABS were obtained from October to December 2013. From the 85 cm cell to the ABS transducer location the suspended sediment concentration profiles sometimes showed affections by other sensors and/or punctual fouling. Therefore, to characterize properly the SSC time series and avoid noisy data, cells from 85 cm to the ABS transducer were removed.

It is worth noting that the calibration of the ABS with in situ sediment under controlled laboratory conditions have to be taken with care because sediment grain size distribution in

suspension can be significantly different from that of the seabed and the suspended sediment grain size can change with time and under different energetic conditions (Davies and Thorne, 2016). Moreover, SSC profiles exhibited minimum concentrations always higher than ~16 mg/l at whatever the depth was measured, which was unrealistic even in a deltaic area as the Ebro Delta. These minimum concentrations were invariable during calm conditions suggesting that overrated minimum concentrations could be consequence of calibrations. While the absolute value of SSC is affected by calibration errors it is expected that the relative variability of measurements in space and time provides a good estimation to the study of the suspended sediment dynamics.

› *Burst-averaged SSC-profiles*

Nielsen (1992) proposed a convection-diffusion-type approach for the time-averaged vertical distribution of the sediment concentration profiles which deal with vortex trapping effects for sediments in oscillatory flows. Accordingly, the vertical transport rate per unit area can be approached as:

$$q_z = -\varepsilon_s \frac{dc}{dz} \quad \text{(eq. 50)}$$

And therefore, the time-averaged vertical distribution of the sediment concentration profile is described as:

$$\omega_s C + \varepsilon_s \frac{dc}{dz} = 0 \quad \text{(eq. 51)}$$

Where w_s is the settling velocity of the sediment grains, C the mean suspended sediment concentration and ε_s the turbulent eddy diffusivity or sediment mixing coefficient.

This is the most common approach to model the suspended sediment transport and it is based on the advection-diffusion theory. The first term of the equation represents the downward transport of sediment by gravity (settling) and the second term represents the upward transport by turbulent processes (mixing), which adopting the diffusion model is proportional to the vertical concentration gradient. The solution of the equation depends on the selected form of the vertical distribution of the mixing coefficient, typically the *exponential* and the *power-law* profiles (Davies and Thorne, 2016).

› *Exponential profile*

The exponential profile resulted from the assumption of a constant-in-vertical mixing coefficient. It implicitly means that the water column is assumed to be well-mixed and given by:

$$C_z = C_0 exp(-z\varepsilon_s/\omega_s) \quad \text{(eq. 52)}$$

Assuming that the dominant processes are convective instead of diffusive, coherent structures in the fluid motion must exist to produce the upward transport of sediment particles. Under non-breaking waves, Nielsen (1992) assumed that the environment is mainly dominated by wave action and therefore, equation can be rewrite as:

$$C_z = C_0 exp(-z/L_s) \quad \text{(eq. 53)}$$

Where L_s is the decay length scale, and C_0 is the reference concentration at bottom ($z = 0$). In this work, both variables (C_0 and L_s) were derived from the adjustment between known concentrations measured with the ABS and the estimated exponential profile approach.

› *Power profile*

The power concentration profile assumes that the sediment diffusivity varies linearly with elevation above the bottom. This approximation is usually employed in environments with combined waves and currents contributing both to the sediment mixing being the sediment suspended within the wave boundary layer and diffused further up into the flow by the turbulence associated with the current (Glenn and Grant, 1987; Soulsby, 1997). The sediment diffusivity is defined as:

$$\varepsilon_s = \gamma k u_{*wc} z \quad \text{for} \quad z/\delta_w < 1 \quad \text{(eq. 54)}$$

$$\varepsilon_s = \gamma k u_{*c} z \quad \text{for} \quad z/\delta_w > 1 \quad \text{(eq. 55)}$$

Where γ (here taken as 1) is a constant accounting for the differences between turbulence diffusion of water and sediment particles.

The mean suspended sediment concentration C_z at a height z above the bottom is given by:

$$C_z = C_{(\delta_w)}(z/\delta_w)^{-\gamma(\omega_s/ku_{*c})} \quad \text{for} \quad z > \delta_w \quad \text{(eq. 56)}$$

$$C_z = C_{(z_0)}(z/z_0)^{-\gamma(\omega_s/ku_{*wc})} \quad \text{for} \quad z < \delta_w \quad \text{(eq. 57)}$$

Being z_0 the height of the bottom roughness, $C_{(\delta w)}$ and $C_{(z0)}$ the reference concentrations at the top of the wave boundary layer and at z_0 respectively.

Accordingly, the power equation approach used here to fit the concentration profiles was:

$$C_z = C_r(z/z_r)^{-\gamma(\omega_s/ku_*)} \quad \text{(eq. 58)}$$

Where C_z is the concentration along the profile (z) given by the ABS measurements and C_r the concentration at the reference level (z_r).

The burst-averaged concentration profiles exhibit strong acoustic signals due to the ABS response to the very strong sound reflection below the real surface of the seabed. Above the strongest acoustic return exists a break-slope point in the SSC-profiles which is considered as the lowest echo uncontaminated by backscatter from the seabed (Lee et al., 2004; Cacchione et al., 2008). In this work the position of the break-slope point along each profile is found when the second discrete derivative converged to zero. One centimetre above this point was here defined as z_r and the reference concentration (C_r) was the concentration estimated at this reference level (z_r). For practical reasons, the reference level is defined here as the position (in cm) relative to the ABS cell.

The SSC-profiles were analysed using the exponential and the power approaches and also separating two approaches from the seabed (SB) to the reference level (z_r) and above it as suggested by some authors (Bolaños et al., 2012; Davies and Thorne, 2016).

› *Intra-burst or time-varying SSC analysis*

The ABS recorded the backscattered signal during 9 minutes at a sampling rate of 1 Hz every hour (one burst), which results on 540 profiles per burst. These 540 SSC profiles are here mentioned as intra-bursts or time-varying SSC-profiles and provided key information about the high-frequency SSC patterns and their evolution in a short temporal and spatial-scale and the potential processes controlling sediment resuspension and transport. The SSC and hydrodynamics relationship was not always direct or evident because of the lack of high-resolution hydrodynamic measurements. In addition sensor internal factors and/or external factors (related to the environment) could modify the direct interconnection or response of the sediment movement induced by the hydrodynamics. Nevertheless, general trends could be observed and inferred.

The spectral analysis is a useful tool to analyse in the frequency domain the SSC rhythmicity at a desired height above the bottom or through the measured profiles. The analysis in frequency domain allows elucidating if the suspended sediment shows rhythmic patterns as a consequence of i.e. gravity waves. Frequency domain was separately analysed into 0.05-0.25 Hz frequencies range potentially triggered by the sea-swell waves with peak periods of 5-20 s and into 0.005-0.05 Hz frequencies range potentially related to infragravity waves or wave groups with peak periods between 20-200 s.

› *Fast Fourier Transform*

The SSC frequencies were evaluated with spectral analysis using the Fast Fourier Transform (fft). Fft has been widely used in studies of sediment and bedform dynamics when high-resolution data is available generally, at the last meter from the seabed. Fft analysis provides identification of the frequencies and domains of the SSC events and potentially linked to

sediment and hydrodynamic interrelations (Kularatne and Pattiaratchi, 2008; O'Hara Murray et al., 2012; Bakker et al., 2016; Bertin et al., 2018). The SSC time series was first detrended by the subtraction of the mean value resulting on a zero-mean time-varying series of SSC at each ABS cell. The zero-mean time series were filtered into infragravity (0.005-0.05 Hz) and sea-swell (0.05-0.25 Hz) frequencies band using a band pass filter and the Discrete Fast Fourier Transform was calculated at each frequency band converting the SSC time series from time domain to frequency domain. Finally, a 5 points window was applied to smooth the spectrum.

› *Wavelet*

Wavelet analysis is a common tool for analysing localized variations of power time series which discomposing into time-frequency space allow to determine the dominant modes of variability and how those modes vary in time (Torrence and Compo, 1998). Wavelet analysis indicates the SSC spectral density oscillations and the frequencies linked to these oscillations in hertz (Hz). One of its distinguished features is the capability to analyse time varying signals with respect to time and space, which let to capture rapid changes in dynamic properties of i.e. surface waves (Liu and Babanin, 2004). This Fourier analysis extension is particularly effective using continuous wavelet transform with the complex valued Morlet wavelet that provides a local energy spectrum for every data point of the time series (Liu and Babanin, 2004). The wavelet transform produces an "instantaneous" estimate or local value for the amplitude and phase of each harmonic and this allows detailed study of nonstationary spatial or time-dependent signal characteristics (Meyers et al., 1993).

The wavelet analysis requires that time series must have zero mean and be localized in time and frequency space (Farge, 1992; Torrence and Compo, 1998). Thereafter, Morlet wavelet function was applied at each ABS cell.

Chapter IV. Contemporary genesis of sand ridges in a tideless erosional shoreface

Part of the content of this Chapter is published in Guerrero et al. (2018): Guerrero, Q., Guillén, J., Durán, R., Urgeles, R., 2018. Contemporary genesis of sand ridges in a tideless erosional shoreface. Mar. Geol. 395, 219–233. doi:10.1016/j.margeo.2017.10.002

1. Introduction

Subaqueous dunes are ubiquitous bedforms on continental shelves with heights ranging from centimetres to several metres and wavelengths ranging from a few metres to hundreds metres (Ashley, 1990). In sandy environments, these bedforms are usually classified as subaqueous sand dunes, sand waves or sand ridges in relation to their genetic mechanism (see Simarro et al., 2015 for a discussion of these terms). In general, the terms sand dunes and sand waves are used to refer to transverse bedforms linked to unidirectional or bidirectional flows, respectively (Allen, 1980; Ashley, 1990). They are usually active in response to present-day hydrodynamics. On the other hand, the term sand ridges is used to refer to bedforms of slightly larger dimensions that can be either active or relict (Yang, 1989; McBride and Moslow, 1991; Dyer and Huntley, 1999). They have a "geological history" from their generation in shallow waters, as sand ridges connected to the shoreface, until they drown as a consequence of sea-level rise, forming a field of isolated bedforms in deeper waters (Stahl et al., 1974; Amos and King, 1984; McBride and Moslow, 1991; Dyer and Huntley, 1999; Snedden and Dalrymple, 1999; Snedden et al., 2011; Nnafie et al., 2014; Simarro et al., 2015; Durán et al., 2016, 2017). When sand ridges are located from the foot of the shoreface to the inner part of continental shelves, they are defined as shoreface-connected (or attached) sand ridges (SFCRs); otherwise they are defined as shoreface-detached sand ridges (SFDRs).

Huthnance (1982) proposed a fluid-dynamic model for linear sand banks in tide-dominated settings which has later been accepted for the genesis of sand ridges on storm-dominated shelves (Dalrymple and Hoogendoorn, 1997; Snedden and Dalrymple, 1999). Based on this model, the requirements for sand ridge development are (i) availability of sufficient sand, (ii)

presence of currents capable of transporting sand and (iii) an initial irregularity in the seabed topography. The availability of sediment is typically associated with ebb-tidal deltas or fluvial deltas (McBride and Moslow, 1991; Dyer and Huntley, 1999; Snedden and Dalrymple, 1999), while sand transport is mainly attributed to near-bottom currents induced by wind storms, waves and/or tide-induced flows at the foot of the shoreface (Trowbridge, 1995; Goff et al., 1999; Snedden and Dalrymple, 1999). Trowbridge (1995) explained SFCR formation on storm-dominated shelves as morphodynamic self-organization related to recurrent storm-driven currents. In this model, the physical mechanism for the development of the sand ridges is the offshore deflections of the storm-driven alongshore flow at the ridge crests and sediment convergence in the offshore direction due to the slope. Successive improvements of the model included bedload, suspended load sediment transport and a depth-dependent stirring of sediment by waves (Calvete et al., 2001; Nnafie et al., 2014). Though all these models assume constant sea level, Nnafie et al (2014) tested the effects of sea-level rise on ridge dynamics. They showed that under sea-level rise the height of the ridges increases and their migration speed decreases until they become inactive because they drown. The time-scale involved in SFCRs has been linked to changes in sea level and is therefore of the same order of magnitude as these eustatic variations (Nnafie et al., 2014). However, the genetic mechanisms and timing required for the development and evolution of SFCRs are currently not well constrained because of the long time-scales usually considered (hundreds/thousands of years).

Sand ridges in the Mediterranean are mostly located from the middle to the outer shelf (Correggiari et al., 1996; Bassetti et al., 2006; Simarro et al., 2015; Durán et al., 2015, 2016). They are located at depths where the present-day hydrodynamics are insufficient to transport enough sand to generate them, and they sometimes contain bioclasts typical of coastal areas (Bassetti et al., 2006). In general, it is accepted that sand ridges on the middle and outer Mediterranean shelves developed as SFCRs in former coastal environments and in a transgressive scenario. Particularly, their genesis is set during periods of sea-level rise deceleration such as the Younger Dryas (Bassetti et al., 2006; Durán et al., 2016). During these periods, the combination of sediment availability and the reduced rates of sea-level rise allowed sand transport and/or reworking, leading to the development of sand ridges. Subsequently, when sea-level rise accelerated, SFCRs were progressively drowned and detached further from the shoreface (Correggiari et al., 1996; Bassetti et al., 2006; Simarro et al., 2015; Durán et al., 2016).

The purpose of this chapter is to analyse the contemporary formation of a sand ridge field on the shoreface of a tideless erosional deltaic system: the Ebro Delta, in the western Mediterranean Sea. We characterize the morphodynamics, geological setting and timing of development of the ridges, and the processes associated with the onset of the field. Finally, we discuss potential

analogies with SFCRs and SFDRs on storm-dominated shelves. With this study we aim to better characterize the initial stages of SFCR formation and improve our understanding of the timing and processes involved in SFDR development, particularly for the middle and outer shelves of the Mediterranean Sea.

2. Holocene Ebro Delta evolution

Direct sediment supply by the Ebro River during the Holocene has allowed the delta to prograde seaward across the inner shelf and develop the Ebro prodelta (Díaz et al., 1990; Somoza et al., 1998). As in other large deltas of the world (e.g. the Mississippi, the Nile, the Yangtze and the Rhone), the base of the sedimentary progradational deposits is attributed to the sea-level stabilization (coinciding with the present sea level) during the last 5000-7000 years (Maldonado and Riba, 1971). The thickness of the Holocene delta deposits ranges from 18 m on the landward side of the delta to 51 m at the delta front (Somoza et al., 1998). The Holocene stratigraphy is formed by retrogradational and progradational high-frequency sequences set within the transgressive and highstand system tract (Somoza et al., 1998). The upper sedimentary sequence of the Ebro inner continental shelf is made of several superimposed prograding delta lobes that developed due to successive channel switches on the delta plain during the last millennium (see Maldonado and Riba, 1971; Díaz et al., 1996; Somoza et al., 1998; Somoza and Rodríguez-Santalla, 2014; for an extended description of the former delta lobes and channels). Other than the present river mouth, traces of three ancient river mouths and their respective lobes can be found on the delta plain (Maldonado and Riba, 1971; Somoza et al., 1998; Somoza and Rodríguez-Santalla, 2014). Each of these former river lobes was developed from its corresponding river channels (Fig. 3 b): (i) the *Riet-Vell Lobe* is the most southern lobe (*Riet* river course) and was active between 1100 and 1300 Anno Domini (AD); (ii) the *Sol-de-Riu Lobe* resulted from the progressive avulsion of the river mouth to the north and was fed by the *Riet Zaida*, the river course that remained active between 1350 and 1700 AD; and (iii) the central lobe (located between the two ancient lobes) consists of the *Migjorn Lobe* developed in the period 1700-1800 AD and the *Buda Lobe*, which developed to the north from the *Migjorn Lobe* and had three river channels: the *Gola del Nord River Channel*, the *East River Channel* and the *South River Channel* (< 1880-1937 AD) (Fig. 13). The *Buda Lobe* constitutes the Cape Tortosa river mouth. In the 1930s, a new river mouth opened to the north of Cape Tortosa, and has progressively become the main river mouth (Guillén and Palanques, 1997b; Somoza et al., 1998). This last change in the river mouth position led to severe coastal retreat (ca. 2500 m between 1947 and 2014, ~37 m/y) at the abandoned river mouth (Cape Tortosa). Here, the loss of delta plain surface occurred at different rates, with the period from 1957 to 1973 the time-span with the largest coastal erosion rates (Jiménez and Sánchez-Arcilla, 1993).

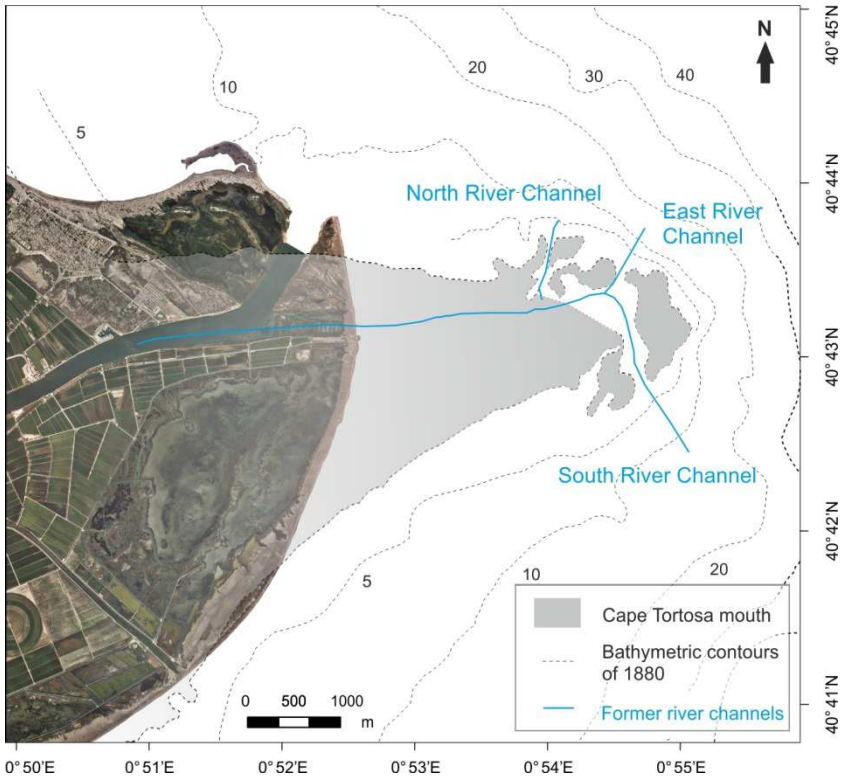

Fig. 13. Ebro Delta aerial photograph of 2014 with the current river mouth course. The bathymetric contours of 1880 are overlapped (dashed lines) and the former Cape Tortosa river mouth is indicated with grey shadow area. The blue lines correspond with the ancient river courses of the *North East and South River Channels* (river channels active during this period).

3. Results

3.1. Sand ridge field characteristics

The grain size analyses of the surficial sediment of the sand ridge field showed a poorly sorted fine sand composition with a d_{50} of 210 μm (91% sand and 9% mud) at the tripod location (Fig. 3 b). The mud content increased and the sediment became silty sand along the corer depth.

Detailed morphobathymetric analysis of the ridge field on the shoreface of the Ebro Delta was carried out for surveys B-2004 and B-2015 and no significant morphometric changes were observed over the study periods. The sand ridge field occupies an area of 6.5 km^2 between the 5 and 15 m isobaths of the B-2015. However, the field probably spreads out in shallower waters beyond the mapped area (Fig. 14). The field is composed of seven major ridges lying over the shoreface of the Ebro Delta. They display straight rectilinear crests arranged approximately 40° from north that often display bifurcations (Fig. 14). The orientation of the crests with respect to the shoreline varies from 18° to 50° because of the circular-shape of the shoreline. The ridges are ~2000 m long over the mapped area, though they could be up to one km longer considering that they probably extend into shallower, non-mapped waters (Fig. 14). Two areas where ridges

display a slightly different morphology are distinguished: the deeper north-northeastern sector, where the ridges are steeper and the crests are narrower; and the shallower south-southwestern sector, where they are smoother and have wider crests. A large amount of rounded hole-like features are found along the troughs of the sand ridges, mostly in the deeper north-northeastern sector. Some of the hole-like features are arranged linearly in a NNW-SSE direction along the troughs of the bedforms (Fig. 14).

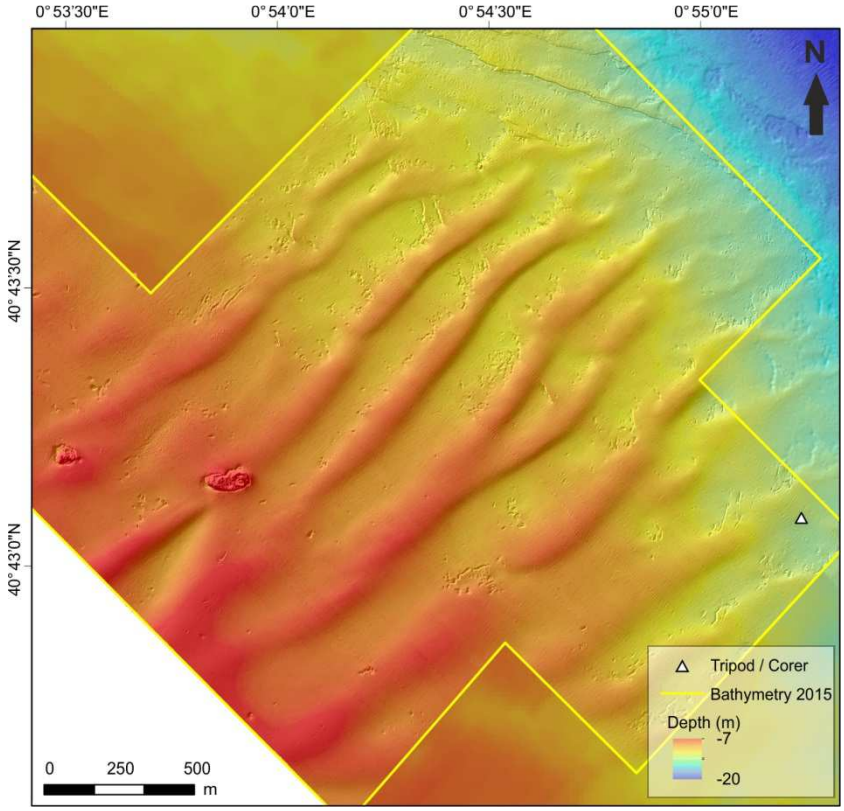

Fig. 14. Very high-resolution bathymetry (0.5 m grid-spacing) acquired in 2015, showing the sand ridge field. The triangle shows the location of the benthic tripod and the sediment sample and the polygon shows the extent of the 2015 survey.

The morphometric analysis using the highest-resolution bathymetry (B-2015) indicates that the ridges are 0.5-2.5 m high with a mean height of 1.36 m (Fig. 15 a). The statistical distribution of the heights shows a smooth gauss-shaped curve with peaks of frequency between 1 and 1.5 m. The highest sand ridges are located in the central and SE sectors of the field and the height decreases progressively towards deeper and shallower areas (Fig. 14). The wavelengths range from 100 to almost 400 m (median 250 m) (Fig. 15 b). As observed in the heights, the wavelength also displayed spatial differences, with larger values in the S-SE sector and in shallower areas, and smaller values in the N-NW sector and in deeper areas, where the crests tend to be arranged progressively closer (Fig. 14). Values of the asymmetry index embraced the

full range from -1 to 1. The gauss-shaped distribution with the peak around zero indicates that the sand ridges are mostly symmetric, though positive and negative asymmetries (lee side facing SE and NW, respectively) are also observed (Fig. 15 c). The sand ridge steepness ranges from 0 to 0.01, with a mean value of 0.005, indicating rather smooth bedforms (Fig. 15 d). The clear unimodal behaviour of the steepness histogram indicates no significant spatial variability in this parameter.

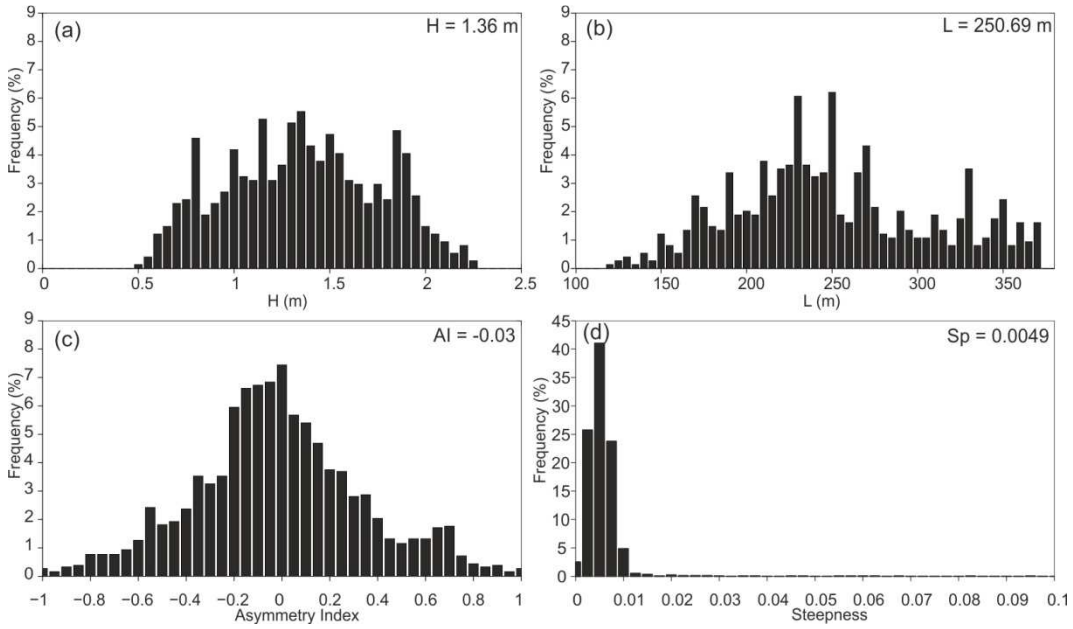

Fig. 15. Distribution of geometric parameters for the sand ridge field obtained from the bathymetry acquired in 2015. The histograms provide statistics for the analysed variables with the values in the top-right corner in each histogram indicating the respective median values of (a) sand ridge height; (b) sand ridge wavelength; (c) asymmetry index; and (d) steepness.

3.2. Sand ridge migration

Sand ridge migration rates were determined by comparison of the ridge crests in the region where bathymetries B-2004 and B-2015 overlap. Figure 16 (a) displays the estimated migration from August 2004 to November 2015 superimposed on the most recent bathymetry (B-2015), where the arrows represent the migration magnitude along the profiles (from the crest position in B-2004 to the analogous crest point in B-2015). Overall, the migration seems consistently towards the SE over the entire field (Fig. 16 a). This migration ranges from ~40 m to 180 m and the migration values displayed a normal distribution, while the mean migration is ~116 m, which nearly coincides with half of the sand ridge wavelength (Fig. 16 b). The migration rate is therefore ~10 m/y (11.33 years between acquisitions of the two bathymetric data sets). Looking at each crest separately, it can be seen that the mean migration ranges from less than 85 m (crest number 5) to more than 140 m (crest number 3) (Fig. 16 a, c). Ridges with longer crests (2, 4, 6,

7 and 9) had similar mean migration values and a narrower range of variability (Fig. 16 c). This lower variability probably results from the fact that longer ridges have more representative statistical variables. Despite large scatter in measurements, it can be observed that in general migration rates decreased with depth (Fig. 16 d). Migration rates predominantly ranged between 60 and 120 m in water depths >10 m and between 80 and 140 m in water depths <10 m.

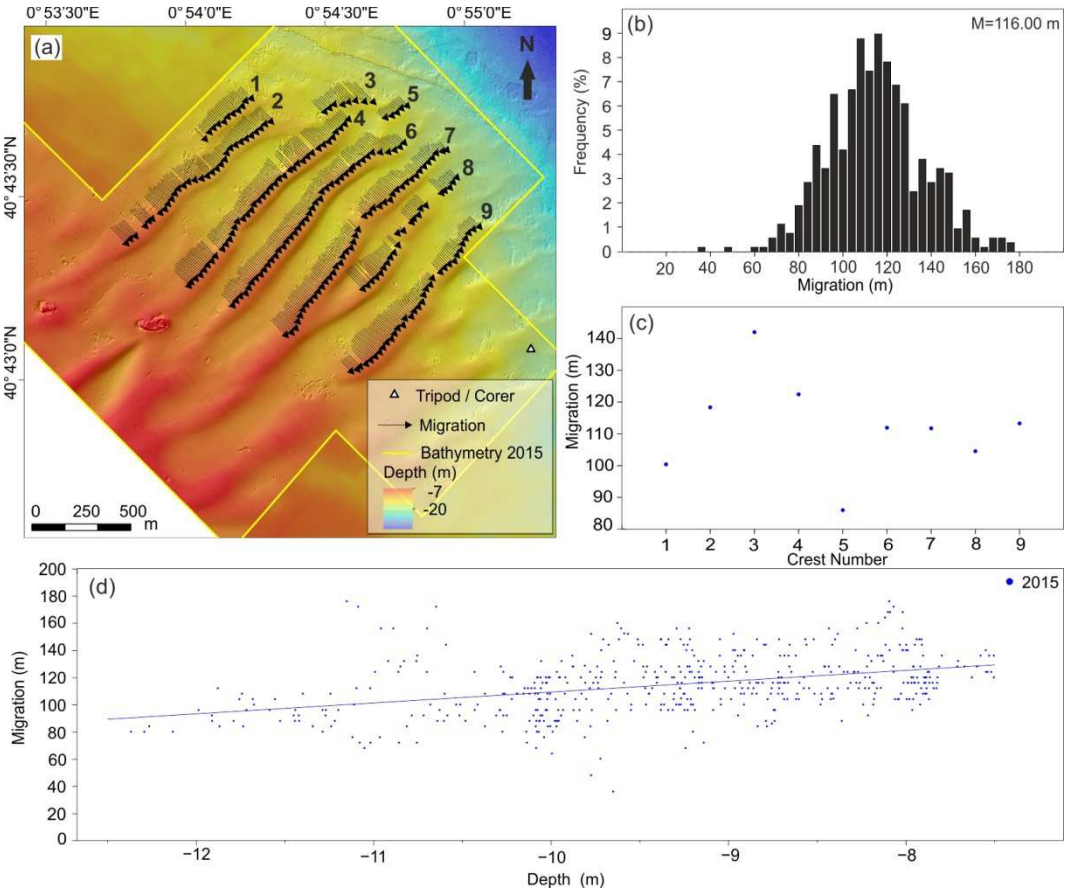

Fig. 16. (a) Migration magnitude along profiles. Arrows display the magnitude and direction of the migration from the initial point (the crest point in the 2004 data set) to the final point (the crest point in the 2015 data set). The numbers refer to the ridge crests in Fig. 16c. (b) Histogram showing migration rate distribution and mean migration rate (top-right corner) (c) Mean migration rates for each crest separately. (d) Migration values as a function of depth for the 2015 data set.

Bathymetric differences between the 2015 and 2004 surveys (Fig. 17) show a banded pattern of alternating negative elevation differences (erosion or sediment loss) and positive elevation differences (sedimentation or sediment gain) in the central sector of the sand ridge field, while erosion took place mostly in the surrounding areas (Fig. 17). Indeed, the ridge crests in 2004 were eroded ~2 m (maximum values of 3 m), while the troughs in 2004 underwent deposition of up to ~2 m of sediment (Fig. 17). This is in agreement with the magnitude of migration of the sand ridges (approximately half the wavelength), in which the trough locations in 2004 were

replaced by the crests in 2015 and vice versa. Therefore, Fig. 17 actually displays the migration of individual sand ridges. A differential thickness relative to depth is also evident in Fig. 17, with higher values in the central and shallower sectors of the survey and a progressive decrease along the crests towards deeper waters. Overall, the sedimentary balance in the area where the two surveys overlaps between August 2004 and November 2015 (~2.6 km²) is $0.635 \cdot 10^6$ m^3 of sediment loss.

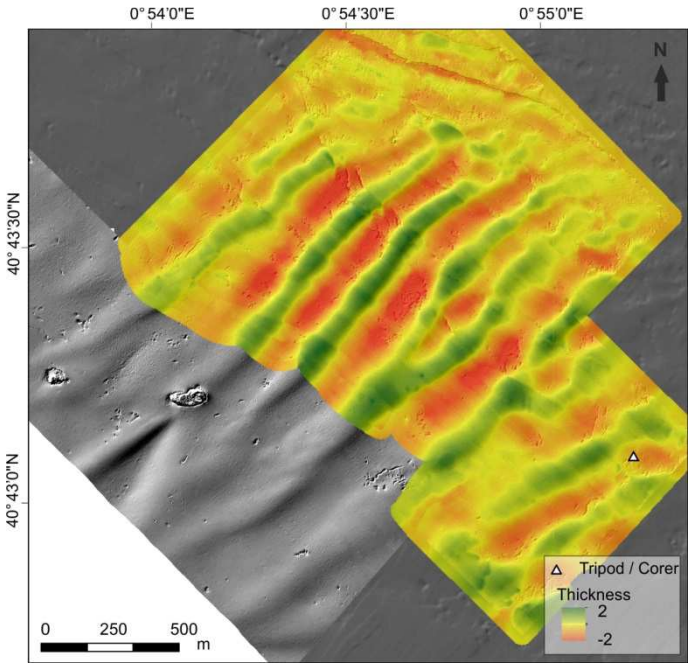

Fig. 17. Sediment erosion/accumulation map obtained from differential bathymetry (2015 minus 2004). Negative elevation differences correspond to erosional areas and positive elevation differences to depositional areas; non-differences are areas displaying only minor changes. The surface is overlaid on the shaded-relief map of B-2015.

3.3. Wind, wave and current time series

Wind speed time series during the tripod deployment period display a cyclic daily behaviour with higher values during days and lower values during nights (Fig. 18 a). High-gust wind speeds of up to 10 m/s were quite frequent, but were especially persistent in November and December and from mid-January to mid-February. From the end of February, the cyclic daily behaviour was accentuated, with diurnal-nocturnal differences of up to 20 m/s. High wind speed events were also frequent from the end of March to the end of the time series data (mid-April). When high wind speeds occurred, the wind direction clearly funnelled towards the SE (Mistral winds), which is the characteristic wind direction in the area.

The wave time series show several periods of increased significant wave height (H_s), especially in November and December, corresponding to the seasonal regime of the area. In general, the

most severe wave-storm events came from the E-SE, although NW wave-storm events also occurred (Fig. 18 b). During the recording period the two largest storms came from the east and had maximum H_s values reaching almost 4 m in November and December (Fig. 18 b).

The near-bottom current intensity measurements showed similar behaviour to the wind and wave data, with the most energetic events in November and December (Fig. 18 c). From January to the end of the recorded time series (April), sporadic high-intensity currents also occurred (Fig. 18 c). The maximum near-bottom currents were between 0.4 and 0.6 m/s, flowing towards the SSE (Fig. 18 c). In general, the current direction funnelled towards the SE when the velocity increased to 0.2 m/s. Wind and current time series reveal that high-intensity events of both variables were simultaneous. In particular, current events flowed towards the SE when wind events came from the NW, suggesting that high-speed near-bottom currents were induced by the NW (Mistral) winds.

The progressive vector of the near-bottom current intensities resulted in virtual displacement of up to 1100 km towards the south and almost 250 km towards the east during the recording period (Fig. 18 d). Most of this virtual displacement took place during the first period of the whole time series, when the most severe wind and wave-storm events occurred. Accordingly, high-intensity near-bottom currents induced by the NW winds and eastern wave-storms governed the hydrodynamics and consequently the sediment dynamics in the area.

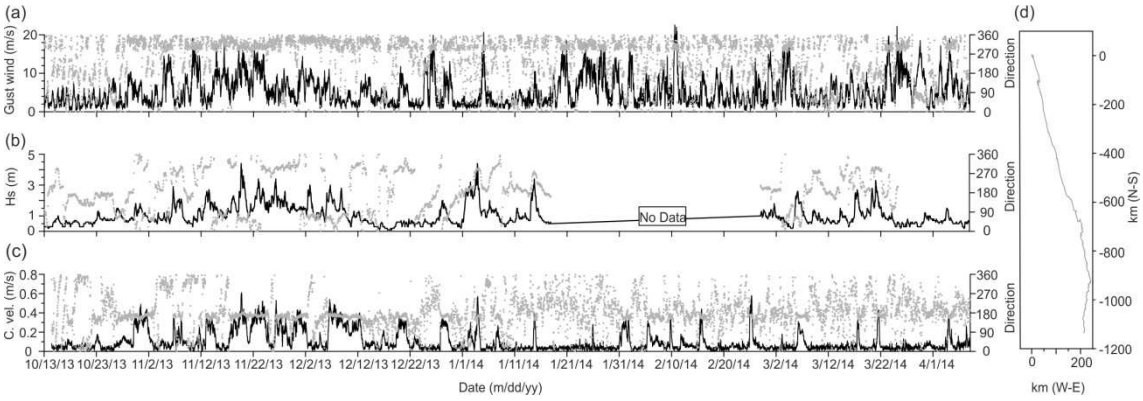

Fig. 18. Time series dataset during the tripod deployment of (a) wind maximum gust speed and the respective maximum wind gust direction at the Buda Island observatory (location in Fig.1). (b) Significant wave height and wave direction propagated from the location of the Tarragona buoy to the tripod location. (c) Current velocity and current direction at the tripod location at ~1 mab. Black lines correspond to the speed magnitudes and dots to the directions for subplots a, b and c. (d) Progressive vector of the current intensities where the y-axis displays the N-S direction and the x-axis displays the W-E direction of the near-bottom current intensities.

3.4. High-resolution sub-bottom profiles

High-resolution seismic profiles display a seafloor with a clear convex-shape typical of a delta lobe with sand ridges lying mostly in the central area (Fig. 19). Differences in the morphologies of the ridges seem to be related to slight changes in the seafloor slope and depth because of the lobe-convex form: the sand ridges are more symmetric and higher in the central area of the delta lobe, becoming progressively smoother and flatter towards deeper water.

On sub-bottom profiles, a major erosional surface defining two major sedimentary units can be traced across most profiles. This surface corresponds to a high-amplitude, fairly continuous albeit irregular, semi-horizontal reflector that emerges at the seabed in places (Fig. 19 a). Though the erosional surface could not be traced at all locations (e.g., beneath the largest sand ridges), it clearly marks the base of the bedforms. The sedimentary unit that corresponds to the sand ridges, limited by this erosional surface and the seafloor, displays very little internal reflectivity (at some points there is even no penetration), probably because of the relatively homogeneous sandy composition of the sand ridges (Fig. 19).

The seismic unit below the erosional surface is characterized by dipping reflections. At the NW tip of the profiles, these reflectors seem to dip to the NW, while in the central and SE sectors of the sand ridges the apparent dip is to the SE (Fig. 19 b). These reflectors are sometimes truncated at the seafloor at the location of troughs and in the deepest part of the ridges' stoss side (see zoom, red rectangle, in Fig. 19 b). In fact, this geometry suggests that the sand ridge troughs have been progressively eroding the lobe sediments, presumably as a result of their migration. Therefore, the occurrence of such an erosional surface suggests an erosional period before or concomitant with the sand ridge development.

In the sand ridge field area there is considerable evidence of fluid (likely gas) expulsion in the form of gas flares (Fig. 19). These gas flares are associated with the hole-like features identified in the swath bathymetry and display a V-shape in profile view, suggesting that the hole-like features are pockmarks linked to fluid migration in the dipping strata below the erosional surface.

The erosional surface tracked along the sub-bottom profiles was interpolated to produce an isobaths map over the sand ridge area (Fig. 20 a). The erosional surface extends from 7 to 19 m below sea level, defining a lobe-like shape. Comparison of the erosional surface with the nautical chart of 1880 suggests that the erosional surface and the former Cape Tortosa river mouth are closely related (Fig. 20 a): the ancient *North, East and South River Channels* can be identified on the erosional surface, especially in the case of the *East River Channel*, the main river channel at that time (white arrows in Fig. 20 a).

The thickness of the sedimentary unit above the erosional surface in 2015 (considering only the sector where both surfaces overlap) ranges from 1 to 2 m in most areas, although it may reach more than 3 m at the bedforms crests (Fig. 20 b). The total sediment volume involved in the sand ridge sedimentary unit (calculated only in the area where the three surfaces overlap, ~2.6 km^2) was about $4.6 \cdot 10^6$ m^3 in 2004 and $3.9 \cdot 10^6$ m^3 in 2015, suggesting that this area of the delta lobe is currently eroding.

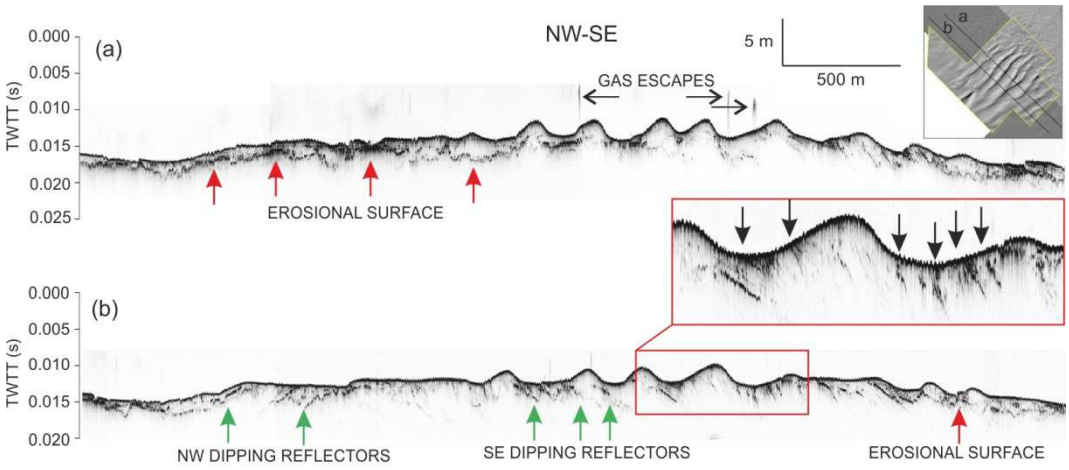

Fig. 19. Detail of two high-resolution sub-bottom profiles (location in top-right corner). The main erosional surface and the NW and SE dipping reflectors are indicated with upwards vertical arrows; acoustic plumes interpreted as gas escape to the seafloor are shown with horizontal arrows. The zoom of Fig.10b represents the dipping reflectors and the base of the sand ridges that outcrops at the seafloor in the troughs and on the stoss side, indicating that trough migration has been eroding progressively downward into the older sediments.

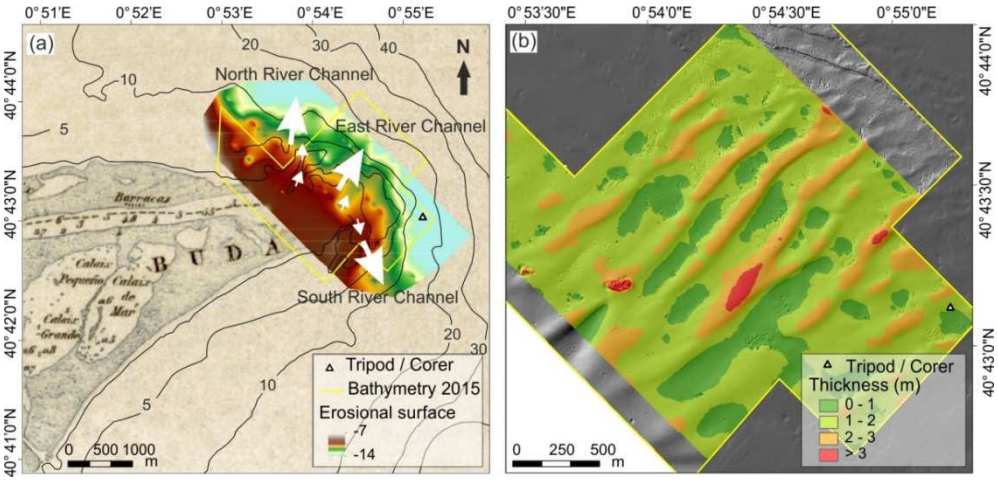

Fig. 20. (a) Erosional surface beneath the sand ridge field obtained from interpolation of tracked depth in sub-bottom profiles. The surface is overlaid on the nautical chart of 1880. Black lines show bathymetric contours from the 1880 nautical chart. Former River channels are also indicated with their names and white arrows, as interpreted on the erosional surface. (b) Sediment thickness of the sand ridge unit calculated between the erosional surface and the B-2015 survey, with the bathymetry-derived hillshade in grey-scale.

4. Discussion

4.1. Evolution of the Cape Tortosa and the onset of the sand ridges

The last change in position and orientation of the Ebro River mouth is chiefly responsible for the morphological variations of the delta plain and sediment dynamics on the shoreface. The contemporary evolution in the Cape Tortosa area can be divided into a progradational period from 1880 to about 1940 and an erosional period from 1940 to the present (Fig. 21).

The circular-shaped configuration of the erosional surface obtained from high-resolution sub-bottom profiles is compatible with the progradational period of the Cape Tortosa river mouth. Furthermore, the delta plain morphology and the 1880 river channels can be identified on this erosional surface (Fig. 20 a). The NW and SE dipping reflectors below the erosional surface identified on the sub-bottom profiles were also arranged to the north and to the south of the main channel in 1880 (the *East River Channel*). Therefore, these reflectors are probably related to progradation of the delta relative to the active period of the Cape Tortosa River mouth.

In the 1940s, a new river mouth opened to the north and progressively became the main river channel (Fig. 21 b, c and d). Thereafter, the former Cape Tortosa river mouth was progressively abandoned and eroded, leading to severe shoreline retreat of ca. 2500 m from 1947 to 2014 (~ 37 m/y) (Fig. 21 d). This shoreline retreat was non-uniform being the highest rates between 1957 and 1973 with maximum values of ~ 70 m/y. After that period ~ 25 m/y was the average rate of the coastal retreat at the Cape Tortosa former river mouth (Jiménez and Sánchez-Arcilla, 1993). Thus, the erosional surface can be interpreted as a ravinement surface that developed during the retreat of the Cape Tortosa river mouth. The sediment eroded from the river mouth after the 40s was transported by waves and currents and redistributed along the delta plain and shoreface, forming the sand ridge field. In most examples around the word sand ridges develop above an equivalent erosional surface caused by marine transgression (Snedden and Dalrymple, 1999; Goff, 2009).

The precise date of the initial development of sand ridges is uncertain, although it can be bounded between later forties and eighties. The first observations of “sand bars” on the Cape Tortosa shoreface were recorded in 1988 (Guillén and Palanques, 1997a), but it is probably that bedforms started to form earlier on, some years (maybe decades) after coastal retreat started during the forties.

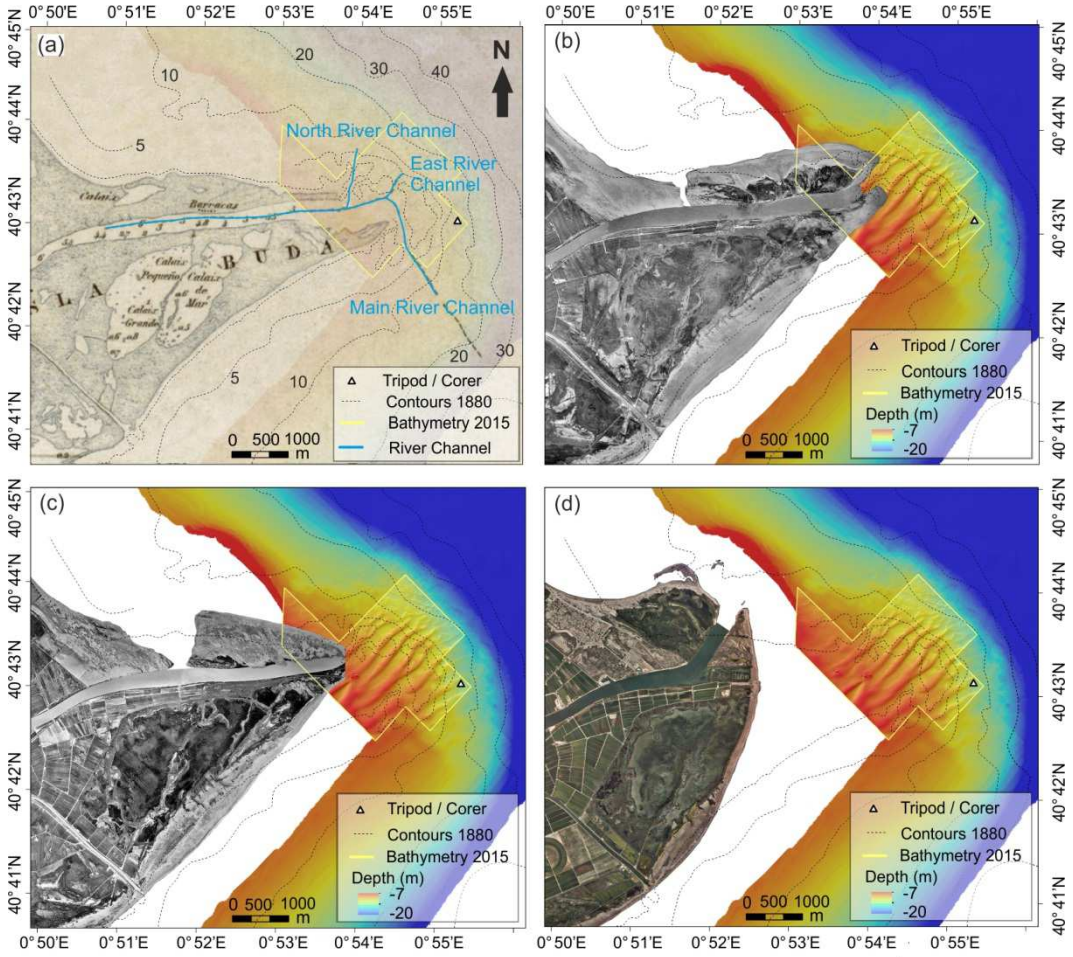

Fig. 21. Ebro river mouth evolution from1880 to 2014. (a) Nautical chart of 1880 with bathymetric contours (dashed lines), which correspond with the progradational period of the Cape Tortosa river mouth, and the corresponding active river channel courses (in blue). (b) 1947 aerial photograph and multibeam bathymetric map of 2015, note that the river channel switched to the north with respect to the previous main river channel. (c) 1957 aerial photograph and multibeam bathymetry (B-2015) when the retreat and erosion of the Cape Tortosa river mouth started, note that then the northern river channel was the main river channel. (d) 2014 aerial photograph and multibeam bathymetry (B-2015) where the shoreline retreat and the erosion of the former river mouth can be observed since the forties. The location of the sand ridges with respect to the Cape Tortosa river mouth can also be appreciated.

4.2. Sand ridge genetic mechanism and dynamics

As previously stated, the requirements for sand ridge development are availability of sufficient sand, the presence of currents capable of transporting sand and an initial irregularity in the seabed topography (Huthnance, 1982). These conditions are fulfilled in the Ebro Delta sand ridges field. First, the sand ridges were formed in an erosive context after the abandonment of the Cape Tortosa river mouth and the bedform development was favoured by the availability of large amounts of unconsolidated (eroded) sand. Second, the presence of waves and currents capable of mobilizing the sandy sediment favoured the scenario for sand ridge formation.

Finally, a ravinement surface full of irregularities such as incised channels could have provided the necessary pre-existing roughness for flow-seabed interaction, and the river mouth sand bar that was emerged in 1880 could even have been an initial precursor and have evolved into sand ridges.

The genesis of sand ridges is commonly linked to unidirectional or bidirectional near-bottom currents induced by tides, wind storms and/or wave-storms in the coastal zone (McBride and Moslow, 1991; Dyer and Huntley, 1999; Snedden and Dalrymple, 1999; van de Meene and van Rijn, 2000; Li and King, 2007; Snedden et al., 2011; Thieler et al., 2014; Simarro et al., 2015) In agreement with these observations, the hydrodynamic measurements acquired in this study, together with the wind field data, show a direct relationship between the strong NW winds (Mistral) and high-speed near-bottom current events (Fig. 18 a and c). A combination of high-speed current and wave-storm events is capable of mobilizing sand (Jiménez et al., 1999; Guillén et al., 2002; Palanques et al., 2002). Accordingly, considering the arrangement of the sand ridges with respect to the present-day Ebro Delta shoreline (18-50°) and the direction of high-speed currents with respect to the sand ridges crests (~50°), the sand ridges were probably generated and mainly maintained by the southeastward currents induced by the Mistral winds, as suggested by Urgeles et al. (2011). The obliquity of the Ebro sand ridges with respect to the shoreline is what leads to the convergence of the sediment flux to the ridges crests and the further offshore deflection, in agreement with Trowbridge (1995).

The sand ridges in the Ebro shoreface migrated ~10 m/y towards the SE between 2004 and 2015. Sand ridges migration displayed a decreasing gradient from shallower to deeper parts of the area. Actually, the sand ridges migration rate is usually related to depth (Nnafie et al., 2014) and ridge height (Van de Meene and van Rijn , 2000). Weakening of the flow-induced bedload sediment transport with depth along the ridge can be a potential contribution to the oblique crestline orientation. On the other hand, the direction of sand ridges migration would therefore imply asymmetries with the lee side of the sand ridges facing to the SE. However, the ridges are mainly symmetric and sometimes even show opposite asymmetries with the lee side facing both to the NW and the SE (Fig. 15 c). This ridge configuration could result from competition between the severe E-SE wave-storm events and the strong currents induced by the NW winds. Both could reshape the sand ridges with the first producing NW-facing lee sides and the second SE-facing lee sides. The combination of the north-westerly directed wave-induced current and the south-easterly directed current induced by the strongest local (Mistral) wind acting in an opposite direction could reshape the ridges to more symmetric geometries (as observed in other areas e.g. Li and King, 2007), particularly in shallower areas where the wave effects are more intense on the seabed and sand ridges display more symmetric geometries. In fact, an active sediment transport inferred from ripple formation and morpho-dynamics caused for both SE

currents and eastern storms has been described in this area (Guerrero et al., 2017). Therefore, sand ridge migration might have taken place by pulses when current events occurred and thereafter been reshaped by the E-SE storms to form more symmetric geometries.

4.3. The Ebro Delta sand ridge field: an analogue for the initial stages of sand ridges

Sand ridges have been observed on many continental shelves worldwide (Swift et al., 1978; Figueiredo et al., 1982). Their abundance is a consequence of the global sea-level rise during the Holocene, which left continental shelves covered by sandy sediments left behind by shore retreatment, in addition to transgressive conditions that favoured the formation and maintenance of the ridges (Snedden et al., 2011). Table IV summarizes the main characteristics of some of the sand ridges (connected and detached from the shoreface) on storm-dominated continental shelves, including the Ebro Delta ones. In general, sand ridges form elongated sand bodies ranging from a few to tens of kilometres long, hundreds of metres to a few kilometres apart, and one to ten metres high. They are all arranged obliquely to the shoreline or to the bathymetric contours (Table IV). Storm-dominated sand ridges are composed of fine to coarse sand and are generally asymmetric.

Storm-dominated sand ridges are usually associated with fluvial/ebb-tidal deltas and barrier islands in a shoreline retreat setting that provide the amount of sand needed for ridge development (Swift et al., 1972; McBride and Moslow, 1991; Snedden et al., 1994; Snedden and Dalrymple, 1999). The erosion of the former Cape Tortosa river mouth is the source of sediment on the shoreface, and the river mouth sand bar that was emerged in 1880 may have acted as a nucleus for the shoreface sand ridge development. The offshore, down-current direction migration rate (~10 m/y) of sand ridges in the Ebro Delta during the study period (2004-2015) lies in the range of storm-dominated SFCR migration, as on the US Atlantic coast (1-7 m/y; Swift et al., 1978; Swift and Field, 1981; Thieler et al., 2014) and Sable Island (5 m/y; Li and King, 2007). This migration rate is also consistent with models using oceanographic forcing conditions similar to those of our study area, where SFCR migration rates are from 1 to 10 m/y (Calvete et al., 2001). Furthermore, the migration of the sand ridges on the Ebro Delta is currently contributing to the shoreface ravinement process, mostly in the troughs (zoom Fig. 19 b). The erosional surface that represents the base of the sand ridges commonly outcrops at the seafloor in the troughs as well as on the stoss side, indicating that trough migration has been eroding progressively downward into the older sediments (zoom of Fig. 19 b). A similar configuration has been described in other storm-dominated SFCRs, where ridge migration combines with wave erosion to foster shoreface ravinement, by eroding the lower shoreface and

transferring sand to the sand ridges (Dalrymple and Hoogendoorn, 1997; Goff, 2014; Schwab et al., 2014b).

Though SFCRs are widespread on continental shelves, there are no present-day examples of SFCR development on the Mediterranean shelves (Table IV). The morphology, the oblique arrangement with respect to the shoreline and the main wind-induced current, the sediment grain size, the down-current migration and the development above an erosional surface are common characteristics of sand ridges located on storm-dominated shelves (McBride and Moslow, 1991; Snedden and Dalrymple, 1999; Calvete et al., 2001) and of the Ebro Delta sand ridges. Hence, taking into account the onset of the Ebro Delta sand ridges, they could be reasonably considered as a modern example of the initial stages of sand ridge development on Mediterranean continental shelves.

Looking further, time-scales involved in the genesis of transgressive sand ridges are thought to be of the same order of magnitude as those of sea-level changes: from hundreds to a few thousand years (Snedden and Dalrymple, 1999; Nnafie et al., 2014). However, here it is observed that sand ridges in a retreating shoreline could develop very rapidly, in a time-scale of the order of tens of years (Fig. 21).

The average estimated present-day Ebro Delta subsidence is 3 mm/y (Canvi Climàtic, 2008; Alvarado-Aguilar et al., 2012). Taking into account the global sea-level rise of ~1.5 mm/y according to the Intergovernmental Panel on Climate Change (IPCC, 2013), the estimated relative sea-level rise (RSLR) in the Ebro Delta was 4.5 mm/y during the period 1992-2007 (Canvi Climàtic, 2008). This RSLR rate for the Ebro Delta is quite similar to that during deceleration periods of the SLR in the Holocene, such as the Younger Dryas (e.g. 5.6 ±0.4 mm/y, Bard et al., 2010), when most of the SFDRs of the Mediterranean shelves are suggested to have developed (Bassetti et al., 2006; Durán et al., 2015, 2016). Therefore, this RSLR seems to favour the development of sand ridges. However, sand ridge preservation is unlikely in the Ebro Delta under the present conditions. If the shoreline position stabilizes, the sediment availability will drastically decrease, exposing the sand ridges to progressive degradation as a consequence of reworking by waves and currents. In fact, the sediment volume comparison of the surficial sedimentary layer suggests that the area is currently eroding. The loss of sediment between 2004 and 2015 (about 0.7 10^6 m^3) results in ~24 mm/y of height loss, of which 4.5 mm/y can be attributed to RSLR and the remainder to erosion of the sand ridge layer (19.5 mm/y). In this regard, it is worth noting that there is no evidence of sand ridge development on the two ancient lobes of the Ebro Delta. Since conditions of coastal retreat and large availability of sand in the shoreface should be equivalent during the former lobes abandonment, it implies that sand ridges (if developed) were eroded. In that case, it is inferred that the preservation of

sand ridges should be associated to the sea level rise and the consequent deepening of sand ridge location. In absence of rapid sea level rise, the shoreline tends to stabilize after several decades retreating, the amount of sandy sediment available decrease and the erosion dominates the shoreface because the high sediment dynamics in shallow waters. Preservation is only feasible when sea-level rise suddenly accelerates (such as during the Holocene after the Younger Dryas). If the sea-level rise accelerates, sand ridges will drown, relocating the SFCRs to the middle/outer shelves as SFDRs in which the near-bottom sediment dynamics is weaker and intense wave effects cannot reach the seabed (Goff et al., 1999; Nnafie et al., 2014). In fact, drowning of sand ridges should occur in a relatively short period just after or during their development; otherwise they will vanish fast because of reworking by waves and/or currents or lack of sediment to maintain them. It is accepted that sand ridge morphologies (height, width and length) do not change significantly beyond ~20 m depth (Goff et al., 1999; Nnafie et al., 2014), so drowning beyond that depth would probably enable the ridges to be preserved.

Table IV. Morphologic characteristics of sand ridges on storm-dominated shelves

Location	Height (m)	Wavelength/width (km)	Length (km)	Angle to the shoreline	Depth (m)	Type	Author
Ebro Delta shoreface	**0.5 to 2.5**	**0.1 to 0.4**	**2**	**~18 to 50° (clockwise)[a]**	**5 to 15**	**SFCR**	
Middle Atlantic Shelf of South America	4 to 10	2 to 8	220 (max.)	~35° (counter-clockwise)	8 to 24	SFCR	(Swift et al., 1978; Figueiredo et al., 1982)
US Atlantic Shelf	1 to 10	1 to 5	6 to tens	~20°-30° (clockwise)	4 to >20-35	SFCR	(Swift et al., 1972, 1978; Swift and Field, 1981; Figueiredo et al., 1982; McBride and Moslow, 1991; Snedden et al., 1994; Schwab et al., 2000, 2013, 2014; Calvete et al., 2001; Thieler et al., 2014; Warner et al., 2014)
Panama City, Florida Gulf of Mexico	1 to 4	-	-	Oblique	8 to 25	SFCR	(Goff, 2014)
Scotian Shelf (Stable Island Bank)	1 to 13	0.41 to 8	5 to 20	Oblique	15 to 40	SFCR	(Dalrymple and Hoogendoorn, 1997; Li and King, 2007)
North Atlantic Shelf	1 to 10	1 to 5	2 to 11	~15°-30° (clockwise)	~20 to >100	SFDR	(Swift et al., 1972, 1973; Stahl et al., 1974; Stubblefield and Swift, 1976; Swift and Field, 1981; McBride and Moslow, 1991; Goff et al., 1999; Snedden et al., 2011; Goff and Duncan, 2012)
Tampa Bay, Florida Gulf of Mexico	1-4	1 to 2	2 to 10	Oblique	5 to >35	SFDR	(Edwards et al., 2003; Harrison et al., 2003)
Adriatic Sea	1.5 to 4.1	0.33 to 0.745	> 2	Normal to the regional contours	20 to 24	SFDR	(Correggiari et al., 1996)
Gulf of Lions	10	1	Few to 5	Oblique	80 to 110	SFDR	(Berné et al., 1997; Bassetti et al., 2006)
Valencia shelf (Spain)	1.5 to 7	0.6 to 1.1	1.1 to 3.1	Oblique	55 to 85	SFDR	(Durán et al., 2015; Simarro et al., 2015)
Murcia shelf (Spain)	1.5 to 3	0.3 to 0.6	1.5 to 3.5	37° to 43°	65 to 76	SFDR	(Durán et al., 2017b)

[a] Note that the orientation of the sand ridges is widely variable because of the lobe-shaped shoreline.

5. Conclusions

High-resolution seafloor mapping allowed us to identify and morphologically characterize a sand ridges field in the former Cape Tortosa river mouth in the Ebro Delta. The sand ridges field extends between 5 and 15 m depth although it probably spreads landwards in shallower waters. The ridges have a maximum height and wavelength of approximately 2.5 and 400 m, respectively, both decreasing towards deeper waters. They are made of fine sand and arranged obliquely to the shoreline. The sand ridges migrated ~10 m/y between 2004 and 2015 and consistent with SE-directed wind-induced currents. Waves during E and SE storm events may reshape the ridges into symmetric geometry.

The genesis of the sand ridge field is closely related to the contemporary evolution of the Ebro River mouth. The switch of the main river course that started in the 1940s led to progressive abandonment of the Cape Tortosa river mouth, rapid retreat of the shoreline and formation of an erosional surface on the shoreface, which limits the progradational deposits below. The development of the sand ridge field above this surface was favoured by large amounts of sand provided by coastal erosion and available for reworking; persistent high-speed currents; topographic irregularities in the erosional surface as potential bedform precursors; and suitable RSLR in the area during the last few decades (similar to the initial phases of SFDR genesis during the Holocene on Mediterranean shelves). The process involves the deposit of a sandy layer above the erosional surface, with a maximum sediment thickness of 3 m (at the crests), which implies approximately $3.9 \cdot 10^6$ m^3 of sediment (considering only the mapped area of ~2.6 km^2).

Though the preservation of contemporary sand ridges remains an open question, it is highly probable that, in the absence of rapid sea-level rise, the Ebro Delta sand ridges will vanish after a life-span of only a few decades. In fact, sediment losses between the 2004 and 2015 surveys suggest that the sand ridges are already disappearing. The formation of the Ebro shoreface sand ridge field provides an example of the first stages of sand ridge development. At least during these initial stages, the time-scale of development of SFCRs (previously estimated as hundreds to a few thousand years) could actually be much shorter-of the order of a few decades.

Chapter V. Dynamics of ripples superimposed on sand ridges in a tideless shoreface

1. Introduction

Small scale bedforms like ripples are ubiquitous morphological features in sandy coastal and shelf sea environments. They display typical wavelengths (λ) of ~0.05–0.5 m and heights (η) of ~0.01-0.1 m (e.g. Allen, 1968; Nielsen 1992). Ripples can be generated by wave-, current- or wave and current-induced flows (Flemming, 1980) and represent intermediate flow conditions, between the thresholds for grain movement and sheet flow (Dalrymple and Rhodes, 1995). When the flow intensity exceeds the critical condition of sediment movement the flat bottom will no longer remain plane becoming unstable, developing seabed irregularities such as ripples. When shear stress is further increased, ripples first reach a maximum in their height and length and then enter a breakoff range until shear stress reaches the sheet flow criterion when ripples are washed-out and upper-plane bed sheet flow occurs (Southard & Boguchwal, 1990; Soulsby and Whitehouse, 2005; Camenen, 2009). On the other hand, if shear stress decreases below the threshold of initiation of sediment motion after ripple formation relict ripples can continue lying on the seabed inactive during low flow conditions (Soulsby et al., 2012).

Morphologically, ripples are generally characterised by their crest alignment as straight-crested (2D-ripples), which occur at lower speeds, or no-straight-crested as 3D-ripples (sinuous, catenary, linguoid, brained or lunate) at higher speeds (Thorne et al., 2009). Ripple geometries can be significantly different under wave or current-dominant conditions: wave-generated ripples are typically symmetrical in shape and with rectilinear crestlines, while in unidirectional flows they are primarily asymmetric and 3D morphological features. In wave-current ripples the morphological pattern is mainly 2D or 3D when the wave-current direction angle is parallel or perpendicular respectively having a combination of the properties mentioned previously (Nielsen, 1992). Likewise, crossing wave trains or large and abrupt changes in wave direction can lead to complicated 3D ripple patterns (e.g. Li and Amos, 1998; Traykovski et al., 1999; Soulsby et al., 2012). Different terms and classifications are used to describe ripples, especially for wave-ripples. Bagnold (1946) classified wave-generated ripples into two groups: rolling-

grain ripples and vortex ripples. Rolling-grain ripples form first on an initially flatbed under low wave action. As the rolling-grain ripples grow, their height causes the boundary layer flow separation behind the crest of the ripple and vortices form. For current-dominated ripples, (Bartholdy et al., 2015) described the development of small embryonic flow-transverse "wavelets" later transformed into mature ripples with increasing flow conditions (Coleman et al, 1994; Zhou and Mendoza, 2005). Clifton and Dingler (1984) categorized ripples with increasing hydrodynamic forcing as orbital ripples, which are scaled to the wave orbital diameter at the seabed, suborbital ripples, as transitional ripples whose spacing depends on wave orbital diameter and grain size, and anorbital ripples, only related to the sediment grain size. Smith and Wiberg (2006) identified two new populations of wave-generated ripples both scaled with the orbital diameter and developed under strong hydrodynamic conditions: "hummocks", long wavelength and low amplitude ripples generated in fine sand, and coarse grained ripples developed in medium to coarse sand.

The accurate prediction of ripple geometry is crucial to the modelling of bottom boundary layer dynamics and sediment transport since the ripple development and bed roughness variation directly control the magnitude of bed stress, skin friction/form drag partition, near bed velocity structure, vertical profiles of suspended sediment concentration (SSC) and bedload rates (Glenn and Grant, 1987; Grant and Madsen, 1979; Wiberg and Nelson, 1992; Li et al., 1996; Li and Amos, 1998). Recent equilibrium ripple predictors based on extensive laboratory and field datasets exist for waves (e.g. Soulsby et al., 2012; Nelson et al., 2013), currents (e.g. Soulsby et al., 2012; Bartholdy et al., 2015) or for combined waves and currents (e.g. Li and Amos, 1998; Soulsby et al., 2012). Under non-steady forcing conditions, active ripple patterns and geometrical characteristics continuously adjust or adapt according to changing hydrodynamic conditions (Traykovski et al., 1999). Equilibrium ripple predictors may not capture this adaptation process, resulting on limited prediction of ripple dimensions during morphodynamically active periods. To solve this issue, time-evolving (non-steady) ripple predictors have recently been suggested (Traykovski, 2007; Soulsby et al., 2012).

Ripples are frequently superimposed on larger scale bedforms. The hierarchical nature of bedforms has long been recognized where often two, three or even four distinct scales of bedform may occur in the same system (e.g. Venditti et al., 2005; Li and King, 2007). Experimental and field data observed ripples and small dunes generally lying on the backs or stoss side of larger bedforms which many of them grow by amalgamation of the smaller bedforms, and small embryonic bedforms continually form on the backs of the larger ones (Allen, 1982; Gomez et al., 1989; Venditti et al., 2005; Reesink and Bridge, 2009, 2007; Naqshband et al., 2014). The size, shape and dynamism of the superimposed forms are function on the relative position with respect to the host bedform and at the same time the host bedform

size, shape and dynamism are, at least partially, function of the superimposed bedform size and dynamics. For example, Cataño-Lopera and García (2006) observed bigger and slightly asymmetric ripples on the crest and smaller and slightly more symmetrical ripples on the trough while between the crest and the trough of the primary bedform were observed to be smaller and very asymmetric.

Ripples are dynamic bedforms that can migrate usually downstream or following the wave skewness (Allen, 1973; Gallagher et al., 1998; Crawford and Hay, 2001). When superimposed ripples migrate and arrive at the crest of a host bedform they affect the shape and migration rate of the larger-scale bedform lee side and influence the nature of deposition of sediment (Reesink and Bridge, 2007). Under unidirectional flow, the superimposed bedforms travel faster than the host bedform and overtake it (Reesink and Bridge, 2007), although the number of superimposed bedforms decreases gradually with the increasing flow velocity (Reesink and Bridge, 2009). In general, both ripples and the host bedforms migrated in the same direction as the wave/current propagation. Typical daily-averaged observed migration rates in shallow waters are about of 24-80 cm, with specific migration episodes ranging from 0.1 to 2 cm/min, mainly depending on the cross-shore location and ripple dimensions (Traykovski et al., 1999; Doucette, 2002; Masselink et al., 2007). Increasing flow speed resulted on faster migration rates but smaller ripple dimensions (Cataño-Lopera and García, 2006). Ripple migration rates are of similar order of magnitude when ripples are superimposed on larger bedforms than when ripples are lying on flatbed although ripple migration rates varied depending on the relative location with the host bedform, being slower ripples over the troughs and faster over the crests (Cataño-Lopera and García, 2006). Back-flow or regressive ripples with opposed or oblique migration directions than host bedform have been observed within the lee side eddy of the primary bedform during specific hydrodynamic conditions (Reesink and Bridge, 2007; Herbert et al., 2015) or during the vertical grow of the host bedform (Cataño-Lopera and García, 2006).

In this chapter, small-scale bedforms were observed lying superimposed on a sand ridge field. The relative location of ripple with respect to the larger bedform corresponded with an extreme of a sand ridge, with symmetric geometry lying on the outer part of the prodelta of the former Cape Tortosa river mouth at 13.3 m depth (Fig. 3). According to (Guerrero et al., 2018) the NW wind-induced currents are the main responsible of sand ridge migration towards the SSE, while waves propagating in the opposite direction were suggested as the mechanism of reshaping to more symmetrical morphologies of these forms. The development and dynamism of ripples under waves and/or currents and the feasibility of ripple migration as a potential contributor to the sand ridges migration are analysed. In addition, the reliability on using ripple predictors and sediment transport estimations are discussed.

2. Results

2.1. Time series of observations

2.1.1. Waves and near-bottom currents

The significant wave height (H_s) time series propagated from the Tarragona buoy to the tripod location with SWAN model ranged from 0.1 m to maximum values of ~3 m with several periods of H_s >1 m (Fig. 22 b). The highest waves (> 2 m) occurred mostly during November and the beginning of December and represented conditions of moderate wave storms with peak wave periods (T_p) between 8 and 12 s. The storms were clearly eastern storms (locally called "Llevantades"), with only one exception on the 24th of December when waves came from the S (Fig. 22 b). Following the waves, the near-bottom orbital velocity (U_w) displays several peaks of > 0.4 m/s mostly between November and the beginning of December and a maximum peak of 0.8 m/s on the 16th of November (Fig. 22 d).

The current speed measurements at ~1 mab show periods of intense currents occurred between November and December similarly than the wave heights (Fig. 22 c). The maximum speed recorded was of ~0.6 m/s and occurred on the 16th of November and the 27th of December. When current speeds increased over 0.2 m/s they always channelled towards the SSE.

2.1.2. Seabed morphological changes and ripple observations

The altimeter was able to measure the topographic variability of the seabed from the beginning of the deployment until the 16th of November when the most energetic measured storm occurred (Fig. 22 e). During this period a settle of ~10 cm was first recorded on the 17th of October probably as a consequence of the structure stabilization (Fig. 22 e). The seabed position measurements alternated steady and oscillating topographic periods (Fig. 22 e). Seabed oscillations were large, with fluctuations in the order of 20 cm, and smaller oscillations in the order of few centimetres (Fig. 23 e). The latter were related with ripple development periods.

Six periods of ripple formation were identified with the images of the video camera during the first month of the deployment (Fig. 22 a, Fig. 23 a). In general, ripples developed during low-moderate energetic hydrodynamic conditions. They were typically generated by the action of waves and/or currents and their size well-correlated with the flow energy exhibiting bigger dimensions under higher-energetic conditions and smaller dimensions under lower-energetic conditions. At the end of each ripple development period, these small bedforms degraded progressively when the energy decreased (Fig. 22 a, Fig. 23 a). 2D-ripples formed during low-energetic hydrodynamic conditions and were associated with waves (H_s~1 m) while under higher (but moderate) energy conditions 3D-ripples formed and were associated with waves and currents (Fig. 23).

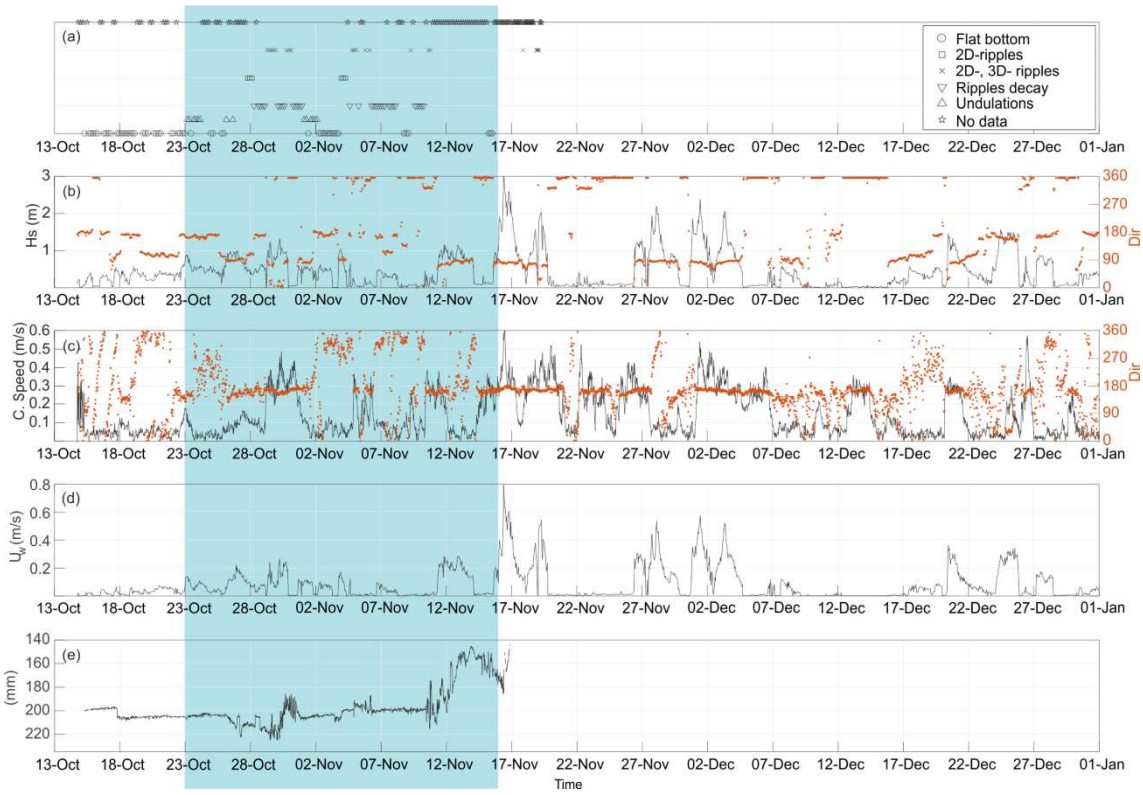

Fig. 22. Time series from October to December of 2013 of: (a) seabed configurations distinguishing the different morphologies or states observed: flat bottom (circle), wave-ripples (square), wave-current-ripples (cross), ripple decay or degradation (inverse triangle), undulations (triangle) and no data (star); (b) propagated significant wave height in m (line) and direction (dots); (c) current speed in m/s (line) and direction (dots) at the tripod location at ~1 mab; (d) orbital velocity (U_w); and (e) seabed topographic variability measured at 20 cmab. The blue shaded area indicates the detail from 23rd of October to the 16th of November of 2013 showed in Fig. 23.

2.2. Ripple classification

Different plane view seabed morphologies were distinguished and classified as: flat bottom; small undulations; 2D-ripples (ripples with rectilinear crests); 3D-ripples (ripples with brained crests); ripple decay or degradation; and no data when images were not available or with low quality to identify any morphology on the seabed (Fig. 22 a, Fig. 23 a). A complete description is addressed by using the images recorded with the video camera, the time series of the propagated significant wave height and direction, current velocity measured at ~1 mab, the seabed topographic variations measured with the altimeter, the measurements of the suspended sediment concentration at ~1 mab and the estimations of near-bottom stresses at the boundary layer.

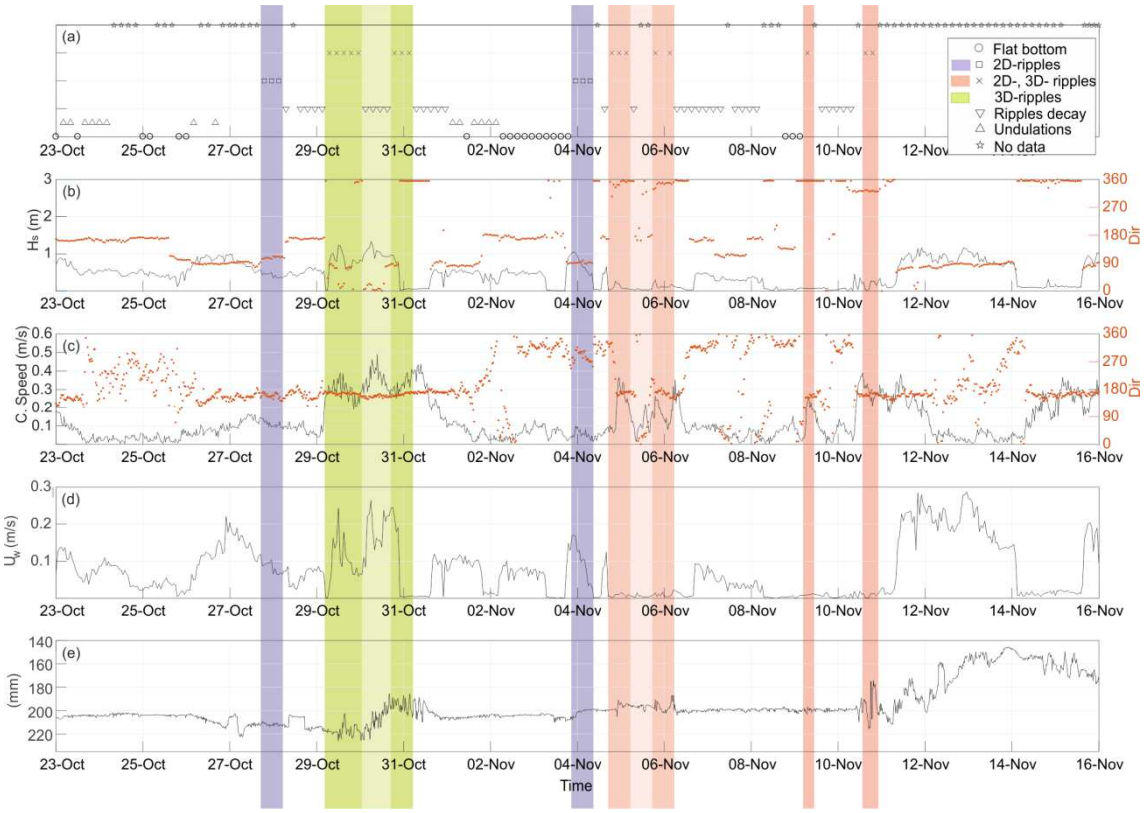

Fig. 23. Detail from the 23rd of October to the 16th of November of the same time series variables described in caption of Fig. 22. The coloured shaded areas indicted the different ripple morphologies observed.

2.2.1. Undulations

During low-energetic hydrodynamic conditions small undulations were observed lying on the seabed (Fig. 24). The small bedforms were not classified as ripple bedforms because they were not well-developed enough showing crests without a clear continuity in length and small dimensions (η < 0.5 cm and λ ~8 cm) (Fig. 24). These undulations formed during periods of waves H_s = 0.5-1 m and low current speed (< 0.1 m/s) (Fig. 23).

Fig. 24. Example of the undulations observed on the instantaneous images from the video record on the 1st of November of 2013 at 19 h.

2.2.2. 2D-ripples

2D-ripples displayed straight rectilinear crests aligned N-S and well-correlated with periods of wave-dominated hydrodynamic conditions (wave-ripples) (Fig. 23 and Fig. 25). Two periods of 2D-ripples development were identified.

2D-ripples were first observed on the 27th of October at 19 h being at 23 h even better developed during a small (H_s < 1 m) eastern storm (Fig. 25 a). Ripples displayed rectilinear N-S oriented crests, with mean $\eta = 1.2$ cm and $\lambda =$ 7-10 cm ($\eta/\lambda \approx 0.15$) (Fig. 25 a). The analysis of the temporal seabed topographic variation and the ripple crest geometries and positions revealed that they were static with neither migration nor dynamism. Previous available images (26th of October) showed the presence of undulations at the beginning of the eastern wave event (H_s ~1 m), suggesting that the pre-existing undulations acted as a precursor of ripple formation (Fig. 23 a). Finally, ripples degraded progressively mainly by the biological activity of the benthic community (Fig. 25 b).

A second period of N-S oriented, straight-crests ripple morphologies with mean $\eta = 0.5$ cm (maximum heights of 1 cm) and $\lambda =$ 6-8 cm ($\eta/\lambda \approx 0.07$) formed between the 19 h and 23 h on the 3rd of November when eastern waves increased until H_s ~1 m (Fig. 25 c). The previous seabed state was "flatbed" with some roughness consequence of the biological activity but any undulations were previously observed. The 2D-ripples also remained static on the seabed with neither dynamism nor migration.

Fig. 25. Example of 2D-ripples formation observed in the instantaneous images (a) on the 27th of October of 2013 at 23 h; (b) benthonic community contribution to ripples degradation on the 28th of October at 19 h; and (c) on the 4th of November of 2013 at 3 h.

2.2.3. Mixed 2D- 3D- ripples

Mixed 2D- 3D-ripples were characterized as dynamic bedforms that changed their arrangement from brained to rectilinear crests and with larger dimensions than the previously described 2D-ripples (Fig. 26). These ripples occurred during current-dominated hydrodynamic conditions (current-ripples) and were observed during three different periods in November (Fig. 23). For example, rippled bed with brained crests and small dimensions developed on the 4th of November at 19 h under high-speed currents (> 0.3 m/s) just after the previous wave-ripples

formation described before (Fig. 23 a; Fig. 26 a). The size of ripples increased/decreased following the current speeds (Fig. 26 a, b, c). Moderate currents (0.2-0.3 m/s) flowing towards the S lead to modify ripple morphologies from 3D- to 2D-ripples (crests oriented W-E), removing completely the residual ripple morphologies from the previous wave-ripple period (Fig. 26 d, e). Finally, ripples degraded displaying rounded crests and poorly-defined shapes under lower current speed (Fig. 26 f). The mean ripple height was estimated around $\eta = 0.8$ cm (maximum > 1.5 cm) and the wavelength (λ) around 10-15 cm ($\eta/\lambda \approx$ 0.05-0.15) considering the whole period of appearance. Ripples migrated towards the SSE with rates of 6-10 cm/h.

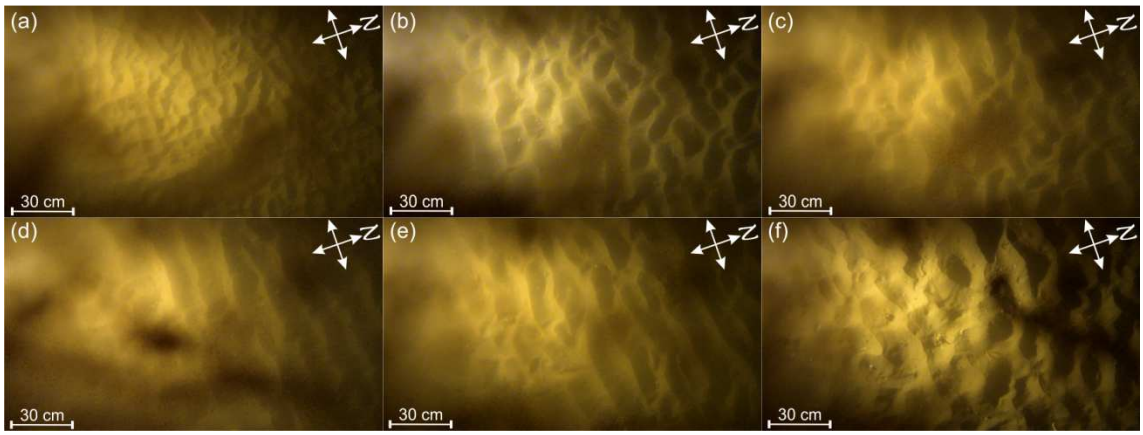

Fig. 26. Example of ripples formation under current-dominated conditions observed in the instantaneous images on (a) the 4th of November of 2013 at 19 h; (b) the 4th of November of 2013 at 23 h; (c) the 5th of November of 2013 at 3 h; (d) the 5th of November at 19 h; (e) the 6th of November at 3 h; (f) the 6th of November at 19 h.

2.2.4. 3D-ripples

3D-ripples displayed brained crests, larger dimension than 2D-ripples and formed under wave-current hydrodynamic conditions (Fig. 23). They migrated towards the S accordingly with the current flow.

On the 29th of October at 7 h 3D-ripples morphologies were observed for the first time (Fig. 27 a) until the 31st of October of 2013 when ripple decline started (Fig. 27 f). Previously to those 3D-ripples development, the seabed configuration displayed small roughness elements, the small undulations, corresponding to the residual morphologies from the former 2D-ripples (Fig. 23 a). The 3D-ripples were progressively readapting their morphologies and sizes by growing, displaying better-defined crests as consequence on the increasing currents and wave heights (e.g. Fig. 27 c-e) however they also slightly degraded during the second and highest current-speed peak (v ~0.5 m/s) and wave heights (H_s = 1.2 m) of the event on the 30th of October (Fig. 27 d). Finally, ripples progressively degraded at the end of this wave-current event (Fig. 23 a,

Fig. 27 f). Ripple mean height was $\eta = 1.9$ cm with maximum ripple height values of ~2.2 cm and $\lambda =$ 7-20 cm ($\eta/\lambda \approx$ 0.10-0.25). The ripples were highly dynamic with migration rates of 5-13 cm/h towards the SSE.

Video-records during these events revealed the presence of fishes swimming against the current flow (perpendicular to ripple crests arrangement) (e.g. Fig. 27 b) and the oscillatory movement (parallel to ripple crests) of sand and shells presumably induced by the eastern waves (e.g. in the video of the instantaneous image Fig. 27 d).

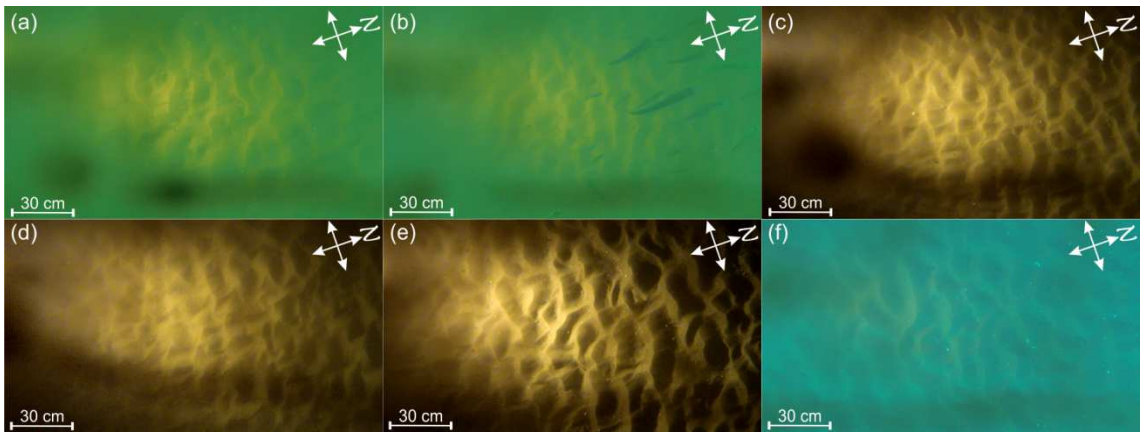

Fig. 27. Example of 3D-ripples formation under wave-current-dominated conditions observed in the instantaneous images on: (a) the 29th of October at 7 h; (b) the 29th of October at 15 h; (c) the 29th of October at 23 h; (d) the 30th of October at 3 h; (e) the 31st of October at 3 h; and (f) the 31st of October at 7 h.

2.3. Estimations of bottom shear stress and bed mobility

The hydrodynamic forcing conditions acting on the seabed during the study period were characterized by estimating the near-bed shear stress generated by waves (τ_w), currents (τ_c) and the combined wave-current (τ_{max}) (Fig. 28 c). The total shear stress (τ_{max}) reached slightly more than 1.8 N/m^2 on the 16th of November and several peaks higher than 0.5 N/m^2 occurred between November and the beginning of December (Fig. 28 c). The maximum contributor to the total shear stress was wave stress (τ_w). However, current shear stress (τ_c) was the main contributor to the total during periods of intense currents and low wave height (e.g. on the 22nd of November Fig. 28 c).

As expected, the Shields parameter time series due to waves and currents followed the same trend than their respective shear stress (Fig. 28 b). The maximum Shields parameter due to waves (θ_w) was reached on the 16th of November and after this event a few peaks of $\theta_w > 0.2$ occurred. Current Shields parameter peaks ranged between 0.1-0.2, coinciding with the highest peaks on the near-bottom current speeds (Fig. 28 b). The estimated Shields parameter thresholds

of motion, wash-out and sheet flow conditions were 0.05, 0.19 and 0.26, respectively (Table V). The comparison between the Shields parameter due to waves and these thresholds suggested that the ~17.2% of the time $\theta_{cr} < \theta_w < \theta_{wo}$, the 1% $\theta_{wo} < \theta_w < \theta_{sf}$ and the 0.4% $\theta_w > \theta_{sf}$. The remainder 81.4% of time the hydrodynamics induced by waves were below the threshold of sediment motion. The Shields parameter due to currents (θ_c) exceeded ~12.9% of the time the theoretical critical threshold of grain motion, but it was always below the threshold of wash-out conditions (Fig. 28 b). In summary and considering both, wave and current Shields parameters, critical conditions for grain movement were exceeded during the 24% of the time and wash-out and sheet flow were only reach during the 1% and 0.4%, respectively under high-energetic waves being the resting 74.6% of time below the critical threshold.

Table V. Shields parameter thresholds for critical, wash-out and sheet flow conditions obtained with different approximations.

Author(s)	$\boldsymbol{\theta_{cr}}$	$\boldsymbol{\theta_{wo}}$	$\boldsymbol{\theta_{sf}}$	$\boldsymbol{\frac{A_w}{d_{50}}}$	**hydrodynamic conditions defined method**
Nielsen (1981)	-	-	1	-	oscillatory flow
Li and Amos (1999)	-	-	0.2	-	combined steady and oscillatory
Kleinhans (2005)	-	-	$\sim\theta_w$ [0-0.56]	-	combined steady and oscillatory
Soulsby and Whitehouse (2005)	-	-	-	~2000	oscillatory flow
Soulsby et al. (2012)	0.05	0.19	0.26	-	combined steady and oscillatory

2.4. Estimation of sediment transport rate

Most of the estimated near-bottom sediment transport occurred in short pulses during severe storms (Fig. 28 d). Peaks of sediment transport ranging 100-400 g/s/m occurred from the mid-November to the beginning of December, with the maximum on the 16th of November of 2013 (Fig. 28 d). Several smaller peaks around ~20 g/s/m were also estimated under moderate conditions (e.g. on the 26th of November or on the 21st of December) (Fig. 28 d). In general, the sediment transport rate was high during events when waves dominated, although most of them were wave -current events (Fig. 28 d). Predictions suggested that the sediment transport was widely dominated by suspended load over the bedload with the 92% and 8%, respectively. This is in agreement with observations of suspended sediment concentration (inferred from turbidity measurements), that displayed a strong relation with high-energetic wave-current conditions (Fig. 28 a). In general, the measured turbidity peaks are well-correlated with periods when the Shields parameter exceeded the critical threshold (grey-shaded areas in Fig. 28 a). The highest turbidity was measured on the 24th of December under high waves and current speed conditions (Fig. 28 a). During periods of 3D-ripples development the 83% of the sediment transport is attributed to suspended load and the resting 17% to bedload.

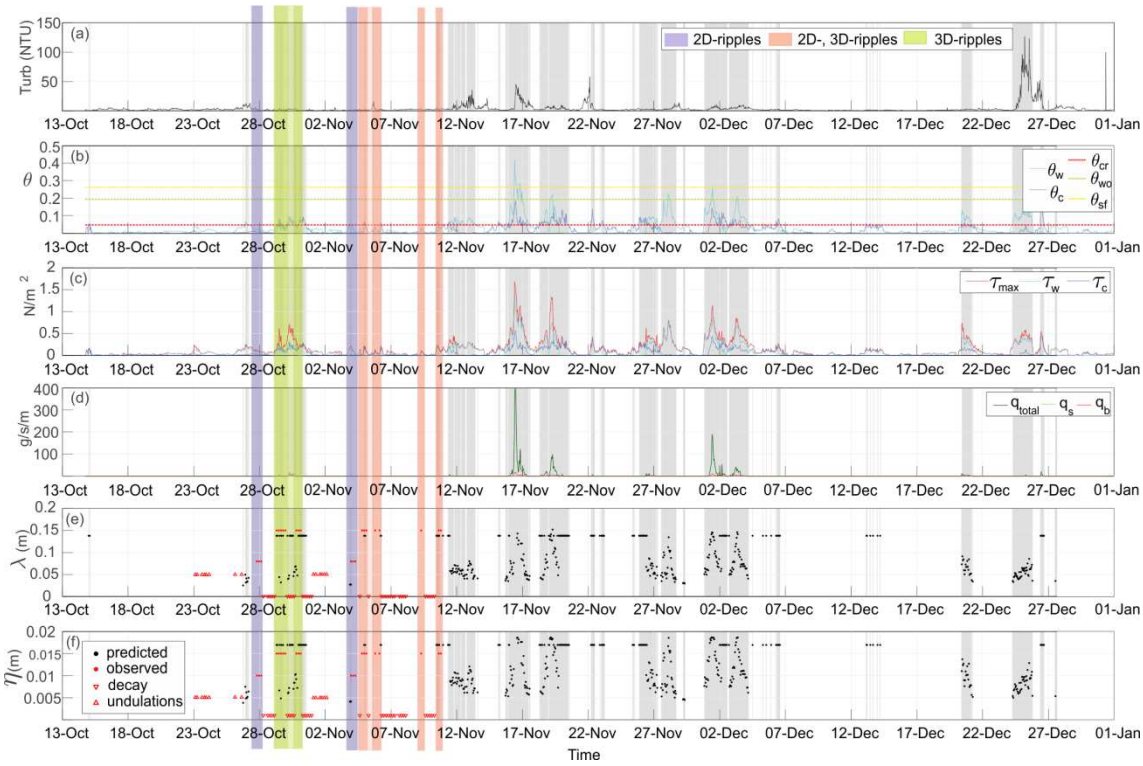

Fig. 28. Time series from October to December 2013 of: (a) turbidity in Normalized Turbidity Units (NTU) measured at ~1 mab; (b) wave and current Shields parameter (θ_w, θ_c) and the thresholds of initiation of sediment motion (θ_{cr}), wash-out (θ_{wo}), and sheet flow (θ_{sf}); (c) maximum combined waves and current shear stress (τ_{max}), wave shear stress (τ_w), and current shear stress (τ_c); (d) total sediment transport rate (q_t), suspended sediment transport rate (q_s) and bedload sediment transport rate (q_b); (e) ripple wavelengths in cm from observations (red dots) and obtained with the Soulsby et al (2012) ripple predictor (black dots); and (f) ripple wavelength in cm from the observations and obtained with the Soulsby et al (2012) ripple predictor (black dots). The grey shaded areas indicate the interval times when the Shields parameters (waves and/or currents) were bigger than the critical threshold, and coloured shaded areas indicate the periods of the ripple development detailed in Fig. 23.

3. Discussion

3.1. Ripple occurrence and prediction

Video observations of ripples in the Ebro Delta are biased, since they are limited to low and moderate hydrodynamic conditions because during storm events the high-sediment concentration prevents seabed video observations. From low to moderate energy, observations suggest a transition from undulations on the seabed, 2D wave-ripples (H_s~1 m), current dominated 2D-, 3D-ripples and the largest wave-current 3D-ripples. Ripple decay also occurred when hydrodynamic regime increased the energy (wash-out), or because of biological activity (mostly the benthic community) that progressively degraded the bedforms (e.g. Fig. 25 b) as observed and suggested previously by (Guillén et al., 2008; Soulsby et al., 2012). Only mixed 2D-3D and 3D-ripples were dynamic, changing morphologies and arrangements adapting to

hydrodynamics as well as migrating towards the SSE accordingly with the current flow direction. However, 2D wave-ripples remained fixed and stable suggesting that only currents produced the ripple migration. Despite wave asymmetry can be an additional mechanism of ripple migration (Traykovski et al., 1999), wave-ripple were static in the Ebro area probably because of near-bottom wave velocities were symmetric or with very small asymmetry during low-, moderate-energetic periods of wave-ripple observations.

Most of ripple formation observations at the study site agree with periods when the Shields parameter exceeded the threshold condition for initiation of sediment motion (θ ~0.05) (Fig. 29). However, undulations can be formed on the seabed below the critical Shields limit under small waves (H_s = 0.5-1 m) and weak currents (v < 0.1 m/s) (Fig. 29, Fig. 22 and Fig. 23). These undulations (η < 5 mm) would be a precursor of the 2D-ripples if waves remained constant or slightly increase, as observed on the 26th of October (Fig. 29). The transition from a plane bed to well-developed ripples through the formation of smaller bedforms (η < 3 mm) as precursor was previously observed with high speed flows (> 0.65 m/s) (Reesink and Bridge, 2007), although this transition occurred during low-energetic wave conditions in the Ebro. The limited available records during higher energy periods inhibit a detailed comparison between theoretical wash-out and sheet flow thresholds with observations. The 3D-ripple decay occurred during a wave-current peak ($\theta_{cr} < \theta < \theta_{wo}$) on the 30th of October and suggests the initiation of ripple wash-out with θ ~0.1 when the measured current speed was above 0.55 m/s (Fig. 29).

The application of the ripple predictor model (Soulsby et al., 2012) roughly fits with ripple appearance since these estimations are based on the previously calculated critical Shields parameter (Fig. 29 a). However, undulations and 2D-ripples were also observed below or near the theoretical threshold of initiation of sediment motion (Fig. 29). The ripple predictor slightly underestimated ripple wavelength (Fig. 29 d) while ripple heights were underestimated under wave-dominated conditions and overestimated during current-dominated conditions (Fig. 29 e). In addition, ripple predictor failed under mixed wave-current conditions, probably because of the assumption that only one of the both mechanisms is the dominant (waves or currents) and because the method is not well-defined for 3D-ripples. Thus, even if the Soulsby et al. (2012) approach has been established to yields one of the best prediction for the ripple characteristics, it suffers uncertainties in the estimation of Shields parameter, it does not take into account properly the inception of sheet flow and largely overestimates the results when ripples were washed-out (Camenen, 2009).

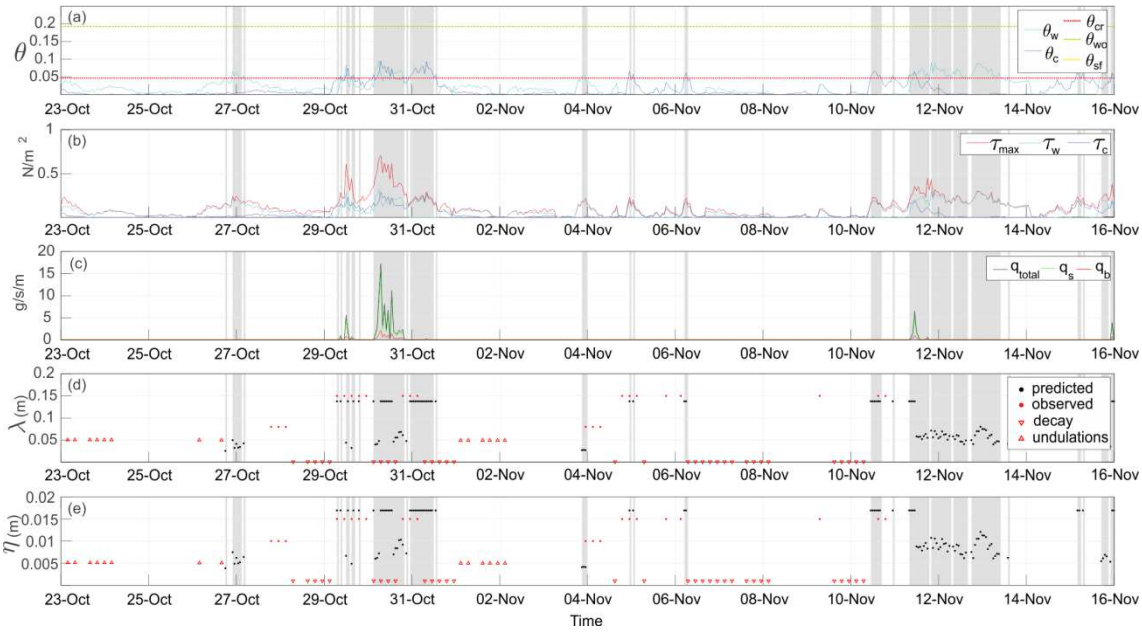

Fig. 29. Detail from the 23rd of October to the 16th of November of time series of: (a) wave and current Shields parameter (θ_w, θ_c) and the thresholds of initiation of sediment motion (θ_{cr}), wash-out (θ_{wo}), and sheet flow (θ_{sf}); (b) maximum combined waves and current shear stress (τ_{max}), wave shear stress (τ_w), and current shear stress (τ_c); (c) total sediment transport rate (qt), suspended sediment transport rate (qs) and bedload sediment transport rate (qb); (d) ripple wavelengths in cm from observations (red dots) and obtained with the Soulsby et al (2012) ripple predictor (black dots); and (e) ripple height in cm from the observations and obtained with the Soulsby et al (2012) ripple predictor (black dots). The grey shaded areas indicate the interval times when the Shields parameters (waves and/or currents) were bigger than the critical Shields parameter.

3.2. Ripples and sand ridges dynamics

Ripples at the study site were lying superimposed on the extreme and deepest part of the SE face of a symmetric sand ridge bedform (Fig. 14). Both ripples and sand ridges migrate towards the SSE as consequence of wind-induced currents and it could be believable some contribution of ripples into sand ridge dynamics. Generally, relatively large-scale bedforms tend to move slower than small-scale features (Venditti et al., 2005). Then, the migrating superimposed bedforms overtakes and avalanche at the lee side of the larger and contribute to the migration of the host bedform (Reesink and Bridge, 2009). The sediment transport involved in the migration represent distinct scales between superimposed and host bedforms, although it can be nearly identical if size and migration rates are proportional between both, i.e. ripples move 10 times faster and is 0.1 time the size of the host bedform (Venditti et al., 2005).

At the study site, the highest sediment transport occurred when the Shields parameter exceed the theoretical wash-out threshold, that was, in absence of ripples. The sediment transport was low (one order of magnitude lower than the highest peaks) between the critical and wash-out

theoretical thresholds (Fig. 28) while, for values of the Shields close to the critical of sediment motion (slightly above or below), when undulations and the 2D wave-ripples developed, the estimated sediment transport was almost null (Fig. 29). Since bedforms were stationary in these low-energy conditions, the sediment transport should be unrelated with the migration of wave-ripples. In presence of 3D-ripples (29th to 31st of October) a peak of sediment transport was estimated with the 83% of the total sediment transport by suspended load and the resting 17% by bedload (Fig. 29 c). Therefore, the bedload transport could be partially attributed to the 3D-ripple migration and dynamism or morphological changes.

Ripple migration was observed during currents and combined waves and currents conditions when flows were lower than 0.55 m/s. The instantaneous ripple migration rates estimated from observations were about ~10 cm/h, which occurs when $\theta_c > \theta_{cr}$. The extrapolation of ripple migration rates to periods when $\theta_{cr} < \theta_c < \theta_{wo}$, provides a rough estimation of the mean ripple migration of 1.3 cm/h during the study period, which should be lower along the year because of the low-energetic summer period. Moreover, the annual sand ridge migration rate was ~10 m/y (Guerrero et al., 2018) that represents a mean rate of 0.11 cm/h. The rude comparison between ripple/sand ridge mean size (0.015 /1.5 m) and migration rates (1.3 /0.11 cm/h) suggests, according to the relationships established by Venditti et al. (2005), that the sediment transport associated with ripple migration could be one order of magnitude lower than the total transport involved in sand ridge migration. This would be a subordinate but non-negligible amount of the bedload sediment transport associated to bedform migration. While most of the sediment transport and sand ridge migration would occur under sheet flow conditions when ripples were wash-out during high-energy episodes, sand ridge migration would also occur during low- to moderate-energetic hydrodynamic conditions.

In a more general perspective, the contribution of small bedforms to the growth of larger bedforms and, after the formation, the presence of ephemeral small bedforms migrating on the backs of the larger ones have been described (Allen, 1982; Gomez et al., 1989; Venditti et al., 2005; Reesink and Bridge, 2009, 2007). The contribution of small bedforms as ripples (or sediment dynamics during low-moderate energy hydrodynamics) can help to understand the formation, dynamics and maintenance of large bedforms with no need to resort exclusively to extreme conditions of high energy. For instance, it was hypothesized that low-moderate energy processes could explain the maintenance of large scale sand ridge in the continental shelf (Simarro et al., 2015). In the shoreface of the Ebro Delta sand ridges could be also dynamic during moderate currents episodes by means of the ripple migration. If this is the case, our vision of large bedforms that remain static during most of the time and only actives during high energy or extreme conditions should be changed.

4. Conclusions

Ripple development is usual under low and moderate hydrodynamic conditions in the Ebro Delta shoreface. Four types of small-scale bedforms were identified which from the critical threshold of sediment motion to wash-out conditions are: (i) small undulations with η <0.5 cm and λ~8 cm, formed as a precursor of wave-ripples when the Shields parameter was close (below) the critical; (ii) 2D wave-ripples with η =1.2 cm and λ =7-10 cm; (iii) mixed 2D-3D current-dominated ripples with η =0.8 cm (max. ~1.5 cm) and λ =10-15 cm; and (iv) 3D wave-current ripples with η =1.9 cm (max. ~2.2 cm) and λ =7-20 cm. Ripple degradation occurred when the hydrodynamic regime increased the energy (wash-out conditions), or under low energy hydrodynamic conditions when ripples progressively decay mainly as a consequence of the biological activity, mostly by the benthic community which contributed flattening the relict ripples.

The applied ripple predictor method roughly fits with ripple appearance. However, ripple morphology was poorly predicted, especially during wave-current conditions. The development of small seabed undulations below the theoretical threshold of grain movement is a major concern in ripple and sediment transport prediction, suggesting the estimated thresholds as progressive ranges rather than abrupt changes.

Most of sediment transport occurred during severe storms under sheet flow conditions. In presence of ripples, only during the development of 3-D wave-current ripples significant sediment transport was estimated. Ripple migration rates were ~10 cm/h during only current and wave-current events. 2D wave-ripples did no migrate and estimations of sediment transport were almost null.

Migration of 3D-ripples is dominated by the wind-induced current towards the SSE and this is the same direction of sand ridge migration in the Ebro shoreface. Accordingly, it was hypothesized that part of the sand ridges migration could be associated with ripple migration. Coarse estimations suggest that the input of ripples to the migration of sand ridges could be roughly no more than one order of magnitude lower than the total transport involved in sand ridge migration. This subordinate amount, however, would represent that large-scale bedforms could be dynamic during low-moderated energetic processes and not only during high energy or extreme conditions.

Chapter VI. Small-scale bedforms in a macro-tidal inner shelf

1. Introduction

The cross-shore sediment transport in coastal areas has been a research hot topic during the last decades mainly for understanding erosion processes in the beach during storms, the post-storm recovery and the prediction of morphodynamic changes in the beach (Wright et al., 1991; Larson and C. Kraus, 1995; Ruessink et al., 1998; Butt and Russell, 2000). Sediment exchanges between the beach and the nearshore are largely better known than between the inner shelf and the nearshore (Wright et al., 1991). In general, the cross-shore sediment exchange between the nearshore and the inner shelf is mainly wave-forced, related to wave asymmetry and wave induced currents (as undertow), although tidal, upwelling (downwelling) currents or wind induced currents can also transport sediment (Wright et al., 1991; Styles and Glenn, 2005; Ruessink et al., 2011;). The net forward bedload transport can occur as wash-out or sheet flow and through ripple migration (Traykovski et al., 1999; Camenen and Larson, 2006; van Rijn, 2007a).

The sediment transport caused by onshore migration of small-bedforms can be higher than the suspended sediment transport in the transition between the inner shelf and nearshore. For example, Traykovski et al. (1999) observed migration rates of 33 mm/h at Beach Haven Ridge (New Jersey) at 11 m water depth or Williams and Rose (2001) estimated migration rates of 0.3-1 mm/s at a sand bank at Middelkerke Bank (Belgium North, Sea) at 20 m water depth. Crawford and Hay (2001) observed offshore ripple migration during storm growth and onshore migration during storm decay, being the bedform migration highly correlated with the near-bed wave orbital velocity skewness in both cross-shore directions. Thus, wave asymmetry seems the main mechanism for ripple migration, while purely linear monochromatic wave motion with no superimposed currents result in equal velocities in both wave directions and thus no sediment transport (bedform migration) (Traykovski et al., 1999). The general understanding of bedform contribution to sediment transport is that bedform component is onshore and large compared with the suspended component in relatively deep water and it is becoming progressively less important towards the shore, through the shoaling and surf zone (Miles and Thorpe, 2015).

One example of nearshore-inner shelf sediments exchanges occurred at the Perranporth coast on the 2013/2014 winter, which is considered the stormiest on record for the Ireland-UK domain since the last 60-years hindcast wave model record (Masselink et al., 2016; Scott et al., 2016). Several storms during 3 months caused a highly unusual sequence of extremely high water levels and very energetic wave conditions resulting in coastal erosion and flooding and therefore, severe coastal impacts and damages especially the southeast part of England. At Perranporth the sediment eroded from the beach was mainly deposited in large subtidal bar systems, located at 6-8 m water depth and part transported offshore (> 14 m water depth) (Scott et al., 2016). After the storms period, progressive beach recovery occurred by onshore bar migration and onshore sediment transport in the nearshore (Masselink et al., 2016; Scott et al., 2016). However, part of the sediment eroded from the beach during storms was still retained in the subtidal bar system and remained inactive on the inner shelf (Scott et al., 2016). Therefore, it has been pointed out that high-energy wave events appear to be essential for the post-storm recovery of the sediment (Masselink et al., 2016).

The potential return of sediment from the distal profile (shoreface/inner shelf) to the nearshore (bar systems) after an erosion period is currently poorly well-understood and it is one focus of this chapter which is involved into the Work Package 1 of BLUEcoast project (http://projects.noc.ac.uk/bluecoast/) that studies the cross-shore and alongshore sediment exchanges in exposed high energy coastal areas with sandy and gravelly coasts as well as rocky headlands. Wave-ripples develop on the nearshore of Perranporth (between 1-6 m depth) under low-energy conditions (orbital velocities < 0.65 m/s) and migrate generally onshore-directed in the shoaling and surf zones, with increasing migration rates through the shoaling zone to a maximum just shoreward of the breakpoint (Miles et al., 2014). The onshore migration of ripples correlated well with positive (onshore) wave skewness, although the direction depends on the competition between velocity skewness, orbital velocity and mean flow, and this is controlled in turn by the position in the surf zone (Miles et al., 2014). The sediment transport rates associated with these bedforms were also onshore directed and increased shoreward which contributed up to the 15% of the total sediment transport (Miles and Thorpe, 2015). Therefore, ripple migration contribution to bedload sediment transport in the nearshore off Perranporth is significant. It is plausible a similar mechanism acting at the inner shelf, but exists a lack of knowledge regarding the interrelation between small-bedforms (ripples) dynamism and sediment transport in the transitional area from the inner shelf to the nearshore.

This research focused on evaluates the potential role and contribution of ripples to sediment exchanges between inner shelf and nearshore. The development and dynamics of these small-scale bedforms (ripples) is analysed to infer the near-bottom sediment dynamics as possible additional relatively long-term beach recovery mechanism during calm and mild energy

conditions and their potential implications to the inner shelf-nearshore sediment exchanges. To gain understanding of these sedimentary processes, an instrumented tripod was deployed at Perranporth in the transitional zone ~20 m depth Ordenance Datum Newlyn (ODN) between the tidal channels (> 30 m depth) and the nearshore area dominated by nearshore bars dynamics and rip currents (Fig. 4 b). A description of the inner shelf area, the morphological and bottom sediment characterisation are first introduced. The time series of wave conditions, water level, currents, morphodynamic of the area recorded with the 3D-Acoustic Rippler Profiler (3D-ARP), ripples observations and bottom shear-stress are described for the period from January to March 2017 and specifically detailed from mid to the end of January 2017. The ripple occurrence and dynamics and the hydrodynamic interrelation, as well as the reliability on using ripple predictors and sediment transport are discussed. These observations can provide new insights about the potential return of sediment from the inner shelf to the nearshore and the potential role of small-scale bedforms in onshore sediment transport during calm and mild energy conditions.

2. Results

2.1. Inner shelf morphology and sediment characteristics

Perranporth continental shelf displays cross-shore profile with slopes of tanβ~ 0.004 and concave-shaped until ~30 m depth (ODN) (Fig. 4 b). Over this area, the seafloor morphology is uniform and homogeneous, limited by rock outcrops at the north and south extremes of the shelf following the emerged cliffs of Devonian rocks (Fig. 4 b). Just at the south of the northern outcrops, at approximately 25 m depth, six subaqueous dunes lie with ~0.5 m high and ~110 m of wavelength, they display asymmetries with the lee side facing to the south. At approximately 30 m depth contour (ODN) an abrupt edge 1 m high appears breaking the seafloor homogeneity. It arranges mainly parallel to the shoreline except at the southern area where the edge appears shallower without apparently any arrangement. Offshore of this edge the seafloor changes to more complex morphologies exhibiting tidal channels aligned NE-SW, 0.3-0.5 m deep (maximum ~1 m) and widths ranging from tens to hundreds of meters. It can be appreciated that the head of these channels are located near the rocky outcrops at the north area of the continental shelf, becoming wider towards the southwest. Thus, the study site is located in the transitional zone between the tidal morphologies (> 30 m depth) and the nearshore bars (< 6 m depth).

The grain size analyses of the surficial sediment showed a moderately sorted medium sand composition with d_{50} of 266 μm at the Mini-STABLE frame location. 97% of the sediment was made of sand in which 7.6, 48.1, 36.5 and 4.8% corresponded to the coarse, medium, fine and very fine sand, respectively and the remaining 3% composed by silt fraction (Fig. 30).

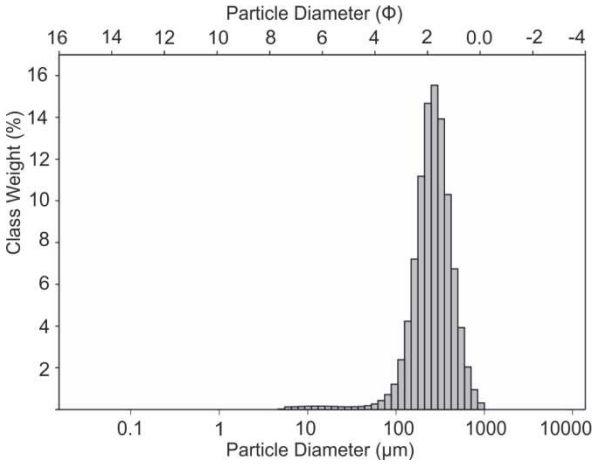

Fig. 30. Grain size distribution of one of the two sediment samples recovered at the Mini-STABLE frame location deployment using the Van Veen Grab during the tripod recovery on the 12th of March of 2017.

2.2. Time series

2.2.1. Wave conditions

The wave time series showed the root mean square wave height (H_{rms}) ranging from 0.5 m to 4 m and mean wave periods (T_z) from 5 to 10 s (Fig. 31 c). The highest waves (H_{rms} > 3 m) took place on the 3rd, 8th and 23rd of February and the 2nd and 5th of March. During these events the T_z varied between 7 and 10 s. Wave directions (data no shown) were clearly unidirectional coming from the W-WNW (mean wave direction of ~280°).

Focusing on the specific period from the 18th of January to the 3rd of February of 2017 (indicated with a blue rectangle in Fig. 31), the H_{rms} ranged between 0.5-2 m and the T_z between 5-10 s until the 1st of February, being the highest waves on the 24th and 31st of January and the 1st of February (H_{rms} ~ 2 m) (Fig. 32 c). The near-bottom wave orbital velocities (U_w) ranged between 0.1 and 0.4 m/s displaying peaks following similar shapes than the wave heights time series (Fig. 32 d). The highest waves occurred at the end of the period on the 3rd of February ($H_{rms} > 3$ m and $T_z = 8$ s), with orbital velocities increasing until 0.6 m/s.

2.2.2. Water level and currents

The water level variation was dominated by semidiurnal tides, with alternating ebbs and floods approximately every 6-7 hours (Fig. 31 d). From the beginning to the end of the water level time series three neap and spring tides displayed minimum amplitudes of 2.5 m and maximum tide amplitudes of ~9 m respectively, coinciding the later with wave events.

At the beginning of the study period (18th of January to the 3rd of February) neap tides showed minimum amplitudes of 2.5 m and spring tides maximum amplitudes of 6.3 m (Fig. 32 b). The

tide directions (obtained from the currents measured with the ADV) indicated that flood tide flowed towards NNE and ebb tide towards S (Fig. 32 b), in agreement with morphological observations in the continental shelf. Each ebb-flood cycle displayed a progressive change in the direction of the currents showing slightly rotational behaviour. The near-bottom currents ranged from 0.2 m/s during ebbs and floods to values nearly zero when the tides changed direction (Fig. 32 d). During springs the tidal currents were larger than during neaps displaying the flood component higher than the ebbs.

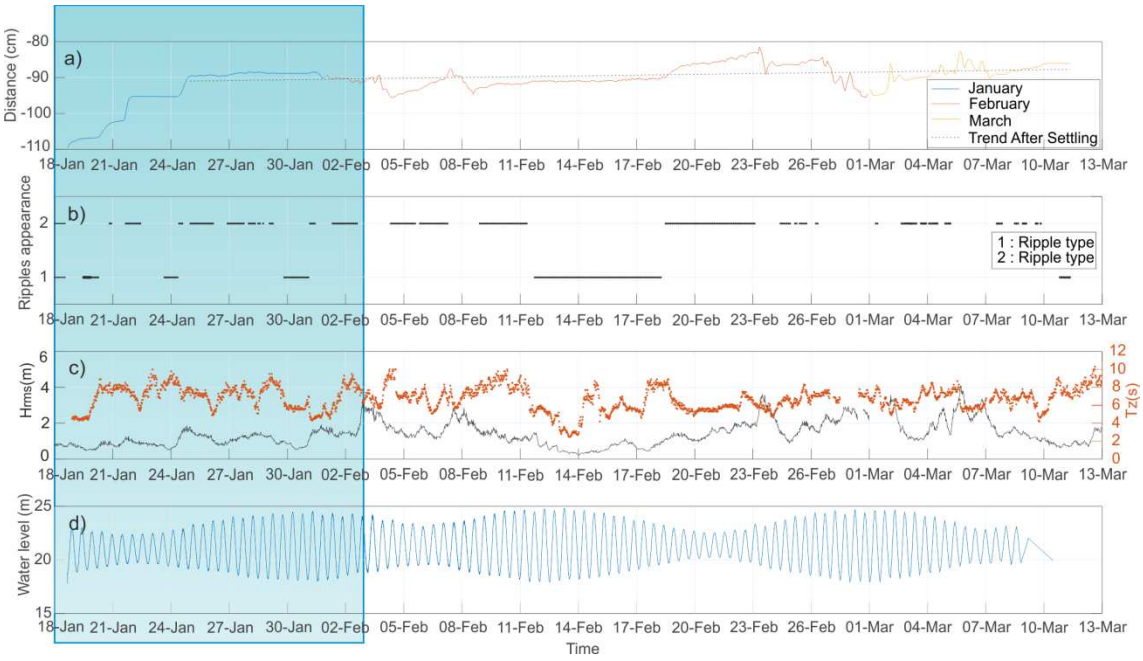

Fig. 31. Time series of the frame deployment of: (a) topographic variability obtained from the 3D-ARP data which represents the relative distance from the 3D-ARP transducer to the seabed; (b) ripple appearance in the 3D-ARP images distinguishing between the two different ripple morphologies observed; (c) wave height and period data from the offshore buoy of Perranporth located at 14 m depth; and (d) water level from the ADCP Signature. The blue- shadowed area indicates the specific period studied (from the 18th of January to the 3rd of February of 2017) detailed in Fig. 32.

2.2.3. Sinking, scour and erosion around the frame

The topographic variations of the bed level displayed three different trends during the study (Fig. 31 a): (i) from the 18th to the 25th of January, when the frame sank in the sand relatively rapid by three times, with total frame settling of ~0.20 m; (ii) four periods when bed level remained more or less constant without significant changes (three after the tripod settlings and one from the 9th to the 19th of February); and (iii) several abrupt seabed level changes with relatively rapid erosion, e.g. on the 4th, 8th or 24th of February or during March when erosion events occurred more frequently (Fig. 31 a). After each erosion period, the bed level progressively recovered. The periods when the topographic variability showed fast erosion

correlated with those periods when wave heights were up to 2 m (Fig. 31). Furthermore, observations from the 3D-ARP indicated that the erosion was the result of relatively big scour formations around the legs of the frame, sometimes even merging between them (Fig. 33 a). The further frame recovery after these erosion periods was the result of the refill of these large scour (Fig. 33 b). After the initial frame settling, the general trend of the seabed was an apparent accumulation of ~0.03 m along the study period (Fig. 31 a, dashed line). The fact that the overall seabed trend was almost zero indicates that the seabed erosion suffered mostly around the frame legs was later recovered with the refill of the scour.

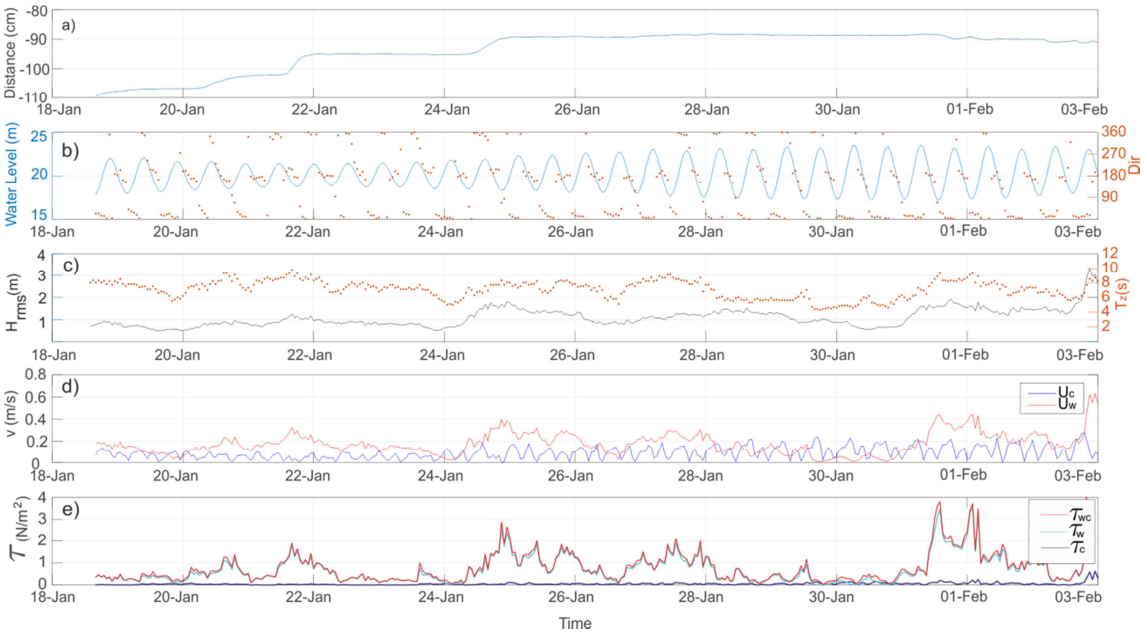

Fig. 32. Specific period of the analysis in this work indicated in Fig. 31 by a blue rectangle showing the time series of: (a) depth-averaged bed level displaying the relative distance between the 3D-ARP transducer and the seabed level; (b) water level depth (line) and direction of tides (dots); (c) root mean square wave height (H_{rms}) (line) and waves mean period (T_z) (dots); (d) orbital velocity (red line) and current speed from ADV (blue line); (e) maximum combined wave and currents shear stress (blue line); wave-alone shear stress (green line), and current-alone mean shear stress (red line).

From the 18th of January to the 3rd of February there were four periods when the distance between the 3D-ARP transducer and the seabed reduced (Fig. 32 a): the first was on the 18th January 2017, sinking 2.6 cm, probably because of the frame deployment; the second occurred on the 20th of January and it happened more progressively with a difference in distance of 4.2 cm; the third was on the 21st of January and the variation in the depth bed level was of 7 cm; and finally the fourth occurred on the 24th of January and distance reduction was of 5.9 cm. Each of these changes last around 16 h and they seemed to be consequence of the frame accommodation and sinking because of its own weight and slightly influenced by the hydrodynamic regime with increasing wave heights. The overall settling was ~20 cm (Fig. 32

a). From the 31st of January to the 3rd of February the distance between de seabed level and the ARP transducer increased around 7 cm meaning erosion of the seabed sediments. Particularly, this erosional period corresponded with the formation of scour around the legs of the frame as mentioned before (Fig. 33 a).

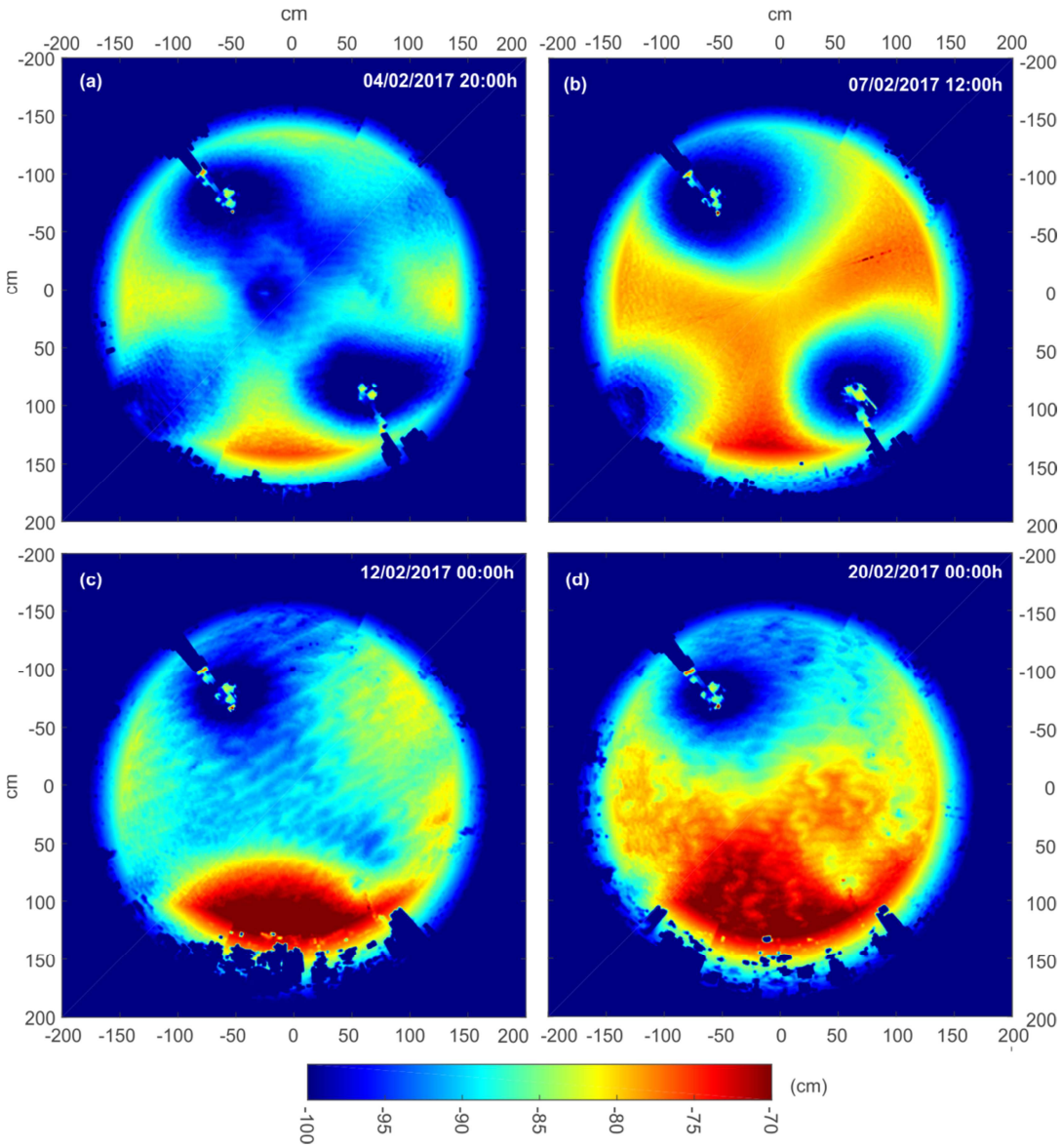

Fig. 33. 2D scan images obtained with the 3D-ARP on the: (a) 04/02/2017 20h showing when two of the scour formed around the legs of the structure and merged; (b) 07/02/2017 12h showing the scour formed around the legs of the structure and the partially refill of the previous scour; (c) 12/02/2017 0h changes on the seabed morphologies with the previous scours at the lower part of the images completely refilled; (d) 20/02/2017 0h other different seabed morphologies identified.

The hydrodynamic forcing conditions acting on the seabed during the study period are here characterized by estimating the near-bed shear stress. The stress was calculated as the maximum combined wave and current shear stress (τ_{max-wc}), shear stress considering only waves input

(τ_w) and shear stress resulted on considering only currents (τ_c) (Fig. 32 e). The maximum contributor to the combined wave and currents shear stress was clearly waves, being only reached and seldom exceeded by the current stress during short periods when the orbital velocities were weak < 0.1 m/s (H_{rms} ~ 0.5 m) on 19th, 24th, 26th, 29th and 30th of January. The combined wave-current shear stress ranged from less than 0.1 to > 3 N/m^2 along the studied period, with several peaks of τ_{max-wc} > 2 N/m^2: the first on the 21st of January with τ_{max-wc}~2 N/m^2; between the 24th and 28th of January some peaks τ_{max-wc} > 2 N/m^2 occurred; on the 31st of January and 1st of February two peaks of almost 4 N/m^2; and finally, at the end of the time series (the 2nd February) resulted on τ_{max-wc} > 4 N/m^2 (Fig. 32 e).

2.2.4. Ripple observations

From the 3D-ARP data, high-resolution scans of ~4 m diameter showed the detailed bed morphologies every 2 h (Fig. 33, Fig. 34). Ripple appearance or presence were identified from the scans and displayed along a time series distinguishing between the different morphologies observed (Fig. 31 b). Despite the scour, ripples continued developing simultaneously with the scour formation and refill intervals (Fig. 33 c, d), although the near-bottom hydrodynamics could be altered modifying the processes related to ripple formation and dynamism. Consequently, the time series data of ripple observations were evaluated during periods when scour were not present or were small enough to consider that they could not severely affect the hydrodynamics and the processes related to the ripples formation and dynamics: from the 18th of January to the 3rd of February of 2017.

Basically, two different ripple morphologies were identified and classified as: (i) ripple type 1 with very rectilinear crests aligned ~180° with respect to the north and (ii) ripple type 2 with apparently smaller dimensions (height and wavelength) and sinusoidal or curved crests, although with similar crest disposition to the previous (Fig. 34 a and c, respectively). During periods when no ripples were observed the scans displayed flat bed and in occasions seabed morphologies with hollows following a zig-zag pattern. The latter could neither be identified nor interpreted pointing to complex morphologies or maybe tridimensional bedforms or perhaps sensor or data acquisition artifacts (Fig. 33 d, Fig. 34 b). Therefore, they were discarded to any further analysis.

The comparison of the mean bed level and the ripple appearance time series indicated that the ripples type 1 only appeared during those periods when the bed level remained stable without large topographic variations (Fig. 31 a, b). During periods of bed level changes by abrupt erosion or scour formation no ripples appeared at the scans. Finally, during periods of seabed level recovery (accretion) ripple type 2 formed (Fig. 31 a, b). It seems that ripple appearance and dimensions followed wave conditions (Fig. 31 b, c). Ripple type 1 occurred under low-

energy wave conditions (H_{rms} < 1 m and T_z < 8 s) and ripple type 2 developed under mild-energy wave conditions (1 m < H_{rms} < 2 m and variable T_z). The angle between the incident waves and the ripple crests was of ~100°. Flatbed was observed during higher-energy periods (H_{rms} > 2 m and T_z ~ 10 s).

The presence of ripples on the seabed at the Perranporth site from the 18th of January to the 3rd of February of 2017 was the most usual situation, since it occurred during the ~64% of the time. The development of type 1 and type 2 occurred during the ~19% and the ~45% of the time studied, respectively. Ripple height and wavelength measurements demonstrated size differences between ripple typology 1 and 2 (Fig. 35 c, d). Ripple type 1 displayed heights up to 2 cm and wavelengths ~15-20 cm, while ripple type 2 displayed lower heights ~1-1.5 cm and wavelengths ~10-15 cm. Based on observations of the seabed morphology, scans from the 3D-ARP pointed to ripple type 1 stationary while type 2 seems to change crest alignment (readjustment) between consecutive scans.

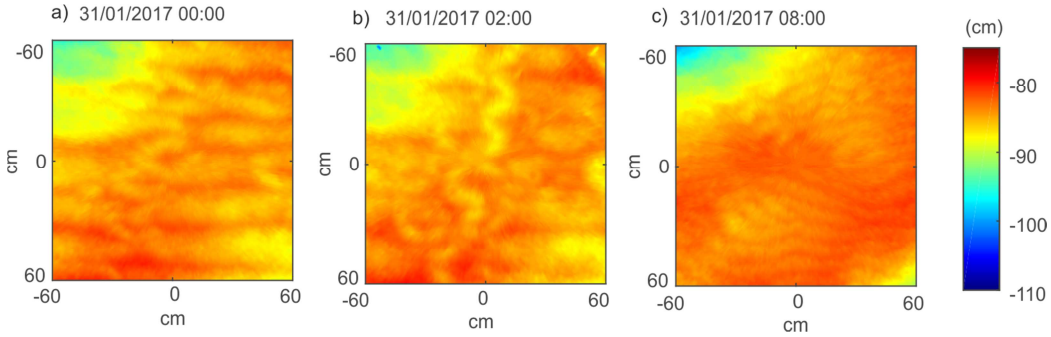

Fig. 34. Examples of 3D-ARP images (2D-scan) for: (a) ripple type 1 morphologies with bigger dimension and rectilinear crests (31/01/2017 0h 2D-scan image); (b) Zig-zag patterns observed in some of the scans (31/01/2017 2h 2D-scan image); and (c) ripple type 2 morphologies with smaller dimensions and sinusoidal or curvilinear crests(31/01/2017 8h 2D-scan image).

3. Discussion

3.1. Seabed alteration induced by the tripod frame

The ARP scan images demonstrated that the seabed was severely altered by the interaction between hydrodynamics and the frame-structure, resulting on scour formation around the legs (Fig. 33). Perranporth observations showed maximum scour dimensions of ~ 0.3 m during periods of moderate growing wave height and low-tidal currents (< 0.2 m/s) (Fig. 31). Both ripples type 1 and type 2 were observed in presence of scours and during refill intervals. However, the presence of instrumented tripods can produce artificial downward vertical velocities, an increase of horizontal velocity under the frame, and enhanced bottom stress that, under large flows, produced considerable scour under the rig (Bolaños et al., 2011). These authors stated a direct relation between tidal speed (from 0.10 m/s to 0.6 m/s) and scour

dimensions (from 0.1 m to 0.8 m) with no scour formation for tidal velocities lower than, 0.10 m/s. Therefore, since the alteration by the frame of the near-bottom hydrodynamics as well as the seabed morphology can modify the processes related to ripple formation and dynamism, the ripple analysis was focus only during the second fortnight of January 2017.

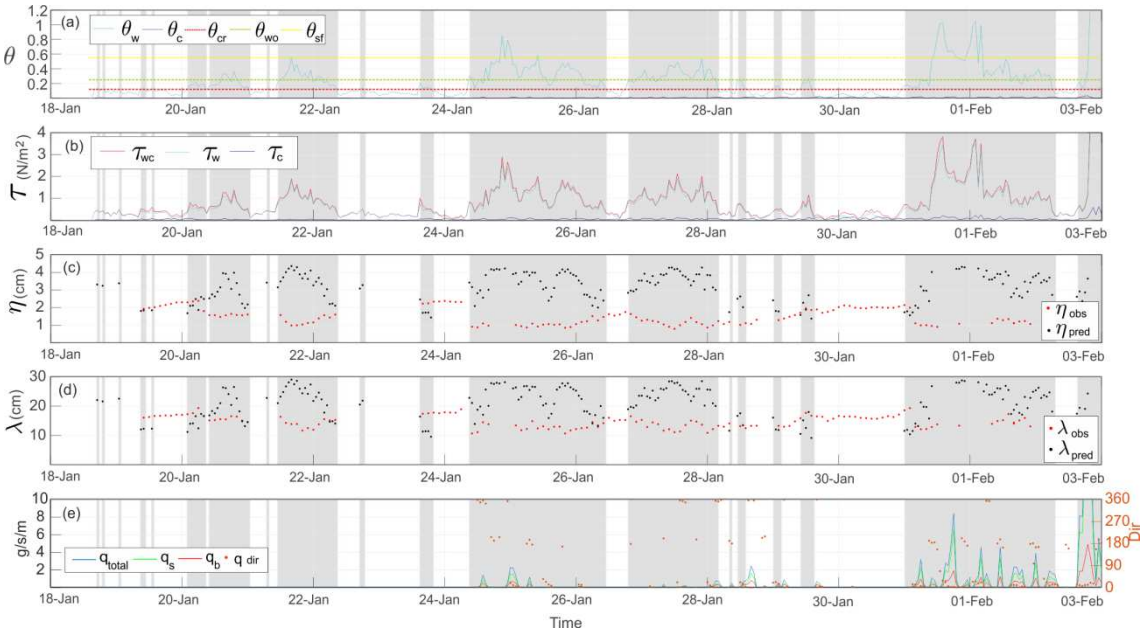

Fig. 35. Time series of (a) Shield parameter due to waves (θ_w, blue line) and currents (θ_c, black line), and threshold of motion (θ_{cr}, dashed red line), wash-out (θ_{wo}, dashed green line), and sheet flow (θ_{sf}, dashed blue line); (b) maximum combined wave and currents shear stress (blue line), wave-alone shear stress (green line), and current-alone shear stress (red line); (c) ripple heights in cm from the 3D-ARP observations (red dots) and obtained with the ripple predictor from Soulsby et al (2012) (black dots); (d) ripple wavelength in cm from the 3D-ARP observations and obtained with the ripple predictor from Soulsby et al (2012) (black dots); (e) total sediment transport (blue line), suspended load sediment transport (green line), bed load sediment transport (red line) and resultant sediment transport direction with respect to N (red dots and right vertical axis). Shaded areas indicate periods when Shields parameter exceeded the threshold of sediment motion.

3.2. Ripple occurrence and development

In general, the presence of ripples and their morphological changes depend on the flow conditions and the ripple ability to adapt to the new hydrodynamic conditions until they reach the equilibrium (Nelson and Voulgaris, 2014). At the Perranporth site, most ripple crestlines (both type 1 and type 2 despite their sinuosity) were oriented N-S, perpendicular to the wave direction approach (W-E) and parallel to the dominant current direction (N-S). Thus, ripple occurrence and evolution was mainly related to wave action. This fact is relevant when considering the effects of bed roughness in the estimation of shear stresses caused by waves and currents since bedform roughness affected the wave induced stress but hardly influenced the current induced shear stress.

The development of ripple type 1 occurred during low-energy hydrodynamic conditions, with wave heights lower than 1 m (orbital velocities < 0.2 m/s) and tidal currents lower than 0.2 m/s. Observations showed gradation from ripple type 1 to type 2 and to flat bottom with increasing Shields parameter (or bottom shear stress) (Fig. 35). Under increasing energetic conditions, ripple type 1 slightly increased their dimensions until a maximum size (~2.4 cm height and ~19.5 cm wavelength) after which, ripple size dropped dramatically (Fig. 35). This drop corresponded with the transition from ripple type 1 to type 2 which was interpreted as ripple degradation when ripple wash-out conditions were reached (e.g. 20th - 21st of January, Fig. 35). Finally, ripples disappeared (sheet flow regime) during the most energetic periods (e.g. 24th-25th or 31st of January and 1st of February, Fig. 35) when the Shields parameter threshold (θ_{sf}) reached a value of 0.55. Inversely, the transition from ripple type 2 to type 1 (ripple growth) was progressive and it occurred when Shields parameter decreased (e.g. 25th - 27th of January, Fig. 35).

Similar transitions in ripple height and wavelength in energetically changing conditions were also observed in other sites (Hanes et al., 2001; Nelson and Voulgaris, 2014). When the flow is energetically changing, ripple dimensions might not be in equilibrium with the flow and they will actively change height, wavelength and orientation until they achieve the equilibrium. In fact, ripples during regimes close to the inception of motion should be only stable if the shear stress stays close or below the critical value, remaining then as a relict bedforms (Bagnold, 1946; Camenen, 2009). At the Perranporth site it was on the 19th, 23rd -24th, 26th, 28th, 29th -30th of January when energy decreased below the threshold of motion and ripples dimensions remained constant without significant changes as relict ripples (Fig. 35).

No ripple migration was detected during the study period. Ripple type 1 remained steady with neither migration nor morphological changes under low bottom boundary layer efforts persisting on the seabed as relict ripples. However, ripple type 2 sometimes exhibited some dynamism by changing the crests curvature between two successive scans which indicated readjustment of these bedforms rather than migration in a particular direction.

3.3. Observations and theoretical approach of ripple prediction

In order to estimate thresholds of initiation of sediment motion the Shields parameter due to waves and currents was first calculated (Fig. 35 a). As expected, the wave Shields parameter followed similar trend than the wave shear stress and the orbital velocities coinciding during higher-energetic peaks reaching values over 0.8. Combining seabed observations and the wave Shields parameter time series, thresholds of motion, wash-out, and sheet flow were roughly estimated and compared with different formulations (Table VI). In spite of the large variability obtained from the different approaches, the threshold values estimated from our observations

are in the same range. These thresholds suggest that the ~62% of the time the θ exceeded the theoretical threshold of grain motion during which the 30% was between the wash-out and sheet flow ($\theta_{wo} < \theta_w < \theta_{sf}$) and the 11% was over the sheet flow. The remainder 38% of the time the hydrodynamics were below the threshold of sediment motion. The Shields parameter considering only current conditions was almost negligible, remaining below the sediment motion threshold during the whole period (Fig. 35 a).

The theoretical estimations of Shields parameter thresholds for starting grain movement and wash-out were lower than suggested from observations while sheet flow thresholds approximations were lower or higher depending on the approximation used (Table VI). Lower theoretical Shields thresholds than suggested from observations in ripple development and disappearance were also previously reported (Bagnold, 1946; Hanes et al., 2001; Camenen, 2009). These differences can be consequence of the strong simplifications involved in calculations (i.e. d_{50} as the representative sediment size and the impossibility of existing completely uniform sediment grain size, bottom boundary layer complexities, etc.) (Traykovski et al., 1999). Similarly, Kleinhans' (2005) diagram considering waves and currents conditions for the Shields parameter and for a given sediment size, located ripples type 1 below the limit of sediment motion and ripples type 2 in the region of linear wave-dominated ripples.

The theoretical sheet flow threshold showed a high variability which depends on the method applied (Table VI). The Li and Amos (1999) and the Soulsby et al. (2012) resulted on the same low and constant value (0.2), probably because of the similarity of the equations and because they only consider the skin-friction case. The constant threshold of Nielsen (1981), the time-varying thresholds of Kleinhans (2005) and Camenen (2009), and the ratio between orbital velocity amplitude and mean sediment grain size overestimated the sheet flow threshold compared with observations.

Table VI. Shields parameter thresholds for critical, wash-out and sheet flow conditions obtained with different approximations

Author(s)	$\boldsymbol{\theta_{cr}}$	$\boldsymbol{\theta_{wo}}$	$\boldsymbol{\theta_{sf}}$	$\boldsymbol{\frac{A_w}{d_{50}}}$	**hydrodynamic conditions defined method**
Nielsen (1981)	-	-	1		oscillatory flow
Li and Amos (1999)	-	-	0.2		combined steady and oscillatory
Kleinhans (2005)	-	-	$\sim\theta_w$ [0-3]		combined steady and oscillatory
Soulsby and Whitehouse (2005)	-	-		~2000	oscillatory flow
Camenen (2009)	-	-	[1-1.2]	-	combined steady and oscillatory
Soulsby et al. (2012)	0.04	0.14	0.2	-	combined steady and oscillatory
Observations	0.12	0.25	0.55	-	combined steady and oscillatory

The discrepancy between observations and theoretical estimations also affect in the application of the theoretical prediction of ripple dimensions since these estimations are based on the previously estimated theoretical thresholds and shear stresses. Therefore, the observed thresholds of the Shields parameter for ripple appearance, degradation and wash-out were applied instead of the theoretic values of critical, wash-out, and sheet flow thresholds (black points in Fig. 35 c and d). Therefore, according with hydrodynamic and morphodynamic observations, the thresholds of Shields parameter for starting ripple formation (θ_{cr}) (ripple type 1), ripple wash-out (θ_{wo}) (transition from ripple type 1 to type 2) and sheet flow (θ_{sf}) regimes were 0.12, 0.25 and 0.55, respectively (Table VI, Fig. 35 a). During the 64% of ripples appearance only the 43% of time were "active" ripples (when ripple appearance and $\theta > 0.12$), whereas the ~21% of time were relict ripples (below the observed threshold of ripples formation $\theta < 0.12$).

Obviously, near-bottom stress had to be equal or exceed the critical condition as a compulsory premise for the predictor estimations. Here, only the wave-generated ripples formulation was applied because of waves dominated the hydrodynamics during the study period (current Shields parameter was always under the threshold of motion, Fig. 35 a). This methodology worked quite well in terms of ripple appearance to estimate equilibrium ripple conditions and only in two occasions the method predicts ripple type 1 when flatbed was observed (Fig. 35 c and d). Ripple type 1 dimensions were estimated quite well under low energy conditions. On the contrary, when the bedforms remained on the seabed as relict ripples flatbed is predicted from the model because $\theta < \theta_{cr}$ (Fig. 35). This almost unpredictable bottom roughness occurs during 21% of time and it can significantly modify shear stress estimations. Actually, the Soulsby et al. (2012) equilibrium ripple predictor suggests pre-existing values for ripple height and wavelength when $\theta < \theta_{cr}$. However, in nature, there are many of these cases where the bed is flat and others when previously formed ripples remain lying on the seabed. A model able to predict this uncertain absence or presence of ripples or relict ripples is challenging as several data indicated the occurrence of ripples whereas the Shields parameter was smaller than the critical value and vice versa.

The ripple prediction for wash-out conditions (ripple type 2) overestimated ripple dimensions and showed wider variability than observations, with ripple heights between 2 and 4.5 cm and wavelengths between 15 and 30 cm (Fig. 35 c and d). Other sites and experiments during wash-out conditions showed similar results (Hanes et al., 2001; Camenen, 2009; Soulsby et al., 2012). Furthermore, the theoretical estimations suggested ripple growth when Shields parameter increased above θ_{cr} and the inverse when Shields decreased because of the equations (depending on the wave orbital velocities). However, the observations showed the opposite

trend, with ripple degradation during increasing energy and ripple growth under decreasing energy (transition from ripple type 1 to 2).

Overall, the theoretical estimation on the Shields parameter thresholds did not fit with our observations probably because of the skin-friction case assumption taking in account only the sediment size non-dimensional parameter and also because of they are generally based on empirical approximations of specific data considered in other studies. Then, theoretical estimations of threshold Shields parameters for ripple prediction should be carefully applied and sometimes only be considered in a semi-quantitative manner. Consequently, observational thresholds of this variable were here applied as we have hydrodynamic and morphodynamic observations and the threshold of motion, ripples wash out and sheet flow can be deducted from the observations. This is the most reasonably option when data and observations are available.

3.4. Are ripples at the inner shelf a potential mechanism of beach recovery after storms?

The two components of hydrodynamics that dominated at Perranporth inner shelf during the period studied were waves coming from the W with a mean approach angle of ~280° and the N-S currents with slightly rotational component of NNE-SSW following the flood and ebb tidal flows (Fig. 36 a). The total sediment transport is mainly related with waves and time series displayed several peaks ranging from ~2 g/s/m to > 20 g/s/m mostly during mild-storm conditions (Fig. 35 e, Fig. 36 b). The estimated suspended load transport widely dominated over the bed load transport (77.2% and 22.8%, respectively).

The dominant sediment transport direction was alongshelf, switching between N and S following the ebbs and floods tidal flows (dots in Fig. 36 b) but with a clear net transport northwards because of flood tidal currents dominated over the ebbs at this point of the inner shelf (Fig. 36 c). This pattern was mainly the result of the sediment resuspension by wave stirring and the further transport due to currents (tidal currents) which is characteristic in environments dominated by waves and currents (Traykovski et al., 1999; van Rijn, 2007a, 2007c). Therefore, most of sediment transport occurred parallel to the ripple crestline and the cross-shelf sediment transport is negligible because of the (almost) absence of cross-shelf currents (Fig. 36 a). However, episodes of alongshelf transport when energy slightly increased can explain the observed changes in the morphology of ripple type 2 (mostly ripple crest realignment) until higher energetic regimes completely washed-out ripples during the highest peaks of sediment transport (Fig. 35). These seabed modifications and ripple dynamisms occurred relatively rapid according to 3D-ARP observations with ripple reorientation between 2 consecutive scans (2 h).

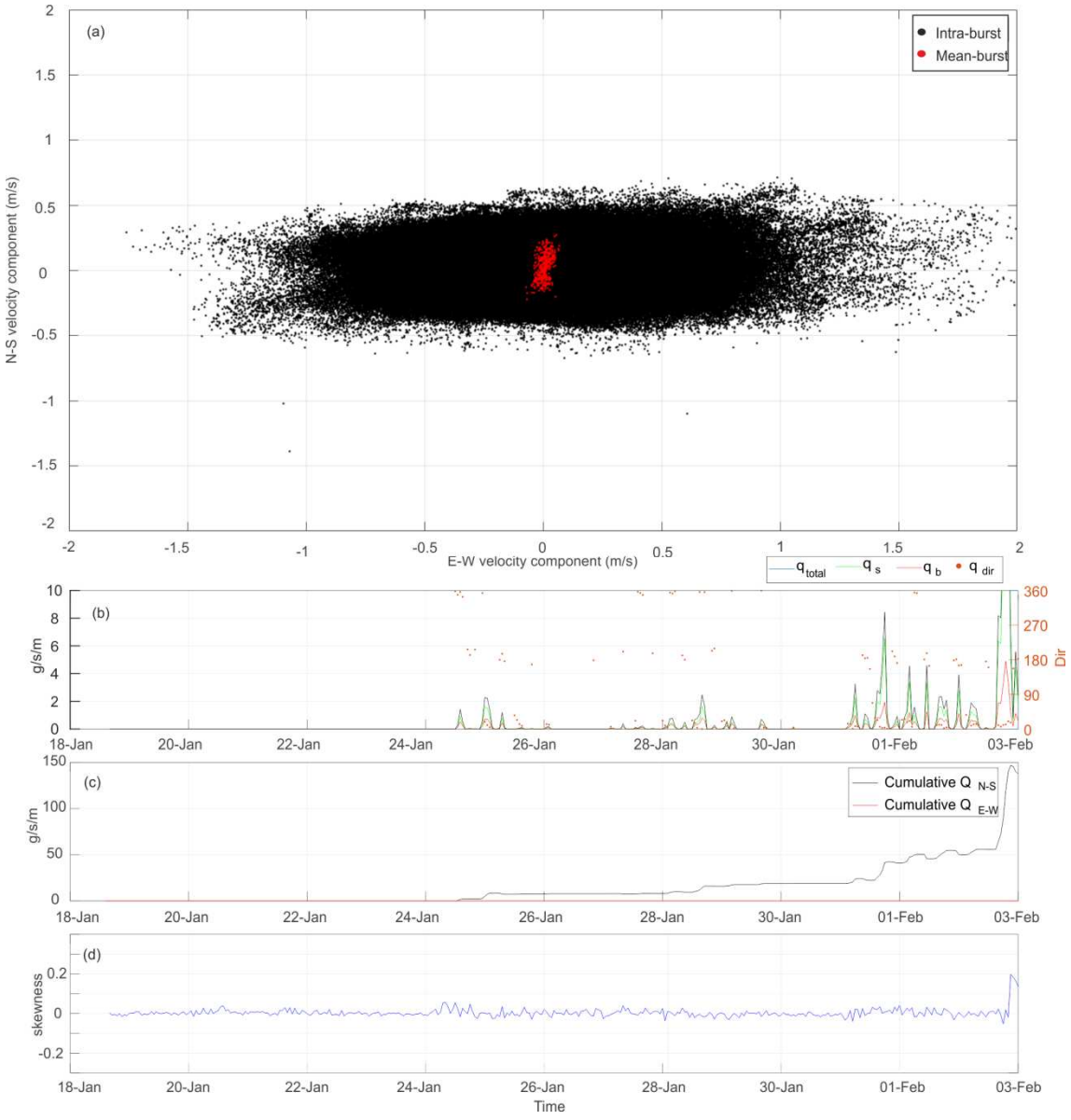

Fig. 36. (a) Dispersion diagram of E-W velocity components (x axes) and N-S velocity component (y axes) considering the E and N components positive values and the W and S components negative values. Black dots corresponds to intra-burst data and red dots the mean-burst data; (b) total sediment transport (blue line), suspended load sediment transport (green line), bed load sediment transport (red line) and resultant sediment transport direction (red dots and right vertical axis); (c) cumulative sediment transport towards the N-S direction (black line) and towards the E-W direction (red line) considering the N and E directions positive; (d) cross-shore (E-W) wave velocity skewness.

In absence of currents crossing the crestlines, wave-dominated ripples would also migrate in response to the asymmetry in the near-bed wave orbital velocities that typically occurs in shallow waters (Traykovski et al., 1999; Crawford and Hay, 2001; Soulsby and Whitehouse, 2005; Miles et al., 2014). Since the wave asymmetry mechanism is not included in the used sediment transport equations, the cross-shore wave velocity skewness was estimated based on the velocity measurements at the Perranporth inner shelf. Results showed quite symmetric near-

bed wave velocities with values of velocity skewness close to zero pointing to no cross-shore sediment transport during most of the study period (Fig. 36 d). The wave symmetry and low-intensity currents parallel to ripple crestlines were in agreement with the stationarity of ripple (no migration) at ~20 m depth (Fig. 36 d). However, positive values of velocity skewness, indicating a potential onshore sediment transport, happened during the highest energy period (3rd of February) (Fig. 36 d). It is worth noting that during that highest energy event, no ripples were observed and sheet flow regime governed the near-bottom sediment transport.

This fact is a relevant difference with respect to observations in the nearshore, where onshore migration of ripples was observed as a consequence of velocity skewness (> 0.2 m/s) during mild waves with wave orbital velocities around 0.25-0.50 m/s (Miles et al., 2014). This could be a mechanism for the beach recovery after storms. It has been pointed out that the post-storm recovery does not necessarily occur during calm periods and in many cases high-energy wave events appear to be essential for recovery of beach sediment (Scott et al., 2016). However, with similar wave orbital velocities, the skewness was lower at the inner shelf than in the nearshore. At the inner shelf, wave skewness around 0.2 m/s was only reached for wave orbital velocities of 0.6 m/s, when ripples were washed-out. Thus, the potential onshore sediment transport at 20 m depth was unrelated with ripple dynamics and only would occur during sheet flow conditions.

4. Conclusions

Morphological observations at Perranporth inner shelf show that the presence of wave-ripples on the seabed is the most usual situation (64 % of time) during low and mild wave conditions.

The presence of the Mini-STABLE rig altered the seabed forming scour around the legs during periods of moderate wave heights and low speed tidal currents (< 0.2 m/s). Therefore, the ripple analysis is focused during the first period of the deployment, when scour were not present or small enough to consider that they were not severely affect the hydrodynamics and the processes related to the ripples formation and dynamics.

Three different general trends on the seabed were linked with changing hydrodynamics: (i) low-energy regime when minimum changes on the seabed morphology happened with steady or relict ripples and negligible sediment transport; (ii) moderate-energy regime characterized by ripples formation which displayed some dynamism by crests-reorientations and small amounts of sediment transport; and (iii) high-energy regime when ripples washed-out, the morphology of the seabed changed rapid by scour formation (erosion around the frame legs) and when sheet flow regime governed and maximum sediment transport rate was estimated.

Ripple occurrence and evolution was mainly related to wave action as most ripple crestlines were oriented N-S, perpendicular to the wave direction approach (W-E) and parallel to the

dominant current direction (N-S). Two categories of ripples were recognized: ripples type 1 with rectilinear crests, η >2 cm and λ =15-20 cm, and ripples type 2 with more sinusoidal or curved crests, η =1-1.5 cm and λ =10-15 cm. Under increasing energetic conditions, ripple type 1 increased their size until a limit which ripple sizes dropped dramatically. This drop corresponded with the transition from ripple type 1 to type 2 which was interpreted as ripple degradation during ripple wash-out conditions. Inversely, the transition from ripple type 2 to type 1 (ripple growth) was progressive and it occurred when Shields parameter decreased.

The application of theoretical ripple predictor fails both in the prediction of the appearance and dimensions. Ripple predictor using thresholds derived from observations improved the capability to forecast ripple appearance, although ripple dimensions were still overestimated.

Alongshelf sediment transport dominated switching between N and S following the ebbs and floods tidal flows with northwards net transport because of flood dominated over the ebbs tidal currents at this point of the inner shelf. Episodes of alongshelf transport when energy slightly increased can explain the observed changes in crests realignment of ripple type 2, until higher energetic regimes completely washed-out them.

The wave symmetry and currents parallel to ripple crestlines were in agreement with the stationarity of ripples (no migration) at ~20 m depth, rejecting the possibility of onshore transport associated to ripple migration. Wave skewness increased during more energetic conditions, being a potential driving for onshore sediment transport during sheet flow conditions.

Chapter VII. Variability of near-bottom suspended sediment concentration by waves and currents above flat and rippled beds (Ebro Delta)

1. Introduction

In shallow marine environments, the suspended sediment is a significant component of the total sediment transport and it is the dominant sediment transport mechanism when fine sediment prevail (van Rijn, 2007c). The variability (spatial and temporal) of suspended sediment has been monitored in controlled laboratory experiments (Ribberink and Al-Salem, 1995; Thorne et al., 2009; Ruessink et al., 2011; O'Hara Murray et al., 2011, 2012; Brinkkemper et al., 2016; Davies and Thorne, 2016) and, less often, in natural environments (Lee et al., 2002; Kularatne and Pattiaratchi, 2008). Most of these studies support that the near-bed suspended sediment concentration on the coastal zone and the inner shelf largely depends on sediment resuspension caused by waves and currents. Understanding the physical processes behind the near-bed suspended sediment dynamics has significant implications for ecology, biogeochemistry, and geomorphology (Schoellhamer et al., 2007; Li et al., 2015).

Under irregular waves, the suspended sediment concentration (SSC) fluctuates from intra-wave frequencies associated with individual waves to infragravity frequencies associated with wave groups (O'Hara Murray et al., 2011, 2012). The initial entrainment process occurred at intra-wave frequencies while at the free stream, sediment suspensions were dominated by the vertical transport of sediment at wave group time scales, having then the waves groups an important role on sediment suspension in both the wave boundary layer and the free stream (O'Hara Murray et al., 2012). Actually, in the shoaling and outer surf zone, the sea-swell waves typically dominates over the infragravity waves (Bakker et al., 2016). Under wave-current dominated conditions, waves generally act as sediment stirring and the resulting suspended particles are transported by the currents (van Rijn, 2007b). Therefore, in the small scale, the suspended sediment variability is the result of the combined effects of local resuspension and sediment advection. Interactions between the flow and the suspended sediment close to the seabed are complex, because of local

nonlinearities of the near-bed oscillatory flow (Ruessink et al., 2011), the seabed roughness (flat or rippled) (Ribberink and Al-Salem, 1995) and the role of currents in sediment dispersion (Ogston et al., 2000). Winds can drive wave and current generation also contributing to the sediment resuspension and transport mostly in shallow coastal waters (Ha and Park, 2012; Carlin et al., 2016). Understanding fetch-limited waves as a function of wind speed and direction, in conjunction with the geometry and/or orography of the area seems to be key to better understand some of the suspended sediment processes (Carlin et al., 2016; Grifoll et al., 2016).

In detail, the suspension of sediment is strongly dependent on the hydrodynamics but also on other factors as the sediment grain size (Davies and Thorne, 2016) or the bottom roughness (Ribberink and Al-Salem, 1995; Li et al., 1996). Exist evidences that diffusion affects the finer fraction of the suspended sediment while the combined diffusion plus advection dominate the distribution of the coarser fractions, with implications in the shape of suspended concentration profiles (Li et al., 1996; Davies and Thorne, 2016). Furthermore, the suspended sediment grain size distribution becomes progressively dominated by finer grains as height above the bed (Davies and Thorne, 2016). In oscillatory flow and above relatively steep ($\eta/\lambda = 0.12$) 2D-ripples, the mixing close to the bed is dominated by coherent process involving vortex formation and shedding, both processes controlling the near-bed sediment suspensions (Nielsen 1992; Thorne et al., 2009; O'Hara Murray et al., 2011, 2012). The resulting intra-wave suspension occurs twice per wave cycle: during the onshore wave half-cycle, a vortex is generated at the lee side of the steep ripple, as flow reverses offshore, this vortex is ejected upward into higher parts of the profile (O'Hara Murray et al., 2011; Amoudry et al., 2016). However, under irregular waves and 3D-ripples vortex formation and shedding will not necessary occurs during each wave half cycle because SSC levels are maintained throughout most wave cycles by the strong orbital velocities, but also by local advection of vortices flow reversal and the transport of sand from other points (O'Hara Murray et al., 2011). Therefore, coherent periodic phenomenon of vortex shedding above steep ripples can entrain more amount of sediment and to considerably higher heights (in a convective layer of thickness 1-2 ripple heights) than above a flatbed (O'Hara Murray et al., 2011; Amoudry et al., 2016; Davies and Thorne, 2016). Above flatbed vortex shedding does not exist and the maximum sediment pick-up occurs at times of peak shear stress at the bed, closely preceding the peak free-stream velocity and it is a diffusive process (Thorne et al., 2009; O'Hara Murray et al., 2011; Davies and Thorne, 2016).

The application of Acoustic Backscattering Systems (ABS) to study the SSC have been gaining acceptance, especially with homogeneous non-cohesive sediments, within flow/sediment/bedforms small-scale sediment processes studies over the last two decades.

Mostly because of the potential to measure non-intrusively and with high temporal and spatial resolution profiles of suspended sediment concentrations (Thorne and Hanes, 2002; Hurther et al., 2011). Unlike in laboratory experiments, field studies have to overcome the difficulties to fully control hydrodynamic conditions and, very often, to the simultaneous presence of cohesive and non-cohesive bottom sediment. In addition, the presence of biological material and bubbles can contaminate the backscattered signal (Thorne and Hanes, 2002). The SSC profiles coupled with flow measurements and bedforms morphology observations with sufficient spatial and temporal resolution allow to insight into wave and current processes and provides new measuring capabilities to advance our understanding of the fundamentals of sediment processes, entrainment and transport but also to improve our capabilities to predict sediment resuspension and transport during storms (Thorne and Hanes, 2002).

This work uses high-resolution acoustic backscatter system (ABS) measurements to examine the near-bottom SSC variability under low- to moderate- energetic hydrodynamic conditions induced by waves, currents and the combined wave-currents in the Ebro Delta inner shelf. We try to find out the main mechanisms controlling SSC variability and the potential role in sediment transport processes using simultaneous measurements of SSC, waves, currents, wind field, suspended particle grain size and ripple observations. The study site is located on a sand ridge field that migrates ~10 m/y towards SSE (Guerrero et al., 2018 and Chapter IV). The area is characterised by persistent strong, dry and usually cold winds that blow from the NW (Mistral wind) through the Ebro valley (offshore wind) during autumn and winter. The Mistral wind influenced by the orography, is channelized into a limited band, forming a seaward wind jet usually developed in a ~50 km wide band offshore (Grifoll et al., 2016). Mistral winds have been suggested to induce strong near-bottom currents that flow towards the SE which are the responsible of sediment transport and sand ridges migration.

Near-bottom SSC measurements in the Ebro continental shelf have been obtained from benthic tripods and moored instruments during the last decades. These observations showed the influence of waves and currents (Guillén et al., 2005, 2002), low-frequency currents (Jiménez et al., 1999) and internal waves (Puig et al., 2001) in SSC variability. Estimations of near-bottom sediment fluxes on the continental shelf were also derived (Cacchione et al., 1990; Jiménez et al., 1999; Palanques et al., 2002). The shape of the SSC-profile was investigated fitting observations to different approaches (Guillén et al., 2002) although they were based on only three punctual measurements above the bottom, preventing a complete characterization of the SSC-profile. Therefore, this work shows a more accurate characterization of the near-bottom concentration profile, its variability at different temporal scales and the potential influence of the bottom roughness.

2. Results

2.1. Waves, currents and winds

Time series of the propagated significant wave height (H_s), current and wind velocities are shown in Fig. 37. From October to December of 2013, the H_s ranged from 0.1 m to maximum values of ~3.5 m, with the highest waves during November and December storms (Fig. 37 a). These waves represent conditions from low to moderate wave storms at the Ebro area. Waves were limited directionally, coming from the E, SE-S and NNW-NE because the existence of a shadow area between 200° and 315°, where winds were fetch-limited and not able to generate large waves in the coastal zone (Fig. 38). The near-bottom current velocities show similar trend than the waves, with the strongest currents during November and December (Fig. 37 b). When current speed increased over 0.2 m/s they channelled towards the SSE. The maximum speed recorded at ~1 mab was ~0.6 m/s on the 16th of November at 11 h (Fig. 37 b). Wind speeds display cyclic daily behaviour with higher speeds during days than during nights (Fig. 37 c). High-speed winds (> 10 m/s) were quite frequent, always towards the SE (so-called Mistral winds), and were especially persistent in November and December (Fig. 37 c). Wind and current time series comparison reveals that the high-intensity periods of both variables occurred simultaneously, with currents flowing towards the SSE meanwhile strong winds came from the NW, suggesting that the near-bottom high-speed currents were induced by the NW winds. Intense Mistral winds generated high waves offshore (at the wave buoy location), although they were unable to produce wave heights higher than 1 m in the coastal area because of the short fetch, as observed in the wave propagation (Fig. 37 a).

In order to study the potential implications of changing hydrodynamic conditions into the near-bottom suspended sediment dynamics, the periods of moderate- to high-energetic conditions of waves and currents were identified, analysed separately and classified as events. Subjective thresholds for each variable were established for waves (H_s > 1 m) and currents (v > 0.3 m/s). Under these conditions, events were classified as: only waves, only currents and wave-current dominated (shaded areas in Fig. 37). The magnitude of the variables was continuously changing, dropping during some intervals below their thresholds and afterwards reaching the threshold again during the same event period. Because of these relatively fast variability in hydrodynamics, two criteria were defined about event duration: (i) during only-wave and only-current events, if the variable remained below its threshold less than 10 h it was considered the same event; and (ii) during wave-current dominated events, if one of both variables drop below its threshold, it was considered the same event until both variables decreased below their respective threshold.

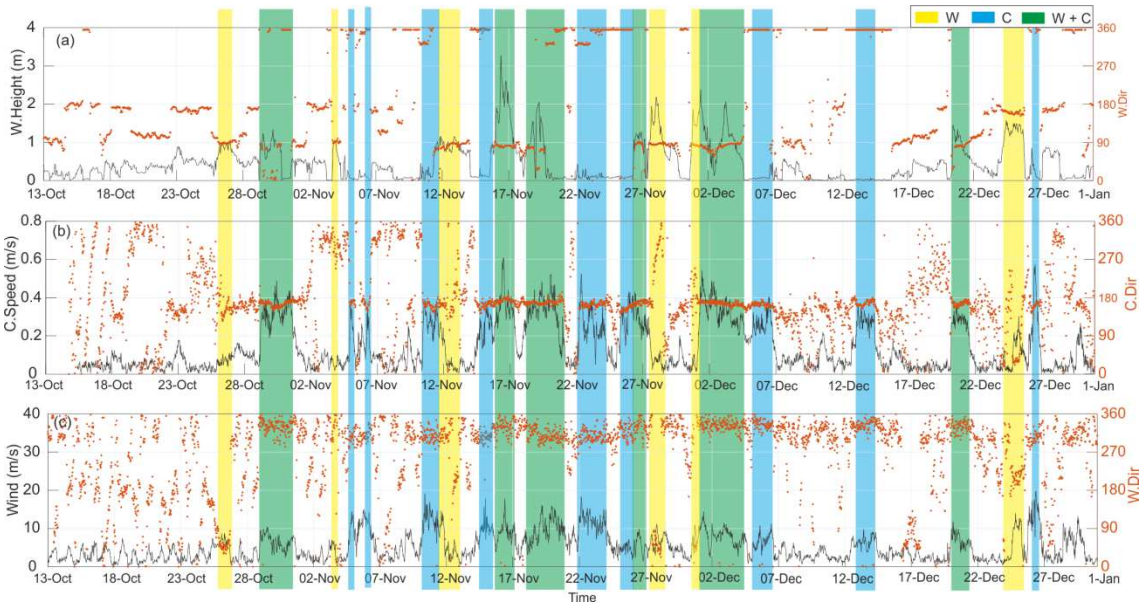

Fig. 37. Time series from 13th of October to the 31st of December of 2013 of: (a) propagated significant wave height in m (line) and direction (dots); (b) current speed in m/s (line) and direction (dots) at the tripod location at ~1 mab; and (c) wind speed in m/s (line) and direction (dots) measured at the Illa de Buda meteorological station. (see locations at Fig. 3). Note that wave directions indicate the direction where the waves came from and current direction indicates the direction towards the currents flowed. The hydrodynamic events classification identified along the period studied are indicated by the coloured shaded rectangles as only-waves (W, in yellow), only-currents (C, in blue), and wave-current (W+C, in green).

Only-wave events are characterized by H_s > 1 m, current velocities < 0.3 m/s and wind speeds < 10 m/s. Only a few exceptions wind speeds were > 10 m/s during wave events (e.g. on the 24th of December, Fig. 37c). During these events, waves always came from the E except one episode of SSE waves at the end of December (Fig. 37 a, Table VII). Six wave events were identified from October to December of 2013 and the main characteristics are summarized in Table VII. The maximum H_s was on the 28th of November when eastern wave heights grew until 2.2 m (Fig. 37 a).

Table VII. Wave height (H_s) and direction in only-wave events identified from October to December of 2013.

H_s (m)	H_s max (m)	Dir (°)	Dir (H_s max) (°)	Start	End
0.9	1	88.2	91.1	26-Oct at 06 h	27-Oct at 01 h
1	1.1	90.3	91	03-Nov at 19 h	04-Nov at 00 h
1.2	1.2	76.9	76.2	11-Nov at 14 h	13-Nov at 06 h
1.5	2.2	86.2	84.9	27-Nov at 13 h	28-Nov at 16 h
1.5	1.9	84.1	85.02	30-Nov at 19 h	01-Dec at 06 h
1.3	1.6	160.3	162.5	24-Dec at 06 h	25-Dec at 18 h

Only-current events were periods characterized by current speed higher than 0.3 m/s and H_s < 1 m (Fig. 37). When current speed increased the velocity always was directed towards the SSE (Fig. 37 b, Table VIII). Most of the current events occurred simultaneously with strong Mistral winds (> 10 m/s), with just only two exceptions: the 25th of November and the 13th - 14th of December 2013 (Fig. 37 c). Nine current events were identified from October to December of 2013 and the main characteristics are summarized in Table VIII.

Table VIII. Current velocity (v) in only current events identified from October to December of 2013.

v (m/s)	v max (m/s)	Dir (°)	Dir (v max) (°)	Start	End
0.31	0.36	166.9	163.5	04-Nov at 21:57 h	05-Nov at 01:57 h
0.3	0.35	157.3	148.4	06-Nov at 04:27 h	06-Nov at 07:57 h
0.3	0.4	161.3	161	10-Nov at 10:27 h	11-Nov at 12:57 h
0.26	0.37	162.5	158.9	14-Nov at 16:57 h	15-Nov at 13:27 h
0.27	0.53	162.9	170.2	22-Nov at 03:57 h	24-Nov at 00:27 h
0.32	0.43	156.1	162.1	25-Nov at 08:27 h	26-Nov at 08:57 h
0.27	0.41	164.3	163.1	05-Dec at 06:26 h	06-Dec at 14:26 h
0.28	0.36	166.5	163.8	13-Dec at 03:26 h	14-Dec at 09:56 h
0.42	0.57	161.2	159.6	26-Dec at 08:56 h	26-Dec at 17:56 h

Wave-current events were defined when simultaneously the current speed was higher than 0.3 m/s and the significant wave height higher than 1 m (Fig. 37). Typically, these events result from a combination of eastern waves and currents flowing towards the SSE, being the angle between the two components almost perpendicular (Fig. 37, Table IX). The most energetic wave-current event reached current speeds of ~0.6 m/s and H_s of 3.3 m on the 16th of November of 2013 (Fig. 37, Table IX).

Table IX. Current velocity (v) and wave height (H_s) and direction in wave-current events identified from October to December of 2013.

m/s m	mean	max	Dir (mean) (°)	Dir (max) (°)	Start	End
v	0.33	0.5	164.7	161.4	29-Oct at 05:27 h	31-Oct at 13:57 h
$\boldsymbol{H_{ss}}$	0.93	1.33	86	19.9	29-Oct at 08:00 h	30-Oct at 18:00 h
v	0.37	0.61	173.7	177.9	15-Nov at 22:27 h	17-Nov at 06:57 h
$\boldsymbol{H_s}$	1.86	3.3	81.8	82.6	15-Nov at 22:00 h	17-Nov at 10:00 h
v	0.36	0.52	167.6	171.9	18-Nov at 05:57 h	20-Nov at 22:27 h
$\boldsymbol{H_s}$	1.25	2.1	72.9	30.8	18-Nov at 11:00 h	19-Nov at 16:00 h
v	0.28	0.43	168.9	166.7	26-Nov at 08:57 h	27-Nov at 09:27 h
$\boldsymbol{H_s}$	1.1	1.3	76.2	87.9	26-Nov at 10:00 h	27-Nov at 06:00 h
v	0.34	0.54	166.6	167	01-Dec at 05:27 h	04-Dec at 12:57 h
$\boldsymbol{H_{ss}}$	1.2	2.4	78.8	85.2	01-Dec at 06:00 h	04-Dec at 02:00 h
v	0.29	0.35	165.1	159.6	20-Dec at 07:56 h	21-Dec at 07:26 h
$\boldsymbol{H_s}$	1.1	1.5	70.1	29.4	20-Dec at 09:00 h	21-Dec at 04:00 h

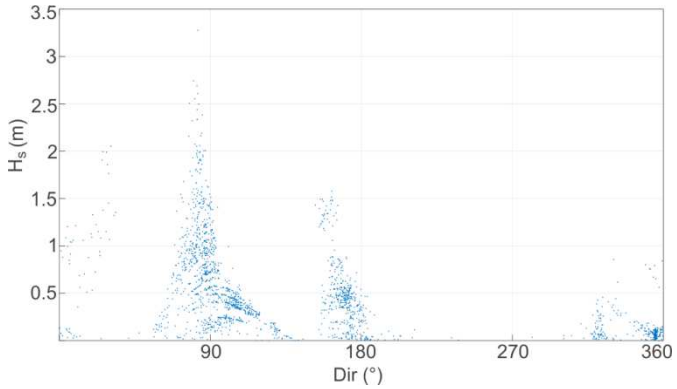

Fig. 38. Propagated significant wave height and wave direction at the tripod location during the deployment.

2.2. Sediment grain size, seabed detection and SSC variability

2.2.1. Sediment grain size

The superficial bottom sediment at the tripod location on the 13th October 2013 was fine sand with a median sediment grain size (d_{50}) of 210 μm. The sediment was composed with two grain size populations: the 91% of well-sorted fine sand with a mode around 230 μm and the 9% of mud mostly silt (Fig. 39).

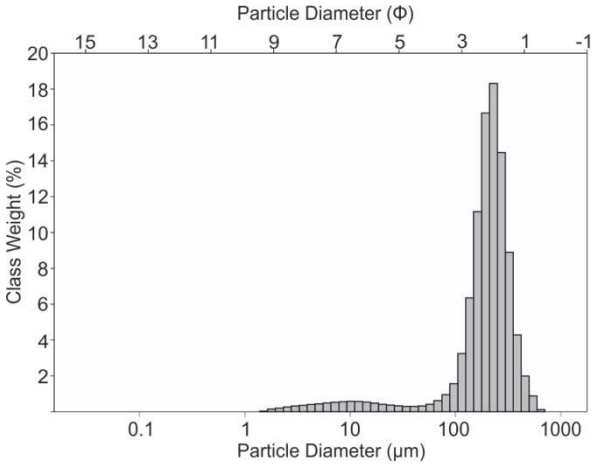

Fig. 39. Bottom sediment grain size distribution of the superficial sample (0-1 cm) at the tripod location on the 13th of October of 2013.

LISST measurements give information about the time series of the suspended sediment grain size at ~20 centimetres above the bottom (cmab) of the deck at the beginning of the deployment (Fig. 40). Useful measurements are available from October to early December when the instrument sank into the bottom. It was specifically since the 7th of December when LISST observations suddenly changed the range of the measurements probably because of the

instrument buried losing confidence on the data (Fig. 40). The grain size of suspended sediment close to the bottom was mostly composed by coarse silt to fine sand (d_{50} = 50-150 µm) with several peaks of coarser sediment (d_{50} > 200 µm) (Fig. 40 a). The minimum and maximum d_{50} were of 23 and 250 µm during the period studied (Fig. 40 a). Fig. 40 (b) shows the grain size distribution at each measurement, indicating that the suspended sediment was mostly composed by fine sand. The grain size was roughly coarser during high-energy events and finer during calm periods, although this trend was not always evident (Fig. 40 a). In general, the median grain size of suspended sediment was finer than the bottom sediment. However, the suspended sediment grain size was similar and even coarser than the bottom sediment during strong hydrodynamic events. Being 250 µm the maximum value that the LISST type B is able to measure, it is plausible that the time-averaged d_{50} of the suspended sediment during these periods could be punctually coarser than the measured (Fig. 40 a). In shorter time-scales, the intra-burst suspended sediment grain size (60 samples per minute) showed a range of variability in d_{50} > 50 µm during only-wave and wave-current events (Fig. 41 a, c) while during only-current events the d_{50} variability was smaller (Fig. 41 b). Since this sediment grain size variability roughly occurs in the same period than waves, these observations suggest a strong control of the wave passage on the near-bottom suspended sediment grain size.

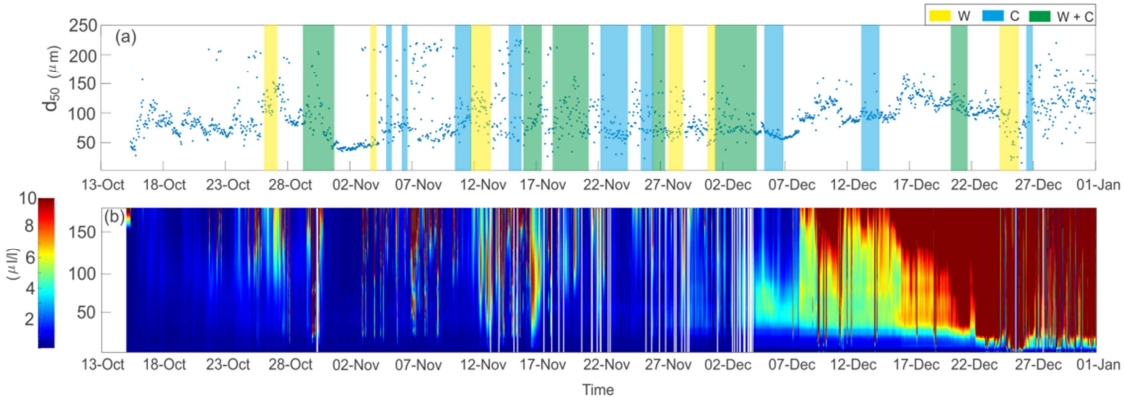

Fig. 40. Time series data of (a) burst-averaged median grain size (d_{50}) and (b) bust-averaged volume concentration of each diameter measured with the LISST instrument located at ~20 cm from ship deck during the tripod deployment.

2.2.2. Seabed location

The seabed location time series obtained with the backscatters of the ABS data indicates an overall decreased in the distance between the transducer and the seabed of ~20 cm from October to the end of December of 2013 (Fig. 42 a, Fig. 43 b). The decrease could be triggered by sedimentation (gain of sediment) or by the partially settling of the tripod structure, or both. A

progressively decrease of the seabed-ABS distance occurred from October to the end of the first fortnight of November (< 10 cm). Afterwards, three major steps of seabed-ABS distance shortening occurred simultaneously with three hydrodynamic events: on the 16th of November (~10 cm), on the 1st of December (~5 cm) and the 24th of December (~6 cm) (Fig. 42 a, Fig. 43 d). After the two firsts, the seabed location was partially recovered during the following days while after the third no recovery of the distance lost was detected (Fig. 42 a, Fig. 43 b).

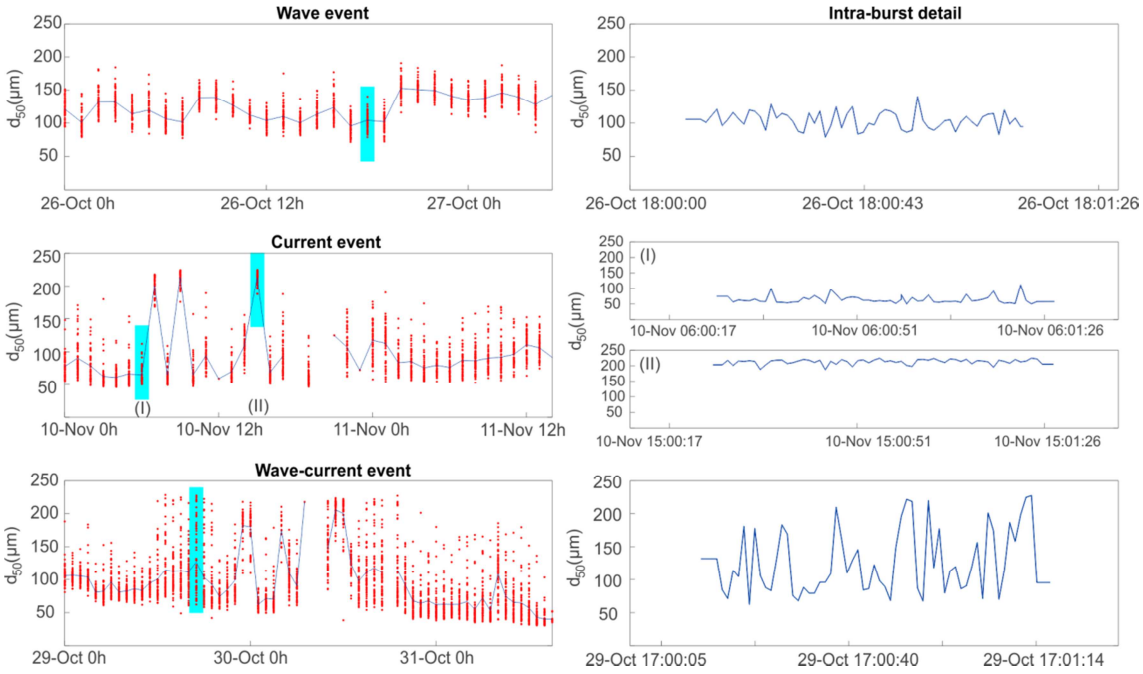

Fig. 41. Suspended d_{50} sediment of the intra-burst (red dots) and burst-averaged (blue lines) measured with LISST (left column plots) and detail of the intra-burst 60 measurements of the shaded blue area (right column plots). First line represents only-wave event; second line only-current event; and third line a wave-current event.

2.2.3. Time-averaged SSC and frequency variability

The burst-averaged or time-averaged SSC time series displays the concentration variability along time and distance from the seabed to the 0.85 m of the ABS-cell (Fig. 42 a). The time-averaged SSC ranged from ~16 mg/l to concentrations higher than 5000 mg/l. The higher peaks of SSC occurred in October (27th and 29th - 31st), in November, especially during the second fortnight when several periods with SSC higher than 500 mg/l reached 0.85 m ABS-cell, and December (1st - 7th and 24th - 26th) (Fig. 42 a). In general, main peaks of SSC occurred at the same time than the hydrodynamic events previously defined (Fig. 37).

A normalized wavelet spectral analysis was applied to the time series of the SSC at 15 cmab (Fig. 42 b). There were large variability of spectral densities and peaks along time, but this variability was similar to that observed with the other parameters described before, in general,

the periods of high spectral densities occurred at the same time than the SSC-peaks and the hydrodynamic events (Fig. 42 b). The majority and the most intense spectral density peaks occurred since the second fortnight of November. During these peaks, the spectral densities increased considerably in frequencies between 0.07 and 0.12 Hz that were equivalent to sea-swell wave peak periods of 8-16 s (Fig. 42 b). Secondary spectral density peaks were observed usually simultaneously than the previous at ~0.03 Hz (Fig. 42 b). This second rhythmicity ranged between 0.02 and 0.05 Hz and can be potentially linked with infragravity waves or wave groups with peak periods of ~20-50 s.

The presence of fishes in the water column between the seabed and the ABS transducer can disrupt SSC measurements e.g. appearing spectral peaks at 0.09 and 0.17 Hz, on the 21st of November under no waves and very slow current conditions (Fig. 42 b). Under high-speed currents, fishes can also mask or introduce noise in the spectral estimations, e.g. on the 25th -26th of November (Fig. 42 b). Therefore, spectral interpretations should be taken with caution when fishes were present mostly during high-speed currents periods.

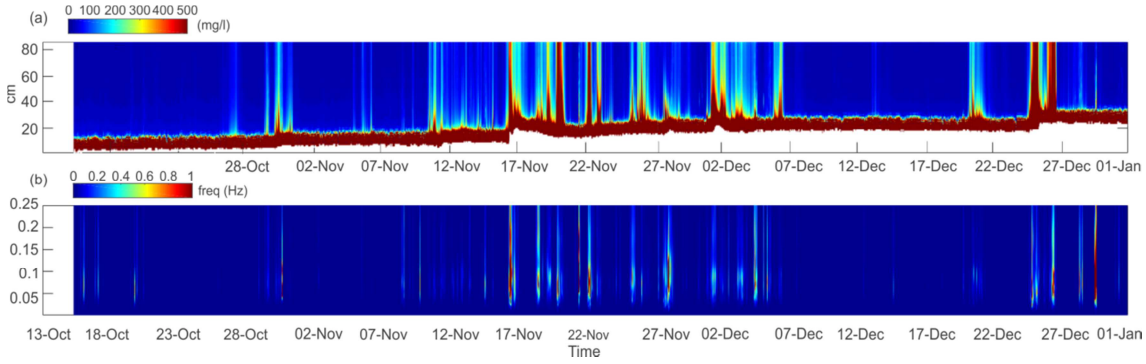

Fig. 42. Time series from 13th of October to the 31st of December of 2013 of: (a) time-averaged SSC (in mg/l) measured with the ABS (at 2 MHz); and (b) normalized wavelet spectral density of the SSC at 15 cmab.

2.2.4. Time-averaged SSC-profiles approaches

Fig. 43 (a) shows the reference concentration (C_r) estimated at the reference level above the bottom (z_r, Fig. 43 b). The C_r time series displayed similar trend than the SSC with several periods of concentration peaks ranging between < 500 and 3000 mg/l (Fig. 43 a). The highest concentration peak occurred during the second fortnight of November on the 22nd of November during a current event. This event was not especially more intense than the other current events to result on such SSC values. However, the Ebro River flow increased until ~700 m^3/s on the 22nd of November, being therefore, the river discharge a potential contributor on the SSC increases during this event. The reference level (z_r) estimations were parallel to the seabed (Fig. 43 b) resulting on a mean distance between the seabed and the z_r of 12 cm (Fig. 43 c).

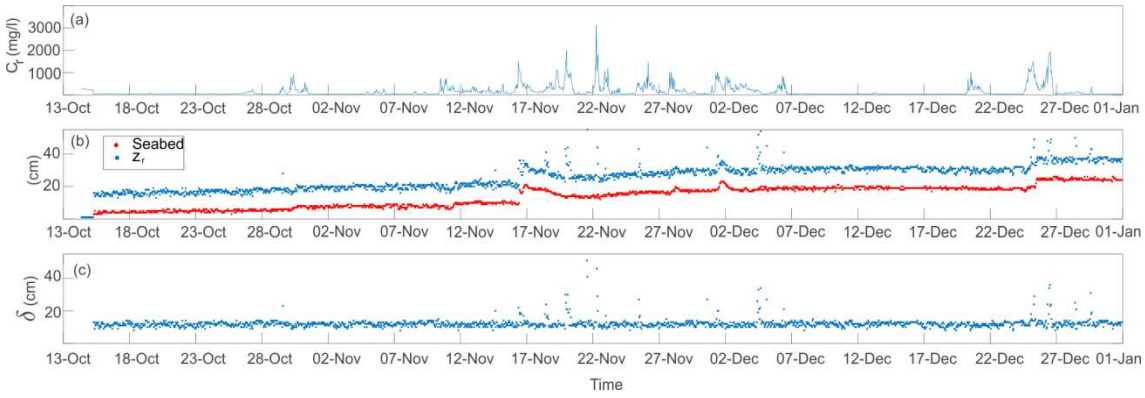

Fig. 43. Time series during the tripod deployment of: (a) the reference concentration (C_r) at the reference level (z_r) obtained with the power SSC-profiles approach from the time-averaged ABS data; (b) reference level above the bottom (z_r) calculated using the second derivative method (see methodology) in blue and seabed (SB) position in red; and (c) thickness or distance between the seabed and the reference level (δ).

The time-averaged suspended sediment concentration profiles (hereafter SSC-profiles) were analysed and compared using the power and exponential approaches (see methodology). When log-linear axes are used to display both profile types the exponential approach gave linear approximations while the power approach Rouse-type shaped profiles (Fig. 44). To determine the best-fit to SSC-profiles at the Ebro Delta site under the different hydrodynamic scenarios, the mean coefficients of determination (r^2) were estimated considering only one fit along the profile and two different approximations along the profile: from the seabed to z_r level (lower profile) and above z_r (upper profile) (Table X).

In general, when only one approach was used the power profiles resulted on better fit (r^2) than the exponential, but r^2 were small in both models (Table X). Consequently, the profiles were estimated separating from the seabed to z_r (lower profile) and above the z_r (upper profile) resulting on considerable improvement on both approaches (Fig. 44 b, d, e, f). Table X shows that the upper and lower profiles were better adjusted with the power function, although with similar r^2 than the exponential at the lower profile. The power profile always fit well, with similar r^2 at the upper and lower profile, while the exponential approach fit better with the lower profiles (Table X). During wave-current events both approaches resulted in the best fit even in presence of ripples (Table X). The power function fit better than the exponential under all hydrodynamic conditions considered and it was consequently selected to graphic representations and analysis hereafter.

Table X. Mean coefficient of determination (r^2) of the power (P) and exponential (E) approaches considering the whole time series, the different hydrodynamic events and the periods with ripples observations.

r^2	Power	P. upper profile	P. lower profile	Exponential	E. upper profile	E. lower profile
All period	0.08	0.79	0.79	0.04	0.71	0.75
Wave events	0.12	0.84	0.85	0.04	0.73	0.79
Current events	0.11	0.83	0.82	0.04	0.72	0.75
Wave-current events	0.14	0.87	0.87	0.04	0.76	0.8
Ripples observations	0.09	0.9	0.8	0.02	0.79	0.77

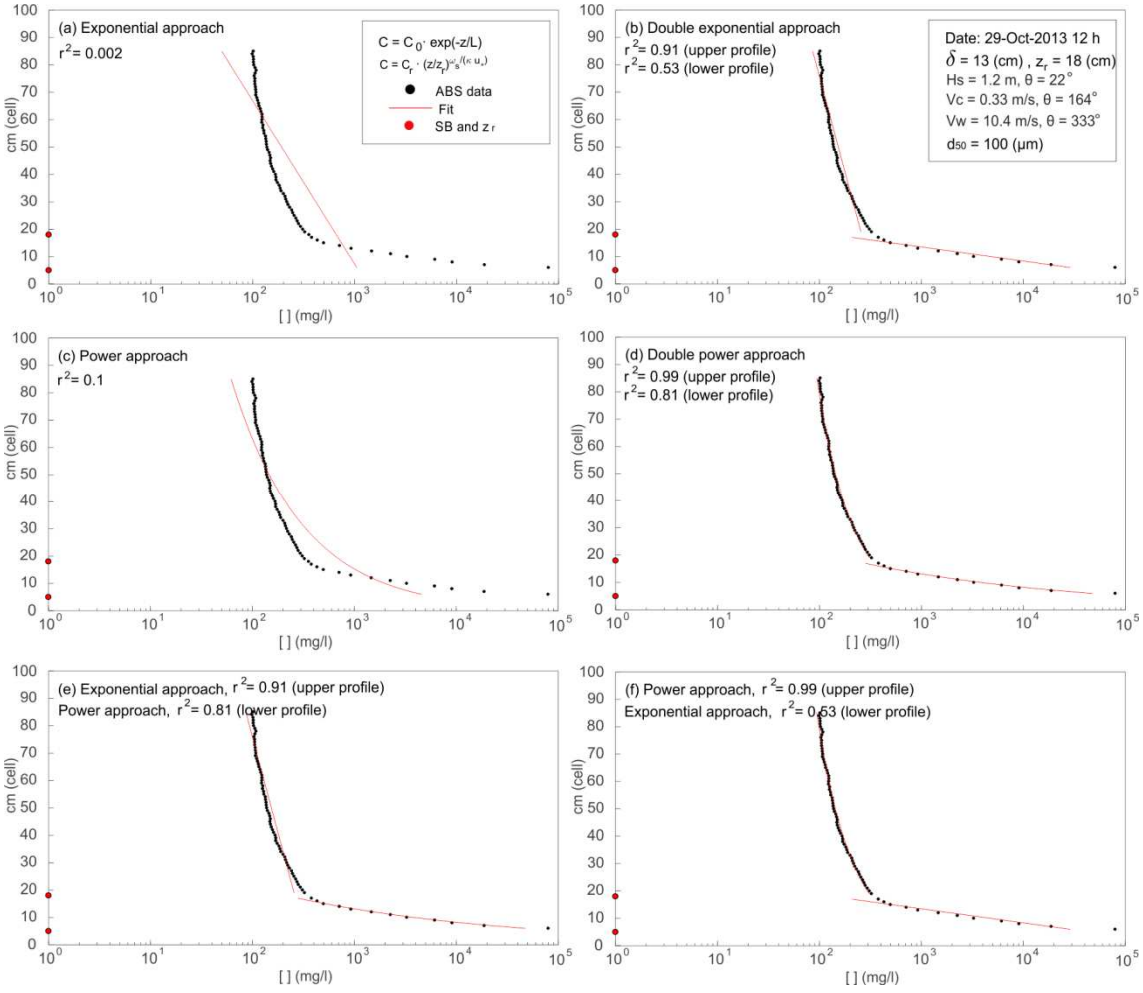

Fig. 44. Example of SSC-profile measured with the ABS (black dots) and the power and exponential approaches (red lines) considering the whole profile and considering the upper and the lower part of the profiles (above and below z_r) separately. The coefficients of determination (r^2) for each case are also indicated. The data selected to give example were on the burst averaged SSC on the 29th of October of 2013 at 12 h during a wave-current event, the details are indicated on the top right of subplot (b). (a) Exponential approach; (b) exponential form for the upper and the lower profile separately; (c) power approach; (d) power approach for the upper and lower profile separately; (e) exponential approach for the upper profile and power approach for the lower profile; and (f) power approach for the upper profile and exponential approach for the lower profile.

2.3. Near-bottom suspended sediment under different hydrodynamic events

In this section the SSC variability is characterized distinguishing between only-wave, only-current and wave-current dominated events. High-resolution ABS measurements of the SSC, allow analysing time scales of days (time-averaged SSC), hours (from burst to burst), minutes (intra-burst time-scale), and seconds (instantaneous SSC profiles). Time-averaged and time-varying (intra-burst) SSC profiles are here described and analysed during these different hydrodynamic events.

2.3.1. Wave Events

As previously described, wave events (H_s > 1 m) formed by eastern waves (waves coming from E) and low-speed currents (v < 0.3 m/s). The wave event from the 27th to 29th of November of 2013 exemplifies the general patterns observed in the suspended sediment variability under these conditions. Fig. 45 shows the time-averaged SSC-profiles and the power approximation of a sequence of 8 h that represents the SSC variability from the beginning of the event, the peak (H_s~2.2 m) and the wave decrease period (Fig. 37). In general, the power approach fit well in the upper and lower profile, giving coefficients of determination > 0.8 except at the beginning of the event (Fig. 45). The reference concentration (C_r) varied between ~70 and 1000 mg/l and the thickness of the high-concentration layer (the distance between the seabed and the reference level) ranged between 10-13 cm, and it was in this layer where SSC showed the highest gradients and variability (Fig. 45). The SSC-profiles at the beginning of the event were quite vertically constant and with low concentration and d_{50} = 101 µm (Fig. 45 a). The near-bed SSC increased progressively with H_s (almost 2 m) the next two hours, resulting on higher gradient concentration profiles and d_{50} = 65-69 µm (Fig. 45 b and c). One hour later, H_s (1.6 m) and SSC decreased although d_{50} increased to 135 µm (Fig. 45 d). The last four hours of the event displayed equivalent wave conditions (H_s ~1.5 m), and SSC-profiles with high-concentration and very fine suspended sediment grain size (d_{50} = 52-67 µm) (Fig. 45 e-h).

Figure 46 shows the intra-burst time series corresponding to the sequence of time-averaged SSC-profiles displayed in Figure 45. The characteristic SSC variability induced by eastern waves showed that the sediment was pumped up and settled down along the profiles with periodicities close to the wave period (Fig. 46). These sediment patterns are visualized as sudden vertical increases and decreases of the SSC. When the sediment pumped up remained suspending during enough time, the following suspended sediment pumped up overlap with the previous, resulting in group-like pattern (Fig. 46, Fig. 47 b). High SSC (> 500 mg/l) were usually observed below the 0.85 m ABS-cell, although occasionally can overpass this position (e.g. Fig. 46 c at 19 h 2 minutes).

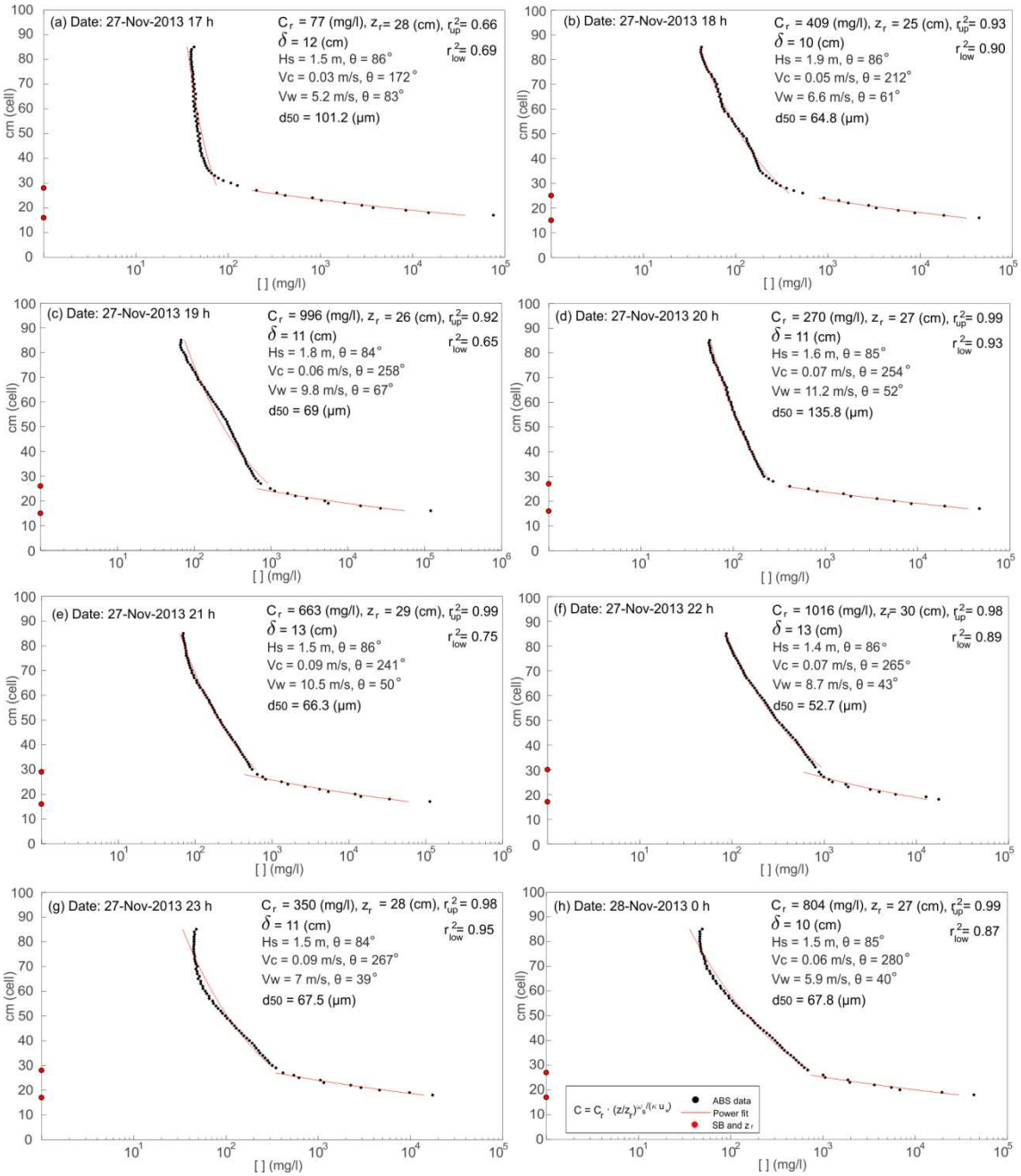

Fig. 45. Time-averaged suspended sediment concentration profiles (SSC-profiles) (black dots) and the power approach (red line) of 8 h sequence during the wave-dominated event from the 27th to the 29th of November of 2013. On the top right corner it is indicated the specific characteristics of the profile: the reference concentration in mg/l (C_r), the reference level in cm (z_r) and the coefficient of determination of the power fit approximation for the upper and lower profiles (r_{up}^2 and r_{low}^2, respectively); the distance between the seabed and the reference level (δ); the H_s and direction; the current speed and direction; the wind speed and direction; and the suspended d_{50} measured with the LISST at ~20 cmab. The lower and the upper red points on the y-axis indicated the seabed (SB) position and the z_r, respectively.

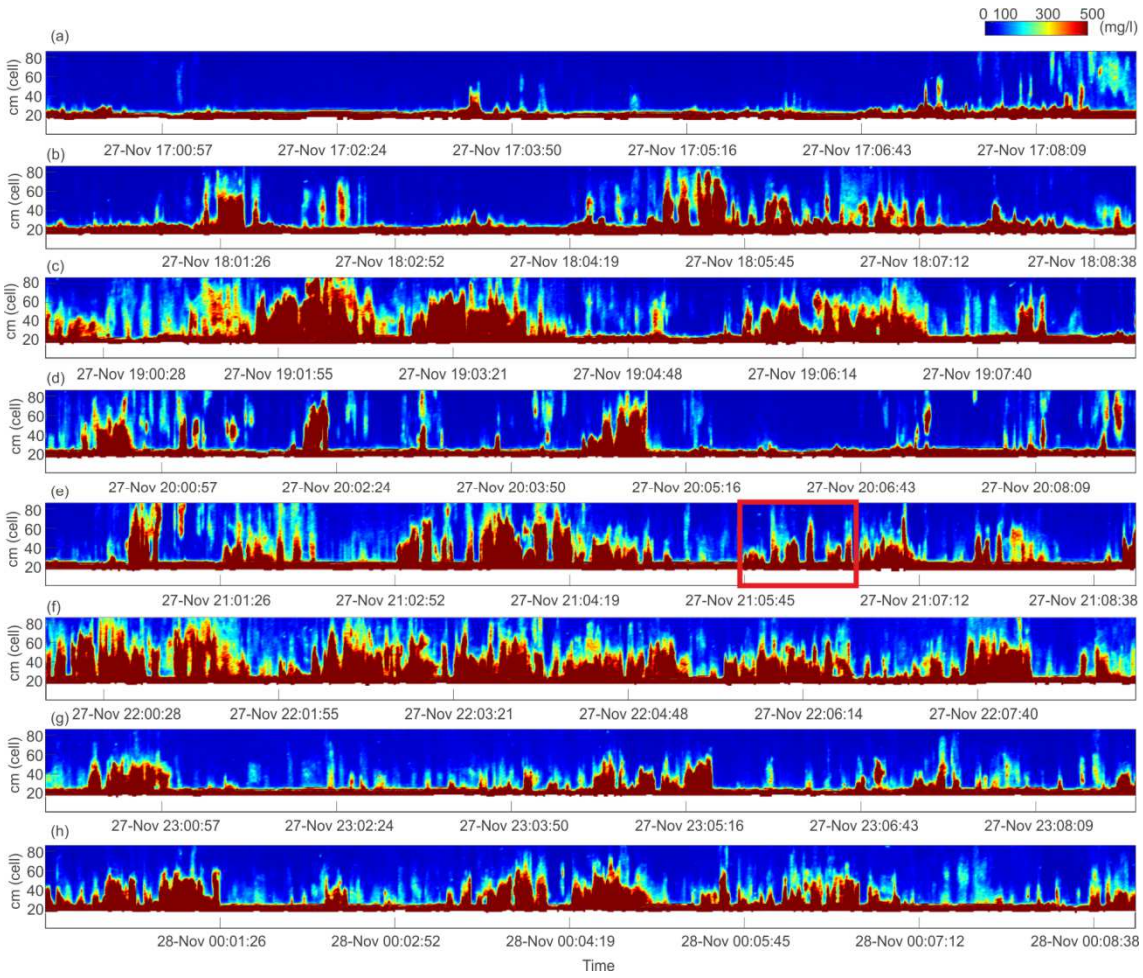

Fig. 46. Time-varying (intra-burst) SSC time series in mg/l corresponding to the time-averaged sequence displayed in Fig. 45. Each subplot represents the 9 minutes of the burst duration showing the instantaneous 540 profiles (1 profile per second) measured every cm along ~0.85 m. The white area at the base of each subplot corresponds to the ABS cells below the seabed location. The sequence corresponds to a period during the only eastern wave event from the 27th to the 29th of November of 2013 (see Fig. 37). The red rectangle indicates the one minute detail displayed in Fig. 48.

Fast Fourier Transform (fft) at 15 cm above the detected seabed position indicates peaks of spectral densities at ~0.1 Hz and at 0.01-0.02 Hz during wave events (Fig. 47 c). These frequencies dominated the SSC variability until ~0.60 m ABS-cell while the lower part of the profile (0.4 m ABS-cell) also was influenced by frequencies at 0.13 and 0.2 Hz (Fig. 47 d and e). Therefore, it is assumed that SSC variability was mainly induced by the resuspension of bottom sediment by waves.

Instantaneous SSC-profiles extracted from the time-varying profiles showed different profile-shapes (Fig. 48 and Fig. 49). They highlighted rapid changes (in seconds) in the SSC and gradient during wave resuspension (Fig. 48). These changes mainly affected the section of the profile close to the bottom although the thickness varied depending on the profile (Fig. 48).

Above this, the SSC-profile tended to a constant value and/or very low-gradient of SSC of ~35-45 mg/l (where the SSC-profile became vertical). It is worth noting that several instantaneous SSC-profiles displayed an anomalous bulge of SSC apparently unrelated to bottom resuspension (e.g. Fig. 49 c and d).

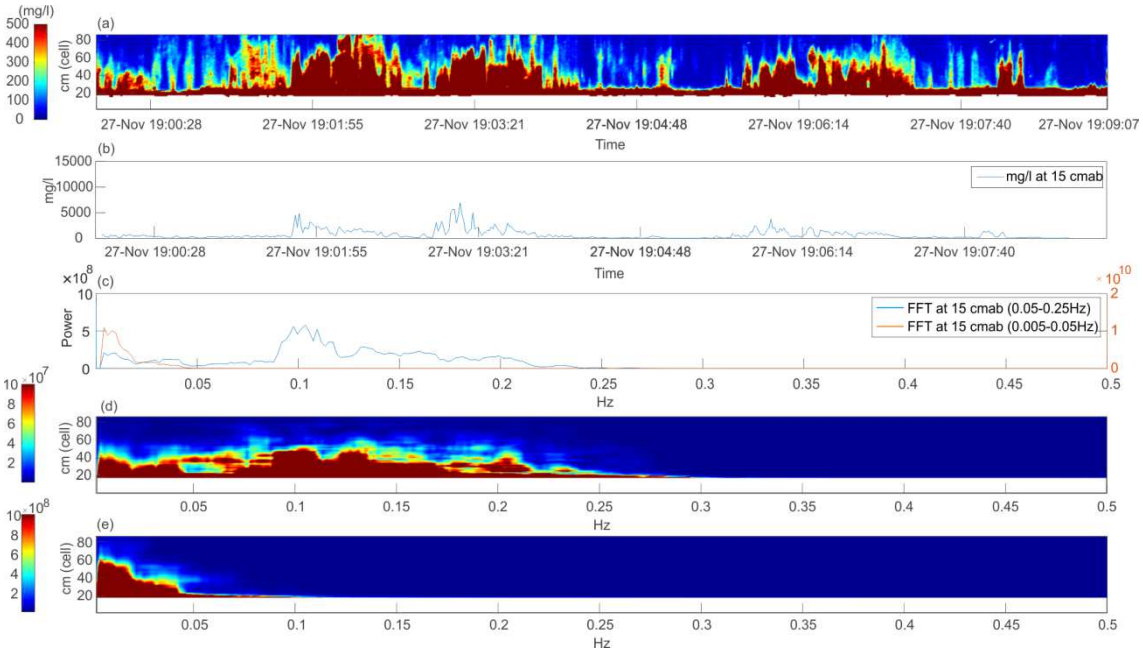

Fig. 47. ABS data during the eastern wave event on the 27th of November of 2013 at 19 h of: (a) the time-varying SSC in mg/l during the 9 minutes of the burst interval showing the instantaneous 540 profiles (1 profile per second) measured every cm along ~0.85 m. The white area at the base of the profiles represents ABS cells below the seabed location; (b) the SSC in mg/l at 15 cmab; (c) the fft power spectral densities of the SSC at 15 cmab after apply the two band pass filters (from 0.005 to 0.05 Hz and from 0.05 to 0.25 Hz); (d) the fft spectral density of the 0.05 to 0.25 Hz frequency band with respect to the distance from the seabed; and (e) the fft spectral density of the 0.005 to 0.05 Hz frequency band with respect to the distance from the seabed.

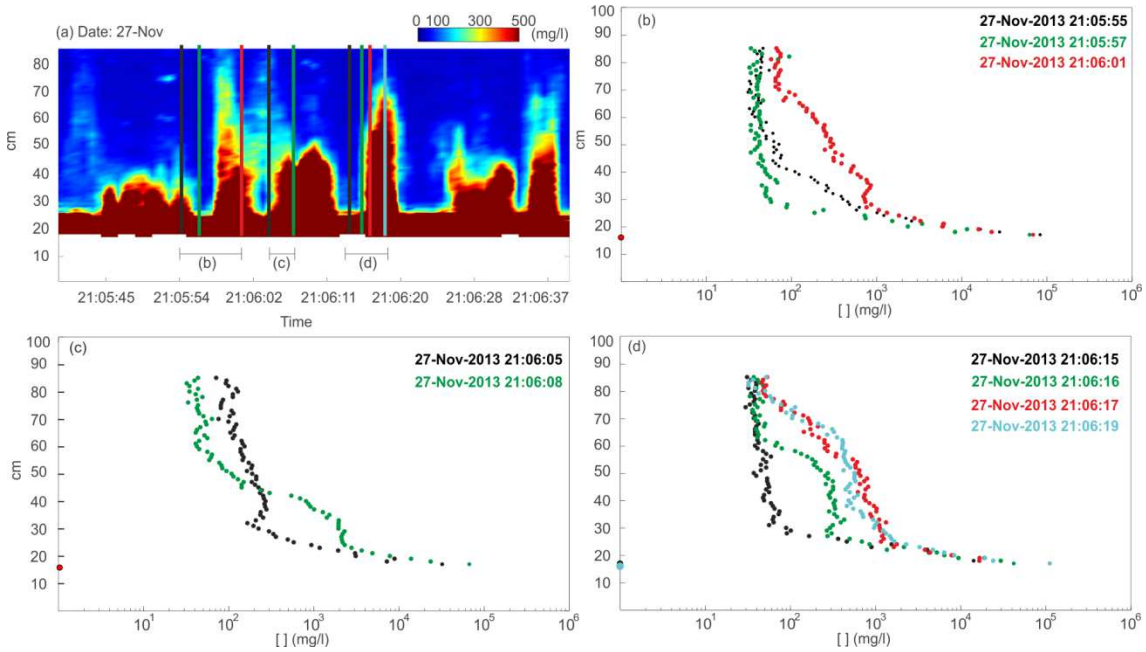

Fig. 48. (a) Detail (one minute) of the intra-burst time series indicated in Fig. 46 (e) with a red rectangle. (b), (c), (d) SSC-profiles at the instances (vertical lines) indicated in (a).

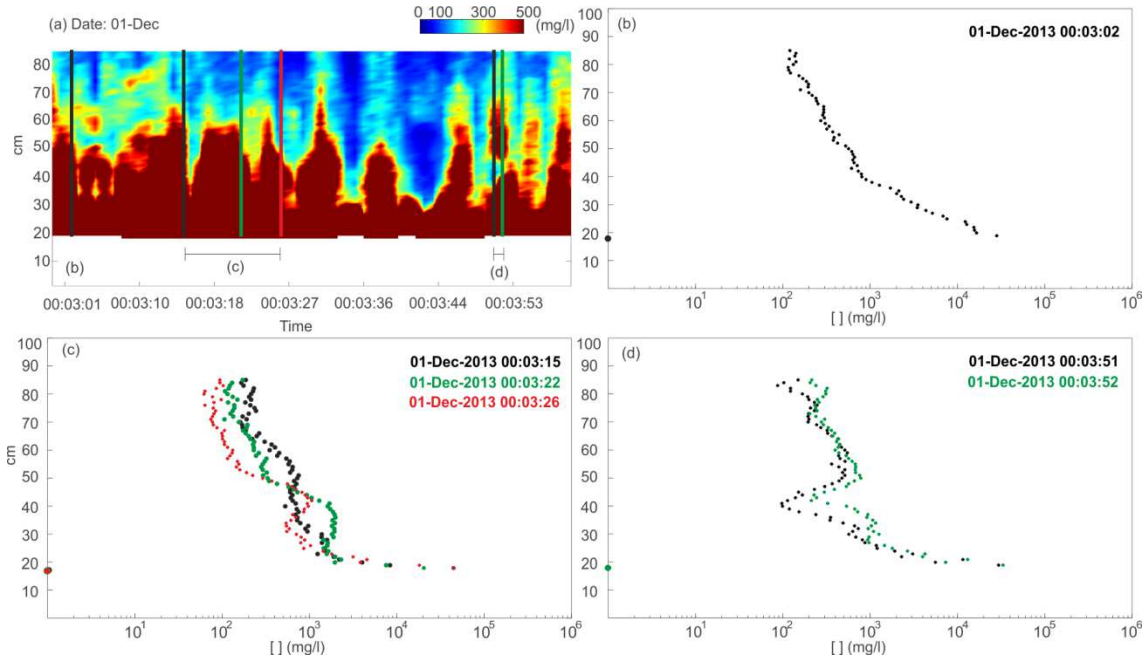

Fig. 49. (a) Detail (one minute) of the intra-burst time series measured on the 1st of December of 2013 at 0 h; (b), (c), (d) SSC-profiles at the instances (vertical lines) indicated in (a).

2.3.2. Current-dominated Events

Current-dominated events were periods characterized by near-bottom current speeds higher than 0.3 m/s and low waves (H_s < 1 m) (Fig. 37). These events generally occurred simultaneously with high speed NW winds (wind speeds > 10 m/s). The 22th-24th of November event, used here as example, showed strong near-bottom currents during two days (maximum peak > 0.5 m/s) and winds (> 15 m/s) that can be separated in three current speed peaks (Fig. 37). Fig. 50 shows the time-averaged SSC-profiles and the power approximation of six bursts immediately before, during and after the first peak of the event (the highest peak). In general, the profiles showed high values of SSC and the typical concave-shaped with decreasing concentration from the seabed upwards (Fig. 50 a-e). The power approach fit well with observations giving C_r between 300-1700 mg/l (Fig. 50 a-e). The highest part of the profile became vertical and tended to low SSC gradient between ~100 and 900 mg/l depending on the current intensities (Fig. 50 a-e). The lower profiles showed variable SSC gradients, higher or lower with thinner (δ ~ 9-10 cm) or thicker (δ ~ 29 cm) thickness between seabed (SB) and z_r respectively (Fig. 50 a-e). The thickness of δ increased with increasing current speeds (Fig. 50 d). The sequence showed high SSC values and strong gradients in the upper profile during the first peak of the event; whereas before and after the peak the SSC-profile was almost vertical and lower (Fig. 50). The coarsest suspended sediment grain size (d_{50} = 128 µm) occurred during the peak of the event, being finer before (d_{50} = 75-95 µm) and after (d_{50} = 58 µm) (Fig. 50).

The intra-burst time series showed the progressive increase of SSC until the first peak of the event (22 November 08 h) and the later progressively decrease (Fig. 51 a-f). The thickness of the layer with high suspended sediment concentrations (> 500 mg/l) increased and decreased with current speed, “filling” the whole measured profile during the peak of the event (Fig. 51 d). As mentioned before, the increase in water discharge (~700 m^3/s) of the Ebro River on the 22nd of November could favour the SSC increase because of the proximity of the study area with the Ebro River mouth. Note that swimming fishes appeared in the intra-burst time series as points of very high-acoustic response when current speeds were moderate (Fig. 51 e and f). Consequently, the time-averaged SSC-profiles were affected by the fishes showing irregular shapes (e.g. Fig. 50 f).

As expected, the fft analysis of the current-dominated event at 15 cm above the detected seabed position showed the spectral densities irregularly distributed along the whole frequency ranges, showing a broad spectrum with minimum affections above the 40 cm of the ABS-cell (Fig. 52 c, d and e).

The detail of the intra-burst SSC-profiles displayed small SSC variability in consecutive profiles maintaining similar shapes (Fig. 53). The background SSC increased from ~200 mg/l before the

peak to ~1000 mg/l during the first peak of the event (Fig. 53). However, some instantaneous profiles showed rapid changes and high SSC variability quite similar than those observed in the wave-dominated events (Fig. 54).

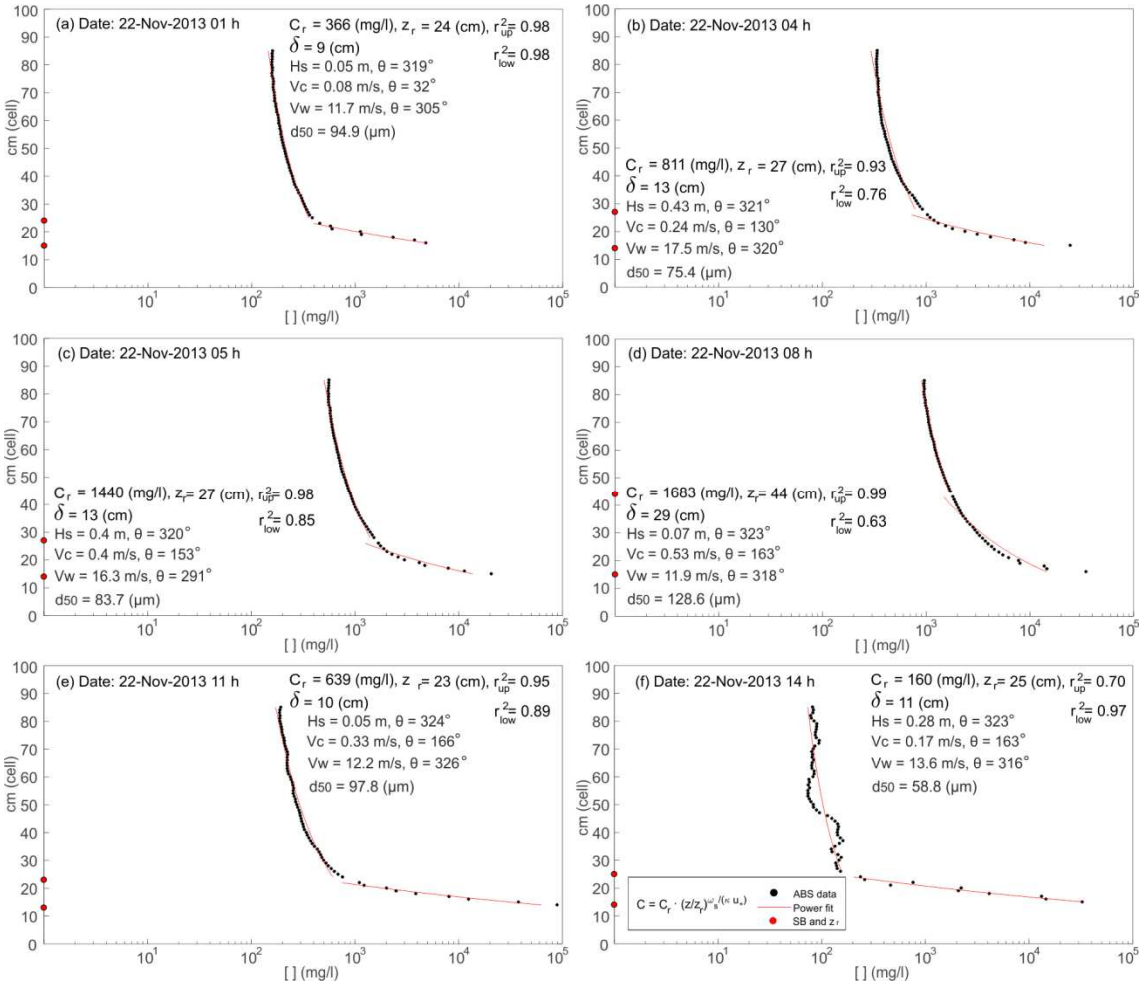

Fig. 50. Time-averaged suspended sediment concentration profiles (SSC-profiles) (black dots) and the power approach (red line) of the current dominated event from the 22th to the 24th of November of 2013. On corners are indicated the specific characteristics of the profiles. See the Fig. 45 caption for the full description of each variable.

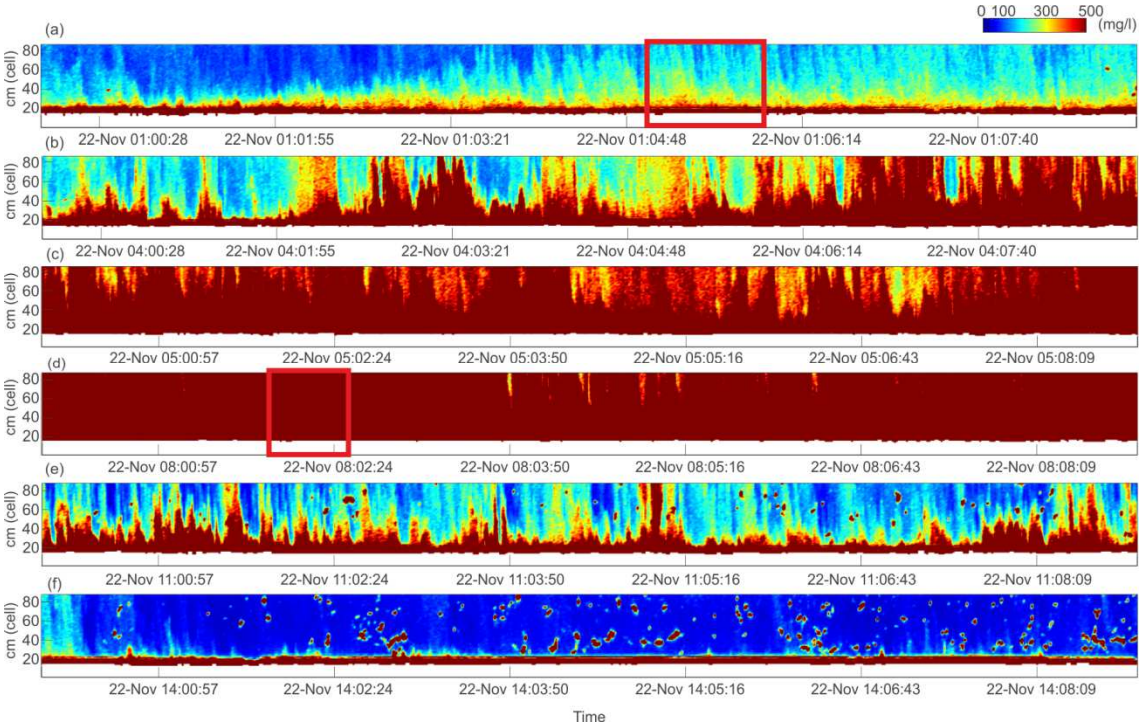

Fig. 51. Intra-burst time series of the SSC in mg/l corresponding to the time-averaged SSC-profiles displayed in Fig. 50. See Fig. 46 caption to full description of the figure. The sequence corresponds to a period during the current-dominated event from the 22th to the 24th of November of 2013 (see Fig. 37). The red rectangles indicate the one and half minute detail displayed in Fig. 53.

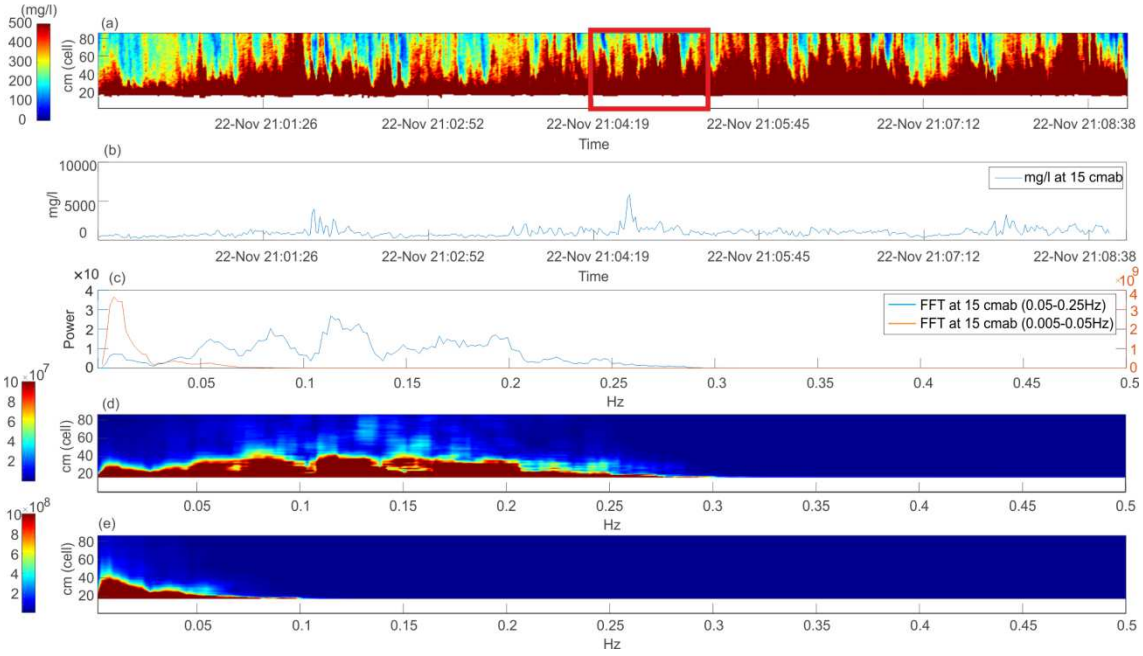

Fig. 52. ABS intra-burst data during the current-dominated event on the 22nd of November of 2013 at 21 h. See Fig. 47 caption for the full description of each subplot. The red rectangle indicates the one and half minute detail displayed in Fig. 54.

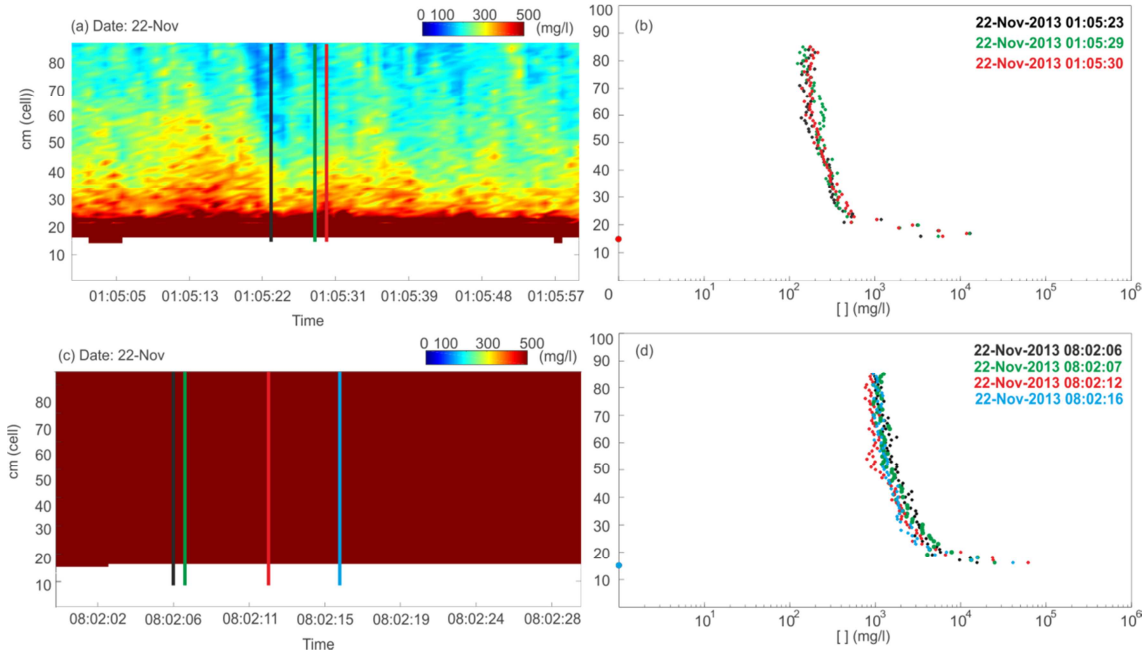

Fig. 53. (a) Detail (one minute) of the intra-burst SSC time series indicated in Fig. 51 (a) with a red rectangle; and (b) SSC-profiles at the instants indicated with the vertical lines in (a); (c) detail (half minute) of the intra-burst SSC time series indicated in Fig. 51 (d) with a red rectangle; and (d) SSC-profiles at the instants indicated with the vertical lines in (c).

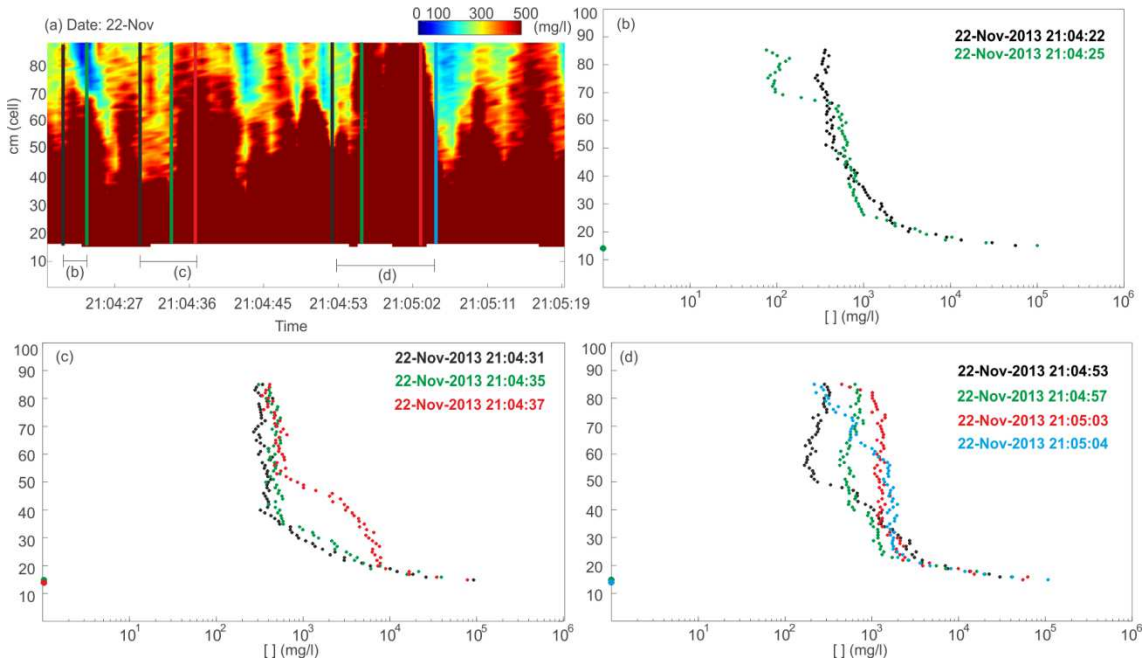

Fig. 54. (a) Detail (one minute) of the intra-burst SSC time series indicated in Fig. 52 (a) with a red rectangle; and (b), (c), (d) SSC-profiles at the instants indicated with the vertical lines in (a).

2.3.3. Wave-current events

These events were defined as periods of high waves (H_s > 1 m) and high current speeds (v > 0.3 m/s) (Fig. 37). In the study area these events typically occurred with eastern waves and southwards currents. The wave-current event from the 1st to the 4th of December was here used to illustrate SSC variability under these hydrodynamic conditions. During this event significant wave height, current speed and wind speed peaks reached values higher than 2 m, 0.5 m/s and 10 m/s respectively (Fig. 37).

The time-averaged SSC-profiles during the first peak of wave height of the event fit well with the upper power profile approach and showed high-gradient in SSC and high minimum concentrations (~400 mg/l) (Fig. 55). The strongest SSC vertical gradient and the highest C_r (> 1000 mg/l), at z_r (~38 cm cell) occurred during the peak of current speed, when the sediment grain size was slightly coarser (d_{50} = 89 µm) than the previous and later hours (d_{50} = 55 and 64 µm, respectively) (Fig. 55 b). The upper power approach profiles fit slightly better than the lower although the determination coefficient was always > 0.7. The distance between the seabed and z_r (δ) increased mainly when the current speed increased, showing maximum values of δ = 20 cm when the current speeds were also maximum and the SSC gradients were lower (Fig. 55 b and c).

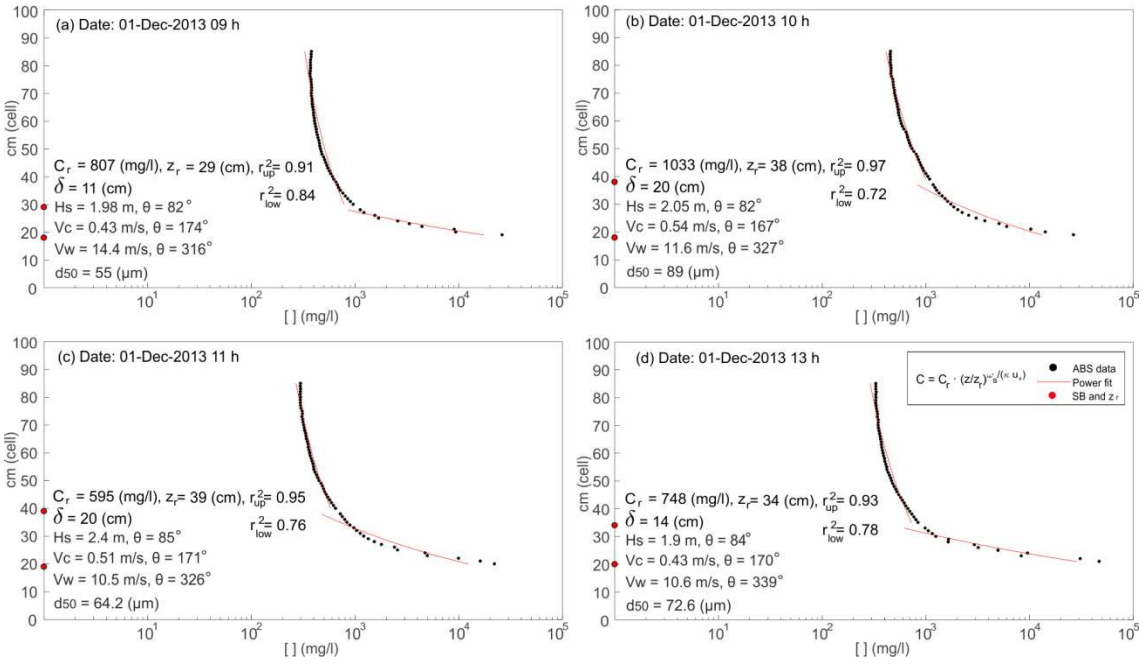

Fig. 55. Time-averaged suspended sediment concentration profiles (SSC-profiles) (black dots) and the power approach (red line) of the wave-current event from the 1st to the 4th of December of 2013. See the Fig. 45 caption for the full description of each variable.

The intra-burst SSC-profiles during the highest peak of the event showed mixed characteristics between the only-wave and only-current cases (Fig. 56). High concentrations of suspended sediment were between 0.20 and 0.85 m ABS-cell, frequently overpassing the ABS position (e.g. Fig. 56 b). Closer to the seabed there was a high concentration band (> 500 mg/l) with intervals of sand pumped up, suggesting pulses of sand resuspensions by waves. These complex SSC patterns resulted on fft analysis with irregular spectrums with broad densities along the whole frequency range (Fig. 57).

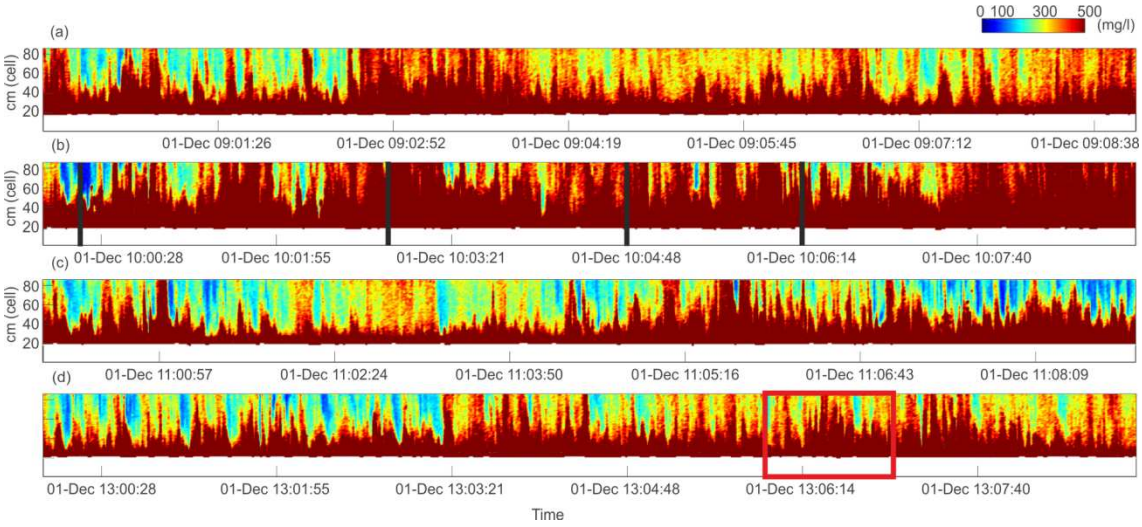

Fig. 56. Intra-burst time series of the SSC in mg/l corresponding to the time-averaged SSC-profiles displayed in Fig. 55. See Fig. 46 caption to full description of the figure. The black lines in (b) and the red rectangle in (d) indicate the instantaneous profiles and the one minute detail displayed in Fig. 58 and Fig. 59, respectively.

The instantaneous SSC-profiles showed high variability in time-scales of seconds (Fig. 58 and Fig. 59). The high concentrations (> 500 mg/l) occupied the whole profile during the peak of the event (Fig. 58). After the peak of the event but still under high energetic conditions, the instantaneous SSC-profiles displayed low-gradient concentrations with minimum concentrations ~300 mg/l (Fig. 59). It is worth noting that there were instants where SSC-profiles displayed a bulge of sediment which unlikely came directly from bottom resuspension (e.g. Fig. 58 c).

When in a wave-current event some of both parameters decreased the SSC distribution and variability changed according to the dominant parameter. When currents dominated over waves, the burst-averaged SSC-profiles were similar than those observed during current-dominated events (e.g. Fig. 60). In the same way, when waves dominated over currents SSC patterns became similar than the only wave events (e.g. Fig. 61). However, in both situations the influence in SSC on the non-dominant parameter was inferred. Under the dominion of currents the influence of waves in the intra-burst SSC was detected, although any clear peak was

detected in the fft analysis (e.g. Fig. 60). Conversely, under the dominion of waves, fft analysis showed clear peaks of the spectral density at ~0.1 Hz (incoming wave frequency) and the SSC-profiles exhibited lower gradient than the current-dominated case (Fig. 61).

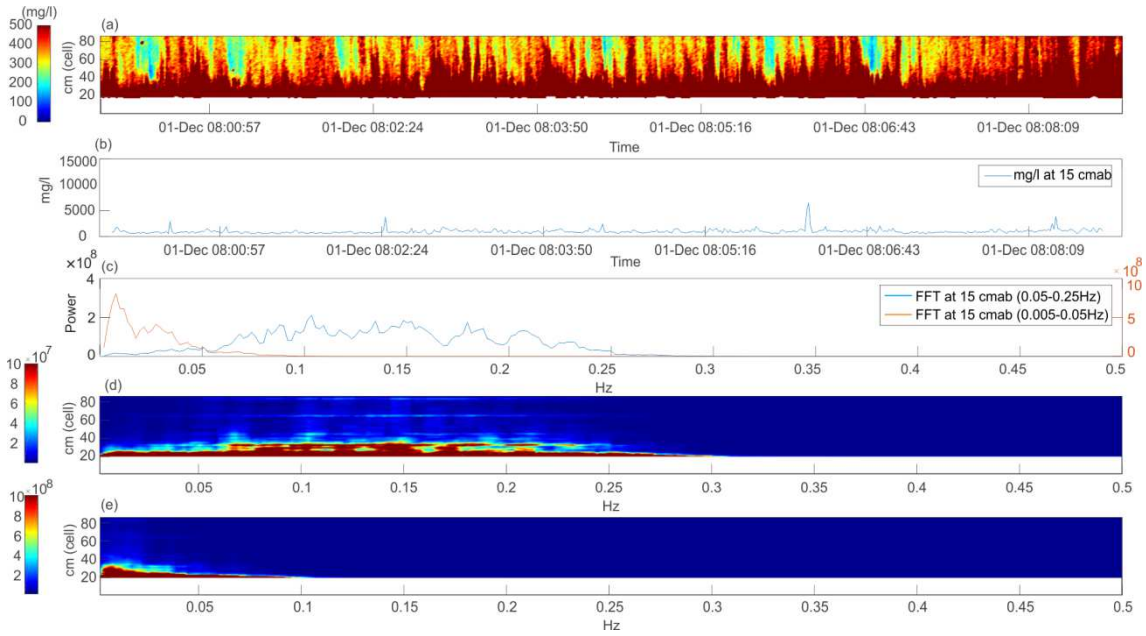

Fig. 57. ABS data during wave-current event on the 1st of December of 2013 at 8 h when H_s = 1.74 m, θ_{Hs}= 79°, v = 0.40 m/s, θ_v = 171°, v_w = 11.9 m/s and θ_w= 335°. See Fig. 47 caption for the full description of each subplot.

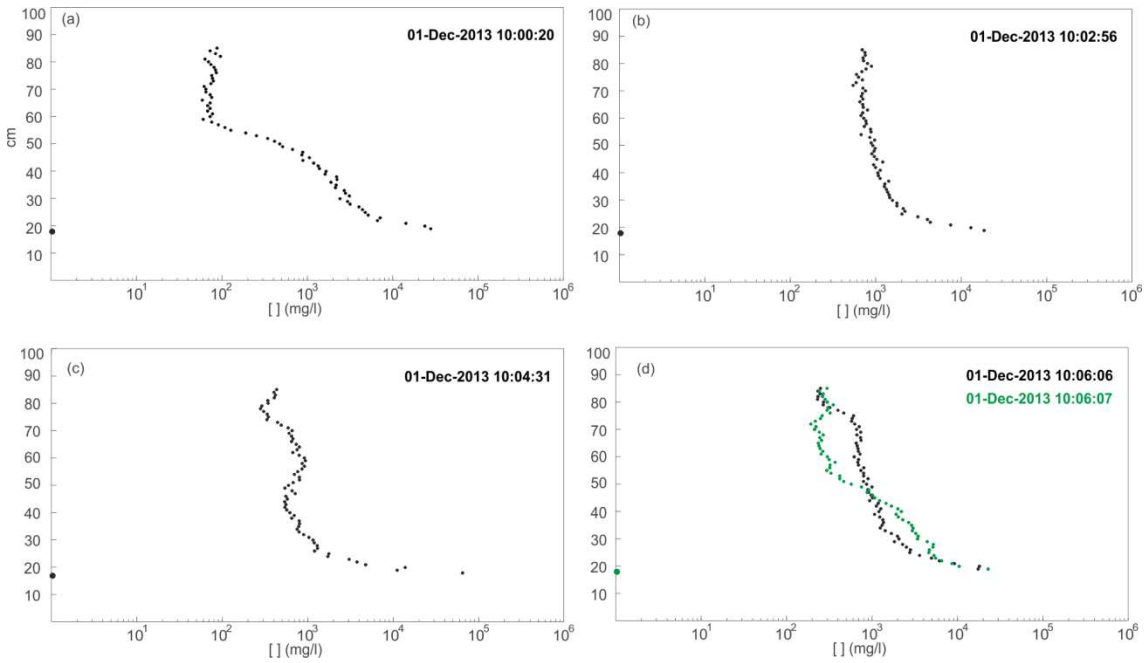

Fig. 58. Instantaneous SSC-profiles during the highest current velocities of the event on the 1st of December at 10 h. The instants are indicated in Fig. 56 (b) as vertical black lines.

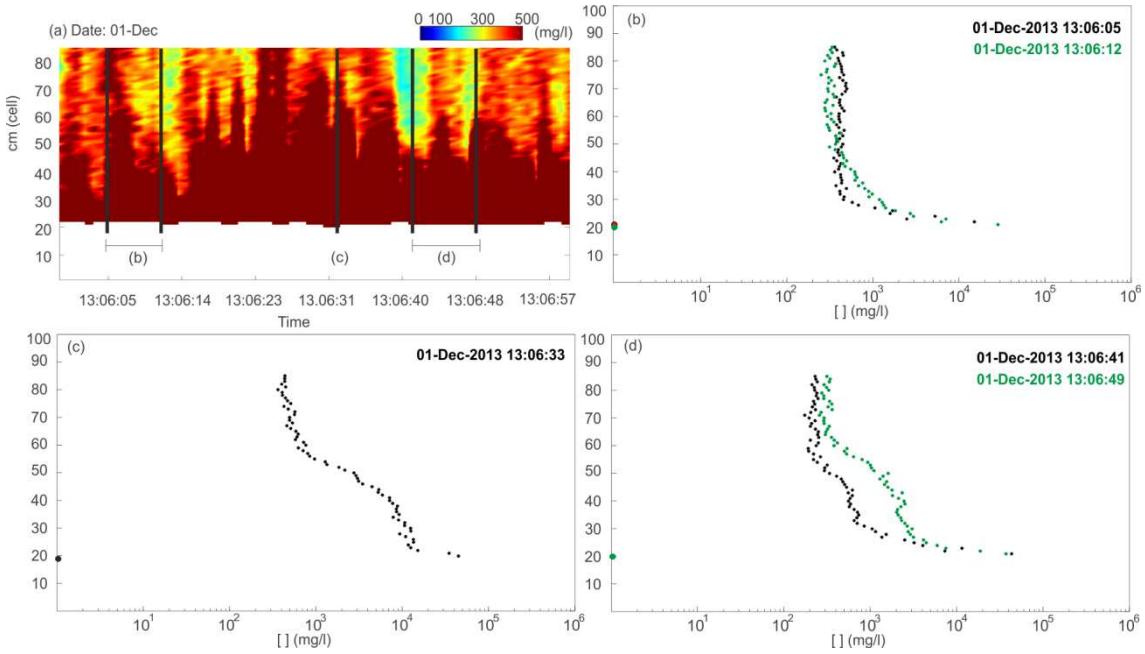

Fig. 59. (a) Detail (one minute) of the intra-burst SSC time series indicated in Fig. 56 (d) with a red rectangle; and (b), (c), and (d) SSC-profiles at the instants indicated with the vertical lines in (a).

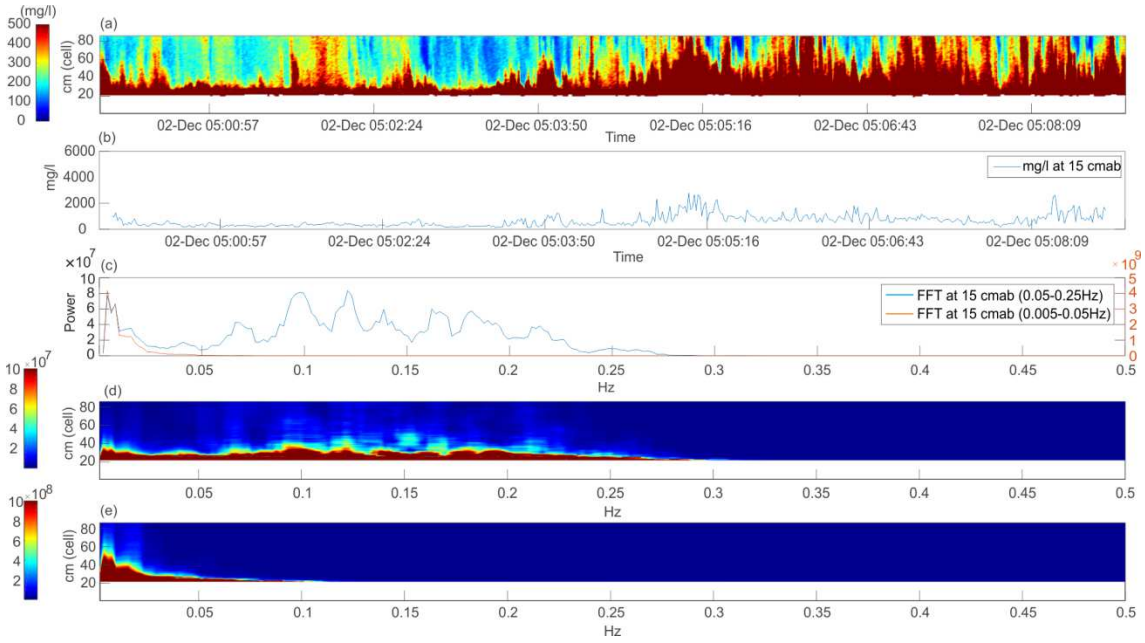

Fig. 60. ABS data during wave-current event under currents dominion on the 2nd of December of 2013 at 5 h when H_s = 0.45 m, θ_{Hs}= 65°, v = 0.41 m/s, θ_v = 171°, v_w = 8.4 m/s and θ_w = 337°. See Fig. 47 caption for the full description of each subplot.

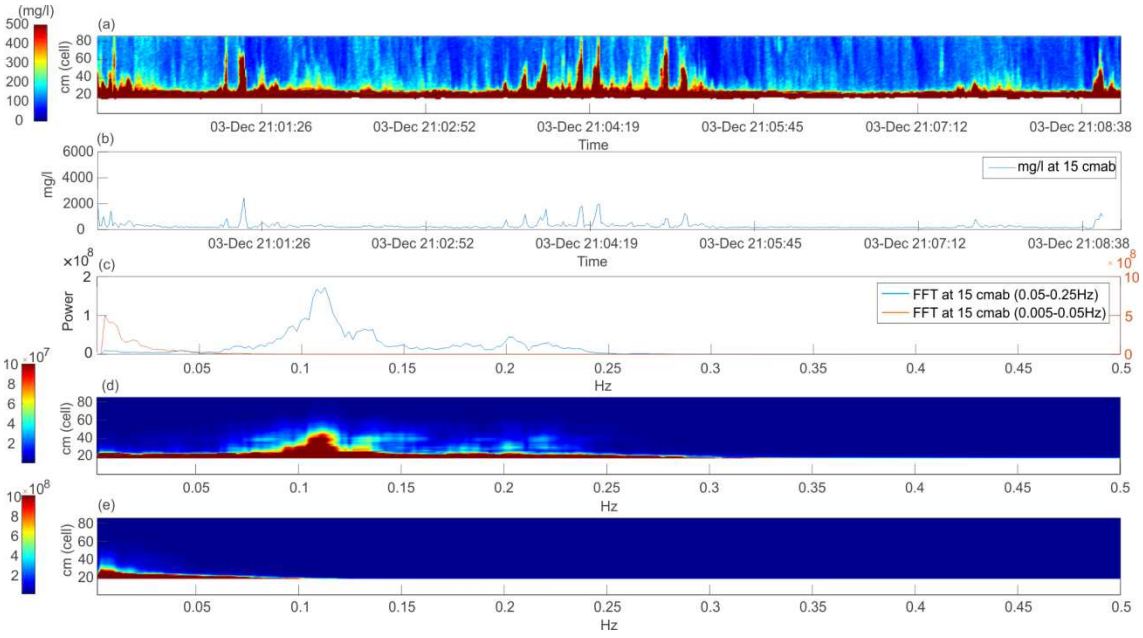

Fig. 61. ABS data during wave-current event under wave dominion on the 3rd of December of 2013 at 21 h when H_s= 1.14 m, θ_{Hs}= 88°, v = 0.26 m/s, θ_v= 161°, v_w = 5.6 m/s and θ_w= 333°. See Fig. 47 caption for the full description of each subplot.

3. Discussion

3.1. Patterns of near-bottom SSC under different flow conditions

In this section it is discussed how the different hydrodynamic conditions and the strong winds affected the SSC and how the SSC dynamics adapted to the rapid changes of these variables during the period studied.

3.1.1. The role of waves, currents and winds in SSC

Most of the periods of high SSC were related to increases on the total shear stress due to waves and currents (τ_{wc}), being the wave shear stress (τ_w) the main contributor to the total shear stress, although current shear stress (τ_c) was also an important contributor (Fig. 62). The highest τ_{wc} peaks coincided with those periods when seabed-ABS distance shortened being the maximum τ_{wc} ~1.65 N/m^2 on the 16th of November (Fig. 62). Maximum values of τ_w and τ_c were ~1.4 and ~0.6 N/m^2 respectively. Direct relation between total shear stress and SSC was accomplished when τ_{wc} > 0.04 N/m^2 (Fig. 63 a). Beyond this threshold, the SSC increased roughly linearly with shear stress, while below this value any obvious relation was observed (Fig. 63 a). This minimum shear stress required to SSC started to increase was observed in previous studies and interpreted as an apparent threshold of sediment resuspension (Ha and Park, 2012; Carlin et al., 2016). Interestingly, when comparing in a scatter plot τ_w and SSC two clouds of points are highlighted (Fig. 63 b). One of them with a stronger correlation linked to τ_w

values higher than 0.04 N/m^2, which was interpreted as the result of sediment resuspension due to waves (Fig. 63 b). The second cloud of points had weaker correlation than the previous showing low τ_w (~0.001 N/m^2) with high SSC and should be associated with high current shear stress (Fig. 63 a, c). However, weak relation was observed between the shear stress due to currents (τ_c) and SSC, displaying more scattered points at low τ_c, where the apparent threshold was at τ_c > 0.03 N/m^2 (Fig. 63 c). Therefore, sediment suspension peaks seem to be mainly related with moderate waves and the highest intensity currents.

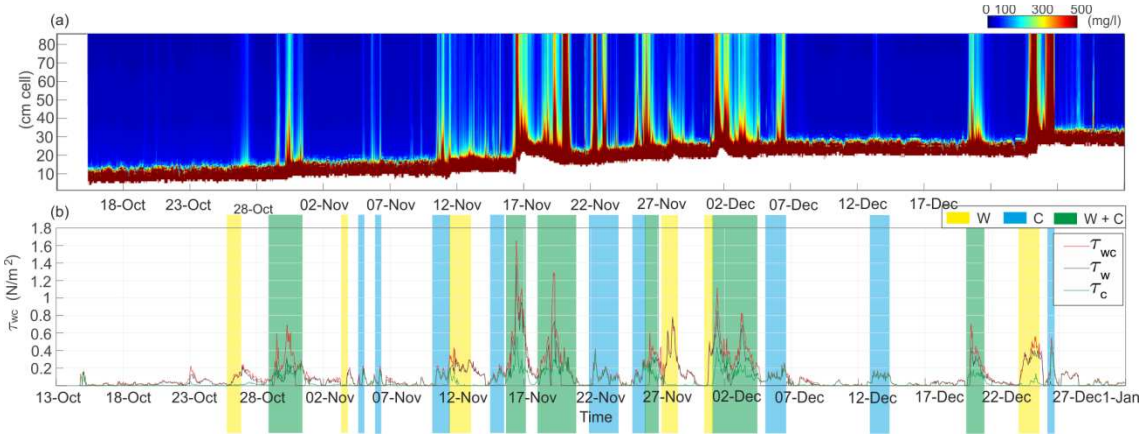

Fig. 62. Time series during the tripod deployment of: (a) time-averaged SSC (in mg/l) measured with the ABS channel 2 (2 MHz); (b) estimations of the maximum combined shear stress due to waves and currents (τ_{wc}), waves shear stress (τ_w) and currents shear stress (τ_c). Only-wave-, only-current and wave-current dominated events are indicated with shaded areas.

The development of wind jets generated by NW winds in the study area during the winter season produces strong wind-induced currents and bimodal wave spectrums (wind generated and offshore generated waves) on the continental shelf (Grifoll et al., 2016). However, the fetch of NW wind was too short at the study site to develop waves with H_s > 1 m and therefore, the strong Mistral winds highly correlated with the SSE high-speed currents (Fig. 64). The simultaneous occurrence of strong winds and currents leads to a direct correlation between wind intensity and the amount of the suspended sediment at different depths (Fig. 63 d). This is a relevant difference with other areas where the SSC was well correlated with the stress generated by winds but unrelated to currents (Carlin et al., 2016).

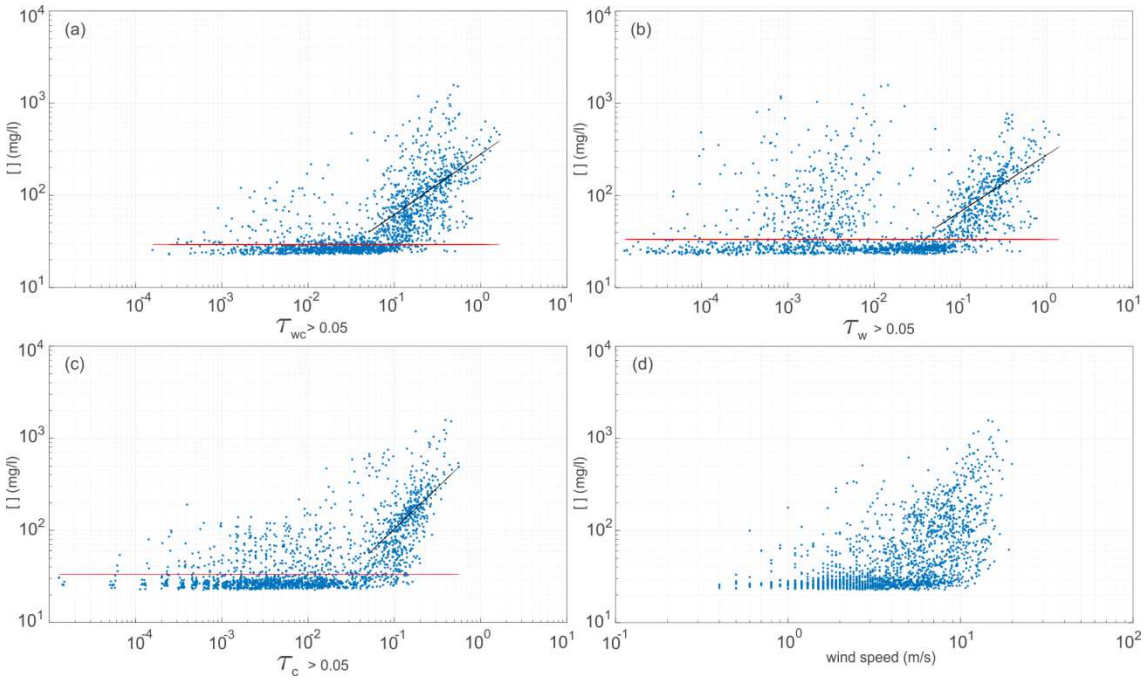

Fig. 63. Logarithmic scatter plot of SSC in (mg/l) measured at 50 cm above the detected seabed location with the ABS and the maximum combined shear stress of (a) waves and currents (τ_{wc}), (b) only-waves (τ_w); (c) only-currents (τ_c); and (d) wind speeds. Trending line for $\tau > 0.05$ N/m^2 and the mean concentrations for $\tau < 0.05$ N/m^2 are plotted (black and red lines, respectively).

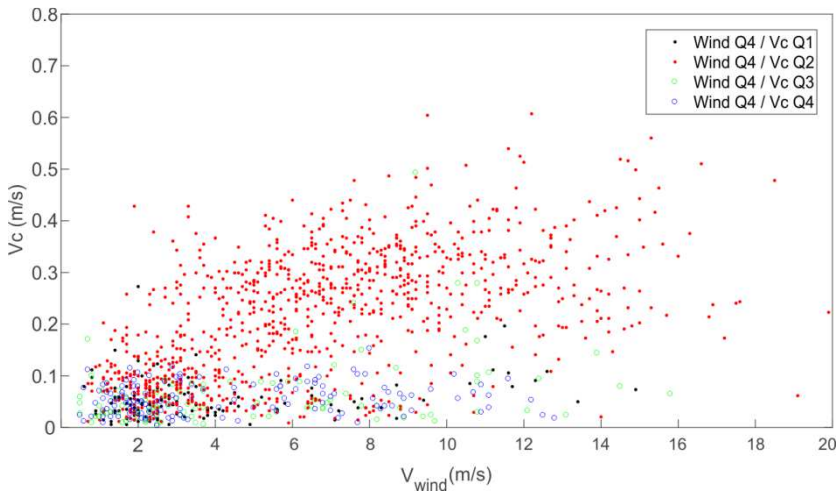

Fig. 64. Scatter plot of the wind speed (fourth quadrant, Q4) and current speed distinguishing between the first (Q1), second (Q2), third (Q3), and fourth (Q4) quadrants measured during the tripod deployment.

3.1.2. The shape of the SSC-profile

The Ebro Delta site is located in a shoaling zone, with non-breaking waves, where hydrodynamics can be dominated by waves or currents or both together and with a flat bottom or with the presence of ripples superimposed to larger sand ridges bedforms (Chapter V). Given

this variety of situations, the concentration profile usually adjusted better to a power form. Time-averaged SSC-profiles exhibited upward-concave shapes and, in general, were well-described with a power function. The choice of power or exponential concentration profile is a controversial issue (Bolaños et al., 2012; Davies and Thorne, 2016). The basic difference between the two predictive models arise in considering height-constant sediment diffusivity (ε_s) for the exponential profiles or considering linearly height-varying diffusivity for the power-law SSC-profile. In the Ebro area, the power profile approach fitted better with the ABS measurements than the exponential (Fig. 44, Table X). In fact, the power approximation is the most used formulae to fit the SSC-profiles in environments with the combination of waves and currents contributing both to the sediment mixing (Soulsby, 1997) and previous studies in areas relatively close to the study site also observed a better fit with the power approach (Guillén et al., 2002).

However, at the uppermost part of the profiles, when sediment concentrations were constant with height (vertical profiles), the power approach presented small divergence from measurements. It probably occurred because of the verticality of the profile due to homogeneity or well-mixing of suspended sediment versus the typically concave shape of the power adjustment. Similarly, Bolaños et al. (2012) observed good agreement of the power and exponential approach for the first 0.2 m above bottom, being the power approach only marginally better than the exponential along these 0.2 m. However, above the 0.2 m they observed a divergence on the exponential form more rapidly with height than the power approach. On the contrary, laboratory observations under only-wave conditions found that concentration profiles very close of the seabed (2η) were better represented by an exponential profile, although the full profile was better described by a power equation (van der Werf et al., 2006).

Based on the shape of the time-averaged SSC-profiles and the parameters estimated from the acoustic device (seabed location and reference concentration) three layers of SSC were usually identified (Fig. 65): (i) high-concentration layer from the seabed (SB) to z_r (with δ thickness); (ii) intermediate layer characterized by strong vertical gradient of SSC; and (iii) upper or background concentration layer with almost constant SSC values with height above the bottom.

The high-concentration layer (high-C layer, Fig. 65), as defined here, should include the sheet flow pick-up layer (Ribberink and Al-Salem, 1995), the wave boundary layer and most of bedload sediment transport, whose typical length scales (few millimetres) (Ribberink and Al-Salem, 1995; Ruessink et al., 2011) are lower than our data resolution (centimetre). In the Ebro site, the thickness of the high-C layer (δ) was typically around 12 cm, but it reached ~30 cm during maximum current speed events accompanied by intense winds (e.g. the 22nd of

November, Fig. 50). High-C layers formation have been observed during stormy weather in coastal areas in mud, silty-enriched (silt and fine sand) or sandy sediment due to horizontal and vertical sediment trapping keeping the sediment in suspension close to the bottom (Traykovski et al., 2000; Lamb and Parsons, 2005; Yan et al., 2010; Yao et al., 2015). The high-C layer formation has been related to the large stirring effects due to oscillatory motion of waves and the sediment-induced buoyancy effects on silty coasts (Lamb and Parsons, 2005; Yan et al., 2010; Yao et al., 2015). Then, during wave-current events, the high-C layer can be related to sand resuspensions from the bottom by sediment stirring by diffusion from the seabed whereas currents were the responsible of the sand/mud transport by horizontal diffusion and advection, occurring then vertical and horizontal diffusion together. The high-C layer was also developed by bottom sediment entrainment generated by strong currents (e.g. Fig. 50). In literature, the near-bottom high-C layer dominated by turbulence has been described in many environments, being their upper boundary the elevation where the concentration is about 10 g/l and SSC range was 3-60 g/l in high-C layers dominated by silt to fine sand sediments (Traykovski et al., 2000; Lamb and Parsons, 2005;Yan et al., 2010; Yao et al., 2015). In the Ebro area, it has been observed in the range of 0.5-10 g/l during the most intense events with an abrupt change in concentrations to lower concentration at z_r, being the concentration at the top of this layer the reference concentration (C_r) used in the SSC-profile model.

The intermediate layer is characterized by a strong decreasing gradient of SSC with height between the top of the high-C layer (z_r) until the level of the profile where the concentration begins to remain almost constant (background layer, see below) (Fig. 65). Time-varying SSC showed that this layer responded to fluctuations in the SSC associated to the entrainment and settling of sediment typically caused by waves (Fig. 48, Fig. 49, Fig. 58 and Fig. 59). These sediment patterns were visualized as sudden/quick vertical increases and decreases of the time-varying SSC and suggest vertical diffusion of fine sand and mud resuspended by waves from the seabed until a specific height (Fig. 46). In this layer, concentrations and the number of high-SSC pulses caused by resuspension decreases progressively with the distance to the seabed and produce a strong vertical SSC gradient in the averaged SSC-profiles (Fig. 45). Similar patterns occurred in current events in presence of waves, suggesting that the effect of small waves could be enhanced by the current and generated rhythmic pulses of suspended sediment (e.g. Fig. 56).

The bulge that disrupted some of the instantaneous SSC-profiles at or slightly above the intermediate layer (Fig. 49 d) suggests that additional processes influence the SSC distribution. Potential mechanisms could be the advection by currents and/or waves, the time lag between the sediment entrainment, and wave flow phases under skewed waves and groups (Ruessink et al., 2011; O'Hara Murray et al., 2012), although in absence of available detailed high-resolution hydrodynamic measurements our data cannot support/discard any of them.

The *background concentration layer* corresponds to the uppermost section of the measured SSC-profile characterized by homogeneous, well-mixing suspended sediments with a roughly constant concentration with height above the bottom (Fig. 65). The small SSC variability was observed in instantaneous, time-varying and time-averaged SSC profiles. The thickness of the background concentration layer tends to maximize at the same time that the sediment concentration decreases during calm conditions while the down-limit can rise above the measured profile during the highest energetic conditions (i.e. Fig. 45 b, c, d, and f).

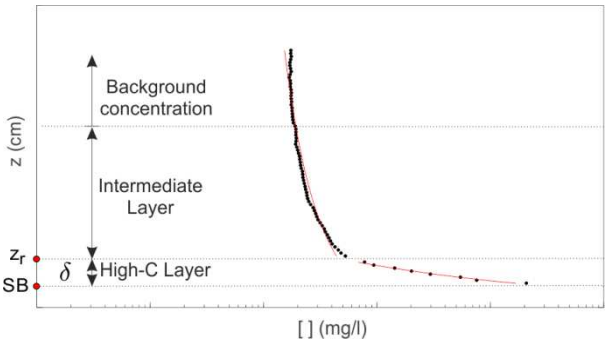

Fig. 65. Model proposed of the time-averaged SSC-profile and the layers identified, where z_r is the reference level, SB is the seabed location, and δ is de distance or thickness between z_r and SB.

3.2. SSC oscillations at wave frequencies

Wave groups and individual waves are characteristic of irregular free surface waves typical in field conditions. Existing field and laboratory works show that the SSC can change over a range of time scales at high-frequencies (intra-waves) associated to individual waves and at low-frequencies (infragravity waves) associated with wave groups (Kularatne and Pattiaratchi, 2008; O'Hara Murray et al., 2011, 2012; Bakker et al., 2016). Time-varying SSC data at the Ebro site displayed SSC oscillations at both incident and infragravity wave frequencies (Fig. 56, Fig. 57, Fig. 66). To show the SSC time scales oscillations and the potential association to individual waves and/or to wave groups, the second fortnight of November was here used as example because it was the period when more high-energetic events occurred under different hydrodynamic conditions (Fig. 66). During wave- and wave-current-dominated events (the latter when waves dominated over currents), SSC oscillations in the intermediate layer were rhythmic, with typical frequencies of 0.07 and 0.12 Hz roughly equivalent to sea-swell waves with periods of 8-14 s (Fig. 66 b, d). In some of these events, secondary spectral peaks at low-frequencies (between 0.03 and 0.01 Hz) appeared simultaneously with the previous (e.g. 28th of November displays second spectral peak at 0.02 Hz, Fig. 66 c). These low-frequency SSC peaks were in the range of characteristic frequencies of infragravity waves or wave groups with

periods 30-200 s also observed in previous experiments (Kularatne and Pattiaratchi, 2008; O'Hara Murray et al., 2012; Bakker et al., 2016).

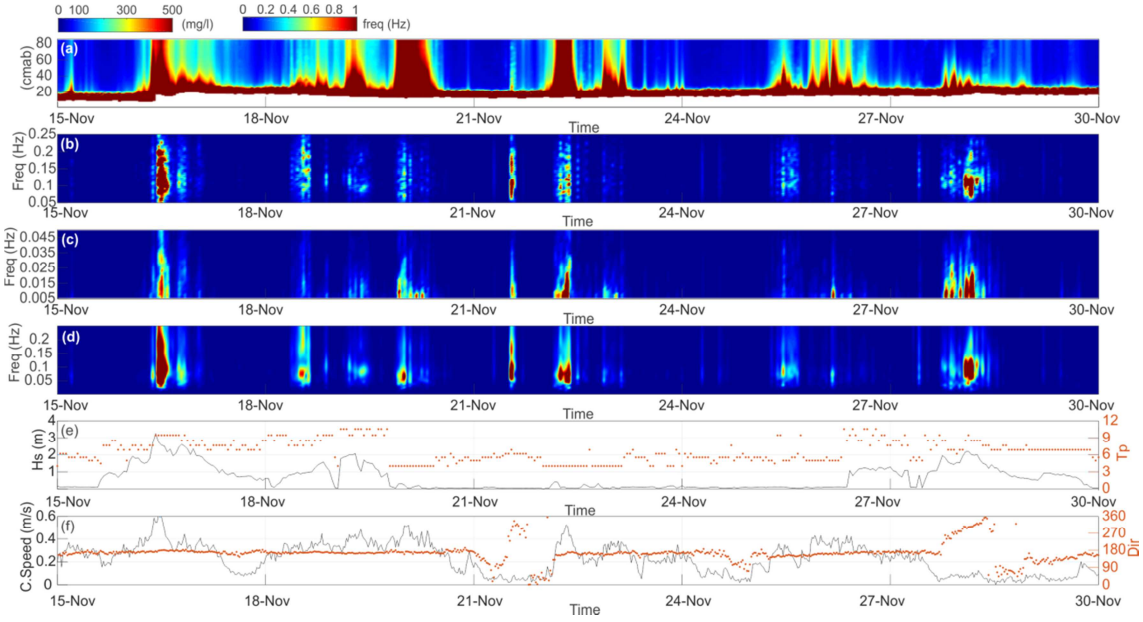

Fig. 66. Time series from the 15th to the 30th of November 2013 of: (a) time-averaged SSC in (mg/l); (b) normalized fft at 15 cm above the detected seabed location for the frequencies between 0.05-0.25 Hz; (c) normalized fft at 15 cm above the detected seabed location for the frequencies between 0.005-0.05 Hz; (d) normalized spectral wavelet at 15 cm above the detected seabed location; (e) propagated significant wave height (line) and peak wave period (dots); (f) current speed (line) and direction (dots).

In pure oscillatory gravity waves, the SSC should displayed two peaks of suspended sediment, during the forward and backwards movement of the water (O'Hara Murray et al., 2011). However, it was observed in shoaling areas that more sand was picked up during the positive than during the negative flow half cycle of waves because of the positively skewed bed shear stress beneath velocity-asymmetric flow (Ruessink et al., 2011). In the Ebro Delta, most of SSC time series spectrums displayed a single peak at gravity wave frequencies suggesting that incoming waves transformed from sinusoidal in deep water, through velocity-skewed in the shoaling zone and the SSC-peak near the seabed should roughly correspond with the onshore wave velocity peak. SSC-peaks wave-like shaped at infragravity frequencies can rise in the water column and most of them reach the uppermost part of the profiles (Fig. 56, Fig. 57).

In the shoaling zone the expected transport associated to the intra-wave skewness is onshore (Kularatne and Pattiaratchi, 2008), while the sediment transport caused by wave groups is typically offshore (Kularatne and Pattiaratchi, 2008; Bakker et al., 2016). The simultaneous occurrence of both frequencies in the SSC time-series in the Ebro site during wave storm conditions suggest that intra-wave frequencies play an important role in the initial resuspension

of sediment within the wave boundary layer, and wave groups can also have a significant role in the near-bottom suspended sediment transport especially at higher elevations above bottom (O'Hara Murray et al., 2012).

3.3. SSC above ripples

Time-averaged, time-varying, and instantaneous SSC-profiles are examined to elucidate if the presence of ripples and their morphological differences significantly modified patterns on the suspended sediment distribution. Ripples developed during low-moderate conditions, while sheet flow regime with flat bottom is assumed to exist during most of the wave-current events in the Ebro area (Chapter V). Observations show that 2D-ripples formed during low- to moderate-energetic conditions associated with waves (H_s~1 m), while 3D-ripples formed under more energetic conditions associated with waves and currents. This is in accordance with the classification of ripples from 2D to 3D transitional to finally plane bed with increasing energy flows (Thorne et al., 2009). In the Ebro Delta, the 2D-ripples remained almost fixed on the seabed while the 3D-ripples migrated towards the SSE and changed their morphologies (Chapter V).

Time-averaged SSC-profiles in presence of 2D wave-ripples showed the same shape as described in wave events (Fig. 67). However, the sequence displayed in Fig. 67 (a-d) exhibits a progressively increase along time of the concentrations, mostly in the high-C and intermediate layers when hydrodynamics remain constant. Therefore, the presence of bedforms potentially be the responsible to that SSC increases. In detail, time-varying SSC showed wave related resuspensions with moderate concentration oscillations but unexpected high SSC measured during small waves suggesting that the presence of ripples could enhance the SSC (Fig. 68). In fact, steep rippled beds can induce vortex formation and entrainment leading to constant sediment diffusivity (O'Hara Murray et al., 2011; Davies and Thorne, 2016). Bulges of SSC increases appeared along the time-varying SSC and the instantaneous SSC-profiles (Fig. 69). These bulges can be compatible with trapped suspended sediment in the shed vortex, which is advected vertically and/or horizontally (O'Hara Murray et al., 2011).

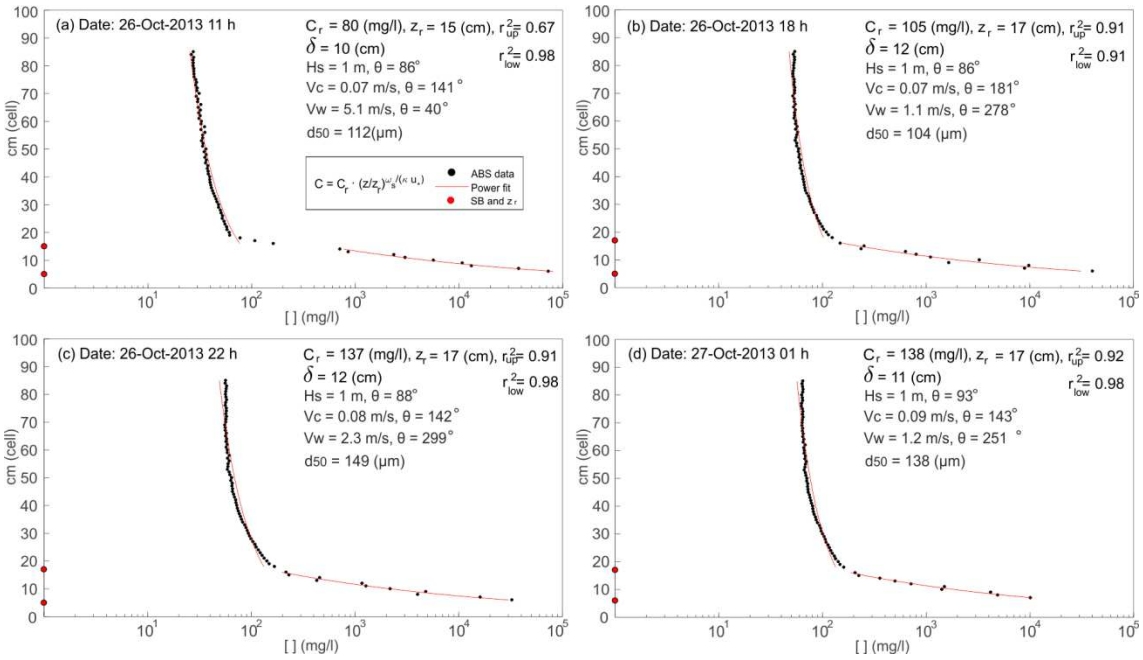

Fig. 67. Time-averaged suspended sediment concentration profiles (SSC-profiles) (black dots) and the power approach (red line) during ripples formation under an eastern wave event. See the Fig. 45 caption for the full description of variables defined in each subplot.

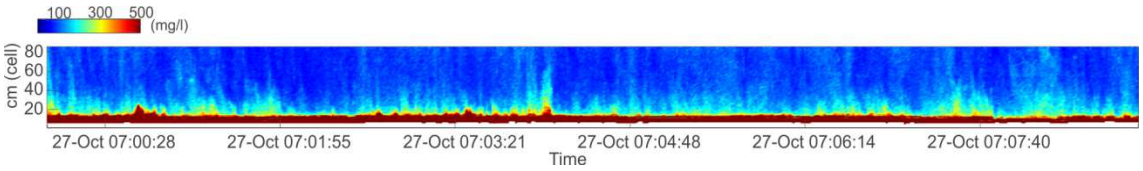

Fig. 68. SSC intra-burst data during the eastern wave event on the 27th of October of 2013 at 7 h when ripples morphologies were observed lying over the seabed.

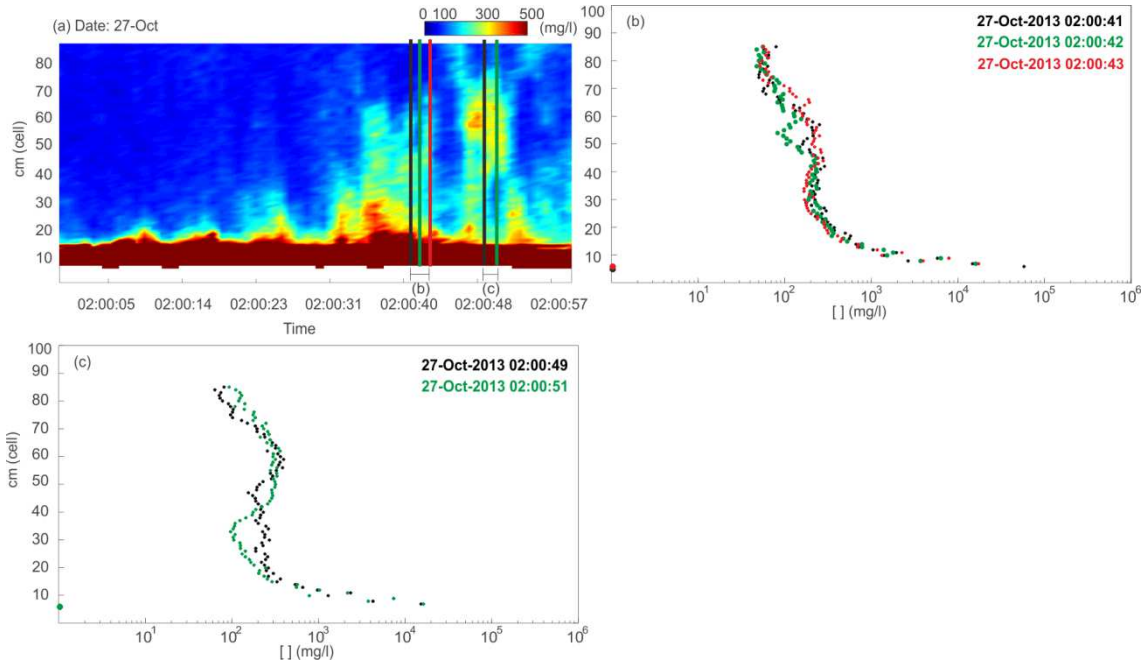

Fig. 69. a) Detail (one minute) of the intra-burst time series measured on the 27th of October of 2013 at 2 h; b, c) SSC-profiles for the instants indicate with the vertical lines in (a).

Rippled bed with brained crests was observed lying on the seabed on the 4th of November at 19 h during a current event (Chapter V). Ripples were very dynamic growing and changing ripple morphologies from 3D to 2D-ripples according to the current speed variations. SSC time series displayed the onset on the suspended sediment increases close to the bottom at the beginning of the event and the progressive augment until the peak on the current speed (Fig. 70 a, Fig. 71). Above current dominated ripples, time-averaged SSC profiles showed thicker background concentration layer (thinner intermediate layer) than in the wave-dominated (Fig. 70). The evolution from 3D brained crests to better-developed 2D rectilinear crests coincided with the increase of the concentration gradient (Fig. 70 a, b, respectively). Instantaneous profiles display wide variability in shapes and thickness of the background concentration (Fig. 71 b, c, d). Below the background concentration layer, SSC exhibit the largest variability displaying different patterns such as: high SSC gradient (Fig. 71 b), bulges development of high SSC close to the seabed (Fig. 71 c) or the progressive decrease of concentrations towards the seabed (Fig. 71 d).

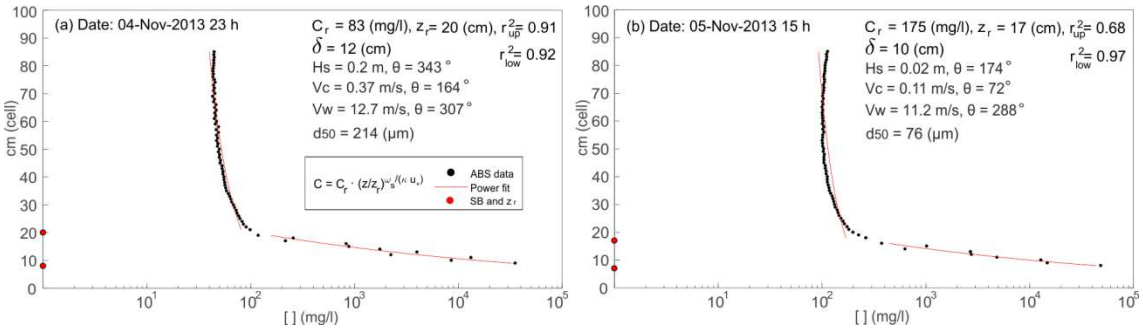

Fig. 70. Time-averaged suspended sediment concentration profiles (SSC-profiles) (black dots) and the power approach (red line) during ripples formation under a current event. See the Fig. 45 caption for the full description of variables defined in each subplot.

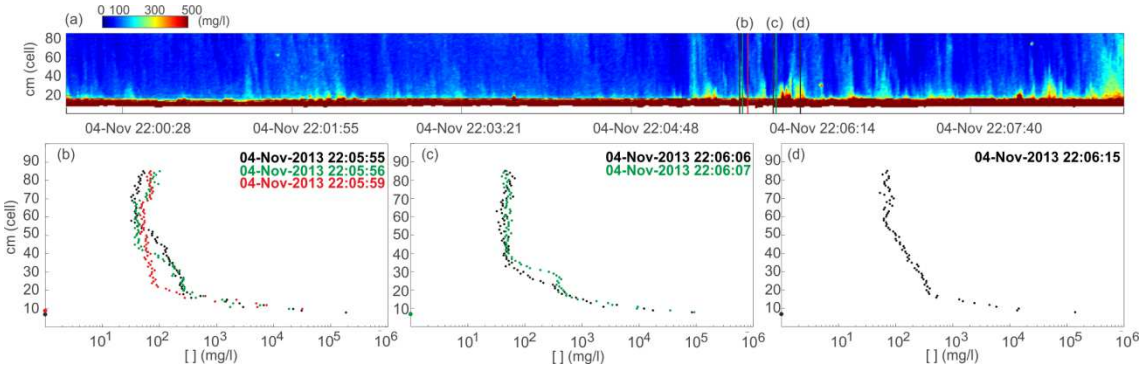

Fig. 71. (a) SSC time-varying of the current event on the 4th of November of 2013 at 22 h; (b, (c), (d) SSC-profiles at the instant indicated in subplot (a).

Finally, 3D-ripples formed during the wave-current event from the 29th to the 31st of October of 2013 (Chapter V). The time-varying profiles show repeatedly suspended sediment pulses above the high-C layer as observed previously in wave-current events (Fig. 72 a). However, some profiles show time-lags on the SSC with height above the bottom at the intermediate layer (Fig. 72 a). These SSC patterns are reflected as abrupt concentration changes along the instantaneous profiles (Fig. 72 b-f). Time-lag SSC with height were also observed to occur consistently just after flow reversal under controlled hydrodynamic conditions in a flume and it was attributed to the ejection of sediment-laden vortices over ripples crests (Hurther et al., 2011) Fig. 9, or Fig. 5 of (O'Hara Murray et al., 2012). This vortex shedding process occurred typically when the orbital diameter is greater than the ripple wavelength (Hurther et al., 2011; O'Hara Murray et al., 2012). In the Ebro, time-lag SSC with height presumably attributed to sediment vortex shedding because of the presence of ripples were only observed during waves and wave-current events.

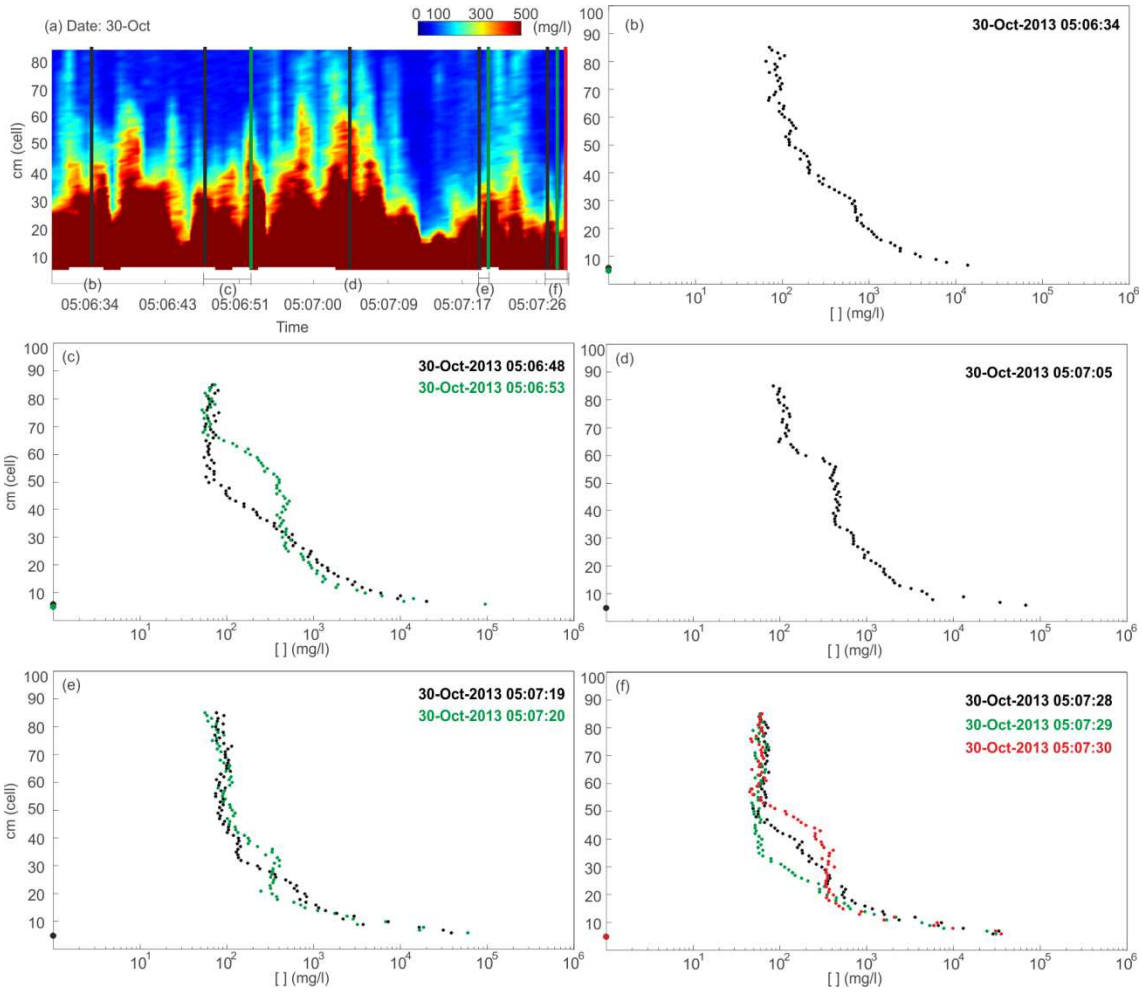

Fig. 72. (a) Time varying SSC during a period of ripples development under wave-current conditions on the 30th of October at 5 h; b, c, d, e, f) SSC-profiles at the instants indicated with the vertical lines in (a).

4. Conclusions

Near-bottom SSC patterns were analysed under only-wave, only-current and wave-current events in the inner shelf of the Ebro Delta area during three months. Inter-burst, burst-averaged (time-averaged) and intra-burst (time-varying) profiles were described for different forcing conditions and the ripple effects in SSC was addressed.

The median grain size of suspended sediment close to the bottom was roughly coarser during high-energy events (d_{50} > 200 µm) and finer during calm periods (d_{50} = 50-150 µm). In general, the suspended sediment is finer than the bottom sediment (d_{50} = 210 µm) except during strong hydrodynamic events, when the suspended sediment is similar and even coarser. The grain size of suspended sediment varies at wave frequencies during waves and combined wave-current events, which indicates that waves control the near-bottom suspended sediment grain size. The variability of suspended sediment grain size is low during current-dominated conditions.

In absence of large sediment river discharges, the total shear stress provided a reasonable prediction of near-bottom SSC, especially during SSC-peaks. Waves are the main contributor to the total shear stress, although strong Mistral winds (NW winds) induced high-speed currents also related with SSC-peaks. An apparent threshold of sediment resuspension was accomplished when τ_{wc} > 0.04 N/m^2.

Three layers were usually identified in the time-averaged SSC-profiles: (i) a high-concentration layer from the seabed to a mean height of ~12 cmab and SSC of 0.5-10 g/l, related to sediment resuspensions due to wave stirring and/or bottom sediment entrainment because of strong currents; (ii) an intermediate layer (few cm to tens cm thick) characterized by an strong vertical gradient of decreasing concentration related to discontinuous resuspensions by wave stirring and diffusion from the seabed and the progressive reduction of concentration and pulses with the height above bottom; and (iii) a background concentration layer at the uppermost part of the profile where SSC is roughly constant and with negligible wave effects.

The variability in the shape of time-averaged SSC-profiles was more related to the energy of the event rather than the trigger factor that induce the sediment mobility (only-waves, only-currents or wave-current). The time-averaged SSC-profile is better fitted to power than exponential profiles under all the studied hydrodynamic conditions. The best fit is obtained applying twice the power profile: at the high-C layer and at intermediate and background layers.

Oscillations of time-varying SSC-profiles mainly occurred at gravity wave frequencies according with bottom sediment resuspension by wave stirring. This is observed even under only current events, when waves are small. When waves dominate, SSC oscillations at typical wave group frequencies enhance the concentration at higher levels above the bottom.

Several changes in the shape of time-varying and instantaneous SSC-profiles were observed in rippled seabed: (i) peaks of SSC with small waves; (ii) increases of the concentration gradient when ripples evolve from 3D brained crests to better-developed (steeper) 2D morphologies; (iii) time-lags in the SSC observed from the bottom to the intermediate layer under waves and combined wave-current events; (iv) bulges of suspended sediment during only-waves and wave-current events which can be compatible with trapped suspended sediment in the shed vortex. However, the shape of the time-averaged SSC profiles remains almost unchanged in presence of ripples.

Chapter VIII. Conclusions and future research

This work undertakes the integrated study of bedform development and sediment dynamics in the inner shelf at different spatial and temporal scales. It is envisaged that small-scale sedimentary processes strongly interact with large-scale processes and therefore, the study of all them is required for their comprehension. For this goal, sand ridges (tens of years-centuries), ripples (minutes-hours) and suspended sediment variations (seconds-hours) were analysed at the Ebro Delta (NW Mediterranean Sea) and Perranporth (Atlantic Ocean) areas.

The diversity of data and techniques has forced to integrate a number of different datasets, data acquisition techniques and methodologies including the use of multiple devices with different sensors (e.g. swath bathymetry, high-resolution seismic reflection, currentmeters, turbidimeters, altimeters, video camera, ABS, seabed profilers), the calibration of the instrumentation, the use of programming tools to process, analyse and plot data; the classification, selection and management of a huge volume of data and information; and the data integration in a Geographic Information System.

The thematic results and conclusions have been explained in the corresponding chapters and then used now to answer the scientific questions raised at the beginning of the thesis.

1. Answers to initial research questions

✓ **What is the temporal scale for the development of shoreface connected sand ridges? Which are the particular conditions required for their formation and potential preservation?**

The Ebro Delta sand ridge field is an example of the first stages of sand ridge bedforms development. During these initial stages, the time-scale of development of SFCRs (previously estimated as hundreds to a few thousand years) was actually much shorter, on the order of a few decades. The genesis of this sand ridge field is closely related to the contemporary evolution of the Ebro River mouth. In the 1940s, the main river course switched and left behind the Cape Tortosa river mouth to its further progressive abandonment, with a rapid retreat of the shoreline and the formation of an erosional surface on the shoreface. Large amounts of sand provided by

coastal erosion available to be reworked favoured the development of the sand ridge field above the erosional surface. The persistent high-speed currents; topographic irregularities in the erosional surface (the potential bedform precursors); and favourable sea level rise in the area during the last few decades instigated and promoted the formation of the Ebro Delta sand ridges, similar to the initial phases of SFDR genesis during the Holocene on Mediterranean shelves.

The sand ridges preservation remains an open question. The existing models and observations about the formation and evolution of SFDR, together with the volume of sediment lost in the sand ridge of the Ebro Delta between 2004 and 2015, encourage thinking that they are progressively degrading and their life-span should be in the order of a few decades. To revert this conjecture a rapid sea-level rise together with large amounts of available sandy sediment should be required.

- ✓ **What is the morphological expression and variability of ripples on the inner shelf under waves, currents and wave-currents conditions? Are they morphologically and/or dynamically different between tideless and macro-tidal environments?**

Seabed morphological observations showed that the presence of ripples is the most usual seabed configuration at the Ebro Delta shoreface and at Perranporth inner shelf during low and mild hydrodynamic conditions.

In the Ebro Delta, four seabed small-scale bedforms were identified. These morphologies sorted from values close (below) to the inception of sediment motion to wash-out conditions are: (i) small undulations with η <0.5 cm and λ~8 cm; (ii) 2D-ripples (wave-ripples) with η =1.2 cm and λ =7-10 cm; (iii) mixed 2D-3D current-dominated ripples with η_{max}~1.5 cm and λ =10-15 cm; and iv) 3D wave-current ripples with η_{max} ~2.2 cm and λ =7-20 cm. The wave-ripples crest alignment were N-S and they were static while ripples under current-dominated conditions and 3D morphologies the crests alignment were W-E and they migrate at mean rates of ~10 cm/h. When the hydrodynamic regime increased the energy, ripple degradation occurred (wash-out conditions) although under low-energy conditions ripples progressively decay mainly as a consequence of the benthic community that contributed flattening the relict ripples.

At Perranporth ripples were related only to waves (wave-ripple) as most ripple crestlines were oriented N-S, perpendicular to the wave direction approach (W-E) and parallel to the dominant current direction (N-S). Two ripple categories were recognized as ripples type 1 with rectilinear crests, η >2 cm and λ =15-20 cm, and ripples type 2 with more sinusoidal or curved crests, η =1-1.5 cm and λ =10-15 cm. The transition from ripple type 1 to ripple type 2 was abrupt and interpreted as ripple degradation or wash-out during increasing energetic conditions while the transition from ripple type 2 to type 1 (ripple growth) was progressive and it occurred when

wave energy decreased. Three general trends were observed at seabed and linked to changing hydrodynamics: (i) during low-energy regimes the seabed was stable and static with steady or relict ripples; (ii) during moderate-energy regimes seabed showed small variabilities with ripple formation and dynamism by crests reorientations; and (iii) during high-energy regimes ripples were washed-out and the seabed formed scour (erosion around the frame legs).

The main difference between both areas is the absence of current-dominated ripples at the Perranporth inner shelf. This occurs because the low-intensity of the recorded tidal currents, which are almost parallel to ripple crestlines. In Perranporth, only two wave-ripples typologies were observed with transitions between them. In the Ebro Delta, small undulations were observed to form under low-energetic conditions (below the critical Shields parameter) as a precursor of the larger well-developed 2D-ripples (wave-ripples) when the energy increased. In both areas, wave-ripples remained stationary suggesting that wave asymmetry/skewness was almost negligible during ripple development. Higher wave asymmetry/skewness was measured at Perranporth during more severe storms and inferred in the Ebro Delta from SSC oscillations during storm events, but in these conditions ripples were wash-out and sheet-flow conditions dominate at the seabed.

- ✓ **Does simple model of ripple prediction satisfactory agree with observations?**

The applied ripple predictor method roughly fits with ripple appearance and it fails in the prediction of ripple dimensions. The development of small seabed undulations below the theoretical threshold of grain movement is a major concern in ripple and sediment transport prediction, suggesting using the estimated thresholds as progressive ranges better than abrupt changes. The capability to prognosticate ripple appearance improved when ripple predictor is applied using thresholds derived from observations, although ripple dimensions were still overestimated.

- ✓ **What are the main mechanisms responsible of the near-bottom suspended sediment variability over flat and rippled bed?**

The mechanisms controlling the near-bottom suspended sediment variability are mainly waves and currents, being the strongest near-bottom currents triggered by the persistent intense Mistral (NW) winds.

The near-bottom SSC is reasonably predicted from the total shear stress, more especially during SSC-peaks. Waves were the main contributor to the total shear stress although high-speed currents induced by strong winds were also associated to SSC-peaks. An apparent threshold of sediment resuspension was achieved when τ_{wc} > 0.04 N/m^2.

The variability in shapes of the time-averaged SSC-profiles is more related to the energy of the event rather than the mechanism inducing sediment mobility (waves, currents or wave-current). Three layers were identified in the time-averaged SSC-profiles: (i) a high-concentration layer related to sediment resuspensions due to wave stirring and/or bottom sediment entrainment because of strong currents; (ii) an intermediate layer associated to wave resuspensions and diffusion where concentrations and pulses progressively reduce with height above bottom; and (iii) a background concentration layer at the uppermost part of the profile where SSC is roughly constant. The time-averaged SSC-profile is better fitted to power than exponential profiles under all the studied hydrodynamic conditions.

The SSC oscillations accordingly with resuspension of sediment induced by the wave stirring at gravity frequencies were observed at the time-varying SSC profiles, even under current-dominated conditions when small wind-induced waves formed. Under wave dominion, SSC oscillations at infragravity wave frequencies enhance the concentration at higher levels above the bottom.

The suspended sediment grain sizes oscillated at wave frequencies during waves and combined wave-current events while during current-dominated events the suspended grain size increased but with reduced (intra-burst) variability. In general, the median grain size of the suspended sediment close to the bottom is finer (d_{50} = 50-150 µm) than the bottom sediment (d_{50} = 210 µm), but during high-energy events it can be coarser (d_{50} > 200 µm).

The shape of time-averaged SSC-profiles remains similar in flat and rippled seabed. However, the time-varying and instantaneous SSC-profiles showed sediment patterns which can be potentially related to ripples lying on the seabed. Some of these changes presumably induced by the presence of the ripples are: peaks of SSC with small waves; increases of the concentration gradient when ripple morphologies changed from 3D brained crests to 2D morphologies; time-lags in the SSC from the bottom to the intermediate layer; bulges of suspended sediment compatible with trapped suspended sediment in the shed vortex during only-waves and wave-current events.

- ✓ **What is the contribution (if any) of ripple dynamics to the migration of sand ridges?**

The integrated analysis of large and small bedforms dynamics at the Ebro Delta suggest that the ripples contribution to the migration of sand ridges could be roughly no more than one order of magnitude lower than the total transport involved in sand ridge migration. This subordinate sediment transport is representative because of it is suggesting that the large-scale bedforms are dynamic during low-moderated energetic processes and not only during high-energy conditions or extreme events. Most of sediment transport occurred during severe storms and under sheet

flow conditions when ripples were washed-out. In presence of ripples, only during the development of 3D wave-current ripples significant sediment transport was estimated and ripple migrated at mean rates ~10 cm/h, dominated (as sand ridge migration) by the wind-induced currents towards the SE.

Observations of small-scale suspended sediment and ripple development also demonstrated that under low- to moderate-energetic conditions 2D-ripples (waves-ripples) form and remain static features (probably because of the wave orbital velocity symmetry). However, when the energy induced by eastern waves increased, the ripples are wash-out and large amount of fine sand and mud was resuspended and available to be transported towards the NW-W (presumably because of wave orbital velocity asymmetry/skewness). Under the latter conditions is when sand ridges can be reshaped to symmetric forms by sheet flow but also through suspended sediment transport.

- ✓ **What is the contribution (if any) of ripple dynamics in the onshore sediment transport from the inner shelf to the nearshore as a potential mechanism of beach recovery?**

The hypothesis of ripple migration as potential contributor to the onshore sediment transport and a beach recovery mechanism under low-, moderate-energetic conditions is discarded based on stationarity of ripples (no migration) that were in agreement with observations of wave symmetry and currents parallel to ripple crestlines at ~20 m depth. The alongshelf sediment transport switched between N and S following the ebbs and floods tidal flows under low-moderate energetic conditions. However, during more energetic conditions, when ripples are wash-out, the wave skewness increases promoting the onshore sediment transport.

2. Future research

The analysis of sand ridges at the Ebro Delta provided valuable information about the formation mechanism, the dynamism, and the involved time scales for the genesis of these large bedforms. In this sense, other field examples of the initial stages of sand ridges formation, embryonic stages, previous to detachment and/or degrading can complement to better define the main controlling processes and the involved time-scales. Field observations can be also valuable information to enrich models of sand ridges formation, evolution and/or vanish. Moreover, observations and models can help to discriminate conditions of sand ridges preservation. In addition, the prolongation of field observations should be recommended to get the seasonal and annual variability of the dynamism of these bedforms.

The precise contribution of small-scale bedforms in the dynamics of large bedforms or in the beach recovery after storms remains an open question that deserves further research. If

significant, it would imply that low-mild-energetic processes (associated to small bedforms) can play a relevant role in the present day morphology of the seabed and in sediment exchanges between the inner shelf and the nearshore. Observations in other inner shelves sites would provide contrasting information about if the cross-shore wave-ripple migration is indeed always restricted to the nearshore zone; and if it is reliable and realistic to be predicted using estimations of wave asymmetry/skewness.

Ripples are usually assumed to be non-equilibrium state features in field with rapid variability (at times even ephemeral) in their formation and dynamism. Therefore, ripple prediction is still under construction and should be improved by adjusting field observations and modelling. The prediction of ripple appearance and dimensions is highly valuable in the estimation of the bed roughness which is decisive in boundary layer parameters (e.g. bed shear stress or sediment transport).

Observation of small-scale processes in the seabed is complex from the technical point of view because the influence of devices deployed. In the future, less intrusive instrumentation will be used from permanent observatories or AUV's devices both incorporating morphological and oceanographic sensors. The integration of high-resolution morphological, hydrodynamic and SSC measurements should make easier data interpretations.

The near-bottom SSC variability and associated trigger hydrodynamic mechanisms interacting with a flat/rippled seabed with changing suspended sediment grain sizes are, at least partially, a "black-box" in our knowledge. Incorporation of new high-quality field measurements (together physical and mathematical modelling) will allow a better understanding of the resuspension and maintenance of sediment in suspension by waves at gravity and infragravity frequencies, wind-induced or tidal-induced currents, the response of the seabed and the resulting sediment transport.

Bibliography

Allen, J.R.L. 1968. Current Ripples: Their Relation to Patterns of Water and Sediment Motion. North Holland, Amsterdam. 433pp

Allen, J.R.., 1982. Simple models for the shape and symmetry of tidal sand waves: (1) statically stable equilibrium forms. Mar. Geol. 48, 31–49

Allen, J.R.L., 1973. A classification of climbing-ripple cross-lamination. J. Geol. Soc. London. 129, 537–541. doi:10.1144/gsjgs.129.5.0537

Allen, J.R.L., 1980. Sand waves: A model of origin and internal structure. Sediment. Geol. 26, 281–328. doi:10.1016/0037-0738(80)90022-6

Alvarado-Aguilar, D., Jiménez, J.A., Nicholls, R.J., 2012. Flood hazard and damage assessment in the Ebro Delta (NW Mediterranean) to relative sea level rise. Nat. Hazards 62, 1301–1321. doi:10.1007/s11069-012-0149-x

Amos, C.L., King, E.L., 1984. Bedforms of the Canadian eastern seaboard: A comparison with global occurrences. Mar. Geol. 57, 167–208. doi:10.1016/0025-3227(84)90199-3

Amoudry, L.O., Souza, A.J., Thorne, P.D., Liu, P.L.-F., 2016. Parametrization of intrawave ripple-averaged sediment pickup above steep ripples. J. Geophys. Res. Ocean. 121, 658–673. doi:10.1002/2015JC011185

Ashley, G.M., 1990. Classification of large-scale subaqueous bedforms: a new look at an old problem. J. Sediment. Petrol. 60, N^{o}1, 160–172. doi:10.1093/teamat/6.1.13

Austin, M., Scott, T., Brown, J., Brown, J., MacMahan, J., Masselink, G., Russell, P., 2010. Temporal observations of rip current circulation on a macro-tidal beach. Cont. Shelf Res. 30, 1149–1165. doi:10.1016/j.csr.2010.03.005

Austin, M.J., Masselink, G., Scott, T.M., Russell, P.E., 2014. Water-level controls on macro-tidal rip currents. Cont. Shelf Res. 75, 28–40. doi:10.1016/j.csr.2013.12.004

Austin, M.J., Scott, T.M., Brown, J.W., MacMahan, J.H., 2009. Macrotidal Rip Current Experiment: Circulation And Dynamics, in: Journal of Coastal Research 10th International Coastal Symposium (ICS 2009). pp. 24–28

Austin, M.J., Scott, T.M., Russell, P.E., Masselink, G., 2013. Rip Current Prediction: Development, Validation, and Evaluation of an Operational Tool. J. Coast. Res. 2, 283–300. doi:10.2112/JCOASTRES-D-12-00093.1

Baas, J.H., 1993. Dimensional analysis of current ripples in recent and ancient depositional environments, Geologica. ed.

Baas, J.H., Best, J.L., Peakall, J., 2016. Predicting bedforms and primary current stratification in cohesive mixtures of mud and sand. J. Geol. Soc. London. 173, 12–45. doi:10.1144/jgs2015-024

Bagnold, R.A., 1946. Motion of waves in shallow water. Interaction between waves and sand bottoms. Proc. R. Soc. A Math. Phys. Eng. Sci. 187, 1–18. doi:10.1098/rspa.1946.0062

Bakker, A.T.M. De, Brinkkemper, J.A., Steen, F. Van Der, Tissier, M.F.S., Ruessink, B.G., 2016. Cross-shore sand transport by infragravity waves as a function of beach steepness. J. Geophys. Res. Earth Surf. 121, 1786–1799. doi:10.1002/2016JF003878

Bard, E., Hamelin, B., Delanghe-Sabatier, D., 2010. Deglacial meltwater pulse 1B and Younger Dryas sea levels revisited with boreholes at Tahiti. Science (80-.). 327, 1235–1237. doi:10.1126/science.1180557

Barnard, P.L., Erikson, L.H., Kvitek, R.G., 2011. Small-scale sediment transport patterns and bedform morphodynamics: New insights from high-resolution multibeam bathymetry. Geo-Marine Lett. 31, 227–236. doi:10.1007/s00367-011-0227-1

Barrie, J.V., Conway, K.W., Picard, K., Greene, H.G., 2009. Large-scale sedimentary bedforms and sediment dynamics on a glaciated tectonic continental shelf: Examples from the Pacific margin of Canada. Cont. Shelf Res. 29, 796–806. doi:10.1016/j.csr.2008.12.007

Bartholdy, J., Ernstsen, V.B., Flemming, B.W., Winter, C., Bartholomä, A., Kroon, A., 2015. On the formation of current ripples. Sci. Rep. 5: 11390, 1–9. doi:10.1038/srep11390

Bassetti, M.A., Jouet, G., Dufois, F., Berné, S., Rabineau, M., Taviani, M., 2006. Sand bodies at the shelf edge in the Gulf of Lions (Western Mediterranean): Deglacial history and modern processes. Mar. Geol. 234, 93–109. doi:10.1016/j.margeo.2006.09.010

Best, J.L. & Bridge, J.S. 1992. The morphology and dynamics of low amplitude bed waves upon upper stage plane beds and the preservation of planar laminae. Sedimentology, 39, 737–752

Bell, P.S., Thorne, P.D., 1997a. Application of a high resolution acoustic scanning system for imaging sea bed microtopography. Seventh Int. Conf. Electron. Eng. Oceanogr. - Technol. Transf. from Res. to Ind. 128–133. doi:10.1049/cp:19970673

Bell, P.S., Thorne, P.D., 1997b. Measurements of sea bed ripple evolution in an estuarine environment using a high resolution acoustic sand ripple profiling system, in: Oceans ’97. MTS/IEEE Conference Proceedings. pp. 339–343. doi:10.1109/OCEANS.1997.634386

Bell, P.S., Thorne, P.D., 2007. Field measurements of wave induced sand ripples in three dimensions. 2nd Int. Conf. Underw. Acoust. Meas. Technol. Results 353–358

Berné, S., Lericolais, G., Bourillet, J.F., Batist, M. De, Reynaud, J.Y., Tessier, B., 1997. Origin of Some Offshore Sand Bodies Around France, in: Proc. Intern. Workshop on “Fluvial-Marine Interations”

Bertin, X., Bakker, A. De, Dongeren, A. Van, Coco, G., André, G., Ardhuin, F., Bonneton, P., Bouchette, F., Castelle, B., Crawford, W.C., Davidson, M., Deen, M., Dodet, G., Guérin, T., Inch, K., Leckler, F., Mccall, R., Muller, H., Olabarrieta, M., Roelvink, D., Ruessink, G., Sous, D., Stutzmann, É., Tissier, M., 2018. Earth-Science Reviews Infragravity waves : From driving mechanisms to impacts. Earth-Science Rev. 177, 774–799. doi:10.1016/j.earscirev.2018.01.002

Bolaños-Sanchez, R., Sanchez-Arcilla, A., Cateura, J., 2007. Evaluation of two atmospheric models for wind-wave modelling in the NW Mediterranean. J. Mar. Syst. 65, 336–353. doi:10.1016/j.jmarsys.2005.09.014

Bolaños, R., Amoudry, L.O., Doyle, K., 2011. Effects of instrumented bottom tripods on process measurements. J. Atmos. Ocean. Technol. 28, 827–837.

doi:10.1175/2010JTECHO816.1

Bolaños, R., Jorda, G., Cateura, J., Lopez, J., Puigdefabregas, J., Gomez, J., Espino, M., 2009. The XIOM: 20 years of a regional coastal observatory in the Spanish Catalan coast. J. Mar. Syst. 77, 237–260. doi:10.1016/j.jmarsys.2007.12.018

Bolaños, R., Thorne, P.D., Wolf, J., 2012. Comparison of measurements and models of bed stress , bedforms and suspended sediments under combined currents and waves. Coast. Eng. 62, 19–30. doi:10.1016/j.coastaleng.2011.12.005

Booij, N., Ris, R.C., Holthuijsen, L.H., 1999. A third-generation wave model for coastal regions: 1. Model description and validation. J. Geophys. Res. 104, 7649–7666. doi:10.1029/98JC02622

Bridge, J. S., Best J. L. (1988). Flow, sediment transport and bedform dynamics over the transition from dunes to upper-stage plane beds: implications for the formation of planar laminae. Sedimentology. Vol 35, Issue 5 pp. 753-763

Brinkkemper, J.A., Bakker, A.T.M., Ruessink, B.G., 2016. Intrawave sand suspension in the shoaling and surf zone of a field-scale laboratory beach. J. Geophys. Res. Earth Surf. 122, 356–370. doi:10.1002/2016JF004061

Butt, T., Russell, P., 2000. Hydrodynamics and cross-shore sediment transport in the swash-zone of natural beaches: A review. J. Coast. Res. 16, 255–268. doi:10.2307/4300034

Cacchione, D.A., Drake, D.E., Losada, M.A., Medina, R., 1990. Bottom-boundary-layer measurements on the continental shelf off the Ebro River, Spain. Mar. Geol. 95, 179–192. doi:10.1016/0025-3227(90)90115-Z

Cacchione, D.A., Thorne, P.D., Agrawal, Y., Nidzieko, N.J., 2008. Time-averaged near-bed suspended sediment concentrations under waves and currents : Comparison of measured and model estimates. Cont. Shelf Res. 28, 470–484. doi:10.1016/j.csr.2007.10.006

Calvete, D., Falqués, A, de Swart, H.E., Walgreen, M., 2001. Modelling the formation of shoreface-connected sand ridges on storm-dominated inner shelves. J. Fluid Mech. 441, 169–193. doi:10.1017/S0022112001004815

Camenen, B., 2009. Estimation of the wave-related ripple characteristics and induced bed shear stress. Estuar. Coast. Shelf Sci. 84, 553–564. doi:10.1016/j.ecss.2009.07.022

Camenen, B., Larson, M., 2006. Phase-lag effects in sheet flow transport. Coast. Eng. 53, 531–542. doi:10.1016/j.coastaleng.2005.12.003

Canvi Climàtic, O.C., 2008. Framework studies for preventing and adapting to climate change in Catalonia. Study N1:Ebro Delta, Oficina Catalana del Canvi Climàtic. Departament de Medi Ambient i Habitatge. Generalitat de Catalunya

Carlin, J.A., Lee, G. hong, Dellapenna, T.M., Laverty, P., 2016. Sediment resuspension by wind, waves, and currents during meteorological frontal passages in a micro-tidal lagoon. Estuar. Coast. Shelf Sci. 172, 24–33. doi:10.1016/j.ecss.2016.01.029

Cartigny, M.J.B., Postma, G., van den Berg, J.H., Mastbergen, D.R., 2011. A comparative study of sediment waves and cyclic steps based on geometries, internal structures and numerical modeling. Mar. Geol. 280, 40–56. doi:10.1016/j.margeo.2010.11.006

Cataño-Lopera, Y.A., García, M.H., 2006. Geometry and migration characteristics of bedforms under waves and currents. Part 2: Ripples superimposed on sandwaves. Coast. Eng. 53, 781–792. doi:10.1016/j.coastaleng.2006.03.008

Cerralbo, P., Grifoll, M., Moré, J., Bravo, M., Afif, A.S., Espino, M., 2015. Wind variability in a coastal area (Alfacs Bay , Ebro River delta), in: Advances in Science and Research. pp. 11–21. doi:10.5194/asr-12-11-2015

Clifton, H.E., Dingler, J.R., 1984. Wave-formed structures and paleoenvironmental reconstruction. Mar. Geol. 60, 165–198. doi:10.1016/S0070-4571(08)70146-8

Coco G. (2017) Bedforms as Self-organized Patterns. In: Guillén J., Acosta J., Chiocci F., Palanques A. (eds) Atlas of Bedforms in the Western Mediterranean. Springer, Cham

Coco, G., Murray, A.B., 2007. Patterns in the sand: From forcing templates to self-organization. Geomorphology 91, 271–290. doi:10.1016/j.geomorph.2007.04.023

Raudikivi, A. J. (1988). The roughness height under waves. *J. Hydr. Res*., 26 (5), 569-584

van Rijn, L. C. (1993). Principles of sediment transport in rivers, estuaries, and coastal seas, Aqua, Blokzijl, The Netherlands

Coleman, S. E. & Melville, B. W. (1994). Initiations of bedforms on a flat sand bed. Journal of Hydraulic Engineering, ASCE, vol. 122, Issue 6, pp 301–310

Correggiari, A., Field, M.E., Trincardi, F., 1996. Late Quaternary transgressive large dunes on the sediment-starved Adriatic shelf. Geol. Soc. London, Spec. Publ. 117, 155–169. doi:10.1144/GSL.SP.1996.117.01.09

Crawford, A.M., Hay, A.E., 2001. Linear transition ripple migration and wave orbital velocity skewness : Observations. J. Geophys. Res. 106, 14113–14128

Dalrymple, R.W., Hoogendoorn, E.L., 1997. Erosion and deposition on migrating shoreface-attached ridges, Sable island, Eastern Canada. Geosci. Canada 24, 25–36

Dalrymple, R.W., Rhodes, R.N., 1995. Estuarine dunes and bars, in: Geomorphology and Sedimentology of Estuaries. Developments in Sedimentology. pp. 359–422

Davidson, M.A., Turner, I.L., Splinter, K.D., Harley, M.D., 2017. Annual prediction of shoreline erosion and subsequent recovery. Coast. Eng. 130, 14–25. doi:10.1016/j.coastaleng.2017.09.008

Davies, A.G., Thorne, P.D., 2008. Advances in the study of moving sediments and evolving seabeds. Surv. Geophys. 29, 1–36. doi:10.1007/s10712-008-9039-x

Davies, A.G., Thorne, P.D., 2016. On the suspension of graded sediment by waves above ripples: Inferences of convective and diffusive processes. Cont. Shelf Res. 112, 46–67. doi:10.1016/j.csr.2015.10.006

Díaz, J.I., Nelson, C.H., Barber Jr, J.H., Giró, S., 1990. Late Pleistocene and Holocene sedimentary facies on the Ebro continental shelf. Mar. Geol. 95, 333–352

Díaz, J.I., Palanques, A., Nelson, C.H., Guillén, J., 1996. Morpho-structure and sedimentology of the Holocene Ebro prodelta mud belt (northwestern Mediterranean Sea). Cont. Shelf Res. 16, 435–456. doi:10.1016/0278-4343(95)00019-4

Dingler, J.R., Inman, D.L., 1976. Wave-formed ripples in nearshore sands. Coast. Eng. no 15, 2109–2126

Doucette, Jeffrey S. (2002). Bedform Migration and Sediment Dynamics in the Nearshore of a Low-Energy Sandy Beach in Southwestern Australia. Journal of Coastal Reseach. vol 18, nº 3, pp. 576-591

Durán, R., Guillén, J., Rivera, J., Muñoz, A., 2016. Holocene evolution of sand ridges in a tideless continental shelf (Western Mediterranean), in: MARID V (Marine and River Dune Dynamics). pp. 61–64

Durán, R., Guillén, J., Rivera, J., Muñoz, A., Lobo, F.J., Fernández-Salas, L.M., Acosta, J., 2017a. Subaqueous Dunes Over Sand Ridges on the Murcia Outer Shelf, in: Guillén, J., Acosta, J., Chiocci, F.L., Palanques, A. (Ed.), Atlas of Bedforms in the Western Mediterranean. pp. 187–192. doi:10.1007/978-3-319-33940-5

Durán, R., Guillén, J., Simarro, G., Ribó, M., Puig, P., Muñoz, A., Palanques, A., 2015. Sand ridges in the mid-outer shelf as potential sand borrows areas (nw mediterranean), in: Proceedings Coastal Sediments. pp. 1–13. doi:10.1142/9789814689977_0111

Durán, R., Rivera, J., Guillen, J., Cárdenas, E. De, Muñoz, A., Acosta, J., 2013. Sandy Subaqueous Dunes on the Murcia Continental Shelf (Western Mediterranean Sea), in: Rapp. Comm. Int. Mer Médit., 40

Dyer, K.R., Huntley, D.A., 1999. The origin, classification and modelling of sand banks and ridges. Cont. Shelf Res. 19, 1285–1330

Edwards, J.H., Harrison, S.E., Locker, S.D., Hine, A.C., Twichell, D.C., 2003. Stratigraphic framework of sediment-starved sand ridges on a mixed siliciclastic/carbonate inner shelf; west central Florida. Mar. Geol. 200, 195–217

Elgar, S., 1987. Relationships involving third movements and bispectra of a harmonic process. IEEE transctins Acoust. speech, signal Process. ASSP-35. N

Farge, M., 1992. Wavelet transforms and their applications to turbulence. Annu. Rev. Fluid Mech. 24, 395–457

Farrán, M. Catalano-Balearic Sea (NW Mediterranean): Bathymetric Chart and Toponyms. Available online: http://gma.icm.csic.es/sites/default/files/geowebs/MCB/CBSbats_cat.htm (accessed on 27 April 2018)

Fenton, J.D., McKee, W.D., 1990. On calculating the lengths of water waves. Coast. Eng. 14, 499–513. doi:10.1016/0378-3839(90)90032-R

Figueiredo, A.G., Sanders, J.E., Swift, D.J.P., 1982. Storm-graded layers on inner continental shelves: Examples from southern Brazil and the Atlantic coast of the Central United States. Sediment. Geol. 31, 171–190. doi:10.1016/0037-0738(82)90057-4

Flemming, B.. W., 1980. Sand transport and bedform patterns on the continental shelf between Durban and Port Elizabeth (Southeast african continental margin). Sediment. Geol. 26, 179–205. doi:10.1016/0037-0738(80)90011-1

Flemming, B.W., 1988. Zur Klassifikation subaquatischer, strömungstransversaler Transportkörper. Bochumer geologische und geotechnische Arbeiten 29, 44-47

Gallagher, E.L., Elgar, S., Thornton, E.B., 1998. Megaripple migration in a natural surf zone. Nature 394, 165–168. doi:10.1038/28139

Glenn, S.M., Grant, W.D., 1987. A suspended sediment stratification correction for combined wave and current flows. J. Geophys. Res. 92, 8244–8264. doi:10.1029/JC092iC08p08244

Goff, J.A., 2009. Evolution and Preservation of Sand Ridges from the New Jersey Middle and Outer Shelf. Search Discov

Goff, J.A., 2014. Seismic and core investigation off Panama city, Florida, reveals sand ridge influence on formation of the shoreface ravinement. Cont. Shelf Res. 88, 34–46. doi:10.1016/j.csr.2014.07.006

Goff, J.A., Duncan, L.S., 2012. Re-examination of sand ridges on the middle and outer New Jersey shelf based on combined analysis of multibeam bathymetry and backscatter , seafloor grab samples and chirp seismic data. Int. Assoc. Sedimentol. Spec. Publ. 44, 121–142

Goff, J.A., Swift, D.J.P., Duncan, C.S., Mayer, L.A., Hughes-Clarke, J., 1999. High-resolution swath sonar investigation of sand ridge, dune and ribbon morphology in the offshore environment of the New Jersey margin. Mar. Geol. 161, 307–337. doi:10.1016/S0025-3227(99)00073-0

Gomez, B., Naff, R.L., Hubbell, D.W., 1989. Temporal variations in bedload transport rates associated with the migration of bedforms. Earth Surf. Process. Landforms 14, 135–156. doi:10.1002/esp.3290140205

Goring, D.G., Nikora, V.I., 2002. Despiking Acoustic Doppler Velocimeter Data. J. Hydraul. Eng. 128, 117–126. doi:10.1061/(ASCE)0733-9429(2002)128:1(117)

Grant, W.D., Madsen, O.S., 1979. Combined Wave and Current Interaction With a Rough Bottom. J. Geophys. Res. 84, 1797–1808

Green, M.O., Black, K.P., 1999. Suspended-sediment reference concentration under waves : field observations and critical analysis of two predictive models. Coast. En 38, 115–141

Grifoll, M., Navarro, J., Pallares, E., Ràfols, L., Espino, M., Palomares, A., 2016. Ocean–atmosphere–wave characterisation of a wind jet (Ebro shelf, NW Mediterranean Sea), in: Nonlinear Processes in Geophysics. pp. 143–158. doi:10.5194/npg-23-143-2016

Guerrero, Q., Guillén, J., Durán, R., Urgeles, R., 2017. Contemporary Subaqueous Dune Field Development Over an Abandoned River Mouth (Ebro Delta), in: Guillén, J., Acosta, J., Chiocci, F.L., Palanques, A. (Ed.), Altlas of Bedforms in the Western Mediterranean. pp. 89–93. doi:10.1007/978-3-319-33940-5_15

Guerrero, Q., Guillén, J., Durán, R., Urgeles, R., 2018. Contemporary genesis of sand ridges in a tideless erosional shoreface. Mar. Geol. 395, 219–233. doi:10.1016/j.margeo.2017.10.002

Guillén, J., Jiménez, J.A., Palanques, A., Gracia, V., Puig, P., Sánchez-Arcilla, A., 2002. Sediment resuspension across a microtidal, low-energy inner shelf. Cont. Shelf Res. 22, 305–325

Guillén, J., Jiménez, J.A., Palanques, A., Puig, P., Gracia, V., 2005. Bottom Sediment Variability in the Active Layer of the Inner Shelf off the Ebro Delta. J. Coast. Res. 21, 482–496. doi:10.2112/03-0056.1

Guillén, J., Palanques, A., 1993. Longshore bar and trough systems in a microtidal, storm-wave dominated coast: The Ebro Delta (Northwestern Mediterranean). Mar. Geol. 115, 239–252. doi:10.1016/0025-3227(93)90053-X

Guillén, J., Palanques, A., 1997a. A shoreface zonation in the Ebro Delta based on grain size distribution. J. Coast. Res. 13, 867–878

Guillén, J., Palanques, A., 1997b. A historical perspective of the morphological evolution in the lower Ebro river. Environ. Geol. 30, 174–180. doi:10.1007/s002540050144

Guillén, J., Soriano, S., Demestre, M., Falqués, A., Palanques, A., Puig, P., 2008. Alteration of bottom roughness by benthic organisms in a sandy coastal environment. Cont. Shelf Res. 28, 2382–2392. doi:10.1016/j.csr.2008.05.003

Ha, H.K., Park, K., 2012. High-resolution comparison of sediment dynamics under different forcing conditions in the bottom boundary layer of a shallow, micro-tidal estuary. J. Geophys. Res. Ocean. 117, 1–14. doi:10.1029/2012JC007878

Hanes, D.M., Alymov, V., Chang, Y.S., Jette, C., 2001. Wave-formed sand ripples at Duck, North Carolina. J. Geophys. Res. 106, 22575–22592. doi:10.1029/2000JC000337

Harrison, S.E., Locker, S.D., Hine, A.C., Edwards, J.H., Naar, D.F., Twichell, D.C., Mallinson, D.J., 2003. Sediment-starved sand ridges on a mixed carbonate/siliciclastic inner shelf off west-central Florida. Mar. Geol. 200, 171–194. doi:10.1016/S0025-3227(03)00182-8

Herbert, C.M., Alexander, J., Martínez de Álvaro, M. j:, 2015. Back-flow ripples in troughs downstream of unit bars: Formation , preservation and value for interpreting flow conditions. Sedimentology 62, 1814–1836. doi:10.1111/sed.12203

Hurther, D., Thorne, P.D., 2011. Suspension and near -bed load sediment transport processes above a migrating , sand-rippled bed under shoaling waves. J. Geophys. Res. 116. doi:10.1029/2010JC006774

Hurther, D., Thorne, P.D., Bricault, M., Lemmin, U., Barnoud, J., 2011. A multi-frequency Acoustic Concentration and Velocity Profiler (ACVP) for boundary layer measurements of fine-scale flow and sediment transport processes. Coast. Eng. 58, 594–605. doi:10.1016/j.coastaleng.2011.01.006

Huthnance, J.M., 1982. On one mechanism forming linear sand banks. Estuar. Coast. Shelf Sci. 14, 79–99. doi:10.1016/S0302-3524(82)80068-6

Inch, K., Davidson, M., Masselink, G., Russell, P., 2017. Observations of nearshore infragravity wave dynamics under high energy swell and wind-wave conditions. Cont. Shelf Res. 138, 19–31. doi:10.1016/j.csr.2017.02.010

IPCC, 2013. Climate Change 2013: The Physical Science Basis. In: Stocker, T.F., Qin, D., Plattner, G.-K., Tignor, M., Allen, S.K., Boschung, J., Nauels, A., Xia, Y., Bex, V., Midgley, P.M. (Eds.), Contribution of Working Group I to the Fifth Assessment Report of the Intergovernmental Panel on Climate Change. Cambridge University Press, Cambridge, United Kingdom and New York, NY, USA (1535 pp)

Jestin, H., Bassoullet, P., Le Hir, P., L'Yavanc, J., Degres, Y., 1998. Development of ALTUS, a high frequency acoustic submersible recording altimeter to accurately monitor bed elevation and quantify deposition or erosion of sediments, in: OCEANS'98 Conference Proceedings (Vol. 1). pp. 189–194

Jiménez, J.A., Sánchez-Arcilla, A., 1993. Medium-term coastal response at the Ebro delta, Spain. Mar. Geol. 114, 105–118. doi:10.1016/0025-3227(93)90042-T

Jiménez, J.A.J.A., Guillén, J., Gracia, V., Palanques, A., García, M.A., Sánchez-Arcilla, A., Puig, P., Puigdefábregas, J., Rodríguez, G., García, M.A., Sánchez-Arcilla, A., Puig, P., Puigdefábregas, J., Rodríguez, G., 1999. Water and sediment fluxes on the Ebro Delta shoreface: on the role of low frequency currents. Mar. Geol. 157, 219–239. doi:10.1016/S0025-3227(98)00153-4

Kennedy, J.F., 1969. The formation of sediment ripples, dunes, and antidunes. Annu. Rev. Fluid Mech. 1, 147–168. doi:10.1146/annurev.fl.01.010169.001051

King, C.A.M., Williams, W.W., 1949. The Formation and Movement of Sand Bars by Wave Action. Geogr. J. 113, 70–85

Kleinhans, M.G., 2005. Phase diagrams of bed states in steady, unsteady, oscillatory and mixed flows, in: SANDPIT End-Book. pp. Q1–Q16

Kleinhans, M.G., Passchier, S., Dijk, T. Van, 2004. The origin of megaripples , long wave ripples and Hummocky Cross-Stratification in the North Sea in mixed flows. Mar. Sandwave River Dune Dyn. 1&2 April 2004 142–151

Knaapen, M.A., van Bergen Henegouw, C.N., Hu, Y.Y., 2005. Quantifying bedform migration using multi-beam sonar. Geo-Marine Lett. 25, 306–314. doi:10.1007/s00367-005-0005-z

Knaapen, M.A.F., 2005. Sandwave migration predictor based on shape information. J. Geophys. Res. Earth Surf. 110, 1–9. doi:10.1029/2004JF000195

Krämer, K., Winter, C., 2016. Predicted ripple dimensions in relation to the precision of in situ measurements in the southern North Sea. Ocean Sci. 12, 1221–1235. doi:10.5194/os-12-1221-2016

Kularatne, S., Pattiaratchi, C., 2008. Turbulent kinetic energy and sediment resuspension due to wave groups. Cont. Shelf Res. 28, 726–736. doi:10.1016/j.csr.2007.12.007

Lamb, M.P., Parsons, J.D., 2005. High-density suspensions formed under waves. J. Sediment. Res. 75, 386–397. doi:10.2110/jsr.2005.030

Larson, M., C. Kraus, N., 1995. Prediction of cross-shore sediment transport at different spatial and temporal scales. Mar. Geol. 126, 111–127. doi:10.1016/0025-3227(95)00068-A

Lee, G., Dade, W.B., Friedrichs, C.T., Vincent, C.E., 2004. Examination of reference concentration under waves and currents on the inner shelf. J. Geophys. Resear 109, 1–10. doi:10.1029/2002JC001707

Lee, G., Friedrichs, C.T., Vincent, C.E., 2002. Examination of diffusion versus advection dominated sediment suspension on the inner shelf under storm and swell conditions, Duck, North Carolina. J. Geophys. Res. 107. doi:10.1029/2001JC000918

Li, G., Wang, X.T., Yang, Z., Mao, C., West, A.J., Ji, J., 2015. Dam-triggered organic carbon sequestration makes the Changjing (Yangtze) river basin (China) a significant carbon sink. J. Geophys. Res. Biogeosciences 120, 39–53. doi:10.1002/2014JG002646.Received

Li, M.Z.., Wright, L.D., Amos, C.L., 1996. Predicting ripple roughness and sand resuspension under combined flows in a shoreface environment. Mar. Geol. 130, 139–161. doi:10.1016/0025-3227(95)00132-8

Li, M.Z., Amos, C.L., 1998. Predicting ripple geometry and bed roughness under combined waves and currents in a continental shelf environment. Cont. Shelf Res. 18, 941–970. doi:10.1016/S0278-4343(98)00034-X

Li, M.Z., Amos, C.L., 1999. Sheet flow and large wave ripples under combined waves and currents: Field observations, model predictions and effects on boundary layer dynamics. Cont. Shelf Res. 19, 637–663. doi:10.1016/S0278-4343(98)00094-6

Li, M.Z., King, E.L., 2007. Multibeam bathymetric investigations of the morphology of sand ridges and associated bedforms and their relation to storm processes, Sable Island Bank, Scotian Shelf. Mar. Geol. 243, 200–228. doi:10.1016/j.margeo.2007.05.004

Lichtman, I.D., 2017. Combined effects of hydrodynamics and cohesive clay on bedform

morphology and migration on sandy tidal flats. PhD Thesis

Liu, P.C., Babanin, A. V., 2004. Using wavelet spectrum analysis to resolve breaking events in the wind wave time series. Ann. Geophys. 22, 3335–3345

Liu, Z., Berné, S., Saito, Y., Yu, H., Trentesaux, A., Uehara, K., Yin, P., Paul Liu, J., Li, C., Hu, G., Wang, X., 2007. Internal architecture and mobility of tidal sand ridges in the East China Sea. Cont. Shelf Res. 27, 1820–1834. doi:10.1016/j.csr.2007.03.002

Maier, I., Hay, A.E., 2009. Occurrence and orientation of anorbital ripples in near-shore sands. J. Geophys. Res. Earth Surf. 114, 1–18. doi:10.1029/2008JF001126

Malarkey, J., Davies, A.G., 2012. A simple procedure for calculating the mean and maximum bed stress under wave and current conditions for rough turbulent flow based on Soulsby and Clarke's (2005) method. Comput. Geosci. 43, 101–107. doi:10.1016/j.cageo.2012.02.020

Maldonado, A., Riba, O., 1971. El delta reciente del río Ebro: descripción de ambientes y evolución. Acta Geológica Hispánica VI, 131–138

Marine Electronics Ltd., 2009. User Manual for the 3D Sand Ripple Profiling Logging Sonar

Mark, C.F. Van Der, Blom, A., 2007. A new & widely applicable bedform tracking tool. Enschede, Netherlands. Univ. Twente

Masselink, G., Austin, M.J., O'Hare, T.J., Russell, P.E., 2007. Geometry and dynamics of wave ripples in the nearshore zone of a coarse sandy beach. J. Geophys. Res. Ocean. 112, 1–19. doi:10.1029/2006JC003839

Masselink, G., Kroon, A., Davidson-Arnott, R.G.D., 2006. Morphodynamics of intertidal bars in wave-dominated coastal settings — A review. Geomorphology 73, 33–49. doi:10.1016/j.geomorph.2005.06.007

Masselink, G., Scott, T., Poate, T., Russell, P., Davidson, M., Conley, D., 2016. The extreme 2013/2014 winter storms: Hydrodynamic forcing and coastal response along the southwest coast of England. Earth Surf. Process. Landforms 41, 378–391. doi:10.1002/esp.3836

Masson, D.G., Wynn, R.B., Bett, B.J., 2004. Sedimentary environment of the Faroe-Shetland and Faroe Bank Channels, north-east Atlantic, and the use of bedforms as indicators of bottom current velocity in the deep ocean. Sedimentology 51, 1207–1241. doi:10.1111/j.1365-3091.2004.00668.x

McBride, R.A., Moslow, T.F., 1991. Origin, evolution, and distribution of shoreface sand ridges, Atlantic inner shelf, U.S.A. Mar. Geol. 97, 57–85. doi:10.1016/0025-3227(91)90019-Z

McLean, S.R., Nelson, J.M., Wolfe, S.R., 1994. Turbulence structure over two-dimensional bed forms: Implication for sediment transport. J. Geophys. Res. 99, 12729–12747

Meral, R., 2008. Laboratory Evaluation of Acoustic Backscatter and LISST Methods for Measurements of Suspended Sediments. Sensors 8, 979–993

Meyers, S.D., Kelly, B.G., O'Brien, J.J., 1993. An introduction to wavelet analysis in oceanography and meteorology: with application to the dispersion of Yanai Waves. Mon. Weather Rev. doi:10.1175/1520-0493(1993)121<2858:AITWAI>2.0.CO;2

Miles, J., Thorpe, A., 2015. Bedform contributions to cross-shore sediment transport on a dissipative beach. Coast. Eng. 98, 65–77. doi:10.1016/j.coastaleng.2015.01.007

Miles, J., Thorpe, A., Russell, P., Masselink, G., 2014. Observations of bedforms on a dissipative macrotidal beach. Ocean Dyn. 64, 225–239. doi:10.1007/s10236-013-0677-2

Murray, A.B., Thieler, E.R., 2004. A new hypothesis and exploratory model for the formation of large-scale inner-shelf sediment sorting and "rippled scour depressions." Cont. Shelf Res. 24, 295–315. doi:10.1016/j.csr.2003.11.001

Naqshband, S., Ribberink, J.S., Hulscher, S.J.M.H., 2014. Sediment transport distribution along developing sand dunes. River Flow

Nelson, J.M., Smith, J.D., 1989. Mechanics of flow over ripples and dunes. J. Geophys. Res. 94, 8146–8162. doi:10.1029/JC094iC06p08146

Nelson, T.R., Voulgaris, G., 2014. Temporal and spatial evolution of wave-induced ripple geometry: Regular versus irregular ripples. J. Geophys. Res. Ocean. 119, 664–688. doi:10.1002/2013JC009020

Nelson, T.R., Voulgaris, G., Traykovski, P., 2013. Predicting wave-induced ripple equilibrium geometry. J. Geophys. Res. Ocean. 118, 3202–3220. doi:10.1002/jgrc.20241

Nielsen, P., 1981. Dynamics and Geometry of Wave-Generated Ripples. J. Geophys. Res. 86, 6467–6472

Nielsen, P., 1992. Coastal bottom boundary layers and sediment transport. Advanced Series on Ocean Eng. vol. 4. World Scientific, Singapore, pp. 324

Nnafie, A., de Swart, H.E., Calvete, D., Garnier, R., 2014. Effects of sea level rise on the formation and drowning of shoreface-connected sand ridges, a model study. Cont. Shelf Res. 80, 32–48. doi:10.1016/j.csr.2014.02.017

O'Hara Murray, R.B., Hodgson, D.M., Thorne, P.D., 2012. Wave groups and sediment resuspension processes over evolving sandy bedforms. Cont. Shelf Res. 46, 16–30. doi:10.1016/j.csr.2012.02.011

O'Hara Murray, R.B., Thorne, P.D., Hodgson, D.M., 2011. Intrawave observations of sediment entrainment processes above sand ripples under irregular waves. J. Geophys. Resear 116. doi:10.1029/2010JC006216

Ogston, A.S., Cacchione, D.A., Sternberg, R.W., Kineke, G.C., 2000. Observations of storm and river flood-driven sediment transport on the northern California continental shelf. Cont. Shelf Res. 20, 2141–2162. doi:10.1016/S0278-4343(00)00065-0

Palanques, A., Puig, P., Guillén, J., Jiménez, J., Gracia, V., Sánchez-Arcilla, A., Madsen, O., 2002. Near-bottom suspended sediment fluxes on the microtidal low-energy Ebro continental shelf (NW Mediterranean). Cont. Shelf Res. 22, 285–303. doi:10.1016/S0278-4343(01)00058-9

Perillo, M.M., Best, J.L., Garcia, M.H., 2014. A New Phase Diagram for Combined-Flow Bedforms. J. Sediment. Res. 84, 301–313. doi:10.2110/jsr.2014.25

Pitman, S., Gallop, S.L., Haigh, I.D., Masselink, G., Ranasinghe, R., 2016. Wave breaking patterns control rip current flow regimes and surfzone retention. Mar. Geol. 382, 176–190. doi:10.1016/j.margeo.2016.10.016

Poate, T., Masselink, G., Russell, P., Austin, M., 2014. Morphodynamic variability of high-energy macrotidal beaches, Cornwall, UK. Mar. Geol. 350, 97–111. doi:10.1016/j.margeo.2014.02.004

Puig, P., Ogston, A. S., Guillén, J., Fain, A. M. V, Palanques, A., 2007. Sediment transport processes from the topset to the foreset of a crenulated clinoform (Adriatic Sea). Cont. Shelf Res. 27, 452–474. doi:10.1016/j.csr.2006.11.005

Puig, P., Palanques, A., Guillén, J., 2001. Near-bottom suspended sediment variability caused by storms and near-inertial internal waves on the Ebro mid continental shelf (NW Mediterranean). Mar. Geol. 178, 81–93. doi:10.1016/S0025-3227(01)00186-4

Raudikivi, A. J. (1988). The roughness height under waves. *J. Hydr. Res*., 26 (5), 569-584

Reesink, A.J.H., Bridge, J.S., 2007. Influence of superimposed bedforms and flow unsteadiness on formation of cross strata in dunes and unit bars. Sediment. Geol. 202, 281–296. doi:10.1016/j.sedgeo.2007.02.005

Reesink, A.J.H., Bridge, J.S., 2009. Influence of bedform superimposition and flow unsteadiness on the formation of cross strata in dunes and unit bars - Part 2, further experiments. Sediment. Geol. 222, 274–300. doi:10.1016/j.sedgeo.2009.09.014

Ribberink, J.S., Al-Salem, A.A., 1995. Sheet flow and suspension of sand in oscillatory boundary layers. Coast. Eng. 25, 205–225. doi:10.1016/0378-3839(95)00003-T

Ribó, M., Puig, P., Muñoz, A., Lo Iacono, C., Masqué, P., Palanques, A., Acosta, J., Guillén, J., Gómez Ballesteros, M., 2016. Morphobathymetric analysis of the large fine-grained sediment waves over the Gulf of Valencia continental slope (NW Mediterranean). Geomorphology 253, 22–37. doi:10.1016/j.geomorph.2015.09.027

Rubin, D.., McCulloch, D.., 1980. Single and superimposed bedforms: a synthesis of San Francisco bay and flume observations. Sediment. Geol. 26, 207–231

Ruessink, B.., Houwman, K.., Hoekstra, P., 1998. The systematic contribution of transporting mechanisms to the cross-shore sediment transport in water depths of 3 to 9 m. Mar. Geol. 152, 295–324. doi:10.1016/S0025-3227(98)00133-9

Ruessink, B.G., Michallet, H., Abreu, T., Sancho, F., Werf, J.J. Van Der, Silva, P.A., 2011. Observations of velocities , sand concentrations , and fluxes under velocity - asymmetric oscillatory flows. J. Geophys. Resear 116. doi:10.1029/2010JC006443

Sánchez-Arcilla, A., González-Marco, D., Bolaños, R., 2008. A review of wave climate and prediction along the Spanish Mediterranean coast. Nat. Hazards Earth Syst. Sci. 8, 1217–1228. doi:10.5194/nhess-8-1217-2008

Schoellhamer, D.H., Mumley, T.E., Leatherbarrow, J.E., 2007. Suspended sediment and sediment-associated contaminants in San Francisco Bay. Environ. Res. 105, 119–131. doi:10.1016/j.envres.2007.02.002

Schwab, W.C., Baldwin, W.E., Denny, J.F., 2014a. Maps showing the change in modern sediment thickness on the inner continental shelf offshore of Fire Island, New York, between 1996–97 and 2011, U.S. Geological Survey Open-File Report 2014–1238

Schwab, W.C., Baldwin, W.E., Denny, J.F., Hapke, C.J., Gayes, P.T., List, J.H., Warner, J.C., 2014b. Modification of the Quaternary stratigraphic framework of the inner-continental shelf by Holocene marine transgression: An example offshore of Fire Island, New York. Mar. Geol. 355, 346–360. doi:10.1016/j.margeo.2014.06.011

Schwab, W.C., Baldwin, W.E., Hapke, C.J., Lentz, E.E., Gayes, P.T., Denny, J.F., List, J.H., Warner, J.C., 2013. Geologic Evidence for Onshore Sediment Transport from the Inner Continental Shelf: Fire Island, New York. J. Coast. Res. 29, 526–544. doi:10.2112/jcoastres-d-12-00160.1

Schwab, W.C., Thieler, E.R., Denny, J.F., Danforth, W.W., 2000. Seafloor Sediment Distribution Off Southern Long Island , New York, U.S. Geological Survey Open-File Report 00-243

Scott, T., Masselink, G., Austin, M.J., Russell, P., 2014. Controls on macrotidal rip current circulation and hazard. Geomorphology 214, 198–215. doi:10.1016/j.geomorph.2014.02.005

Scott, T., Masselink, G., O'Hare, T., Saulter, A., Poate, T., Russell, P., Davidson, M., Conley, D., 2016. The extreme 2013/2014 winter storms: Beach recovery along the southwest coast of England. Mar. Geol. 382, 224–241. doi:10.1016/j.margeo.2016.10.011

Shepard, F. P., Submarine geology: Harper and Row, New York, 348 p. 1948

Simarro, G., Guillén, J., Puig, P., Ribó, M., Lo Iacono, C., Palanques, A., Muñoz, A., Durán, R., Acosta, J., 2015. Sediment dynamics over sand ridges on a tideless mid-outer continental shelf. Mar. Geol. 361, 25–40. doi:10.1016/j.margeo.2014.12.005

Smith, J. J., and P. L. Wiberg (2006), Ripple Geometry in Wave-Dominated Environments Revisited, paper presented at Eos Trans. AGU, 87(36), Ocean Sci. Meet. Suppl., Abstract OS35D-24

Snedden, J.W., Dalrymple, R.W., 1999. Modern Shelf Sand Ridges: From Historical Perspective To a Unified Hydrodynamic and Evolutionary Model. Soc. Sediment. Geol. 64, 13–28. doi:10.2110/pec.99.64.0013

Snedden, J.W., Tillman, R.W., Culver, S.J., 2011. Genesis and Evolution of a Mid-Shelf, Storm-Built Sand Ridge, New Jersey Continental Shelf, U.S.A. J. Sediment. Res. 81, 534–552. doi:10.2110/jsr.2011.26

Snedden, J.W., Tillman, R.W., Kreisa, R.D., Schweller, W.J., Culver, S.J., D. Winn, R.J., 1994. Stratigraphy and Genesis of a modern shoreface-attached Sand Ridge, Peahala Ridge, New Jersey. J. Sediment. Res. B64, N^{o}4, 560–581. doi:10.2110/pec.99.64.0147

Somoza, L., Barnolas, A., Arasa, A., Maestro, A., Rees, J.G., Hernandez-Molina, F.J., 1998. Architectural stacking patterns of the Ebro delta controlled by Holocene high-frequency eustatic fluctuations, delta-lobe switching and subsidence processes. Sediment. Geol. 117, 11–32. doi:10.1016/S0037-0738(97)00121-8

Somoza, L., Rodríguez-Santalla, I., 2014. Geology and Geomorphological Evolution of the Ebro River Delta, in: Landscapes and Landforms of Spain, World Geomorphological Landscapes. pp. 23–35. doi:10.1007/978-3-319-11800-0

Soulsby, R.L. 1997. Dynamics of marine sands. A manual for practical applications. Thomas Telford, London, ISBN 0-7277-2584-X

Soulsby, R.L., 2006. Simplified calculation of wave orbital velocities, in: Sand Transport in Oscillatory Flow. HR Wallingford, p. 12

Soulsby, R.L., Clarke, S., 2005. Bed Shear-stresses Under Combined Waves and Currents on Smooth and Rough Beds, Estuary Processes Research Project (Est Proc)/Defra project FD1905

Soulsby, R.L., Hamm, L., Klopman, G., Myrhaug, D., Simons, R.R., Thomas, G.P., 1993. Wave-current interaction within and outside the bottom boundary layer. Coast. Eng. 21, 41–69. doi:10.1016/0378-3839(93)90045-A

Soulsby, R.L., Whitehouse, R.J.S.,1997. Threshold of sediment motion in coastal environments.

In: Proceedings of the Pacific Coasts and Ports'97 Conference, Centre for Advanced Engineering, Christchurch,NZ, pp.149–154

Soulsby, R.L., Whitehouse, R.J.S., 2005. Prediction of Ripple Properties in Shelf Seas - Mark 1 Predictor (Report TR 150)

Soulsby, R.L., Whitehouse, R.J.S., Marten, K.V., 2012. Prediction of time-evolving sand ripples in shelf seas. Cont. Shelf Res. 38, 47–62. doi:10.1016/j.csr.2012.02.016

Southard, J.B., 1991. Experimental determination of bed-form stability. Annu. Rev. Earth Planet. Sci. 19, 423–455

Southard, J.B. & Boguchwal, L.A. 1990. Bed configurations in steady unidirec- tional water flows. Part 2. Synthesis of flume data. Journal of Sedimentary Petrology, 60, 658–679

Stahl, L., Koczan, J., Swift, D., 1974. Anatomy of a Shoreface-Connected Sand Ridge on the New Jersey Shelf: Implications for the Genesis of the Shelf Surficial Sand Sheet. Geology 2, 117. doi:10.1130/0091-7613(1974)2<117:AOASSR>2.0.CO;2

Sternberg, R., 2005. Sediment transport in the coastal ocean: a retrospective evaluation of the benthic tripod and its impact, past, present and future. Sci. Mar. 69 (Suppl-, 43–54. doi:10.3989/scimar.2005.69s143

Storms, J.E.A., van Dam, R.L. & Leclair, S.F. 1999. Preservation of cross-sets due to migration of current ripples over aggrading and non-aggrading beds: Comparison of experimental data with theory. Sedimentology, 46, 189–200

Stubblefield, W.L., Swift, D.J.P., 1976. Ridge Development as Revealed by Sub-Bottom profiles on the Central New Jersey Shelf. Mar. Geol. 20, 315–334

Styles, R., Glenn, S.M., 2005. Long-term sediment mobilization at a sandy inner shelf site, LEO-15. J. Geophys. Res. 110. doi:10.1029/2003JC002175

Swift, D.J.P., Duane, D.B., McKinney, T.F., 1973. Ridge and Swale Topography of the Middle Atlantic Bight, North America: Secular Response to the Holocene Hydraulic Regime. Mar. Geol. 15, 227–247

Swift, D.J.P., Field, M.E., 1981. Evolution of a classic sand ridge field: Maryland sector , North American inner shelf. Sedimentology 28, 461–482

Swift, D.J.P., Holliday, B., Avignone, N., Shideler, G., 1972. Anatomy of a Shoreface Ridge System, False Cape, Virginia. Mar. Geol. 12, 59–84

Swift, D.J.P., Parker, G., Lanfredi, N.W., Perillo, G., Figge, K., 1978. Shoreface-connected sand ridges on American and European shelves: A comparison. Estuar. Coast. Mar. Sci. 7, 257–273. doi:10.1016/0302-3524(78)90109-3

Thieler, E.R., Foster, D.S., Himmelstoss, E.A., Mallinson, D.J., 2014. Geologic framework of the northern North Carolina, USA inner continental shelf and its influence on coastal evolution. Mar. Geol. 348, 113–130. doi:10.1016/j.margeo.2013.11.011

Thorne, P.D., Davies, A.G., Bell, P.S., 2009. Observations and analysis of sediment diffusivity profiles over sandy rippled beds under waves. J. Geophys. Res. 144

Thorne, P.D., Hanes, D.M., 2002. A review of acoustic measurement of small-scale sediment processes. Cont. Shelf Res. 22, 603–632. doi:10.1016/S0278-4343(01)00101-7

Thorne, P.D., Hurther, D., 2014. An overview on the use of backscattered sound for measuring

suspended particle size and concentration profiles in non-cohesive inorganic sediment transport studies. Cont. Shelf Res. 73, 97–118. doi:10.1016/j.csr.2013.10.017

Torrence, C., Compo, G.P., 1998. A Practical Guide to Wavelet Analysis. Bull. Am. Meteorol. Soc. 79, 61–78

Traykovski, P., 2007. Observations of wave orbital scale ripples and a nonequilibrium time-dependent model. J. Geophys. Res. Ocean. 112. doi:10.1029/2006JC003811

Traykovski, P., Geyer, W.R., Irish, J.D., Lynch, J.F., 2000. The role of wave-induced density-driven fluid mud flows for cross-shelf transport on the Eel River continental shelf. Cont. Shelf Res. 20, 2113–2140. doi:10.1016/S0278-4343(00)00071-6

Traykovski, P., Hay, A.E., Irish, J.D., Lynch, J.F., 1999. Geometry, migration, and evolution of wave orbital ripples at LEO-15. J. Geophys. Res. 104, 1505–1524. doi:10.1029/1998JC900026

Trincardi, F., Normark, W.R., 1988. Sediment waves on the tiber prodelta slope: Interaction of deltaic sedimentation and currents along the shelf. Geo-Marine Lett. 8, 149–157. doi:10.1007/BF02326091

Trowbridge, J.H., 1995. A mechanism for the formation and maintenance of shore-oblique sand ridges on storm-dominated shelves. J. Geophys. Res. 100, 16071–16086. doi:10.1029/95JC01589

Urgeles, R., Cattaneo, A., Puig, P., Liquete, C., De Mol, B., Amblàs, D., Sultan, N., Trincardi, F., 2011. A review of undulated sediment features on Mediterranean prodeltas: Distinguishing sediment transport structures from sediment deformation. Mar. Geophys. Res. 32, 49–69. doi:10.1007/s11001-011-9125-1

van de Meene, J.W.H., van Rijn, L.C., 2000. The shoreface-connected ridges along the central Dutch coast-part 2: morphological modelling. Cont. Shelf Res. 20, 2325–2346. doi:10.1016/S0278-4343(00)00049-2

van den Berg, J.H., van Gelder, A., 1993. A new bedform stability diagram, with emphasis on the transition of ripples to plane bed in flows over fine sand and silt. Spec. Publs Int. Ass. Sediment. doi:10.1002/9781444303995.ch2

van der Werf, J.J., Ribberink, J.S., O'Donoghue, T., Doucette, J.S., 2006. Modelling and measurement of sand transport processes over full-scale ripples in oscillatory flow. Coast. Eng. 53, 657–673. doi:10.1016/j.coastaleng.2006.02.002

van Rijn, L. C. (1993). Principles of sediment transport in rivers, estuaries, and coastal seas, Aqua, Blokzijl, The Netherlands

van Rijn, L.C., 2007a. Unified View of Sediment Transport by Currents and Waves. I: Initiation of Motion, Bed Roughness, and Bed-Load Transport. J. Hydraul. Eng. 133, 649–667. doi:10.1061/(ASCE)0733-9429(2007)133:7(776)

van Rijn, L.C., 2007b. Simple General Formulae For Sand transport In Rivers, Esturies and Coastal Waters

van Rijn, L.C., 2007c. Unified View of Sediment Transport by Currents and Waves. II: Suspended Tranport. J. Hydraul. Eng. 133, 668–689. doi:10.1061/(ASCE)0733-9429(2007)133:7(776)

Venditti, J.G., Church, M., Bennett, S.J., 2005. Morphodynamics of small-scale superimposed sand waves over migrating dune bed forms. Water Resour. Res. 41, 1–14.

doi:10.1029/2004WR003461

Warner, J.C., List, J.H., Schwab, W.C., Voulgaris, G., Armstrong, B., Marshall, N., 2014. Inner-shelf circulation and sediment dynamics on a series of shoreface-connected ridges offshore of Fire Island, NY. Ocean Dyn. 64, 1767–1781. doi:10.1007/s10236-014-0781-y

Wiberg, P.L., Harris, C.K., 1994. Ripple geometry in wave-dominated environments. J. Geophys. Res. 99, 775–789. doi:10.1029/93JC02726

Wiberg, P.L., Nelson, J.M., 1992. Unidirectional flow over asymmetric and symmetric ripples. J. Geophys. Res. 97, 12745–12761. doi:10.1029/92JC01228

Williams, J.J., Rose, C.P., 2001. Measured and predicted rates of sediment transport in storm conditions. Mar. Geol. 179, 121–133. doi:10.1016/S0025-3227(01)00191-8

Wright, L.D., Boon, J.D., List, J.H., 1991. Models of cross-shore sediment transport on the shoreface of the Middle Atlantic Bight. Mar. Geol. 96, 19–51. doi:10.1016/0025-3227(91)90200-N

Wynn, R.B., Masson, D.G., 2008. Chapter 15 Sediment Waves and Bedforms. Dev. Sedimentol. 60, 289–300. doi:10.1016/S0070-4571(08)10015-2

Wynn, R.B., Stow, D. a V, 2002a. Recognition and interpretation of deep-water sediment waves: Implications for palaeoceanography, hydrocarbon exploration and flow process interpretation. Mar. Geol. 192, 1–3. doi:10.1016/S0025-3227(02)00546-7

Wynn, R.B., Stow, D.A. V, 2002b. Classification and characterisation of deep-water sediment waves. Mar. Geol. 192, 7–22. doi:10.1016/S0025-3227(02)00547-9

Yalin, M. S., 1964. Geometrical properties of sand wave. Journal of the Hydraulics Division. Vol. 90, Issue 5, pp. 105-119

Yan, B., Zhang, Q.-H., Lamb, M.P., 2010. Time-averaged turbulent mixing and vertical concentration distribution of high-density suspensions formed under waves, in: Coastal Engineering Proceedings. pp. 1–8. doi:10.9753/icce.v32.sediment.20

Yang, C.S., 1989. Active, moribund and buried tidal sand ridges in the East China Sea and the Southern Yellow Sea. Mar. Geol. 88, 97–116. doi:10.1016/0025-3227(89)90007-8

Yao, P., Su, M., Wang, Z.B., Chen, Y., 2015. High concentration layer over silt-sand mixtures under waves, in: E-Proceedings of the 36th IAHR World Congress 28 June – 3 July, 2015, The Hague, the Netherlands

Zhou, D., and Mendoza, C. 2005. Growth model for sand wavelets. J. Hyd. Engrg., ASCE, 131(10), 866-876